Aeolian geomorphodynamics in endorheic basins of the Mongolian Gobi Desert

D i s s e r t a t i o n

am Fachbereich Chemie, Pharmazie und Geowissenschaften
der Johannes Gutenberg-Universität Mainz

zur Erlangung des Grades
"Doktor der Naturwissenschaften"
im Promotionsfach Geographie
vorgelegt von

Nils Hannes Hempelmann

Mainz, 01.Juli 2010

Acknowledgment

First of all I would like to give my special thank to Prof. Dr. Jörg Grunert, my doctoral advisor, who was always trying to support me with all his possibilities. He gave me the chance to realize many of my ideas, as far as they have nothing to do with "human geography". Further more my special thank is directed to Prof. Dr. Franz X. Meixner, group leader in the Biogeochemistry Department of the Max Planck Institute for Chemistry. His always optimistic mood, the affinity to ambitioned ideas and his open mind was the essential combination to, at least, realizing this work. Also thanks Prof. Dr. Michael Bruse, for his willingness to supervise this thesis. His ultra quick e-mail reply with the very good qualitative answers was a very calming support.

Thanks to Thomas Felauer, Dr. Alexandra Hilgers and Daniela Hülle, the colleagues of the DFG project, for sharing ideas, the very helpful support by realizing some analysis and last but not least the good time we had together in Mongolia and at the few project meetings.

Thanks also to Dr. Kurt Emde, laboratory leader in the Geographical Department of the University of Mainz for the discussions, and the trust while I was working in the lab.

The helping hands in the laboratory and computer lab during the project of Janine Grossjean, Deborah Raulin (alias Debbi) and Lea Schneider for their benefit and the many questions reflecting the right way to focus in the target.

Thanks to Dr. Dariush Hinderberger laboratory leader at the Max Planck Institute for polymer research for his very kind authority to access the ESR applications.

A very special thank is dedicated to my colleague and friend Dr. Philippe Kersting for the interesting discussions, while loosing a game of boule or just spending so many time together in the same office.

Thanks to Prof. Dr. Dr. hc Michael Walther, who supported me in many questions of circumventing difficulties in Mongolia and moreover, for the great time we had together in the Gobi desert. Very special thanks are dedicated to Tschimgee Altangerel, Prof. Dr. Dechingungaa Dorjgotov, and Jugder Dulam for the excellent cooperation and support in Mongolia and for the possibility to find a scientific access to their great country.

I am deeply thankful to all that people helping, inspiring or encouraging me directly or indirectly to progress and complete this dissertation.

Abstract

The following thesis about actual aeolian geomorphodynamics in endorheic basins of the Mongolian Gobi desert was facilitated by the DGF Project "Late Holocene, Pleistocene and actual geomorphodynamics in endorheic basins of the Mongolian Gobi desert". The working area is situated in the south of Mongolia in the northern Gobi desert. Along with some Saharan sites (*Heintzenberg*, 2009), especially the Bodélé region in northern Chad (e.g. *Washington et al.*, 2006a; *Todd et al.*, 2006; *Warren et al.*, 2007) Central Asia is assumed to be a very important source area for particle emission into the global atmospheric system (*Goudie*, 2009). Explicitly the endorheic basins with their temporary lakes are source areas for particle emission and particle dispersion of their sediments.

The vulnerable bare soil of the dried out lake sediments in the endorheic basins is the main contributor of particle emission and their dispersion. In a geomorphological context of landscape development and the connectivity of the basin sediments to the hill slope depositions, as published in *Grunert and Lehmkuhl* (2004) based on ideas of *Pye* (1995), are numerical modelled.

The following study attempts to model the dust dispersion on a regional scale (simulation site 200x150 km) based on punctual sampling sites. The sampling sites represent the distinct geomorphological system parts assumed to be contributing to aeolian geomorphodynamic. The surface covered by pavement, typical for the Gobi region, and their surface sediment, focusing on the grain size distribution, were investigated.

Furthermore a 10 year time series (Jan 1998 to Dec 2007) of data of 32 Mongolian governmental weather stations was analyzed, with regards to the conditions of aeolian geomorphodynamics and parts of the data set used to perform the simulation. Additional atmospheric investigations focusing on the changing of atmospheric stability during night and day time with kite born measurements were done.

The values of the field investigations and the laboratory analyses as well as the time series of the Mongolian governmental weather stations and the kite borne atmospheric investigations were used as input parameter for the simulations. Particle emission for the sampling sites and their dispersion in a 3D diagnostic wind field afterwards were performed to model connectivity of basin sediments to the hill slope deposits.

In case of high mechanical turbulence in the atmospheric surface layer (i.e. high wind friction velocity (U*)) the atmospheric stability was determined as neutral in this period and particle emission and dispersion was calculated for this condition.

The calculation of the dust production was performed in a simplified particle emission model following

suggested models (*Laurent et al.*, 2006; *Darmenova et al.*, 2009; *Shao and Dong*, 2006; *Alfaro*, 2008). The 3D wind field calculation as well as the performed Lagrange simulation of aerosol transport was realized with the commercial programem LASAT®. This program is based on the Lagrange algorithm and calculates the dispersion and deposition of single particles in a stochastic possibility. The study is showing different particle concentrations in the near ground air masses and their deposition rates depending on the grain size in a spatial distribution.

A second part of this study is the investigation of the geochemical property of the distributed sediments of different sites in the area of interest. The geochemical properties should be used to track the simulated dispersion transects of particles in their spatial distribution. In case of the sediments the investigations show a relative homogeneity irrespective to different source areas or grain size fractions. Trace element investigations on single coarse sand grains with a laser application revealed only small variations depending on the different source regions. The mineral and elemental distribution pointing towards granite rock formations as being the sediment contributor. It was concluded that wide spread maphic and ultramaphic alkaline granitoides (*Jahn et al.*, 2009) are basically responsible for the sediment production. Beside the element investigations the quartz characteristic of the light mineral fraction was investigated focusing on the amount of quartz, crystallization of the quartz crystal grid and the electron spin resonance signal of the E'_1 -center in defect oxygen vacancies in the SiO_2 grid. The investigation follows studies of *Sun et al.* (2007) to determine fingerprints of sediments based on these values. The relative homogeneity was also detectable in these proxies.

Zusammenfassung

Die vorliegende Arbeit ist im Zuge des DFG Projektes ``Spätpleistozäne, holozäne und aktuelle Geomorphodynamik in abflusslosen Becken der Mongolischen Gobi´´ entstanden. Das Arbeitsgebiet befindet sich in der südlichen Mongolei im nördlichen Teil der Wüste Gobi. Neben einigen Teilen der Sahara (*Heintzenberg*, 2009), beispielsweise das Bodélé Becken des nördlichen Tschads (z.B. *Washington et al.*, 2006a; *Todd et al.*, 2006; *Warren et al.*, 2007) wird Zentralasien als ein Hauptliefergebiet für Partikel in die globale Zirkulation der Atmosphäre gesehen (*Goudie*, 2009). Hauptaugenmerk liegt hierbei besonders auf den abflusslosen Becken und deren Sedimentablagerungen.

Die, der Deflation ausgesetzten Flächen der Seebecken, sind hauptsächliche Quelle für Partikel die sich in Form von Staub respektive Sand ausbreiten. Im Hinblick auf geomorphologische Landschaftsentwicklung wurde der Zusammenhang von Beckensedimenten zu Hangdepositionen numerisch simuliert. Ein von *Grunert and Lehmkuhl* (2004) publiziertes Model, angelehnt an Ideen von *Pye* (1995) wird damit in Betracht gezogen.

Die vorliegenden Untersuchungen modellieren Verbreitungsmechanismen auf regionaler Ebene ausgehend von einer größeren Anzahl an einzelnen punktuellen Standorten. Diese sind repräsentativ für die einzelnen geomorphologischen Systemglieder mit möglicherweise einer Beteiligung am Budget aeolischer Geomorphodynamik. Die Bodenbedeckung durch das charakteristische Steinpflaster der Gobi - Region, sowie unter anderem Korngrößenverteilungen der Oberflächensedimente wurden untersucht. Des Weiteren diente eine zehnjährige Zeitreihe (Jan 1998 bis Dez 2007) meteorologischer Daten als Grundlage zur Analyse der Bedingungen für äolische Geomorphodynamik. Die Daten stammen von 32 staatlichen mongolischen Wetterstationen aus der Region und Teile davon wurden für die Simulationen verwendet. Zusätzlich wurden atmosphärische Messungen zur Untersuchung der atmosphärischen Stabilität und ihrer tageszeitlichen Variabilität mit Mess-Drachenaufstiegen vorgenommen.

Die Feldbefunde und auch die Ergebnisse der Laboruntersuchungen sowie der Datensatz meteorologischer Parameter dienten als Eingangsparameter für die Modellierungen. Emissionsraten der einzelnen Standorte und die Partikelverteilung im 3D Windfeld wurden modelliert um die Konvektivität der Beckensedimente und Hangdepositionen zu simulieren.

Im Falle hoher mechanischer Turbulenz der bodennahen Luftschicht (mit einhergehender hoher Wind Reibungsgeschwindigkeit), wurde generell eine neutrale Stabilität festgestellt und die Simulationen von Partikelemission sowie deren Ausbreitung und Deposition unter neutraler Stabilitätsbedingung berechnet.

Die Berechnung der Partikelemission wurde auf der Grundlage eines sehr vereinfachten Emissionsmodells in Anlehnung an bestehende Untersuchungen (*Laurent et al.*, 2006; *Darmenova et al.*, 2009; *Shao and Dong*, 2006; *Alfaro*, 2008) durchgeführt. Sowohl 3D Windfeldkalkulationen als auch unterschiedliche Ausbreitungsszenarien äolischer Sedimente wurden mit dem kommerziellen Programm LASAT® (Lagrange-Simulation von Aerosol-Transport) realisiert. Diesem liegt ein Langargischer Algorithmus zugrunde, mittels dessen die Verbreitung einzelner Partikel im Windfeld mit statistischer Wahrscheinlichkeit berechnet wird. Über Sedimentationsparameter kann damit ein Ausbreitungsmodell der Beckensedimente in Hinblick auf die Gebirgsfußflächen und -hänge generiert werden.

Ein weiterer Teil der Untersuchungen beschäftigt sich mit der geochemischen Zusammensetzung der Oberflächensedimente. Diese Proxy sollte dazu dienen die simulierten Ausbreitungsrichtungen der Partikel aus unterschiedlichen Quellregionen nach zu verfolgen. Im Falle der Mongolischen Gobi zeigte sich eine weitestgehende Homogenität der Minerale und chemischen Elemente in den Sedimenten. Laser Bebohrungen einzelner Sandkörner zeigten nur sehr leichte Unterschiede in Abhängigkeit der Quellregionen. Die Spektren der Minerale und untersuchten Elemente deuten auf graitische Zusammensetzungen hin. Die, im Untersuchungsgebiet weit verbreiteten Alkali-Granite (*Jahn et al.*, 2009) zeigten sich als hauptverantwortlich für die Sedimentproduktion im Untersuchungsgebiet. Neben diesen Mineral- und Elementbestimmungen wurde die Leichtmineralfraktion auf die Charakteristik des Quarzes hin untersucht. Dazu wurden Quarzgehalt, Kristallisation und das Elektronen-Spin-Resonanz Signal des E'_1 -Centers in Sauerstoff Fehlstellungen des SiO_2 Gitters bestimmt. Die Untersuchungen sind mit dem Methodenvorschlag von *Sun et al.* (2007) durchgeführt worden und sind prinzipiell gut geeignet um Herkunftsanalysen durchzuführen. Eine signifikante Zuordnung der einzelnen Quellgebiete ist jedoch auch in dieser Proxy nicht zu finden gewesen.

Abbreviation

asl above sea level

ASTER advanced spaceborne thermal emission and reflection radiometer

b intersection ground level

CI crystallinity index

DEM digital elevation model

DFG Deutsche Forschungsgemeinschaft

D_p particle diameter

E fraction of erodible surface

ESR electron spin resonance

F_h saltation flux

F_p particle emission flux

$F_{(gen)}$ generalized particle emission flux

fS fine sand (germ. Feinsand)

f frequency

FWHM full width at half maximum

g acceleration of gravity

GPS geographical positioning system

$H_{(w)}$ water content correction

h_a height of the anemometer above ground

ICP Inductively Coupled Plasma

IPCC Intergovernmental Panel of Climate Change

k v. Kármán constant

L lagrange function

LASAT® Lagrange simulation of aerosol transport

m gradient

MARCC Mongolia: Assessment report on climate change

mS middle sand (germ. Mittelsand)

MS mass spectrometer

N_i dust number flux

PEM particle emission model

$R_{(z0,z0s)}$ drag partition correction

REE rare earth element

RFA X–ray fluorescence analyse

ρ_a air density

SEM Scanning electron microscope

SRTM shuttle radar topography mission

U wind velocity

U* wind friction velocity

U_t^* threshold friction velocity

TA Luft Technical Instructions on Air Quality Control (Technische Anleitung zur Reinhaltung der Luft)

TOMS total ozone mapping spectrometer

v_{s-n} south-north component of wind speed

v_{w-e} west-east component of wind speed

W water correction

WMO World Meteorological Organisation

$\bar{x}$ arithmetric averages

XRD X–ray diffractometry

z_0 roughness length

α wind direction

τ time period

v_d deposition velocity

List of Figures

List of Tables

Contents

1. Introduction

High atmospheric dust loadings in Central and Eastern Asia cause reduction of life quality and even the risk of serious health problems (*Jäkel*, 2006); hence, they generate the necessity to investigate the process-interaction of sand and dust transport mechanisms. Supplementary, this part of the environmental process-interaction is leading to general scientific importance. The process interaction of particles in motion, generates uncertainties due to the relationship of certain components of the geomorphological system.

This work thesis has been made within the context of the DFG Project "Late Pleistocene, Holocene and actual geomorphodynamics in endorheic basins of the Mongolian Gobi desert". It was a cooperation project between the Geographical Department of the RWTH Aachen, Geographical Department of the University of Cologne, the Geographical Department of the University of Mainz, and the Geographical Institute of the Mongolian Academia of Science in Ulaanbaatar and investigates the landscape development in the Gobi desert with their surrounding mountain ranges. While the geographical departments of Aachen and Cologne are working on the Pleistocene and Holocene environmental conditions, this thesis is dealing with the actual processes in the context of landscape development, basically aeolian geomorphology. The thesis is a suggestion of combining computer based simulation modeling with field investigations and laboratory analyses. Figure 1.1 shows the relation of the distinct parts.

The following work focuses on the **"actual aeolian geomorphodynamics in endorheic basins of the Mongolian Gobi desert"** to fill uncertainties of the process interaction within the different geomorphological system parts. A dust dispersion model published by *Grunert and Lehmkuhl* (2004) based on the ideas of (*Pye*, 1995) assumed an interaction of basin sediments and hill slope depositions which is now simulated with a Lagrange simulation of aerosol transport (LASAT®) in this thesis. To simulate the particle dispersion, the particle emission (fig.: 1.2) from different sampling sites was estimated. A suggested generalized particle emission flux ($F_{(gen)}$) (*Shao*, 2004) was modified by the sampling site condition and a particle emission flux (F_p) was calculated for each site. The particle emission, meteorological parameter and additional informations (e.g. the digital elevation model (DEM)) generates the input parameter to

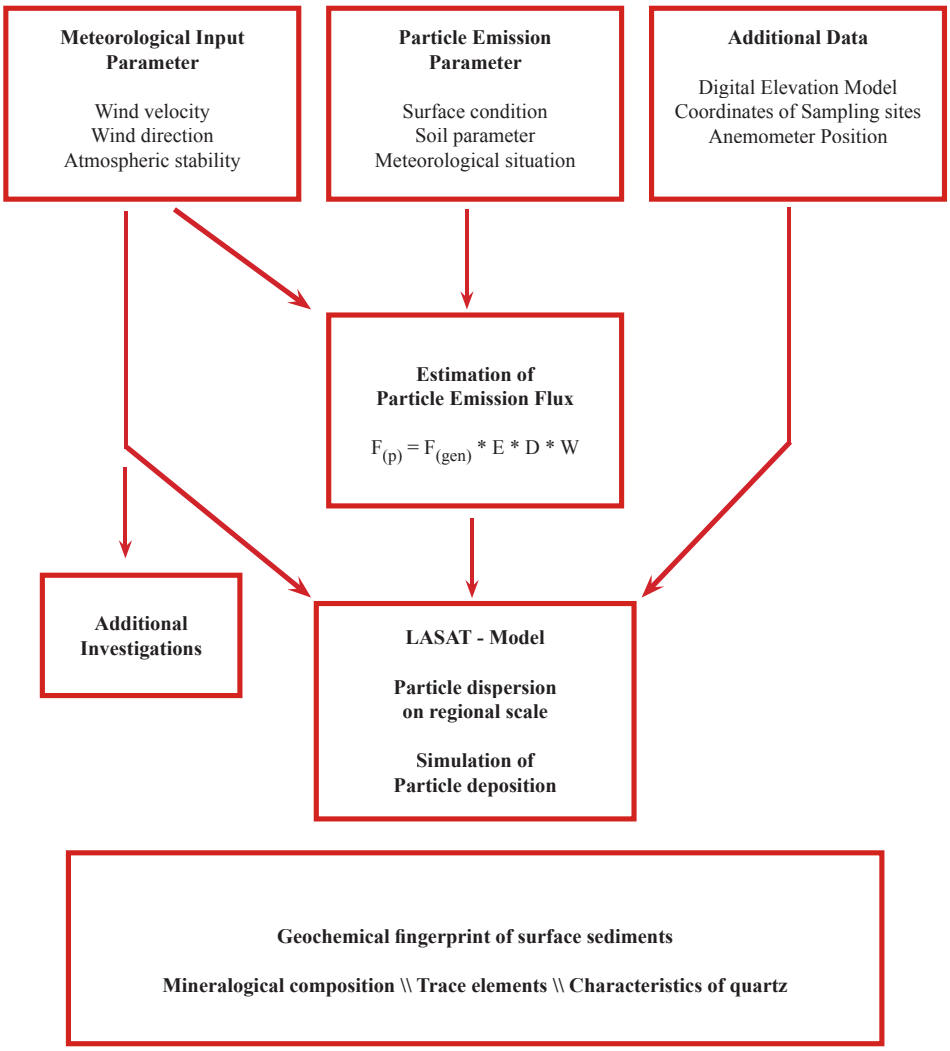

Fig. 1.1.: Concept of the thesis

calculate particle dispersion and spatial distributed particle deposition. Four field expeditions have been done to sample surface sediments and field informations in August 2007, April and August 2008 and August 2009.

The necessary meteorological input parameter comes from a data set of 32 meteorological stations situated in the Mongolian Gobi and was investigated focusing on general conditions in the Mongolian Gobi desert. The investigations were done as additional information and to prove the data base of the Mongolian governmental meteorological stations due to their quality. The values of one station were taken as input data (basically wind direction and wind velocity) to model the dust dispersion exemplary on regional scale (150 x 200 km simulation site).

Furthermore it was tried to determined the simulated results by geochemical properties of the sediments in the assumed source region. These geochemical properties should be used as fingerprint to track the simulated particle dispersion. The assumed and simulated connectivity of basin and hill slope sediments should be underlined by tracking of a specific finger print. Heavy mineral determination and the amount and distribution of trace elements were used to identify differences of the several sources. The mineral spectrum was surprisingly homogeneous and pointing towards plutonic rock formations as being responsible for the particle production in the area of interest. Therefore further investigations were done to identify differences of several assumed sources. These investigations were focusing on the content of quartz in a qualitative and quantitative way. The total amount of quartz of the light mineral fraction, their crystallinity index (CI) and the electron spin resonance (ESR) were determined and coupled to separate the different sources as well. It proved to be, that the sediments of different sources as well as separated to the grain size fractions, were also very similar based on their geochemical characteristics.

Irrespective of the very complex geological formations, the main contributors to particle production are plutonic alkaline granites with a high amount of feldspar regardless of source area and grain size. Also the ESR and crystallinity are not pointing towards a significant cluster. Thus, the geochemical characteristic of the quartz content seems not to be different for the several subsamples, the ESR lines showing uncertain differences hinting at investigation possibilities of probably significant signal differences of the electron spin resonance of the quartz content.

Thus, the initial idea to validate the simulation based on the tracking of the geochemical fingerprint failed. The detailed description of the sediment character was identified the wide spread plutonic alkaline feldspar granites (*Helo et al.*, 2006) as the main contributor to sediment production in the Mongolian Gobi region. Therefore the investigations could resolve several other uncertainties in process understanding or other laboratory applications like problems of performing the OSL dating of sand sediments (*Hülle et al.*, 2009).

1.1. State of the art

Aeolian geomorphological processes are the initial phase for sand and dust storm development (*Livingstone and Warren*, 1996; *Livingstone et al.*, 2007). Particles in the global atmospheric system are leading to several uncertain processes including radiative forcing or biogeochemical cycling (**?**)Goudie2008).

Especially during the spring in March, April and May while the meteorological situation favours the development of sand and dust storms by cyclonal cold fronts (*Natsagdorj et al.*, 2003) translocation of

Fig. 1.2.: Particle emission of the Orog Nuur lake basin

different grain sized particles is responsible for aeolian geomorphodynamics. The occurrence of sand and dust storms and their spatial and temporal distributions for Central Asia has been published not only for Central Asia (e.g. *Wang et al.*, 2008b) as well as for the Aral region (e.g. *Darmenova and Sokolik*, 2007) or the huge SAMUM project focusing on Saharan sites (*Heintzenberg*, 2009) but also for several other sites in a global distribution (e.g. *Hugenholtz et al.*, 2009).

Several investigations based on satellite remote sensing (*Chung et al.*, 2003; *Kinoshita et al.*, 2005; *Lee and Sohn*, 2009), are a common technique to monitor sand and dust store events. Dust as an aerosol in the atmospheric processes has high importance in context of chemical processes. The total ozone mapping spectrometer (TOMS) is indicating that most of the mineral dust sources are situated in the norther hemisphere (e.g. *Prospero et al.*, 2002; *Jones and Christopher*, 2007).

Beside the satellite investigations, ground based observations (e.g. *Mukai et al.*, 2005) are a common way to report aeolian geomorphodynamic. Weather stations of the Mongolian government are reporting dust storm events; corresponding investigations predict an increasing frequency in Mongolia (see, Mongolia: Assessment report on climate change (MARCC) (*Dagvadorj et al.*, 2009) or Intergovernmental Panel of Climate Change (IPCC) (*on Climate Change*, 2007). Field observations can also be done experimentally with transportable wind tunnels (e.g. *Fister and Ries*, 2009) or by laser particle counters (*Mikami et al.*, 2005). The increasing dust storms have also several socioeconomic effects (*Batjargal et al.*, 2006) as well as high agricultural effects and connections sink areas (*Hoffmann et al.*, 2008). The connection between source and sink and the exact atmospheric transects can be estimated by trajectory calculations (e.g. *Kim*, 2008; *Vandenberghe et al.*, 2006) of air mass movements.

To identify the dust sources and connect them with potential sinks geochemical fingerprints are made or searched for in the assumed source areas. Geochemical analyses of source areas or airborne dust in China, Korea and Japan are done by focusing REE, Isotopes (Sr, Rh, Pb or Ne) as well as the coupling

of ESR and crystalinity index (*Nagashima et al.*, 2007; *Sun*, 2002; *Sun et al.*, 2007, 2008).

Further more it was tried to calculate dust emission and atmospheric distribution based on numerical models. Several dust emission models have been developed or improved in Saharan (*Laurent et al.*, 2008) and Central Asians regions (*Wang et al.*, 2000) or existing calculations were verified and validated by field experiments (*Mei et al.*, 2006).

For a general geomorphological process understanding of sediment budgets the links between basin and hill slope sediments are of relevant interest (*Livingstone et al.*, 2007; *Washington et al.*, 2006b). The model of assumed basin hill slope sediment interaction published by *Grunert and Lehmkuhl* (2004) in a study case of West Mongolia were based on ideas from *Pye* (1995).

2. Regional setting

Mongolia is extending from N 52°08′ to 41°34′ latitude and from E 87°45′ to 119°55′ longitude in Central Asia (fig. 2.2) and its territory comprises 1.566 000 km^2, which is 1.2% of the land surface in the world. It is a mountainous country with an relatively flat area in the east.
In the western and central parts, several mountain ranges are dividing the Mongolian plateau with altitudes up to more than 4000m asl. They are running north-west to south-east (e.g. the Mongolian Altai, the Gobi Altai, Gurvan Saichan, Khangai etc).

Fig. 2.1.: Study site at Nugin Els Dune field. Baga Bogd Mountain in the background

The Gobi desert in the southern part of Mongolia, were the working area is situated, occupies a third of the country (*Barthel et al.*, 1962). With a population density of 1,7/km^2, Mongolia is the least populated country of the world. More than 50% of the people are residential in the capital city Ulaanbaatar, with an increasing tendency (*Kahl*, 2007). Excluding Ulaan Baator, a population density less than one per km^2 is given, and even more sparsely in the desert regions of the Mongolian Gobi. Typical for the region of interest is a relative high relief energy (fig. 2.1) superimposed on a highland plateau more than 1000m above sea level (*Haase*, 1983). Due to the geographical location of Mongolia, the several mountain ranges and the continental climate, the variety of the vegetation zones reaches from taiga in the north to desert in the arid and hyper arid regions in the south.

2.1. Environmental characteristics of the Mongolian Gobi

According to the definitions of *Haase* (1983), the sample sites and simulation areas are situated in south eastern part of the Valley of the Great Lakes, the Gobi Altai range with the Gurvan Saykhan as its most eastern part. Foothills and the depressions of the Transaltai Gobi are included. Generally this regions is, due to the long distance from the sea, characterized by extreme continental conditions. High seasonal temperature and precipitation variations can be recorded. Furthermore, the continental conditions and the orographic surrounding mountains are causing aridity and hyper aridity. Precipitation is generally expectable in summer during the influence of the Indian (SW) and Chinese (SE) monsoon (compare chapter 2.1.2).

The dust storm appearance in the area of interest is mentioned to 20-30 and even more than 30 stormy days per year (*Natsagdorj et al.*, 2003).

The occurrence of geological rock formations at the surface is covering a timespan from the Archaicum up to now. Generally the landscape development is better investigated in the norther and western part of Mongolia (e.g. *Schwanghart et al.*, 2009) and less investigated in the area of interest. Even the landscape development during Pleistocene and Holocene can only be reconstructed with uncertainties.

A major factor of landscape development are the presence and their causing influence of human activity. Especially in sensitive ecosystems vegetation and soil surface can be dramatically changed by the presence of herders (*Wesche et al.*, 2001). The detectable anthropogenic influence was concluded in eastern Tibet by *Schlütz and Lehmkuhl* (2009) as a so called "nomadic anthropocene" which can be divided in three phases around 12,700–10,400 cal yr B.P. for flat basins; 7000–5000 cal yr B.P. for the main valley floors; and 3000–1000 cal yr B.P. for the higher terrace surfaces. It also can be assumed with variations for the Mongolian Gobi region.

A gradient of landscape variation in the working area from the Valley of the great lakes in the north to the Transaltai Gobi is perceptible from desert steppe to hyper arid desert (*Dill et al.*, 2006).

Focusing estimates of dust sources, small lake basins (e. g. the Orog Nuur Lake basin) can be assumed to be responsible for dust emission (*Koren et al.*, 2006; *Laurent et al.*, 2008; *Zhang et al.*, 2008, e.g.) as well as the pediments and alluvial fans (*Wang et al.*, 2008a, e.g.).

Beside the always present weathering processes as the initial phases for sand and dust production an actual desertification trend (*Batkhishig and Lehmkuhl*, 2003) increases the vulnerability of the surface by increasing the covering vegetation. The desertification trend, which can be reported globally is much stronger in the Central Asian region (*on Climate Change*, 2007), the increasing of the herders activity

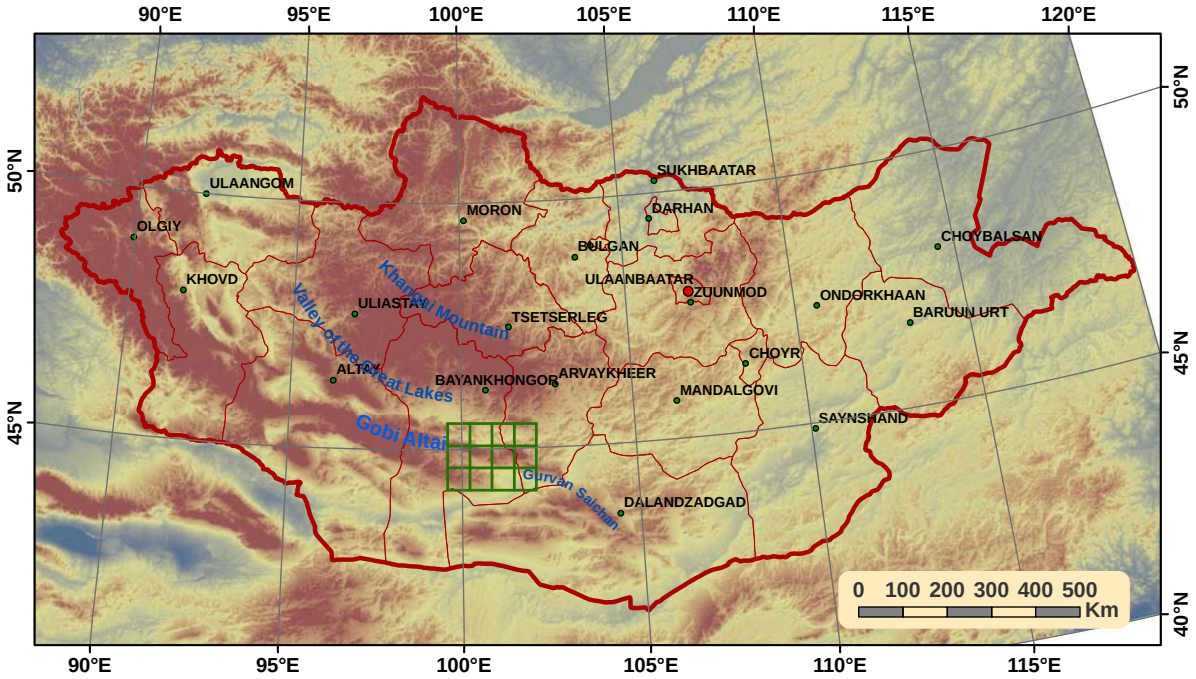

Fig. 2.2.: Shape of Mongolia with the capital City Ulaanbaatar. Area of the dust distribution simulation in green.

intensify that trend.

Due to the high annual climatic variability the periodical occurrence of hazard years (so called Dtzud) are regulating the amount of cattle (*Wehrden and Wesche*, 2007). *Wesche and Retzer* (2005) scrutinized the degradation in the Gobi region as a major problem in semi-desert environments.

2.1.1. Geology

The geological situation in Mongolia is due to the very old surface and the tectonic activity very complex. In the area of interest Upper Archean and Lower Proterozoic polymetamorphic complexes are included as the oldest stratified geological formations found in the Gobi area. These are mainly consisting of quartzite-marble-gneiss (*Badarch et al.*, 2002). Remarkable primary marine Riphean sedimentary deposits such as quartz-albite-chlorite and albitemuscovite schist and sandstone-carbonite-quartzite are also distributed in the study area and belonging to the Icht Bogt, Baga Bogt (*Vassallo et al.*, 2007) complex and in the Gobi-Altai mountain range of the Gobi area (*Lamb et al.*, 2008).

The study area is also representing one of the biggest part of Ordovician and Silurian deposits distributed in Mongolia (*Kozakov et al.*, 2008). It includes a volcanogenic-tuffite member, containing andesite,

andesite-basalt lava, tuff and tuffaceous-sedimentary rocks. Occurence in the Gurvan Seichan Montains and the mountain range of Nemengt Uul as well as reef limestone and carbonate–volcanogenic or Low Devonian deposits of the Ehiin gol suite are distributed in the Gobi Tenger mountain can be seen as schistose sandstone, siliceous siltstone, red chert and sometimes effusive and a lenses of limestone with the remains of brachiopods and crinoids (*Badarch et al.*, 2002).

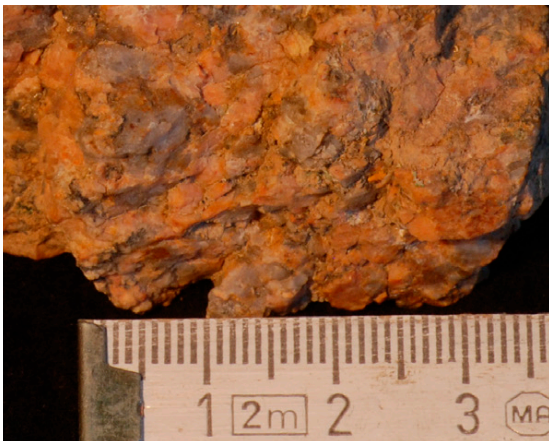

Fig. 2.3.: Alkaline Granite

Middle Devonian deposits in the Gobi Altai, the 600-700 m thick Togoot suite is predominantly composed of limestone sandstone and siltstone, and intermediate volcanic rocks.

Some sites in the study area are representing Carboniferus rocks (Bajanbuurun depression and Gurvan Seichan Montains) which are consisting of various subarial volcanic rocks, tuffs, sandstone and siltstone. In the southern part of the Gobi, flysch-terrigenous Permian deposits are distributed.

Due to aeolian geomorphodynamic one of the most important rock formations are the Mesozoic-Cenozoic stratified deposits. They are mainly concentrated in the variously formed and sized superimposed basins, depressions and valleys, located in the Gobi part (*Cari*, 2004). Triassic deposits are presented by continental molasse series. Jurassic deposits consist of continental deposits, which are composed of brown red, red and sometimes variegated coarse breccia, conglomerate and sandstone. In the depressions of many valleys of the Gobi, siltstone, sandstone, gravel and gravel stone of the Sharil formation are distributed.

Beside the very important middle and upper Mesozoic sedimentary rock formations in the depressions of the Gobi region, Cenozoic deposits are widespread mainly all over Mongolia (*Badarch et al.*, 2002). In many cases polymethamorphic sedimentary and volcanic rocks (*Dobrezow*, 1992), intrusive rock formations play an important role due to aeolian geomorphodynamic in the study area. In case of the Gobi region, Carboniferous intrusive rocks are widespread. Permian granites can be found in the Gobi Altai Montains of Shin Jinst (*Johnson et al.*, 2007). Mostly basement rocks of alkaline and alkalineous granites comprises the rock complexes (*Kovalenko et al.*, 2007). In case of the Khan Bogt (south of Dalanzadgat) the pluton is controlled by an intersection of the Gobi – Tien Shan Rift Zone and consists of alkali granite association (fig. 2.3). It is proposed, that this pluton formations was a hot spot in the paleoocean during

the collision of the Hercynian continent (*Kovalenko et al.*, 2006)

2.1.2. Climate

The paleoclimate was reconstructed based on tree ring analysis (e.g. *Jacoby et al.*, 1996, 1999) and concluded an increasing of temperature. The longest tree ring series over more than 1700 years is showing an increased temperature for the past 100 years (*Pederson et al.*, 2001) also the 20^{th} century is the warmest century of all in that proxy.

In present times the systematic meteorological observations began in the early 1940s (*Batima*, 2006). The actual climate in the area of interest is characterized by a very high seasonal and annual variability. Summer is dominated by monsoon influence with a surface pressure of more than 1.035hPa (i.e. global maximum for this altitude level) is causing frequent clear skies and high atmospheric stabilities.

During winter a very stable anticyclone over Siberia with more than 1.035hPa (globally maximum due to this altitude) is causing clear sky and a very high atmospheric stability with calm days and rare snowfall. Also because of the absence of clouds absolute minima of temperature can be recorded (*Harmel*, 2010). The World Meteorological Organisation (WMO) station in Dalanzadgad (operated by the Mongolian government)registered -13,5řC mean temperature in January. (Data were collected from the climatological data base, which operates in the Institute of Meteorology and Hydrology; they were provided to the project for the period Jan 1998 – Dec 2007; compare chapter 3.3).

Beside low temperatures the winter is characterized by very low precipitation rates; >5mm mean total precipitation for Dec, Jan, Feb. in Dalanzdgad (*Harmel*, 2010). Generally snow contributes less than 20% to total annual precipitation total annual precipitation (*Batima*, 2006).

Depending on the ecliptic of the earth causing a shifting of the jet stream during the year and the destabilization of the Siberian anticyclone in spring because of higher convections caused by rising soil surface temperatures, the westerlies are more and more dominating the atmospheric weather conditions. Connections with the arctic oscillation can also be recorded by the occurrence of storms (a shifting from south to north) during spring time (*Han et al.*, 2008b). It is the most active time for aeolian activities. The mean wind speed increases to maximum more than 15 – 20 m/sec. Protected only by a partiand thin snow cover the dried out soils and lake basins are very vulnerable for wind deflation (*Kimura and Shinoda*, 2010).

Summer is influenced by the weak tails of Chinese (SE) or Indian (SW) monsoon. These air masses are

loaded with higher humidity. About 85% of the total precipitation falls from April to September, about 50-60% of which falls in July and August. Only 50 – 100 mm of annual precipitation can be registered in the Gobi Desert (*Batima*, 2006); and even less in the South–West of the working area. Although annual precipitation is low, its intensity can be high. Local intense rainstorms with 40-65 mm precipitation in a single hour is recorded. The absolute daily maximum precipitation of 138 mm recorded since 1940 occurred on 5 August 1956 at Dalanzadgad, and 121 mm/day on 11 July 1976 at Sainshand, both village centers are located in the Gobi Desert area.

In modelled future scenarios climate of Mongolia is generally getting warmer and slightly drier. For the Gobi regions the rate of winter warming varies from 0,9K to 8,7K, while the summer temperature increase varies from 1,3K to 8,6K. Furthermore the precipitation will increase basically in winter by between 12.6 -119 %, while the summer rainfall decreses in a variety from 2.5% to 11.3% (*Batima*, 2006). Dryer summer are causing a higher vulnerability of the surface in context of eolian activity. In observation studies about the the variability of dust storms an increasing of such storm events are recorded (e.g. *Dulam*, 2005; *Fu et al.*, 2008; *Goudie*, 2009; *Han et al.*, 2008a). This tendencies were also recognized in some variations by the local nomadic herders (*Marin*, 2010).

2.1.3. Soil surface

The soil surface in the area of interest is basically characterized by the relief, the geology and the actual climatic conditions. Pedogenetic processes vary basically due to the altitude. The resulting soil types are shown in the digital soil map of Mongolia. The data were provided by the Geographical Department of Mongolia, Ulaanbaatar in 2008 and the soil distribution in the working area can be visualized (Fig. A.4). The soil type determination is based on the Russian taxonomy (*Vostokova et al.*, 1995). Main soil types can be classified as govi brown, semi desert brown and desert gray brown soil. *Haase* (1983) determined this areas as Burosems (in variation typical or light). For FAO determination this soils are generally classified as calcisols.

In the mountainous regions kastanozems in different variations can be found. Also inter zonal areas of Takyr and Solonchaks (variation: Solonetz) are developed in the basin regions. Furthermore, sandy regions without detectable pedogenetic processes are distributed. Due to actual geomorphological activity, the most important issue is the condition of the soil or sediment surface (*Alfaro*, 2008). The surface of the Gobi desert is characterized by the presence of gravel. These pavement can be found in different variations. Four soil surfaces types were classified by *Wang et al.* (2008a) depending on its density of the

pavement. The different geomorphological system parts varies on their soil surface types. All of these four types, from open bare soil to highly protected sediment, can be found in the study area.

There is a quite controversy discussion about the contribution of different surfaces to the dust emission. While *Wang et al.* (2008a) focuses on the large pediments and alluvial fans *Zhang et al.* (2008) concluded, based on remote sensing methods,that single spots, like dried out lake sediments are responsible for dust development.

2.2. Area of surface investigations

More than 60 surface samples have been taken in the area of interest during four field expeditions (Aug 2007, April 2008, Aug 2008 and Aug 2009 fig. A.5). It was tried to cover up the different geomorphological system parts in a sampling scheme. The whole study area can be divided into several subareas: The Orog Nuur Lake basin north of the Altai Gobi Mountains Icht Bogd and Baga Bogd. In the east of the Orog Nuur Lake the dune field Nugin Els is situated. The river Tuin Gol in the north of the Orog Nuur Lake Basin is draining large parts of the Khangai mountains situated in the north of the area of in-

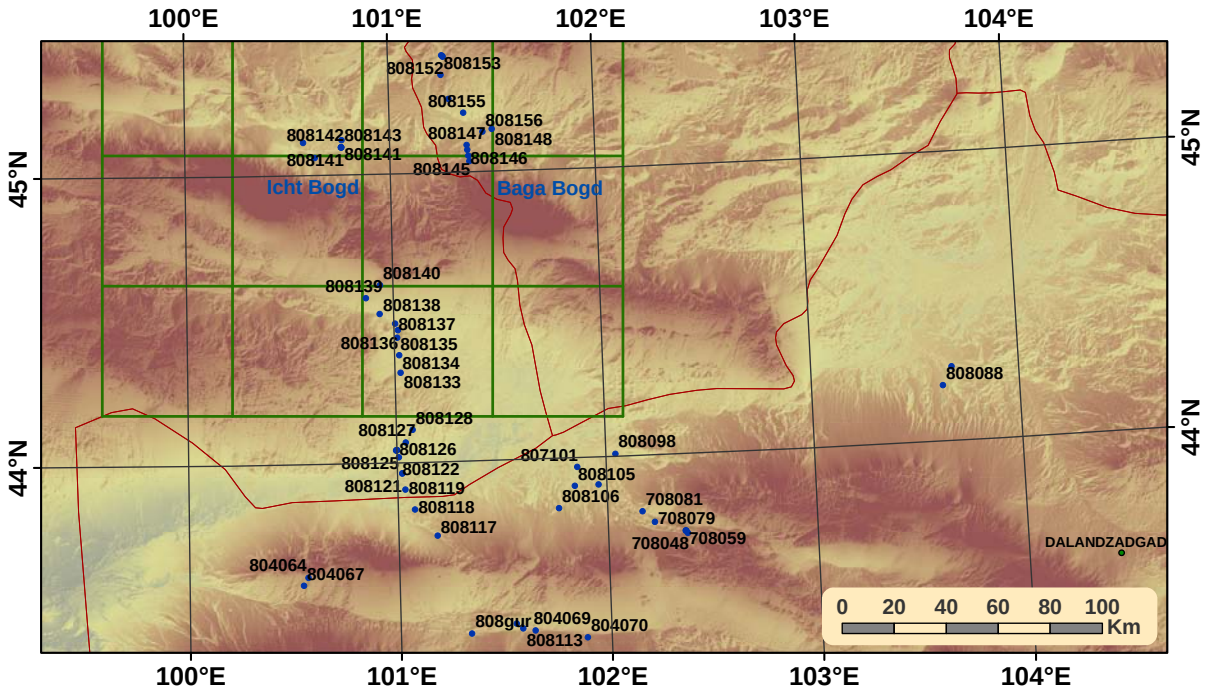

Fig. 2.4.: Sampling sites in the area of interest. Blue points are marking sampling sites

terest. An other river, the Tazin Gol, also with a catchment area of large parts in the Khangai mountains is situated north of the Nugin Els and is draining into the very small lake Tasin Tzagnan Nuur. South of the Altai Gobi Mountains Icht Bogd and Baga Bogd a wide depression ($\approx 200 km\emptyset$) is situated. Samples were taken in all these areas (Fig. 2.4). In a systematically taken transect in the large depression, every 7 – 10 km following a S - N direction 16 samples were taken. Due to the difficult road conditions the transect is situated near the western margin of the basin. Furthermore few samples where taken in the center as well as at sites of the eastern part of the basin. Here the beginning of the huge dune field Khongoryn Els is situated. Furthermore samples south of the Nemegt Uhl Mountain complex were taken. The Orog Nuur Lake basin with the Nemegt Uhl Dune field and the surrounding area is a main study area and taken as the exemplary simulation region to model the particle dispersion. Several surface samples were taken from different geomorphological system parts. Additionally, bottle traps were placed in a transect with high resolution ($\approx 300m$) in the west, and assumed main wind ward direction. The transect is starting from in the center of the valley and running up to the beginning of the alluvial fan of the Icht Bogt mountain. Additionally three samples were taken from the dried out Ulan Nuur basin southwest of Mandal Ovoo Sum center.

2.3. Numerical simulation area

The topographical situation around the mountain complexes Icht Bogd (3957m asl) and Baga Bogd (3590m asl) was used for modeling the particle dispersion on a regional scale (fig.: 2.5). A pass between Icht Bogd (to the west) and Baga Bogd (to the east) is connecting both mountains in an altitude of 1633m asl. In the northern foreland the Orog nuur lake basin (1216m asl) is situated. Furthermore the Nugin Els dune field is situated north of Baga Bogd, were the Tasin gol drain into the Tasin Tzagnan Nuur lake (1235m asl). Southward of the mountain range big alluvial fans are bordered by a large depression. Three sum centers with Mongolian governmental weather stations including anemometers are situated in the simulation area. They are symbolized in the figure as gray towers. Baruunbayan-Ulaan (ID 45201400; 1242m asl) north of the Tasin Tzagnan Nuur lake, Bogt Horiult (ID 45200800, 1308m asl) north of the Orog Nuur lake and Bajangovi (ID 44702200, 1570m asl) at the western margin of the wide depression south of the mountain Icht Bogt.

A SRTM DEM of these area was taken in a square of 150 x 200km. Following the work flow to perform the particle dispersion simulation with LASAT®, the terrain profile was converted into a text file to be

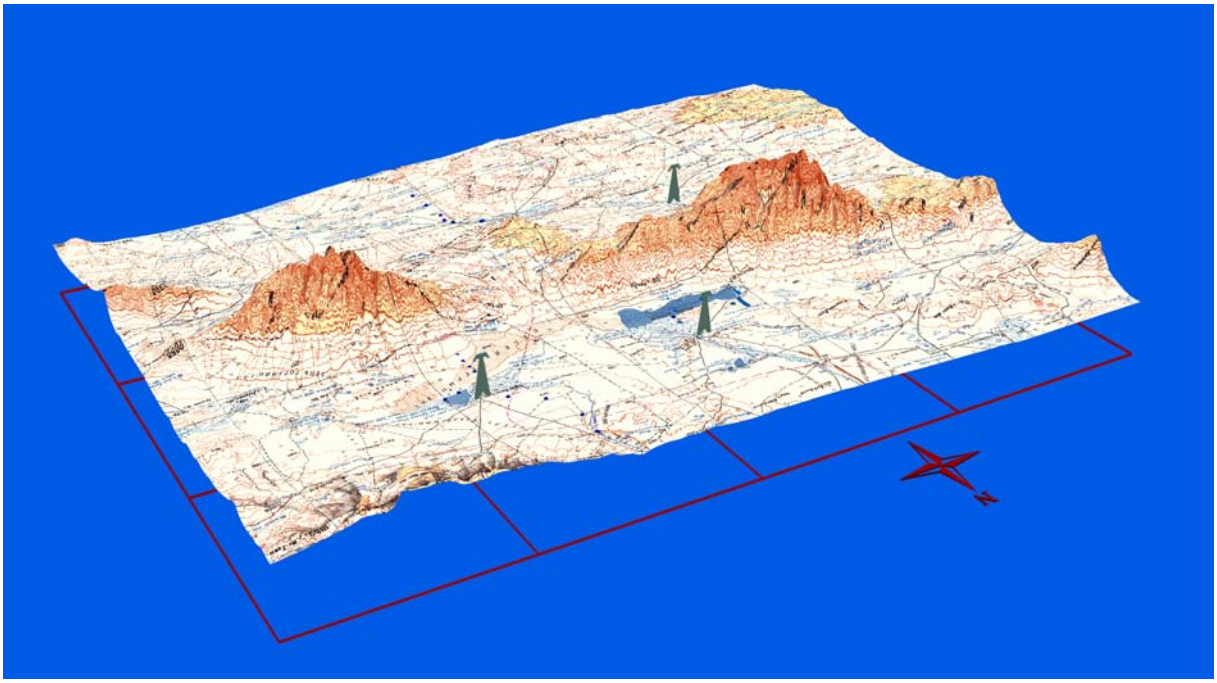

Fig. 2.5.: 150x200 km DEM of the simulation area. blue points – Sample sites; anemometer – gray tower

usable for a dispersion calculation. The conversion is realized with the preprocessor programme IBJgrid. 63 surface samples (symbolized in the figure as blue points) has been taken in the simulation area (2.4) while six of them were used to model the particle dispersion. Due to the road conditions, the samples are in order of transects covering the different geomorphological system parts of pediment, alluvial fans, sandy areas and the temporarily dried out lake sediment of Orog Nuur.

3. Data and methods

The data set resulted from the investigations done during four field expeditions fig. A.5). The expeditions of Aug 2007 and Aug 2008 have been realized according to the DFG project proposal, while the expedition of April 2008 were possible due to a bursary of the DAAD and the support of the Max Planck Institute for Chemistry (Mainz) which has also sponsored the fourth expedition Aug 2009.

To prepare the field work several satellite pictures (Landsat7 and MrSid [NASA Data base 2000]) edited in ERDAS9.3 were taken for orientation. Furthermore, the Mongolian Geographical Department of the MAS was providing topographical maps 1:500000 (whole Mongolia), 1:200000 (central part), and 1:100000 (95% Mongolia) as scanned digital images. The necessary parts were transformed into *.tif format and geo referenced using ArcGis9.2. Coordinate field control of coordinates was performed by a hand-held GPS (Garmin®). Digital elevation Models DEM from the shuttle radar topography mission (SRTM) and advanced spaceborne thermal emission and reflection radiometer (ASTER) were taken for projection as well as for generating input surface data to calculate 3D wind fields as one of the first steps for performing the particle distribution calculation. Additionally the Mongolian Institute for Meteorology and Hydrology was providing weather data in high resolution (Jan 1998 to Dec. 2008) of 32 governmental weather stations.

The data set was very inconsistent and with some curiosities, but nevertheless the best meteorological data set available up to now for this (very) remote region. A detailed description of the data structure, organized in an Access Database, and some first analyses can be found in *Harmel* (2010). Several calculations were performed in MatLab2007a, while wind rose graphics were realized in WRPlotview. The text of this paper is set in LaTeX.

3.1. Field investigations

Regarding the concept of this thesis (fig.: 1.1), the following chapter is divided into two sections. The methods focusing on the dust emission parameter are listed in subsection 3.1.1; Sediment surface investigation. Methods focusing on meteorological parameters are described in subsection 3.1.2; Atmospheric investigation.

3.1.1. Sediment surface investigations

One of the main value in the process complexity of aeolian geomorphodynamics, is the condition of the soil surface. With several laboratory methods and numerical models the time resoluted particle emission

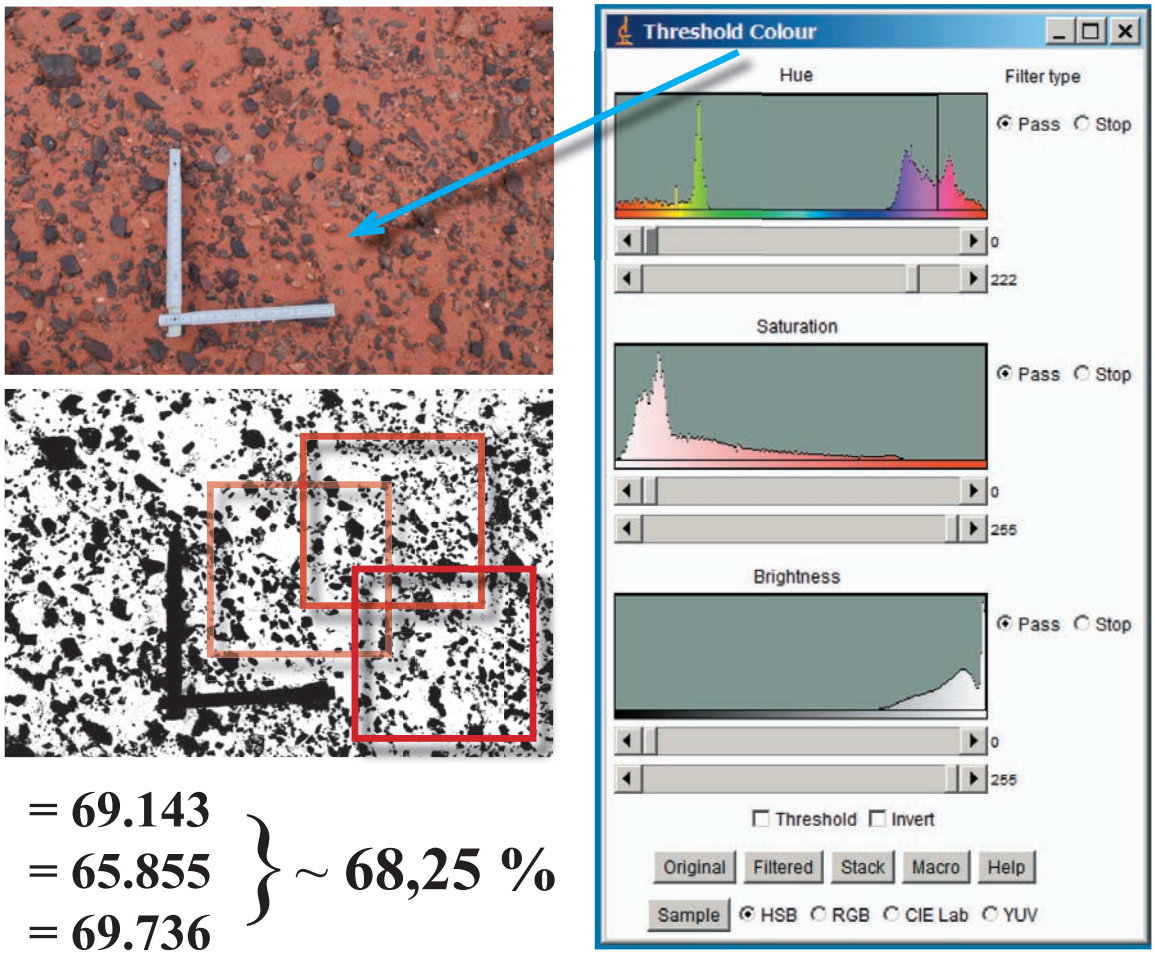

Fig. 3.1.: Calculation of the vulnerable bare soil

were estimated. The estimation is based on

$$F_{(p)} = F_{(gen)} * E * D_p * W \tag{3.1}$$

while F_p is the particle emission flux for a grain size; $F_{(gen)}$ is the generalized particle emission flux and taken from suggested published numbers (*Shao*, 2004; *Darmenova et al.*, 2009). The fraction of erodible surface (E) is basically the proportion of uncovered bare sediment surface and the D is the proportion of the calculated D_p and the W is the water correction. How to calculate the Variables is described in detail in the following text.

For that particle emission model (PEM) 60 sediment samples for laboratory analyses were taken from 2cm of the top soil surface. The samples were taken after removing the covering gravel, using a core cutter or a small shovel. It was tried to choose the sites in a systematical grid raster in the study area, as far as it was possible in the very vast area with only rough infrastructure (Fig.2.4).

Besides the investigation of soil samples to calculate the potential particle emission of the site the vulnerability of the surface is an important value for aeolian geomorphodynamics. A photo graphical method was used to estimate the fraction of erodible surface (E) with regard to the protection of the pavement. The surface of each site was photographed including a measuring rod as a reference. Colour, skewness and brightness of the pixel values corresponding to the bare soil surface area in the picture were determined with the colour threshold plugin of the ImageJ programme. The photos were converted into an 8bit black and white image depending on the committed threshold. For an area of approximately 20x20 cm surface (in order to the measuring rod), the vulnerable bare soil were determined tree times. The average of the investigations were taken as representative for the site (fig.: 3.1). This value is taken as the fraction of erodible surface (E) in the PEM.

To get an idea about the airborne particles and their distribution pattern, simple plastic bottles were installed at the luv (western) border of Orog Nuur basin as a low budged trap system. The bottles were prepared with small wholes as wind outlet on the lee side of the bottle's orifice. The bottles were buried by 2/3 into the subsurface soil and were used as particle traps along a 10km transect and a distance of 300 to 500 m to each other. The trap entry was positioned in the assumed main wind

Fig. 3.2.: Low budget "bottle trap"

direction at at a standardized distance (7cm) from the soil surface (Fig.3.2). The installation of the traps was performed during the expedition in August 2007; the traps were removed after sampling the trapped particles during the expedition in April 2008.

3.1.2. Atmospheric investigation

For the calculation of particle dispersion the airborne motion creates the importance of exact values of meteorological situations. As one of the main input values for the particle dispersion calculation, meteorological input parameters have to be used.

After the expedition in April 2008, the Mongolian Institute of Hydrology and Meteorology was providing a ten year time series of 32 official meteorological stations (fig. A.2). The data were fractionated sub datasets per email in various formats and had to be organized in an Access database. Several uncertainties, time series of 2012 for example, were found in the data files and generates the necessity to prove the dataset carefully. In general, all meteorological quantities were read out and observed by the station personnel in an 3 hour interval (02:00, 05:00, 08:00, 11:00, 14:00, 17:00, 20:00 and 23:00) or three times a day (08:00, 14:00 and 20:00). Air temperature (Stevenson screen 2m above ground), wind speed and wind direction (plate anemometer 10m above ground) were determined. For some stations also data for barometric pressure, precipitation and relative humidity are available, as well as the soil temperature and soil moisture. In chapter 2.1.2 Fig. A.2 is showing the locations of all official Mongolian weather stations situated in the working area. An overview and closer description of the data set is given in *Harmel* (2010).

This data set was used to detect seasonal periodicities of the wind; they were also used for the calculation of the 3D wind field in the model region which is necessary to simulate the dust dispersion.

Additional meteorological investigations have been done during the field expeditions by a mobile weather station (Driesen und Kern®) with sensors for temperature, wind speed and direction (2D ultrasonic), relative humidity precipitation, barometric pressure and global radiation (fig.3.3) in a time resolution of up to 2 sec. This mobile station was used as a reference to the data set of the governmental weather stations as well as the ground station for kite borne investigations to determinate the atmospheric stability.

A third part of the meteorologic investigation was done with kite borne sensors. Sensors for temperature, barometric pressure and humidity (Driesen und Kern®) as well as a sensor for wind speed (ADC Silva®) were installed in the kite. The same combination of sensors was also hooked on a lift, driving

up and down on the kite line with an electro engine. The determined profiles were taken to estimate the variability of the atmospheric stability depending on day and night time, as well as on different wind conditions. These values were used to estimate the atmospheric stability, which is a necessary parameter to determine the diagnostic 3D wind field. Mathematical steps are described in subsection 3.3.

Wind data (wind velocity (U) and wind direction (α)) are also used for the numerical simulation of the 3D wind field in LASAT®. Values of the anemometers situated in the simulation region are available. The best resouluted values are from the governmental weather station of Horiult (ID 45200800; 1308m asl; Bogt Sum center $100°45'46,218"E$ $45°11'8,878"N$). Therefore the values of this weather station were taken as input data to calculate the particle dispersion. The values are used to calculate the 3D diagnostic wind field using the preprocessor programme *Lprwnd* of LASAT®. This time resoluted 3D diagnostic wind field is necessary for the particle dispersion calculation. The values are available in a 3 hour resolution and one value is taken as representative for a period 2 hours before to one hour after the real determination time. In case of '0'-value a wind speed of 0.5 m/sec. is committed to keep the possibility of the afterwards particle dispersion calculation. It was necessary to query the data base of the meteorological weather data to convert the structure into compatible input data (fig.: 3.4).

(a) **(b)** **(c)**

Fig. 3.3.: Atmospheric measurements: a) governmental weather station (Bajangovi), b) mobile automatic weather station, c) kite borne sensor lift

```
=========================================================== meteo.def
- LPRAKT 3.0.1: time series I:/mong_lasat/orog/horihult.dmna
- Umin=0.7  Seed=11111
.
  Version = 2.1  ' boundary layer version
  Z0 = 0.02      ' surface roughness length (m)
  D0 = 0.03      ' displacement height (m)
  Xa = 84176.0   ' anemometer (measurement) x-position (m)
  Ya = 113162.0  ' anemometer (measurement) y-position (m)
  Ha =  10.0     ' anemometer (measurement) height above ground (m)
  Ua = ?         ' wind velocity (m/s)
  Ra = ?         ' wind direction (deg)
  KM = ?         ' stability class according to Klug/Manier
  HmMean = ' terrain-corrected mixing layer heights for unstable stratification
           { 0, 0, 0, 2415, 2715, 2715 }
  WindLib = ~lib    ' wind field library
_
!            T1             T2     Ua     Ra   KM
-(ddd.hh:mm:ss) (ddd.hh:mm:ss)   (m/s)   (deg) (K/M)
Z       00:00:00       03:00:00  5.000    360   3.1 ' 1998-01-01.03:00:00 GMT+01
Z       03:00:00       06:00:00  0.700    353   3.1 ' 1998-01-01.06:00:00 GMT+01
Z       06:00:00       09:00:00  0.700    347   3.1 ' 1998-01-01.09:00:00 GMT+01
Z       09:00:00       12:00:00  6.000    340   3.1 ' 1998-01-01.12:00:00 GMT+01
Z       12:00:00       15:00:00  0.700     14   3.1 ' 1998-01-01.15:00:00 GMT+01
Z       15:00:00       18:00:00  0.700      8   3.1 ' 1998-01-01.18:00:00 GMT+01
...
```

Fig. 3.4.: Example of an meteo.def file. The Klug/Manier class is set to neutral in this case

3.2. Laboratory methods

To generate the input data for the particle emission model (PEM) laboratory methods were used. Further more, as mentioned in the introduction, a geochemical fingerprint as a characteristic signal to identify source areas and track the particle dispersion several laboratory investigations have been done. Most of the applications could not be done in the geoecological laboratory of the Geographical Department, University of Mainz, because of the lack of special equipment. Thus most of the analyses were carried out by other laboratories. The Scanning electron microscope (SEM) was done at the Geological Department of the University of Mainz. X–ray diffractometry (XRD) could be realized at the Geographical Department of the University of Cologne. After sample preparation at the Geographical Department, University of Mainz, the Beckmann Coulter particle scanner was used at the Geographical Department of the University Aachen, with the friendly help of Thomas Felauer. Moreover it was possible to use the combined Laser-ICP-mass spectrometer (MS) system (Thermo Finnigan Element2) of the Geochemistry, Department of the Max Planck Institute for Chemistry (Mainz) to realize the trace element laser investigations at single coarse sand grains. The electron spin resonance (ESR) signal of quartz worked out as one of the most important parameter to determinate the geochemical fingerprints of sediments. For this it was possible to use the application Miniscope 2000 at the Max Planck Institute for Polymer Research in Mainz.

3.2.1. General properties

For all samples of the soil surface (fig. 2.4), pH-values (DIN 19684) in H_2O and $CaCl_2$ solution, amounts of $CaCO_3$ (Scheibler method) and organic content (weight reduction 2g of each sample at 550° C in muffle furnace) were determinated at the bulk samples.

For grain size analyses organic and carbonate matter have been removed with hydrogen peroxide and hydrochloride acid (10%) of 0.5 to 1 g of sample material. To separate possible aggregates into single particles Natriumpyrophosphate in water solution was used. The grain sizes were determinated by scanning with Beckmann Coulter. Three scans were done for each sample, at a scan range 0.04 to 2000 μm with 200 steps. The procedure was repeated three times per sample. The average of the three samples were taken as a proportion of the grain size distribution and taken as input parameter to calculate the particle emission model (PEM).

Besides a wet chemical method, dry sieving was used to separate the samples into sub samples. Four grain size fractions $2000 > 630; 630 > 200, 200 > 125; 125 > 63$ were separated. This separation was done by dry sieving to preserve the geochemical character of pseudo micro soil aggregates as well as to find out the methodical error of different grain size analyzes.

The SEM pictures were performed with Zeis DSM 962 with a voltage of 4 and 15 kV and a magnification up to x500. The samples were prepared with Carbon.

3.2.2. Geochemical analyses

Heavy minerals were determined from the finest sand fraction ($> 125 > 65\mu m$). Separation of the grain size fraction were done by dry sieving and separation of the heavy minerals in a separation funnel with Bromoform. The separated heavy minerals were conserved after cleaning and drying on a glass disc with Epoxidharz. Besides the bulk analyses further investigations were done by taking fractions of some selected bulk samples.

For element analyses, 5-6 g of sediment sample were grained down to 63μm with a ball mill and pressed into powder tablets using Alterite®. Several elements were detected by x-ray fluorescence analyses.

Furthermore from four selected sites ten single coarse grains were drilled three times by the combined Laser-ICP-Mass-Spectrometer system (Thermo Finnigan Element2). Each grain has been drilled for 68 sec forming a hole of $65\mu m$ in diameter three times at a random spot. The results of the analyzed elements were related to silicon (Si).

3.2.3. Electron spin resonance, cristallinity index and quartz content

Sun et al. (2007) proposed to identify the source areas of dust by coupling of the two parameters: signal intensity of the electron spin resonance (ESR)–signal of the E'_1 -center in defect oxygen vacancies of crystalline SiO_2 (Fig. 3.5) and the CI mentioned by *Murata and Norman* (1976). In case of such a defect, an unpaired electron can be trapped into the vacancy (*Rudra and Fowler*, 1987), the presets of γ-radiation is therefore necessary. To concentrate the quartz contents, samples of different dry sieved grain sizes of the light mineral fraction have been separated. The separation was done with solutions of sodium polytungstate (TC Tungsten® Compound) at a density of 2.74, 2.73, and 2.74 g cm^{-3}. The separation of 48 size-separated sub-samples (twelve bulk samples) was done by centrifugation (30 min 1500 revs/min).

To remove the superficial Fe contamination, the samples were pretreated with HCl (10%) in a warm water quench.

The ESR signal intensity of the E'_1 -center was determined with a ESR spectrometer (*Miniscope*® 2000). It was conducted of 0,2-0,5 g sample material at room temperature with a magnetic field modulation of 500 mG, 27 dB MWatten, a BO field of 3357,24 with a sweep of 28,83 and a sweep time of 30. Scans have been repeated 10 times per sample. The scans were measured with a gain of 400, 600 or 800 and linearly converted to gain 600 afterwards. Baseline correction was realized by the Matlab function get-miniscope.m.

The conduction was repeated after irradiation with a total dose of 71,2 Gy γ-radiation (using a ^{60}Co-source at the University of Düsseldorf) of 1-2g pretreated sample. The defect oxygen vacancies are not necessarily engaged by an unpaired electron, and can synthetically be padded with electrons by using γ-radiation. After irradiation the samples were tempered for 15 min at 300° C to trap the electron radicals in the defect oxygen vacancies as E'_1 -center.

To couple the ESR signal with the crystallinity index (CI) the value of the CI have to be determined. The CI is defined by *Murata and Norman* (1976) of the pretreated grain size separated sub samples has been grained $> 63\mu$ with a ball mill and determined using the XRD application at the Geographical Department of the University of Cologne. The XRD measurements ran three times in a scan range from 66ř to 69ř (2θ) with a resolution of 500 steps at a total scanning speed of 1.5 min. The irradiation was done with a Cu source (Alpha 1=1.5406 Å), a voltage of 40 kV current of 20mA. *Murata and Norman*

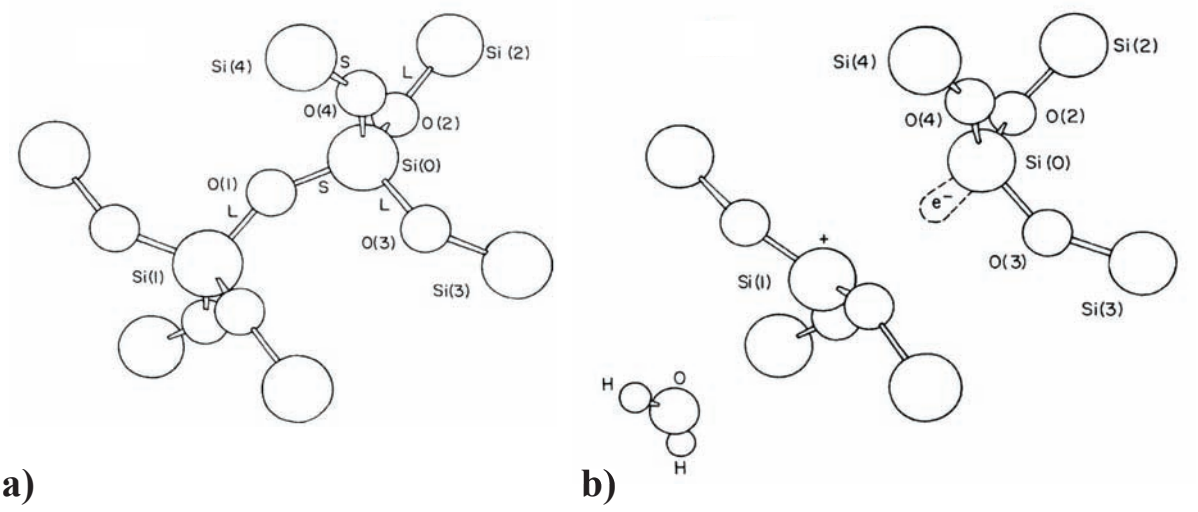

Fig. 3.5.: Normal (a) and defect (b) oxygen vacancy in a quartz cristal grid. (*Rudra and Fowler*, 1987)

(1976) defined the CI by the degree of resolution at d(2 1 2) reflection of quartz at 1.382 Å. The ESR signal intensity has to be calculated up to the signal of pure quartz. For that matter, the relative **quartz content** in the separated light mineral fraction of the sub samples has to be known.

Klug and Alexander (1974) mentioned the internal standard method to determinate the amount of one component in a multicomponent system. Silicon Powder (Alfa Aesar, crystalline, -325mesh, 99.5% metals basis) was taken as the internal standard with a principal peak at $28,4$. The peak intensity (I_{Si}), in combination with the full width at half maximum (FWHM), is coupled with the intensity of the $d(1\ 0\ 0)$ diffraction peak of quartz around $20,9$ (I_{Qtz}). The measurements have been conducted three times and the quartz content was calculated as:

$$Qtz_{Sample+Si} = \left(\frac{W_{Si}}{W_{Sample}}\right) \cdot \left(\frac{I_{Qtz} \cdot (FWHM)_{Qtz}}{I_{Si} \cdot (FWHM)_{Si}}\right) \tag{3.2}$$

where W_{Si} and W_{Qtz} are the weights of silicon standard and the sample. The $Qtz_{Sample+Si}$ have to be assigned with a calibration line (Fig. 3.6) and calculated to the Qtz content of the pure sample Qtz_{Sample}.

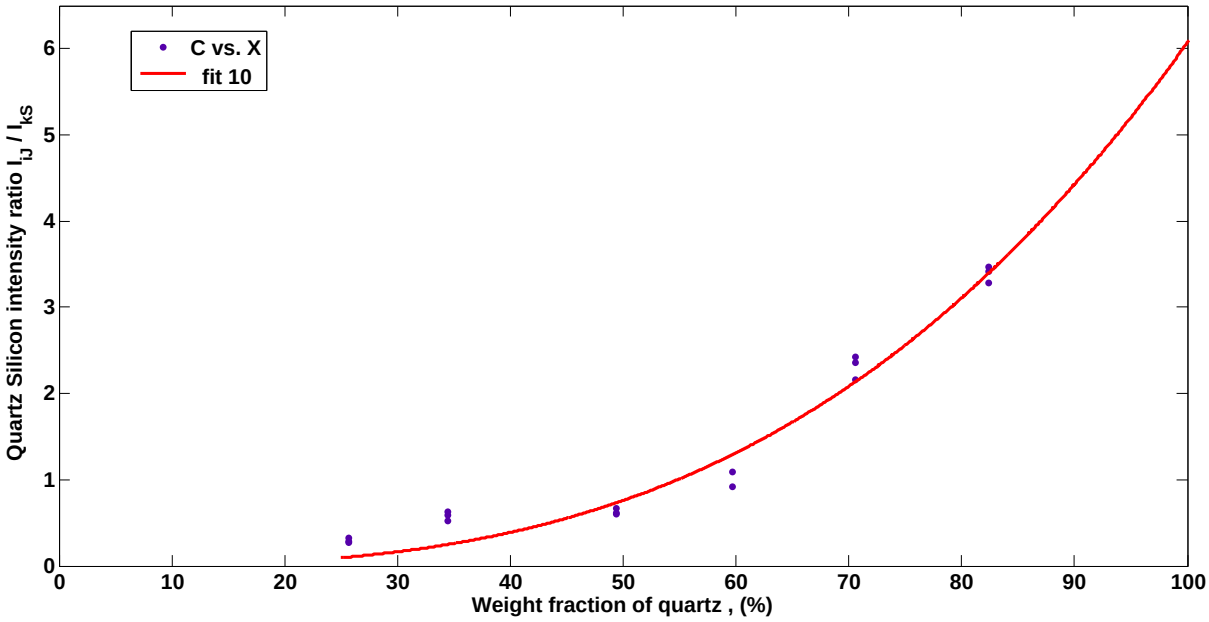

Fig. 3.6.: Calibration Line to determinate the quartz content

3.3. Mathematical methods

Calculations were done at several stages in the work flow of this study. Due to the general concept several input parameter had to be generated as input data for the several steps calculating the particle emission, their dispersion and deposition. Furthermore, the additional information are important to prove the data set of the Mongolian governmental weather stations and to get information about the climatological condition in the area of interest. In this section, the numerical simulation of particle emission, dispersion and deposition was stressed out while the calculations of laboratory and field work based determinations was already described in the last sections.

3.3.1. Time series analyses

The main data set of 32 official meteorological stations (fig. A.2) were organized in an Access data base in order of their identification number, the time stamp and the values. Stations with a 3 and 6 hour intervals were organized in two separate tables. The missing 2.00am value were substituted with the 20pm value and place holder numbers like 164898 were removed. Available precipitation values were added into the tables in order of their time stamp.

Temporal arithmetric averages ($\bar{x}$) for temperature and pressure were determined with

$$\bar{x} = \frac{x_1 + x_2 + ... + x_n}{n} \tag{3.3}$$

while for the determination of temporal averages of wind speed and wind direction the south-north component of wind speed (v_{s-n}) and **vwe!** (**vwe!**) from individual U and α data have to be calculated:

$$v_{s-n} = U \cdot \sin\left(\pi \cdot \frac{90 - \alpha}{180}\right) \tag{3.4}$$

$$v_{w-e} = U \cdot \cos\left(\pi \cdot \frac{90 - \alpha}{180}\right) \tag{3.5}$$

Temporal averages ofU and α are given by

$$\bar{U} = \sqrt{\bar{v}_{w-e}^2 + \bar{v}_{s-n}^2} \tag{3.6}$$

$$\bar{\alpha} = 90 - \frac{180}{\pi} \cdot \arctan\frac{\bar{v}_{s-n}}{\bar{v}_{w-e}}. \tag{3.7}$$

for west-east component of wind speed (v_{w-e}) < 0 and

$$\bar{\alpha} = 270 - \frac{180}{\pi} \cdot \arctan\frac{\bar{v}_{s-n}}{\bar{v}_{w-e}}. \tag{3.8}$$

For $v_{w-e} \geq 0$.

Temporal trends of meteorological quantities are assumed to be linear. Therefore, linear regressions with time were computed:

$$y = mx + b \tag{3.9}$$

while m is gradient and b the intersection with the y-axes. The trend were subtracted before calculating the frequencies and the power spectrum and has been performed with the matlab function 'detrend'. The frequency analyses were performed to investigate the informations in the meteorological data set. Beside the removing of trend tendencies, the 29^{th} Feb. were removed, to equalize the sampling periods. To calculate the frequencies, a blackman turkey analyses were performed based on

$$X_{xx} = \sum corr_{xx}(k) e^{i2\pi fk/f_s}. \tag{3.10}$$

The calculation has been done with matlab and the theoretical foundation is based on a complex Fourier transform $X(f)$ of the autocorrelation sequence $corr_{xx}(k)$ where M is the maximum lag and f_s the sampling frequency (*Trauth*, 2008).

3.3.2. Particle emission of surfaces

One of the main issues of aeolian geomorphodynamics is the estimation of the surfaces particle emission. This emission depends basically on the erodibillity of the sediment surface. Surface erodibility facilitates dust emission during aeolian geomorphodynamics. The particle emission is depending on atmospheric conditions as well as on surface characteristics. The already suggested equitation (3.1) to calculate the F_p needs the values of the generalized particle emission flux ($F_{(gen)}$) as an suggested value (*Shao*, 2004; *Darmenova et al.*, 2009). To determinate the $F_{(gen)}$, the calculated particle diameter and the wind friction velocity (U*) have be taken (see. fig. 3.7). For the atmospheric conditions, the U* is a main value to estimate the particle emission and calculated for conditions of neutral atmospheric stability is given by

$$U* = \frac{u \cdot k}{\ln(\frac{z}{z_0})} \tag{3.11}$$

where the v. Kármán constant (k) is 0.4, and the time dependent wind velocity (U) is provided by the wind observations of from the highest resoluted Mongolian governmental meteorological station Bogt

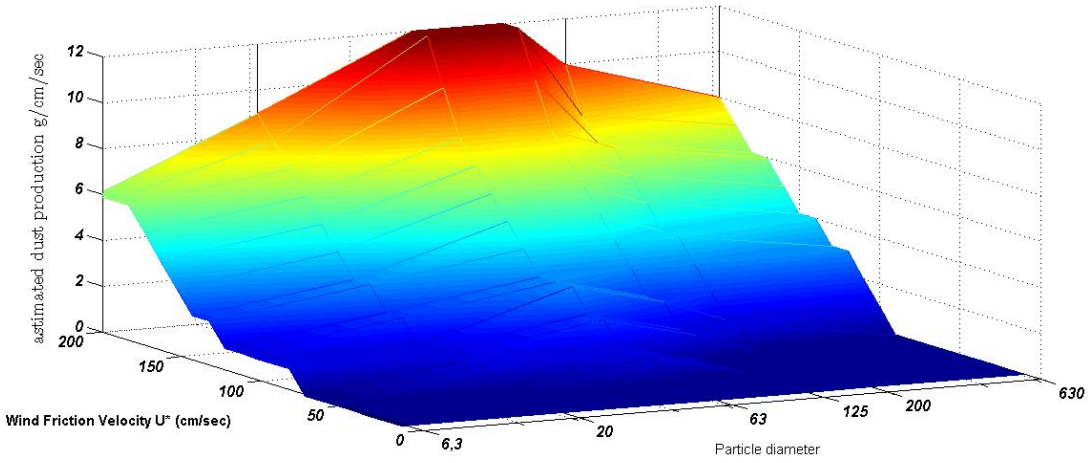

Fig. 3.7.: Particle production ($mg/m^2/sec$), depending on grain size and wind friction velocity (U*)(suggested in *Darmenova et al.* (2009)).

Horiult (ID 45200800, 1308m asl $100°45'46,218"E$ $45°11'8,878"N$; 3h resolution). The U is determined in an altitude of 10m (z) and roughness length (z_0) is taken as 0.02 m (fig.: 3.3). The fraction of erodible surface (E) is the value determined as mentioned in the section 3.1.1 with a photo graphical method by investigating the pixel values of color, skewness and brightness of digital surface photos. The value for the proportion of the calculated particle diameter (D_p) is determined with the grain size scanning of the sediment sample (subsec.: 3.2.1).

The particle emission flux (F_p) is than calculated for the particle sizes 20, 63, 125, 200 and 630 ţm depending on the resulting wind friction velocity based on suggested values published in *Shao* (2004); *Darmenova et al.* (2009) for each sites.

Furthermore the soil moisture is a very important parameter, while the binding energy of the surface particles are increasing due to the soil moisture (*Alfaro*, 2008; *Ishizuka et al.*, 2009). Gravimetric soil moisture values are only available for meteorological Station in Dalanzadgat (ID 43604400) in a 10 day resolution. Therefore the 10 day resolution is interpolated up to a 3 h resolution(fig.: A.19) and the values taken as a factor.

3.3.3. Particle dispersion

Next step after the calculation of the time resoluted particle emission flux (F_p) the dispersion of the single particles have to be simulated. Due to aeolian geomorphodynamics in context of landscape development, a main focus is set on the dispersion of heavy aerosols (Focusing diameters of $20-630\mu m$). To realize these particle dispersion a commercial program performing a LASAT® were used for the simulations. It is a common program to calculate dispersions of particles or gases on a regional scale (up to 200 km distances) and better known under the name Austal2000. This is part of the stipulated work flow of the Technical Instructions on Air Quality Control (Technische Anleitung zur Reinhaltung der Luft) (TA Luft) appendix 3 to calculate industrial emissions. Several preprocessors are included for example to calculate the 3D wind field, turbulences in the Prandl Layer or the boundary layer as a boundary to the free atmosphere. Also several post processors are implemented for example to merge concentrations of different time intervals. The following description is a very short introduction and can be found in detail in the program manual (*Janicke*, 2008).

Diagnostic wind field model

A three dimensional diagnostic wind field model was needed to generate potential flow solutions according to the DEM in the simulation area for several wind velocity situations. Wind fields were generated under the assumption of neutral stability of the atmospheric boundary layer. The preprocessor program of LASAT® *Lprwnd* is realizing the modeling and generates the flow in order to the topography.
An initially uniform divergence free background wind (the average wind speed and wind direction of the total input wind data) is taken for all grid cells and adapted to the DEM. After the terrain profile the vertical air flux (turbulence) was taken into account. The turbulences appear at the near ground depending basically on the roughness length, wind speed and atmospheric stability. This near ground layer is called the Prantdl layer and is included into the diagnostic wind field by imposing a vertical wind velocity profile. It is necessary to avoid a deviate of the wind values at anemometer position after having taken the terrain profile and the Prandl layer into account. For that reason two diagnostic wind fields were generated in advance and any wind field can be created, using the linear combination of the two base fields in such a way that the wind speed and direction exactly match to the predefined wind values at the anemometer position. For that matter a wind field library was created with two diagnostic wind fields calculated with the average wind velocity of the whole input data and two wind directions (in this case wind direction (α) of 270 and 360). All the calculations were performed with the general assumption of neutral atmospheric stability. While performing the dispersion of the particles, the wind field was calculated for each wind situation as described for the anemometer position with the values of the weather station data set (resolution of 3h). Furthermore before performing the particle dispersion, the boundary layer is calculated taking into account the the roughness length (z_0), the height of the anemometer above ground (h_a), the wind velocity measured at the anemometer, the wind direction (α) the stability class and the height of the mixing layer (adjusted according to the terrain).

Dispersion Model

The central part of this thesis is the performance of a Lagrange simulation of aerosol transport, which is realized with the commercial program LASAT® and simulates the turbulent diffusion of particles (or gases). It is a simulation of discrete (single) particles, with a random motion of the particles during the simulated transport by the predefined wind field. The particles were defined with diameter and specific weight which lead to the particle velocity, implifying sedimentation and deposition velocities. With the

intern algorithm the positions of each particle could be calculated according to the wind field and the time period. The distributions of the single particles were averaged for a given time period.
The distribution calculation was realized with a lagrange function (L). This is an amelioration of the euklidic algorithm which can be basically described with

$$L = f(x_1, x_2) + \lambda(x_1, x_2) \tag{3.12}$$

while $f(x_1, x_2)$ is the basic function and $\lambda(x_1, x_2)$ are describing the additional conditions. Taking several additional conditions into account, the algorithm starts up to become very complex. A detailed description can be found in the program manual (*Janicke*, 2008). This method guarantees a simulation close to reality but limits the simulation region in resolution (grid size) and extent (maximum extent at 200km).
The final deposition under dry conditions is described in an empirical way by a specification of a deposition velocity (υ_d). Particles that are hitting the ground are always reflected and leaving with a certain probability, to keep the sampling error small.

4. Results

Due to the concept of this study the results containing a general part presenting general properties (3.2.1) of the surface samples to get the first ideas of the conditions for aeolian geomorphodynamics in the Mongolian Gobi desert. Furthermore the central part of the study, the exemplary simulation of particle emission, dispersion and deposition are presented in the section of numerical modeling (4.2). The simulation were performed by defining the sampling site as point sources emitting single particle size fractions, to investigate the distribution transects. After selecting the most important site for particle emission (situated in the lake basin) the corresponding geomorphological unit was mapped out and taken exemplary as a polygon source of particle emission. Furthermore in a third section about the geochemical properties (4.3) the detailed search for a geochemical fingerprint of different assumed source areas were presented and interpreted. The initial idea was an underlining of the simulated particle dispersion by tracking characteristic geochemical signals as fingerprints of the particle distribution of different sources. But due to difficulties characterizing significant differences of the sampled surface material, this part is basically a suggestion of methods with their advantages and disadvantages to investigate a geochemical fingerprint.

4.1. General properties

Several laboratory analyses were done to collect input data to calculate the particle emission depending on the soil sediment condition for each sampling site. The results show local differences in grain size distribution, content of organic matter, $CaCO_3$ and slight differences of pH–values. The values are used for interpretation of ongoing aeolian geomorphodynamic activities. The surface sediment samples are representative for the typical soils (compare chapter 2.1.3) generally in arid and hyper arid regions. They are sand dominated and the organic content is low. To have an idea of the contribution of aeolian activity, wet chemical processes or fluvial transport as well as a process interaction SEM images were done. They were taken to investigate the morphology of the single grains in general to get a first information about

the contribution of aeolian dominated processes. They show sharp edges of the single sand grains (fig.4.1 and A.6) in most of the cases, while the breaking edges vary depending on the mineralogical composition. The very sharp edges point out short transport distance to the source. Furthermore on the grains hints for chemical weathering can be seen as a rough surface. The surfaces of the grains are generally clean and without any contamination, but still in some cases, clay particles contaminate the grain surfaces and show micro soil aggregates which have to be considered while interpreting the simulation of grain size fractionated particle emission. The shape of the morphology of the grains gives a hint to assume the transport mechanism dominated by aeolian processes, but also shows the presents of chemical weathering processes, only possible under the presence of at least a small amount of water. Thus, regardless to the aridity fluvial erosion also has to be considered in the process interaction of aeolian geomorphodynamics. The annually precipitation during the summer time and the plain flood causes a translocation of surface particles. That fluvial process part is the providing of the surface with erodible particles. To keep aeolian geomorphodynamics an ongoing process the plain flood events are a necessity.

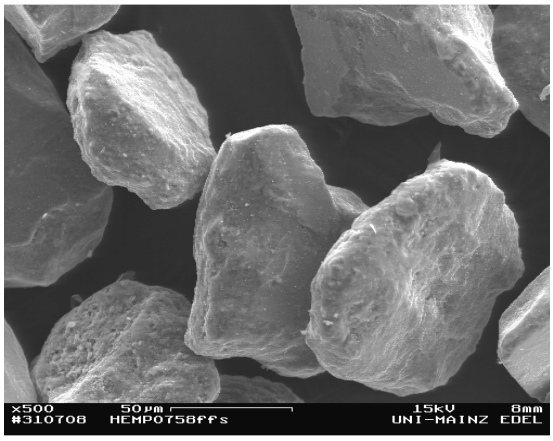

Fig. 4.1.: SEM picture of sand grains

All pH–values are showing an alkaline environment with values between pH 7,3 and 9,0 in a aqueous solution and values of pH 8,5 to 10,2 in a $CaCl_2$ solution (fig. A.7 and A.5). It is assumed that the pH values are basically resulting out of surface high salinity, $CaCO_3$ content as well as the first hint that the wide spread alkanoide granites are the the main contributers for aeolian sediment production.

The sparse causal connection to a low production of organic matter results in a low amount of organic matter in almost all samples as well. Except the samples 708114; 808087; 808134 and 808142 the organic matter is always lower than 2 % (fig. A.9 and fig.: A.11 is shown the spatial distribution.).

All samples with exceptionally high amounts of organic matter are taken from small depressions. These cases are not representative for the general surface properties, but were assumed as single dust sources with high emission rates in case of wind friction velocity above the threshold. To investigate the uncertainty focusing the contribution of particle emission out of different geomorphological system parts the small spots were sampled and their corresponding particle emission were calculated.

In contrast to the pH – values and the organic content, the $CaCO_3$ content varies within the different

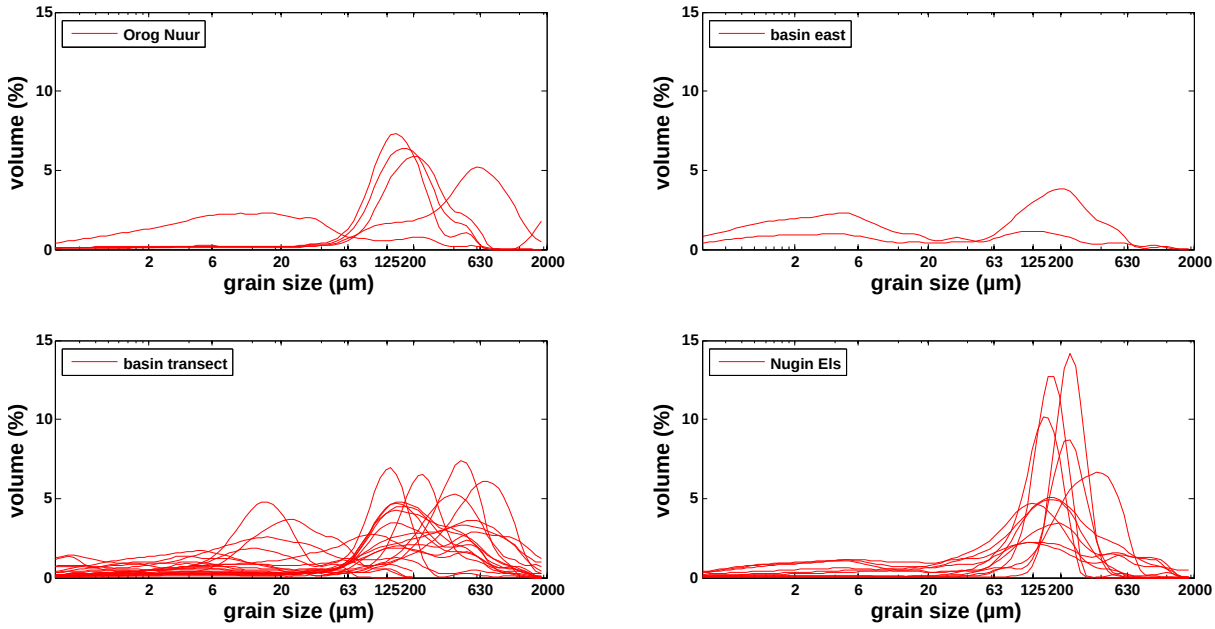

Fig. 4.2.: Particle size distribution of all samples

sampling and pointing out regional differences [fig.: A.8 and fig.: A.10 is shown the spatial distribution.). The samples situated in the wind corridor south of the Icht Bogd Mountain (samples of the depression transect 0808124 - 140) are containing a much higher relative amount of $CaCO_3$. This is also the case for the samples collected in the river delta of Tazin Gol. It can be an evidence for the long distance transport of particles into the region.

The grain size distribution varies within the different locations but correlates to the contents of organic matter and the $CaCO_3$-content. The pH-values dont't show a significant variation correlated to the localization. In case of the sandy dominated areas (The Nugin Els and Sandy sites of Orog Nuur with a peak $\approx 630\mu m$,), the silt and clay fraction are very low (Fig 4.2). In most of all samples the grain size volume peaks point out the coarse silt at $125\mu m$ and the finest sand grain size fraction at $200\mu m$. Two samples were taken in the east of the depression basin showing a clear reduction of sand and coarse silt fraction. Instead of these fractions (besides a remarkable peak at $200\mu m$) the spectrum is shifting to more finer grain size fractions of fine silt and clay. Also in the transect taken from the western part of the depression basin, the grain size spectrum is very broadly spread. Besides many detectable peaks, pointing out coarse sand and middle sand, at around $630\mu m$ the finest sand and coarse silt are also represented. Most of the lines have a maximum at around $125\mu m$. Furthermore the samples of the transect in the depression also have a remarkable content of fine silt as well as an important amount of clay.

This spectrum of grain size distribution variations of the surface sediments is in contrast to air borne

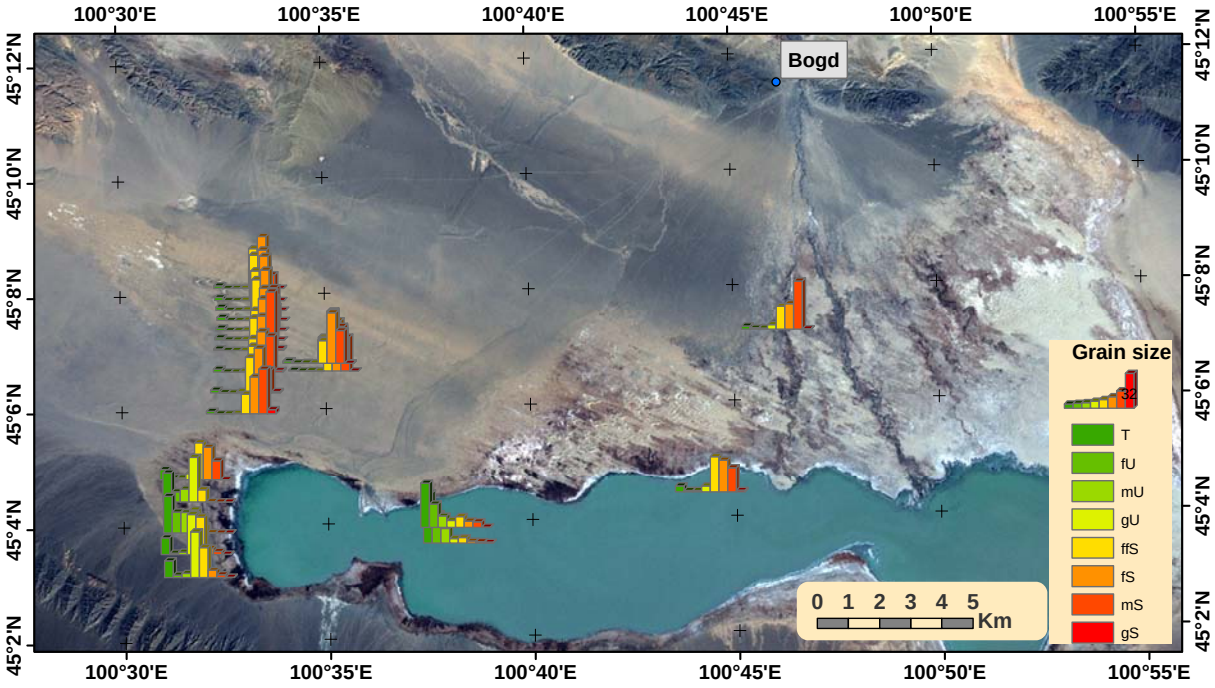

Fig. 4.3.: Bottle trap transect. Grain size distribution of air borne particles at Orog Nuur

particles collected in the northern part of the valley west of the Orog Nuur basin using the "low budget bottle" traps (fig.: 3.2). This transect is running through the valley bottom and continuing up to the beginning alluvial fan to the south, where the Icht Bogt Mountain is located. Fig 4.3 is showing the grain size distribution of the samples. The grain sizes were determined in contrast to the particle scanning method taken for all the other samples by the Köhn method (subsec.: 3.2.1) and showing a variable spectrum of the grain size distribution. While in the deeper parts of the valley the fine sand (germ. Feinsand) (fS) and middle sand (germ. Mittelsand) (mS) is dominating the spectrum, with an increasing of the altitude up to the alluvial fan of the Icht Bogd in the south, the grain size distribution of air born particles is shifting to the finer grain sizes. Also the content of clay is increasing. Also the content of clay is increasing within the interim from the valley up to the alluvial fan. In some cases a clay fraction is even detectable with more than 5%. These cases are related to a local occurence of asumed high soil moisture caused by a small spring, where the ground water conditions as well as vegetation and range land situation differs to the sourounding conditions. It is also an area with high frequented range land and settling of local nomades. Some of the bottle traps could not be found, couple of mounth later or had considerable signs of trampling.

Beside the bottle trap –transect several surface samples were taken from the lake basin surface (the lake

was dried out in the sampling time) as well as samples out of the delta region of the Tazin Gol. The lake sediment is shows remarkable contents of fine and middle silt as well as contents of finest sand in case of the delta area. A huge amount of clay in the basin region was determined, while sandy compartments were missing in the samples of the lake sediment but were detectable at the delta locations (Table of exact contests in the attachment A.6).

The values of this parameter in their spatial distribution can be concluded as different aeolian geomorphodynamics due to the location. The whole study is characterized by the temporarily strong winds. Several light yellow stripes orientated in north-west to south-east direction the satellite picture (4.3) are showing the transects of moving particles, which can be detected in other locations in the same orientation too. They are situated in the valley and point out the main wind directions.Thus the whole location is under the influence of temporarily high wind speeds and the presence of particles in motion vary enormous. The results of the bottle trap transect are pointing out a high variability of different grain size distributions within a small scale. In some cases of the dune Field Nugin Els, Khongorien Els and Zungol Els the dune formations show a barchanoid orientation pointing out the main wind direction with high wind speeds from the north west. Furthermore nebkas and abrasions on the Mesozoic-Cenozoic stratified deposits in the central part of the depression south of Icht Bogd and Baga Bogd point out the main wind direction (fig.: A.13). Furthermore fraction of erodible surface (later on used as the factor E in the particle production model) is changing due to the location. While the surface of the depression basin, where the surface sample is located at its western margin, a dense pavement is covering the surface. The grain size distributions shift to a higher relative dominance of middle and coarse silt which can be concluded to an aeolian geomorphodynamics characterized by relatively less particles in motion. In contrast to the depression the lake basin of Orog Nuur north of Icht Bogd and Baga Bogd pointed out a high content of middle silt (mU) and coarse silt (gU) especially in the delta region of the Tuing gol river. This grain size fractions are highly vulnerable to wind erosion and main contributors to particle emission from surfaces. The lake basin (in case of water absence) can therefore be mainly responsible for aeolian geomorphodynamics.

4.2. Numerical Modelling

The following section is divided into several subsections. In context of the thesis concept, the numerical methods are used to investigate the process of aeolian geomorphodynamics in endorheic basins. First of all the wind conditions in the area of interest were investigated focusing on general parameters. Wind values of Mongolian governmental weather stations, basically wind velocity (U) and α were analyzed. Furthermore temperature, precipitation and soil moisture (values representative for the depth layer 0-5cm) were analyzed and taken into account while performing the estimation of the dust production rate for several surfaces. Averages and standard deviations gave preliminary ideas about the conditions in the area of interest. Furthermore the wind conditions in a time resolution were taken into account, for investigating the periodicities and oscillations as far as possible due to the relative short time series available. Frequencies pointed out the wind periods for an annual as well as a daily period and were used to generalize the simulation input parameter.

The final simulation of particle dispersion under several conditions was exemplary modelled in a 200 x 150 km simulation site. Three meteorological weather stations are situated in that location.

To simulate the dust distribution and interaction between basin sediments and hill slopes, dust emission rates were calculated by performing a particle emission model (PEM). The input parameter was taken from the analyses of the Mongolian meteorological data set as well as the values out of the soil samples investigations. Additionally the vulnerable bare soil was calculated with the interpretation of pixel values of digital photos taken from the surface.

As a third part, the final Lagrange simulation of aerosol transport (LASAT®) was performed. Single emission sources were taken to follow the transects of heavy aerosols dispersion. A calculation of a 3D diagnostic wind field in a time resolution was necessary. The following particle dispersion simulation allowed to model the dust loads of the air masses, as well as sedimentation rates of different grain sizes.

4.2.1. Data of governmental Mongolian weather stations

To use the data set provided by the Mongolian Institute for Hydrology and Meteorology, for particle dispersion modelling, the data first had to be checked to reduce uncertainties. First investigations testing the validity of the data were performed by *Harmel* (2010) focusing on the temperature values of different sites. In this study the main interest is directed to the wind conditions and therefore, the values of wind velocity (U) and wind direction (α) were investigated. The analyses are focusing different time periods.

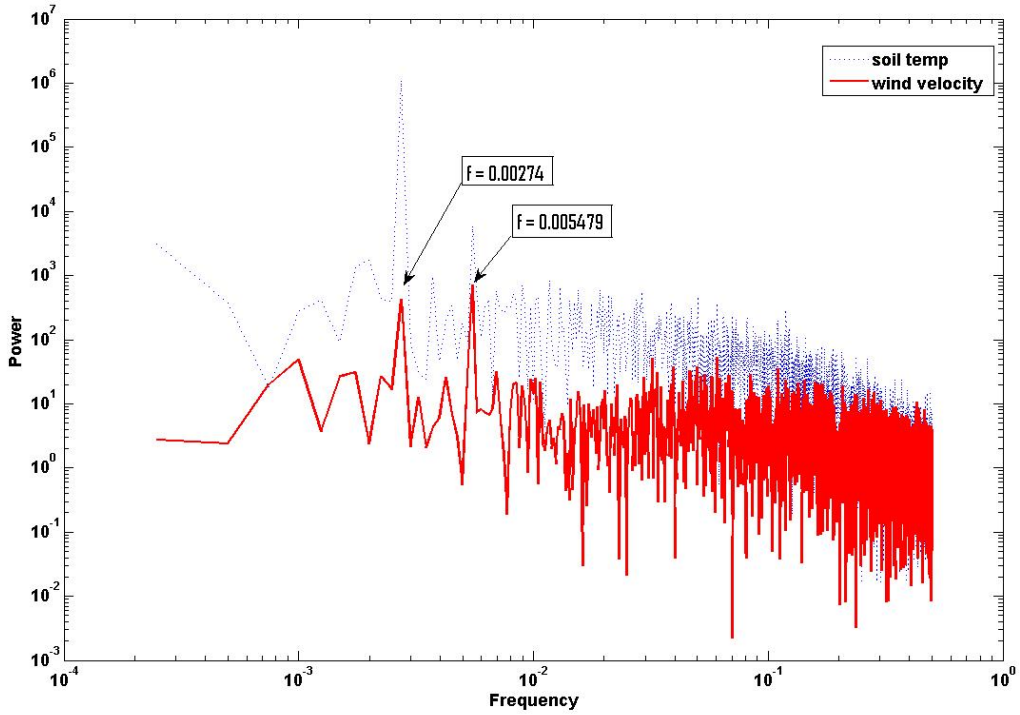

Fig. 4.4.: Blackman Turkey frequency analyses for all averaged wind speeds of the Gobi desert weather stations

As already mentioned in the climate subsection of the environmental characteristic (cha. 2.1.2), the weather has a high annual periodicity. The overlying frequencies of different periods can be detected with a Blackman turkey autocorrelation. Depending on the intensity the frequency of a period is corresponding to the power value. A high intensity is showing a high value at the power axes. Fig.: 4.4 shows frequencies in case of a general daily average of the wind velocity. The input data are the wind velocity values for all stations situated in the Mongolian Gobi desert. As an additional signal information the available values of the soil temperature is taken. Two remarkable peaks pointing out two overlying periods. A frequency (f) of 0,00274 which is equivalent to a time period (τ) = 364,96 sampling intervals (≙1 year) with a very high power intensity. In case of the soil temperature, this annual period with a power of $1.09x10^6$ the signal is even much clearer. Nevertheless, the annual wind period is even detectable in the power spectrum. Furthermore a second remarkable peak can be detected at f = 0,005479 which points out τ = 182,52 (≙1/2 year). Two periods with a frequency of one year respective half year are detectable with a high intensity of their occurrence. The frequencies are overlying and the two signals are amplifying each other. It results in a main wind season in spring time and a lower but detectable minor wind season in autumn (fig.: 4.6). As already mentioned in the chapter of the environmental characteristics,

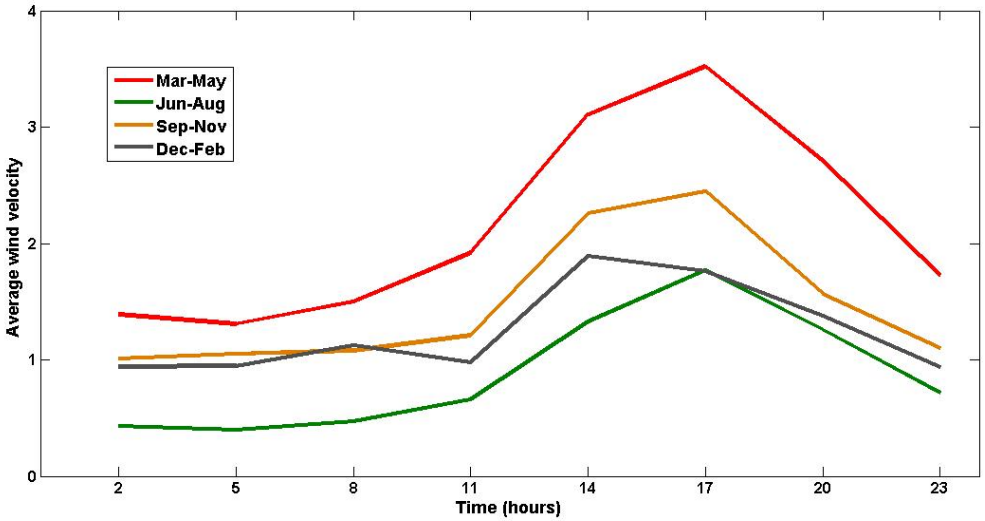

Fig. 4.5.: Variation of wind velocity during the daytime (Peking time). Average of 32 stations

the two wind seasons apply to the situation of the area of interest mainly influenced by the westerlies. The shifting of the westerlies is coupled to the jet stream. The Mongolian Gobi is under this influence in spring and autumn (*Han et al.*, 2008a). These are the main wind seasons (detected in the power spectrum), while in winter, the influence of the Mongolian Siberian anticyclone is blocking the westerlies and in summertime the area is under the influence of the south eastern monsoon. The are no more serious peaks in the power spectrum. The uncertain line detecting oscillations with a period of several years is uncertain. Thus the oscillations of the hazard years with a periodicity of three respectively seven years are due to the short time series of the provided meteorological data not detectable. Furthermore shorter periods are regarding to the noise of the signal also not detectable.

Besides the frequency of a daily resolved average of all stations, the wind velocity distribution during the daytime is of relevant interest. Fig. 4.5 is showing a clear increasing of expectable wind velocity at anemometer height (10m) during the day time. As a characteristic of desert energy balances high temperature variations can be notable in the air respective soil temperature values. The effect of latent and sensible heat flux is also influencing the atmospheric stability. The loss of vegetation, the bare soil, covered with black stones (≙low albedo) and the cloudless sky increases that effect. The negative energy flux during night time and the high energy input during daytime changes the atmospheric stability. While the establishing of a night boundary layer is reducing the wind velocity at the near ground, strong convections during the daytime are resulting an instable atmospheric stability. In the afternoon, when the energy input of the sun is decreasing, cyclonal - antycyclonal pressure differences on larger scales,

can establish higher wind velocity in the afternoon (*Stull*, 1988). The differences of the four seasons are fitting to the seasonal wind conditions. The spring time with the highest expectable wind velocities and the autumn nearby are under the influence of the westerlies with their cyclonal cold fronts. The high Siberian-Mongolian anticyclone causes very stable stratifications with strong inversions and thus blocks the wind velocity in general. Just slow wind velocities occur due to the anticyclional influence out of the north can be recorded. In contrast to these seasons, the summer is characterized by very low wind speeds during the influence of the east Asian monsoon.

Another important parameter is the presence of precipitation and within an increasing of soil moisture of the top soil layer. With an increasing soil moisture the cohesion and binding energy of particle aggregates increases and the vulnerability of the surface decreases. The soil moisture is one of the input parameter for the PEM and influences the particle emission flux (F_p), which are the necessary parameters to perform the Lagrange simulation of aerosol transport (LASAT®). Therefore, the soil moisture is a very important parameter for calculations of eolian geomorphodynamic, but in most cases not continuously determined.

4.2.2. Data of station Bogt (ID 45200800)

Three governmental meteorological weather stations are situated in the area taken for particle dispersion simulation (fig.: 2.5). The stations Bajangovi (ID 44702200, 1570m asl) and Baruunbayan-Ulaan (ID 45201400; 1242m asl) have a sampling interval of every 6 hours, while the Station of Horihult (Bogt at lake Orog Nuur ID 45200800, 1308m asl) records the weather conditions in an interval of 3h. The values of this station were taken for the later performed simulation of particle dispersion. Within the data set of this station (ID 45800200) there are no missing values during the recorded period of 11 years (Jan 1998 to Dec 2008) and situated next to the basin of the lake Orog Nuur. The other two stations ID45201400 and ID44800300 are also situated in the simulation area but have lower temporal resolution and were not taken into account.

As already detected by the Blackman Turkey power spectrum the annually and half annually frequency is recognizable in the averaged wind velocity. Fig.: 4.6 shows the wind velocity of recorded values at the anemometer position (z = 10m) of the Horihult/Bogt Station (ID 4200800). There is a smoothed line plotted in red and visualizes the main wind season in spring time and a second wind season in autumn with generally relative lower wind velocities. The figure shows the typical situation of wind conditions

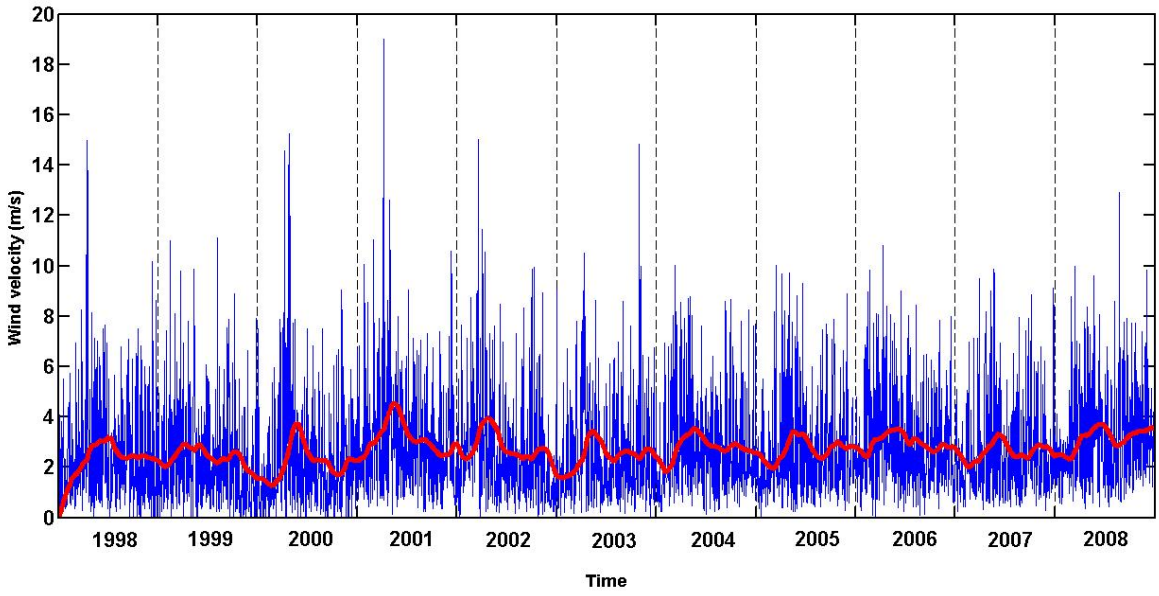

Fig. 4.6.: Wind velocity of Station Bogt; ID 45200800 (n=32144)

in south Mongolia (*Dagvadorj et al.*, 2009), already detected in the power spectrum analyses of the generalized averages of all stations.

The wind velocity (U) at anemometer height (h_a = 10m) is several times high enough, that the resulting wind friction velocity (U*) exceeds the threshold friction velocity (U_t^*), to move particles and emits them from the surface. This threshold depends on several parameters and is discussed in the several sections of the particle emission model (PEM) (subsec.: 4.2.4). The highest values were recorded at the end of April 2001, during a strong dust storm. This event is well known in the community as the "perfect dust storm" (*Nakano et al.*, 2005) and therefore the later performed particle dispersion is calculated with the values of the year 2001.

Besides the wind velocity (U), the wind direction (α) is an important parameter to understand the eolian geomorphodynamic. The wind directions in case of the weather station ID45200800 are shifting (fig.: 4.7). The main seasons in spring and autumn are basically influenced by the westerlies and theirfore north west winds are dominating the wind direction (α) during that time. Besides the main wind seasons with expectable high wind velocity, summer and winter are dominated by low wind speeds. Influenced by the tails of the south east and east Asian Monsoon and air masses from south east and eastern direction are influencing the weather condition during the summer in south Mongolia. Furthermore the high pressure of the Siberian Mongolian anticyclone generally reduces the horizontal air flux. Winter is

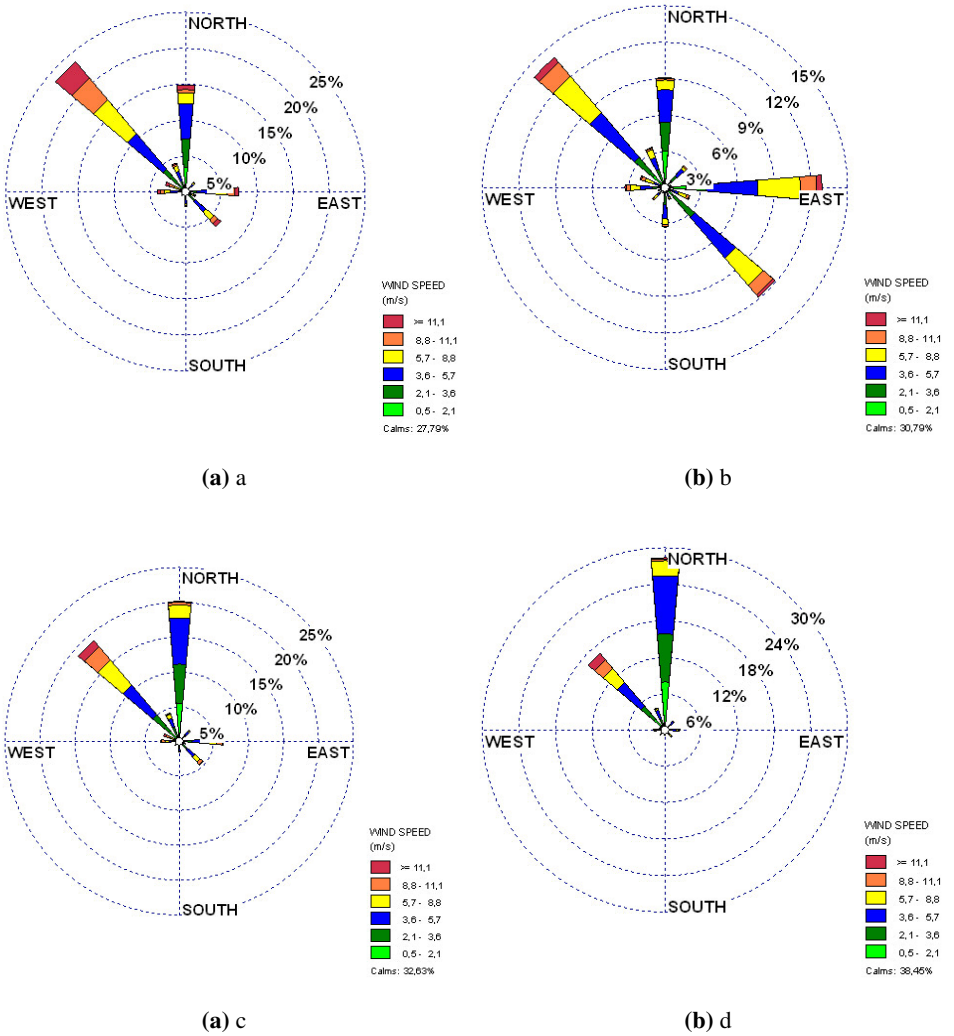

(a) a **(b)** b

(a) c **(b)** d

Fig. 4.7.: Wind roses of station ID 45200800. a) Mar-May, b) Jun-Aug, c) Sep-Nov, d) Dez-Feb.

dominated by very calm situations ($38,45\%$) and low wind speed mainly from the north.

Within the influence of air masses out of different regions, the humidity is changing. While in most of the cases, the relative humidity is very low, the summer with the east and south east winds increase the relative humidity accomparrid by the precipitation risk increases. In context of aeolian geomorphodynamic, the presence of precipitation is important in several points. First the wash out of airborne particles and a resulting wet deposition, and second the increasing of soil moisture which leads to higher binding energies of the sediment particles. Unfortunately there are no soil moisture values available for the station ID 45200800. This circumstance nesessitates to rely the soil moisture data of Danlanzadgat (ID 43604400) ($\approx 250km$ to the south east). Furthermore the soil moisture is just determined manually every 10 days and the variation of the values is enormous. Besides the error of taking the values of a more or less far

away station as representative, the ten days values were interpolated linearly (skript.: **??**) to calculate the necessary input parameter (fig.: A.19) for the moisture correction while estimating the particle emission of the several sites.

4.2.3. Atmospheric stability investigation

Besides wind direction (α) and the wind velocity (U) the atmospheric stability was an uncertain factor in the beginning of the study. Generally in desert regions, with the absence of vegetation and an high energy input from the sun, the energy flux during night and day shows high differences. It is responsible for the establishment of near ground boundary layers respectively instable atmospheric stabilities due to high convections. The stability situations are therefore shifting during day and night, which have a high influence to the horizontal and vertical wind velocity. The analyses of the wind velocity values of the Mongolian governmental weather stations shows the resulting increasing of the wind velocity in general (fig.: 4.5). Focusing on the aeolian geomogphodynamics, dust storms are also recorded basically during the after noon (*Natsagdorj et al.*, 2003; *Kim*, 2008). To investigate the atmospheric condition, kite borne measurements as well as a lift running up and down the kite line were used to measure the profiles. It was able to measure a low level jet at the Bajan Onjul Oasis ($96°45'29,859"E$ $44°55'18,889"N$) at the 17.08.2009 (fig.: 4.8). Low level jets are less investigated phenomena with an assumed high importance for particle dispersion (*Washington and Todd*, 2005; *Warren et al.*, 2007). That is why this phenomenon is presented here. The figure shows an instable wind profile in the beginning of the investigation resulting in low differences of wind speed between the kite borne sensors and the automatic weather station at ground. The corresponding temperature (fig.: A.15) show a instable profile too. During the sunset the situation is shifting. A nigh boundary layer starts to establish and the warmer air masses were cut of the ground friction by a near ground inversion. The larger scaled pressure differences of the cyclone and anticyclone resulting a wind velocity above the near ground inversion. The warmer air masses are moving with wind speed up to 15 m/sec and probably more (the anemometer could only record 2000 datasets, and therefore the measuring stops at around 22:00). The corresponding values recorded at 2 m above ground with the automatic weather station shows a calm wind situation and low temperatures $\approx 10°$ C. The night boundary layer was established up to an altitude of $\approx 200m$ then the kite drops down. While the particles basically emitted by the presence of high wind speeds at near ground the stability situation can be detected as neutral for these times. The later on performed particle emission and their

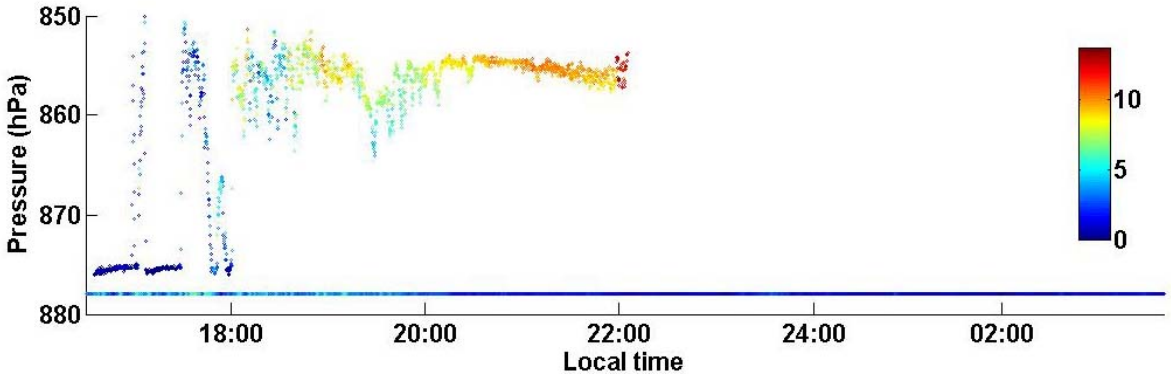

Fig. 4.8.: Kite borne measured windprofile showing a low level jet (values in m/sec)

dispersion were calculated under the estimation of a neutral athmospheric stability. This necessity is also due to the limited possibilities to define the wind profiles in LASAT®. But for the estimation of expectable errors in the dispersion calculation the investigations of the atmospheric stability are useful and have to be improved in future times.

4.2.4. Particle emission model

To calculate the time resolute emission rate for the sampled sites, the necessary input parameter were generated. These are due to the suggested equation ((3.1)) the generalized particle emission flux ($F_{(gen)}$), taken as suggested values published in *Darmenova et al.* (2009), the fraction of erodible surface (E) determined by the photographic method based on the pixel values of the digital surface photos, the proportion of the grain size fraction (D) and the moisture correction. All this parameters were taken as input data to calculate the particle emission flux (F_p).

The particle emission is calculated generally as a result of the time resolute weather condition in correspondence with the surface condition of each sampling site. Fig. 4.9 shows the effective particle emission for a generalized site with no gravel cover and a log normal distribution of particle sizes fractions; simulated for the year 2001, which was taken for the simulation. The two wind seasons in spring time and autumn can be recognized. During the winter period the dust production is very low due to the low wind velocity conditions. Furthermore during summer the dust production is again reduced, resulting out of the generally moderate wind velocities as well as the higher soil moistures, causing an increase of the particle binding energies and therefor a reduction of the particle emission (*Alfaro*, 2008; *Ishizuka et al.*, 2009).

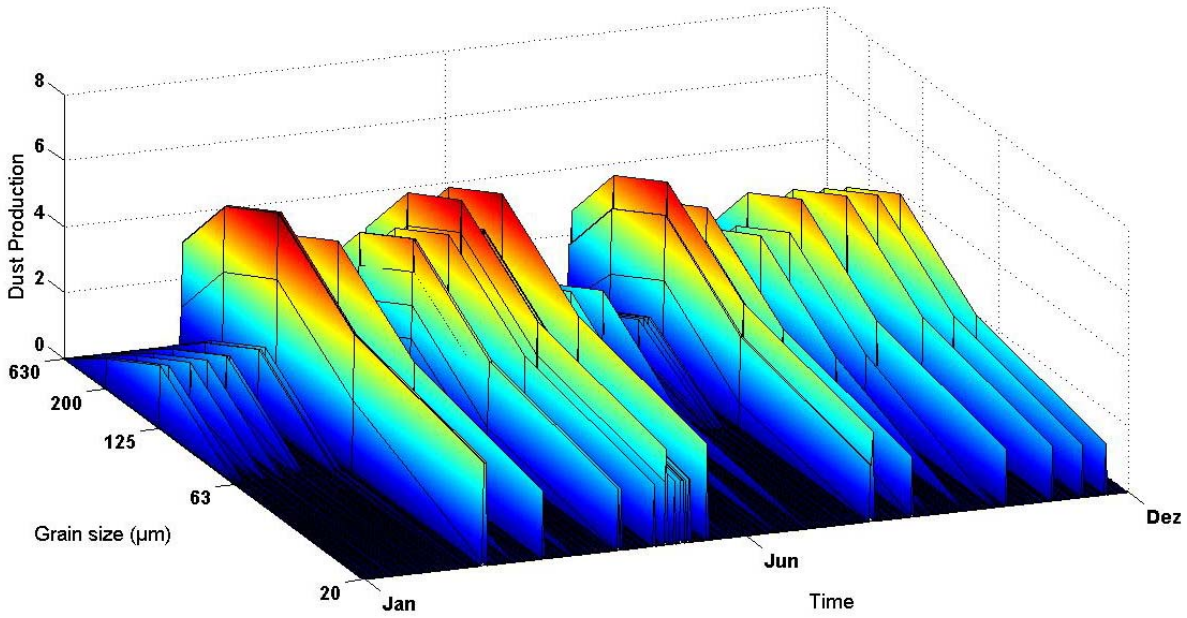

Fig. 4.9.: Particle production. Dependence of the grain size during time

The particles of different grain sizes are due to the relation between their own roughness length and their total weight differently vulnerable for particle emission. That causes a different contribution to the total dust production depending on the grain size. The main contributors are the grain sizes of around $125\mu m$ and therefore the predominat peaks of dust production can be found at around this grain size. Basically this silt size grain fraction (up to $200\mu m$) was also detected as the dominated grain size in most of the sediment samples, which is a sign for the aeolian activity as the main geomorphological process in that region. In case of the Orog Nuur lake basin with the uncovered sediment there are explicit good conditions for particle emission. Furthermore it is assumed, that the dust production might be even more, because of the presence of the nearby sand dunes (fig.: 4.3) leading to a sand blasting. Coarse sand grains in motion have a high kinetic energy to crack the binding energy of the soil micro aggregates at the surface and increase the particle emission. In contrast, the basin of the depression south of the Icht Bogt mountain is only a very minor contributor to particle production. Most of the surface is covered with gravel and therefore protected against deflation. The grain size distribution of the surface shows a lower amount of silt. North of the orographic barriers Icht Bogt and Baga Bogt similar surfaces can be found. The proportion of vulnerable bare sediment is relatively small and the grain size distribution of the sediments similar (fig.: 4.2).

4.2.5. Diagnostic wind field

With the selection of the simulation area with an extension of 150 x 200 km and the corresponding subset of the digital elevation model (DEM), the wind values of the year 2001 (the year of the perfect dust storm) and the performance of the particle emission model (PEM) all necessary input parameter were generated to start the work flow of the particle dispersion simulation with LASAT®.

The first step is the calculation of the time resoluted diagnostic wind fields. They are a result of the calculations performed with the preprocessor program *Lprwnd* implemented in the LASAT® utilities. The grid resolution of 1 x 1 km and several different heights consider the topographical condition and calculate the Prandl layer to take the turbulences into account, as well a terrain corrected height of the boundary layer. The roughness length is set to a general parameter of $z_0 = 0.02$, and the values were taken from the anemometer at Bogt Horiult (ID 45200800, 1308m asl; fig.: 2.5). During the performance of the particle dispersion calculation the wind fields were calculated continuously, considering the values at anemometer hight. The figure 4.10 shows a separately visualized diagnostic wind field for a wind

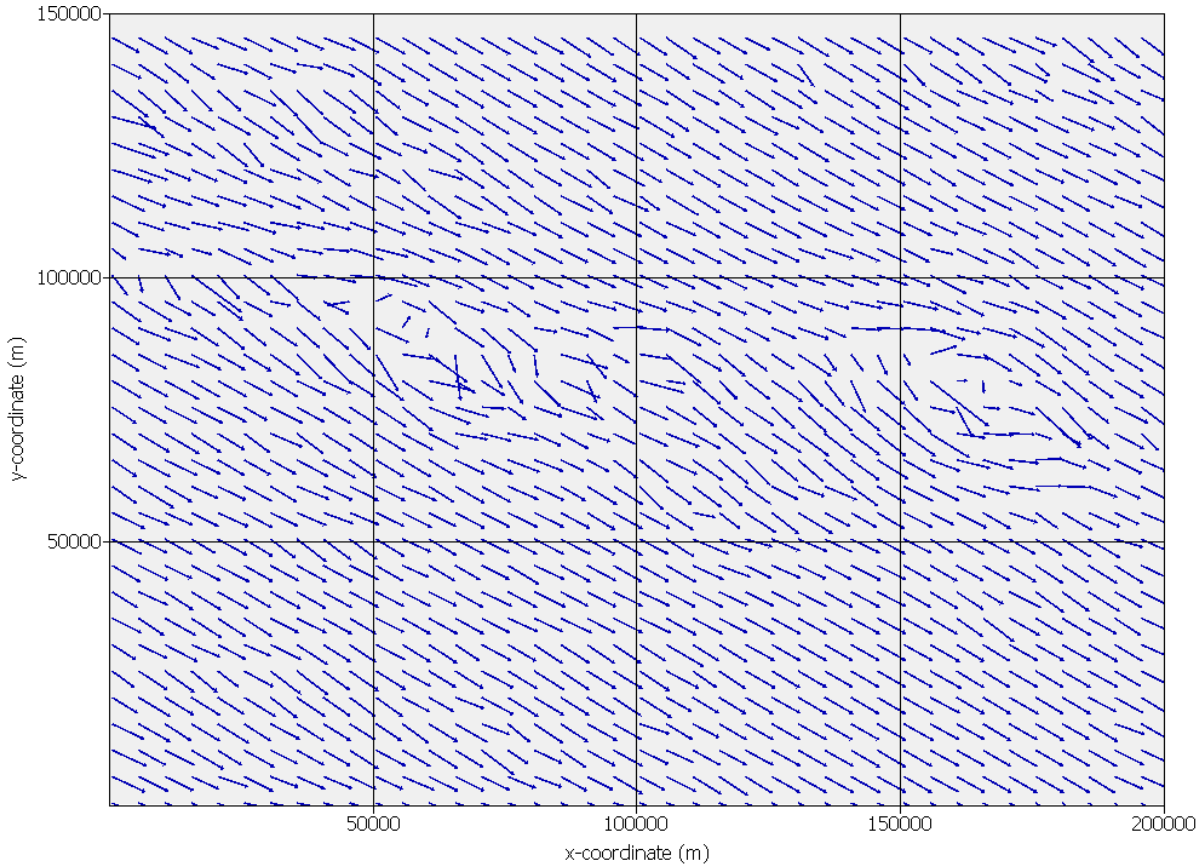

Fig. 4.10.: Diagnostic wind field. Wind direction = 315; Wind velocity = 4.3 m/sec at anemometer position

direction (α) of 315 (north west) and a wind velocity (U) of 4.3 m/s, which is the suggested value to calculate the diagnostic base wind fields.

The two orographic barriers of the mountains Icht Bogt (west) and Baga Bogt (east) are clearly detectable in the deflection of the general main wind direction. The air masses surrounding the mountains as well as the flow over the small pass area of the air masses is shown in the figure.

4.2.6. Simulation of particle dispersion

Besides the particle emission and their afterwards following spatial dispersion is a main part of the investigation to understand the actual aeolian geomorphodynamic in endorheic basins on the Mongolian Gobi desert. In the context of landscape development and the uncertainties regarding the connectivity of the basin sediments to the hill slope depositions the simulation of particle dispersion is a central part of this thesis. The simulation was performed with the values, generated as mentioned in the previous sections with field investigations during four field campaigns (fig.: A.5), laboratory analyses to determinate necessary input data for the PEM and numerical calculations to generate the input data for the particle dispersion model. They are basically meteorological parameter, particle emission values and additional data (fig.: 1.1).

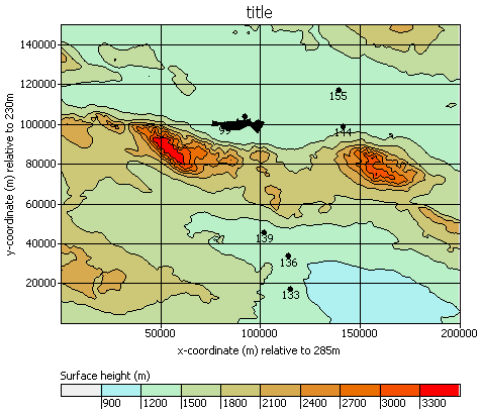

Fig. 4.11.: Simulated sites for particle dispersion. Single spots and the Orog Nuur lake basin as polygon source

Particles were simulated and distributed exemplary form single spots, to investigate the contributers of particle production and to enlighten the spatial transects of moving particles. The simulation area includes several geomorphological system parts; a lake basin (Orog Nuur), two orographic barriers (the mountains Icht Bogt and Baga Bogt) in the south of the Orog Nuur lake basin, further south a huge depression which is basically gravel covered and alluvial fans. All of these system parts have different surface conditions due to there pavement and grain size distribution of the surface sediment and sampled sites shows different responsibility for the particle emission. It worked out that the most responsible site for particle production (Site 99 and 141) in the study area is the Orog Nuur lake basin and therefore it is simulated as a polygon source as well (fig.: 4.11)

The particle emission differs from site to site, depending on the surfaces grain size distribution and the condition of the pavement as well as on the time. The differences of particle emission for the several sites are resulting in differences for the values of particle concentrations in the near ground air masses (0-3 m above ground) (fig.: 4.12). Within the concentration of the air mass, the final deposition is changing as well (fig.: A.25 to A.31). Besides differences of distances depending on the grain size, the figures A.33 (a) to (l) shows the differences during the year 2001 in monthly resoluted averages of deposition rates (in mg / m^2 / sec). The most aeolian activity in form of particle dispersion were simulated for April. It is also the time were the so called "perfect dust storm" could be observed (*Nakano et al.*, 2005). Exemplary simulations were therefore shown in figures A.25 to A.30 for the different particle sizes 20, 63, 125, 200 and 630 μm during April 2001 as an average of the particle deposition (in mg / m^2 / sec).

The conspicuous radial form of the dispersion resultes out of the low resolute values of the wind direction (α) input data. But nevertheless the observed main wind direction from the north-west can also be seen in the dispersion simulation. Furthermore a slight higher concentration in the luv site of the orographic barriers (the mountains Icht Bogt and Baga Bogt) were detectable. To focus on the different geomorphological system parts, the spots for the sites WP008099 and WP0808141 were the main contributor in the process interaction of aeolian geomorphodynamics. In contrast, the sites situated in the depression south of the orographic barrier respective at the alluvial fans north of the orographic barrier shows lower particle emission, thus they just play a minor role for the particle dispersion. To focus on the Orog Nuur lake basin, it is justified to simulate the shape of the lake as an polygon source with open bare, highly vulnerable, surface (fig.: A.14) and a grain size distribution represented for the WP 0708099.

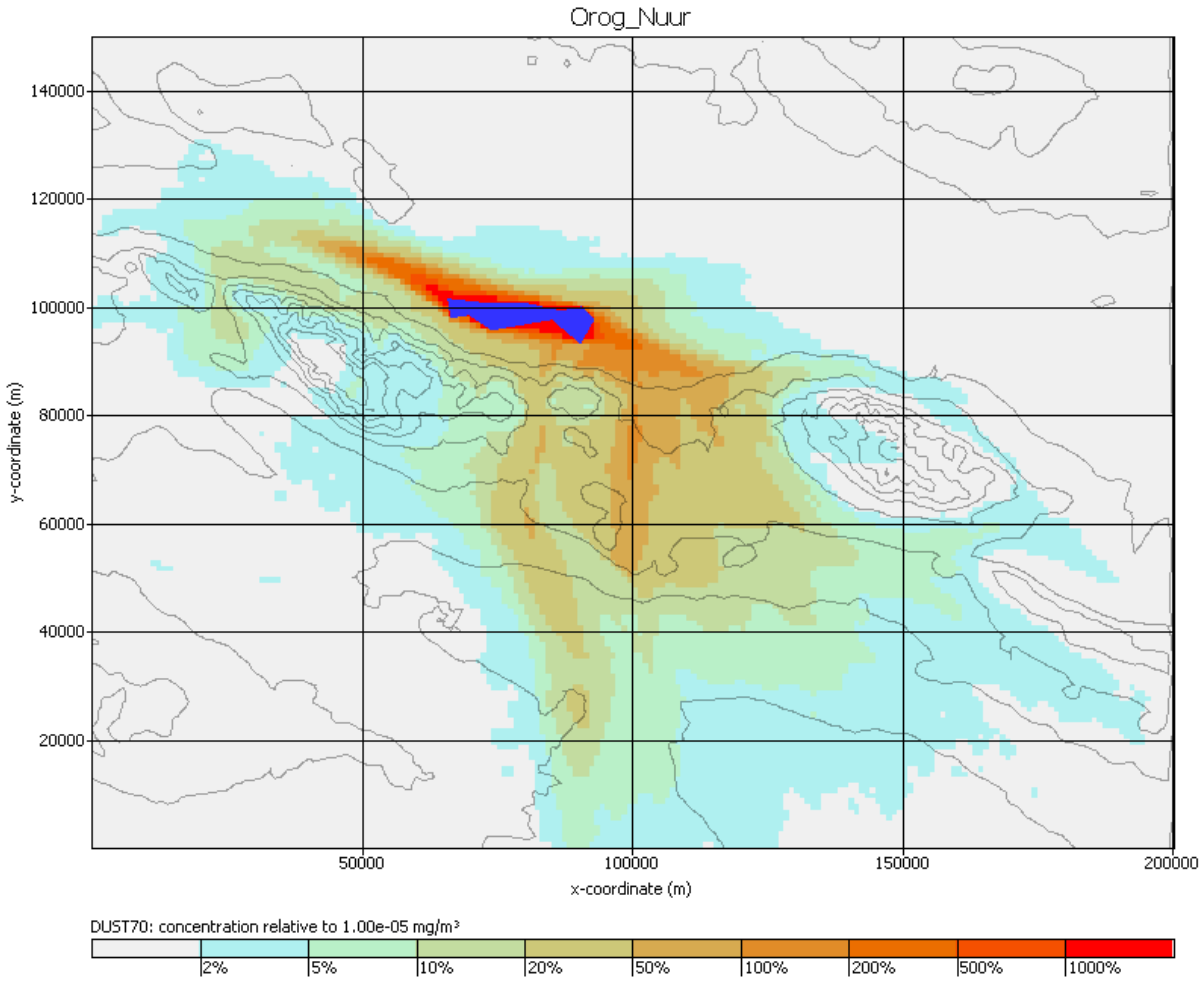

Fig. 4.12.: Dust dispersion

4.3. Geochemical and -physical properties of the surface sediments

During the performance of the simulation of either the PEM or the LASAT® calculations, several difficulties have to be handled and assumptions are unavoidable due to the relative few input data available for complex simulations. The concerning points will be discussed in detail in chapter 5.

Based on these expected uncertainties, the basic idea of this study was a concept with a tool to validate the modelled aeolian activity on a geochemical basis. By characterizing the geochemical properties of the surface sediment in the assumed dust source, it might be possible to track the geochemical signal along the simulated particle dispersion as a finger print.

The geology of the Mongolian basement rocks at the surface show a high variety of very different rock formations corresponding to several time periods (comp. 2.1.1).

Due to that complex geology it was very difficult to cluster the geochemical values significant to the different sources. It worked out, that the geochemical signals were very similar with reference to the grain size fraction or the source area, thus the initial idea had to be dropped and the responsible basement rock for sediment production were found.

The following sections are trying to fill the gap of uncertainties focusing on the geochemical fingerprints of the surface sediments, separated in grain size fraction sub samples. Until now only few preliminary investigations on the geochemical characteristics of the Mongolian Gobi surface sediments exist (*Baasan*, 2004). Some knowledge is already available resulting out of the dating problems of quartz samples originated from these regions. The contamination of the quartz with other minerals or elements in the light mineral fraction distracts the detectable signals (*Hülle et al.*, 2009).

The following results are also a history of several analytical steps, showing the difficult search to find a typical characteristic for each assumed source area.

Besides general questions of investigations to separate the bulk samples, dry sieving, pipett–method or particle laser scanning are compared, the fingerprints were searched by classical methods in the beginning and ended up with high end techniques to be improved in the future. Heavy mineral determinations and SEM images were used to get the first impressions of the actual aeolian geomorphodynamic. Furthermore X–ray fluorescence analyse (RFA) investigations were used to assign the sandy sediments to a rock formation.

Even single coarse sand grains were investigated in their distribution of element compartments. Focus-

ing the homogeneity of these single coarse grains, they were drilled with a laser application and the out coming particles of the laser drilling were analyzed by a mass spectrometer (MS).

Besides the investigation of trace elements, the focus is set on the quartz content of the sediments. Section 4.3.3 is dealing with the results of analysis of the light mineral fraction of several sub samples. Focusing the character of quartz in the light mineral fraction, basically two parameters were determined. One is the crystallinity index (CI) and the second is the electron spin resonance (ESR) of the E'_1 -center in a defect oxygen vacancies of the quartz crystal grid. All the methods have been described in detail in chapter 3.2.1.

4.3.1. Heavy mineral analyses

Heavy mineral analyses are the classical way of determining provenance regions, and were done as one of the first determinations during this study. The analyses were done of selected samples to trace regional differences and to relate the surface sediments to a rock formation of the surrounding basement. A map in the attachment (A.12) shows the spatial distribution of the sites taken for the heavy mineral determination. The determination shows the surprising result of a relative homogeneous determination of the

Table 4.1.: Values of the heavy mineral determination

	70835	**80435**	**80436rock**	**80436eros**	**70840**	**70841**	**70842**	**70851**	**70854**	**70858**	**80469**	**80470**	**80462**	**80466**	**80473**	**80474**	**70886**	**Camp04**	**NO 0303**
Anatase	-	-	+	-	-	-	-	-	-	-	+	-	+	1	-	1	-	-	-
Epidote	48	33	62	57	50	50	50	44	40	40	48	46	52	41	17	29	30	42	43
Mica	3	-	1	-	1	1	-	-	1	-	1	-	-	-	-	-	-	-	-
Garnet	3	8	16	9	9	4	6	12	5	12	7	8	11	9	7	6	5	5	5
gr Amph.	45	51	1	6	36	37	41	35	47	37	35	38	1	43	55	47	51	46	45
br Amph.	-	2	-	-	+	+	-	-	-	1	2	+	-	2	+	1	1	1	+
Rutile	-	-	-	+	-	-	-	-	-	-	-	1	-	-	+	1	+	+	-
Staurolite	-	2	1	+	-	1	+	1	+	-	1	1	-	-	-	-	-	1	-
Titanite	+	+	-	-	-	+	-	-	-	-	1	+	-	-	-	-	+	+	1
Turmaline	+	2	3	2	2	2	1	3	3	3	2	2	1	-	1	4	-	2	-
Zircon	+	2	15	25	2	4	1	6	3	7	3	3	34	4	18	11	12	1	6
Opaque	18	21	62	82	37	41	25	45	39	52	54	60	61	48	58	47	51	52	47
Alterite	51	47	75	61	39	41	41	33	49	40	45	30	32	40	53	45	43	49	55

occurring minerals. Remarkably high contents of epidote (17-62%) and amphibole (35-55% mostly the green variation) can be found in all samples regardless of the sampling site. Only the sediments 80436 taken directly from the cretacous rock formation in the assumed source region and 80462 out of the sandy region in Khongoryn Els have a content of only 1 - 6 % amphibole. Furthermore garnet (3-16%), turmaline (1-4%) and zircone (1-34%) were detectable in nearly all samples. Also mica and staurolite are present in a remarkable amount while anatase, rutile and titanite are represented in very low contents. The spectrum is typical for maphic and ultra maphic rock formations (*Okrusch and Matthes*, 2009).
It is necessary to point at the huge amount of opaques (composition mineral), which can be interpreted as an evidence for maphic genesis of the origin rock formation. As well as the very high amount of minerals unable to be determinated, due to the intransparent quality of the single grain in the polar microscope. These are indeterminable (alterite 18-82%) as well as the very high content of opaque grains in the samples, especially in case of the two samples from site 80436, reducing the plausibility of the determination. Nevertheless the spectrum is shows a very clear picture: that the contributing rock formation for particle production and thus basically responsible for aeolian geomorphodynamic is related to maphic and ultramaphic formations.

4.3.2. Element analysis

The concluded ideas of the heavy mineral determinations, that the surface sediments basically belong to maphic and ultramaphic rock formations, the investigations were furthermore focusing the elemental contents. The pointing out maphic or ultra maphic heavy mineral spectrum can correspond to the alkaloid granites wide spread in the area of interest (*Gerel et al.*, 2006; *Kovalenko et al.*, 2006) and can also be linked to the amount relations of the main elemental compositions. Besides the manually performed heavy mineral determinations, X–ray fluorescence analyse (RFA) investigations of 30 sub samples representing 17 different sites are shown homogeneous element relations without any significant variations due to the different location. Furthermore the data of the grain size fractionated subsamples are show no significant differences due to their grain size as well.
A typical line of the element amounts of Sc, V, Cr, Co, Ni, Cu, Zn, Ga, Rb, Sr, Y, Zr, Nb, Ba, Pb, Th and U is to be seen in fig.4.13. Some general characteristics of the element contents can be pointed out. The relative high variability of V (14-137ppm), Cr(1- for 200ppm), Co(2-11ppm), Ni (4-31ppb) and Cu(5-27ppb) is remarkable compared with the very constant amount of Ga ($\approx$ 10), Rb ($\approx$ 100) and Pb

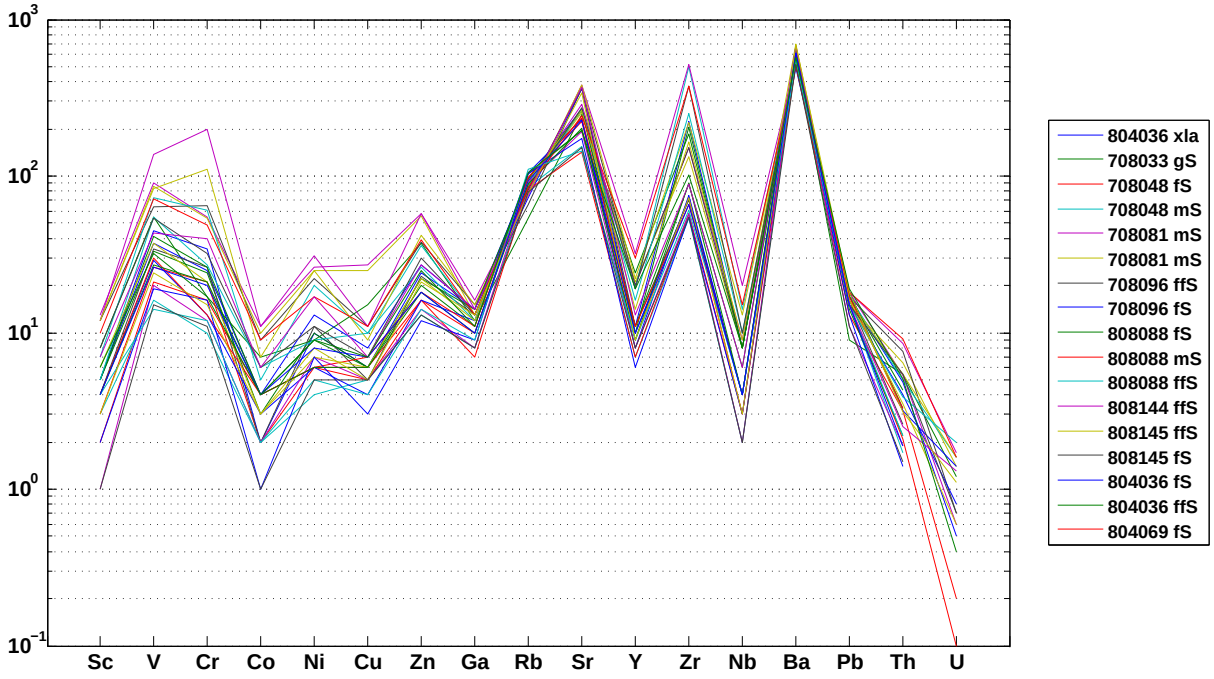

Fig. 4.13.: Values (in ppm) of the X-ray fluorescence analyses

(≈ 5) in the lower section of all the samples. The same homogeneity can be recognized by the values of Sr (≈ 250), and Ba (≈ 500), with a high amount in all samples. Furthermore Zr (55-514 ppb) and Nb (2-20 ppb) hold the same relations but show high variances. *Kozlovsky et al.* (2006) published the element contribution of the alkali granites situated in the area of interest and exposed to weathering.

While the RFA analyses are consolidating the assumption, that the feldspar granite rock formations are the main contributors to the sediment production in all study sites, the determination of the source regions' fingerprint has to be done in more detail.

For that matter single coarse grains were investigated. Laser applications were used to determinate the content of several elements in single coarse sand grains using an Inductively Coupled Plasma (ICP) MS. All values are related to the amount of ^{29}Si, which is set to the value 1.0 (see ch. 3.2.1).

The element resultes is resulting in a data spectrum showing a remarkable averaged amount of Na ($1,37;4,3x10^{-1};4,52^{-1};6,96x10^{-3}$) and Al ($2,99;2,68;5,47x10^{-1};5,04x10^{-1}$) for the samples 0733 0759 08114 and 0836. Especially in the 7033 and 7059 samples with are related to the Khongoryen Els dune field. Also Mg ($6,76x10^{-2};4,77x10^{-1};9,67x10^{-2}$ and $3,28x10^{-3}$) are related to Si in all samples is relatively high (fig 4.14). It is necessary to point out the standard deviation of the detected values for one site. With the values up to $\sigma 4,33$ in case of Al the grains show a very high internal inhomogeneity.

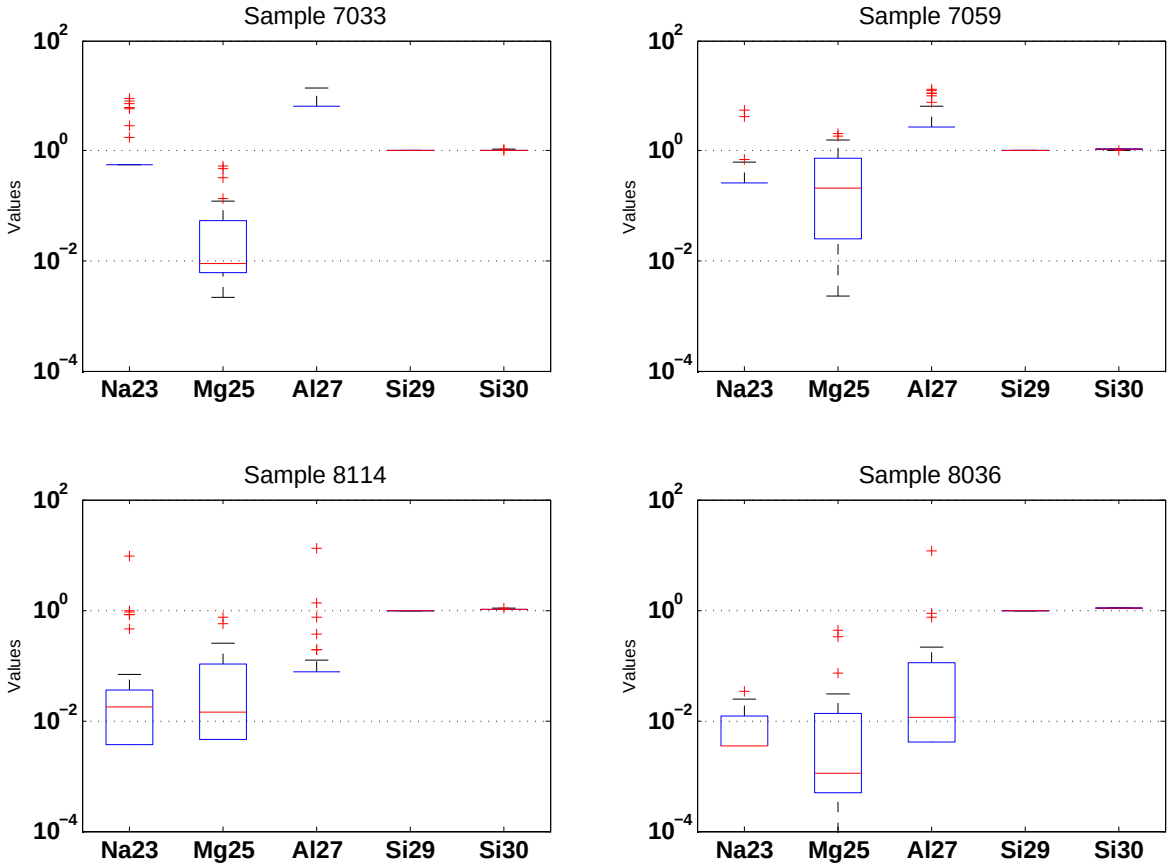

Fig. 4.14.: Single grain determination. Values of the main elements

While performing the investigation, the heterogeneity could be seen by high magnification as single intrusions of different colour values.

Na, Mg and Al are the main components of the feldspar mineral Albit or related minerals (*Okrusch and Matthes*, 2009) which have also been detected during the dating performance of Khongoryn Els dune sand samples (*Hülle et al.*, 2009). Furthermore elemental components of Fe (averaged with values of $1,10x10^{-1}$;$4,5x10^{-1}$;$1,06x10^{-1}$;$7,93x10^{-2}$ for the four sites 0733; 0759; 08114 and 0836) and the relative high values of Ti (fig. 4.15) are resilient hints underlining the detected Fe/Ti related heavy minerals titanium, rutile as well as the very high amount of amphiboles.The MS determination is representing high amounts of Sr ($1,51x10^{-1}$;$1,72x10^{-1}$;$1,1x10^{-1}$;$2,05x10^{-2}$), Ba ($4,99x10^{-2}$;$5,04x10^{-2}$;$3,57x10^{-2}$ and $1,32x10^{-2}$) and Zr ($6,66x10^{-2}$;$3,64x10^{-2}$;$1,44x10^{-2}$;$6,98x10^{-3}$) which have been already detected with the RFA investigations. But the resolution is due to the technique much more in detail and can be related to several other elements investigated in the single grains. Besides relative high values of Sr, Ba and Zr, in case of the Khongoryn Els samples (7033 and 7059) the amounts of Y ($1,63x10^{-2}$

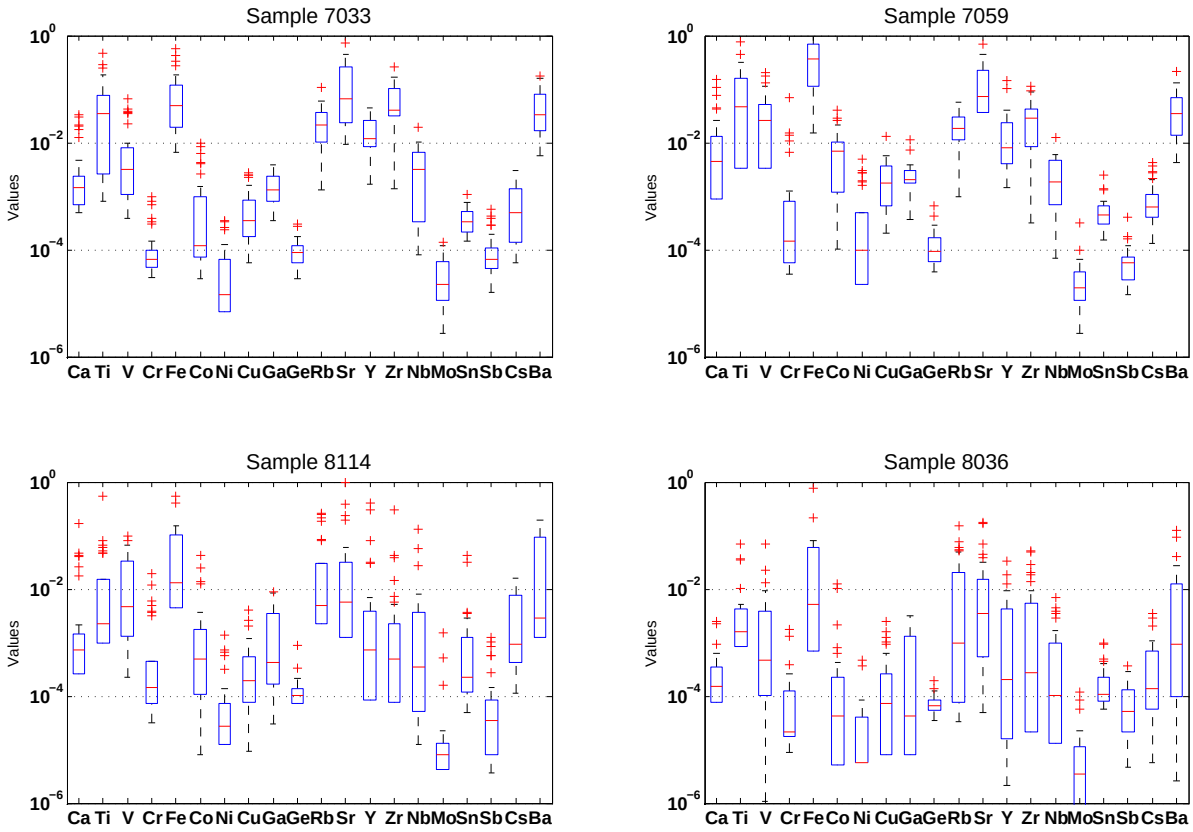

Fig. 4.15.: Single grain determination. Values of trace elements

and $1,93x10^{-2}$) and Rb ($2,63x10^{-2}$;$2,22^{-2}$) are higher than the samples 08114 and 0836 ($2,19x10^{-2}$ and $3,65x10^{-3}$ for Y and $4,89x10^{-2}$ and $1,83x10^{-2}$ for Rb). A slight variation is also detectable for the amount of Co. With an approximately equal value for the samples 7033 and 8114 ($1,37x10^{-3}$ and $3,78x10^{-3}$) a high value is characterizing sample 759 ($8,73x10^{-3}$) and a low amount in case of sample 0836 ($9,3x10^{-4}$). These slight varieties are besides the different standard deviations, which are generally much higher in case of sample 8114 and 8036, one of the few differences of the study areas. Some general remarks have to be pointed out furthermore; a low amount of Ni ($5,98x10^{-5}$,$7,08^{-4}$;$1,47^{-4}$;$4,29^{-5}$) Mo($3,93x10^{-5}$;$3,58x10^{-5}$;$8,08x10^{-5}$;$1,35^{-5}$) and Sn ($3,97x10^{-4}$;$5,68^{-4}$;$3,2x10^{-3}$;$2,09x10^{-4}$).

A classical way to interpret the value distribution of element amounts is the line spectrum of rare earth element (REE) (*Liang et al.*, 2009; *Yang et al.*, 2007). In case of the four sites, the REE are showing a typical shape of the light to the heavy rare earth elements. Besides this decreasing line of the rare earth element content significant to the element size, the typical negative Eu anomaly was found. But the Eu anomaly is just in a slight development (fig. 4.16). In case of sample 8114 the amount of Sm are even

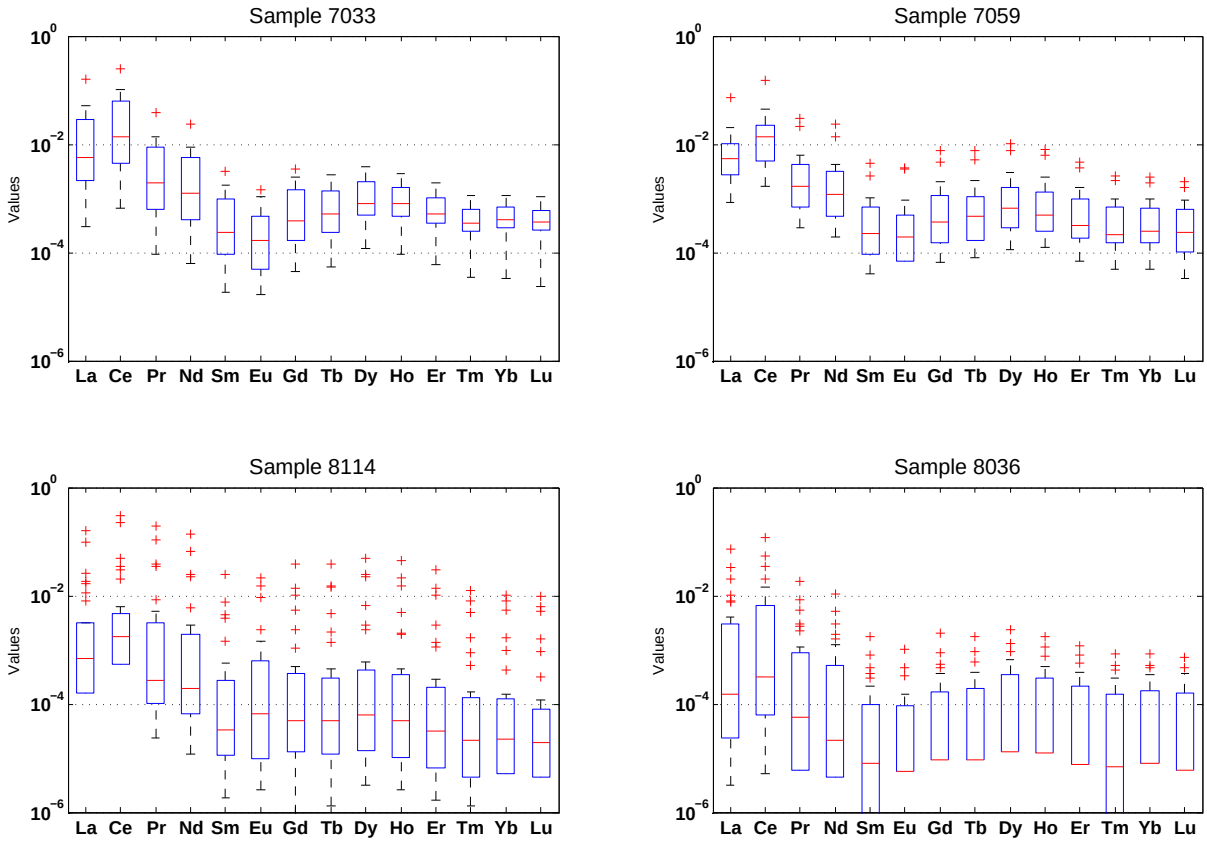

Fig. 4.16.: Single grain determination. Values of the rare earth elements

lower ($5,84x10^{-4}$). As well as for the most elements already mentioned, the standard deviation are much higher in case of the samples 08114 and 08036.

In fig. 4.17 the values of the elements Hf, Ta, W, Au, Tl, Pb, Bi, Th and U are graphically visualized. Remarkable difference is the low amount of Hf ($4,84x10^{-4}$) in case of the sample 8114.

The element spectrum of the single grain determination shows the relation to the maphic plutons situated in the working area (*Gerel et al.*, 2006) as well. The results show that these rock formations are mainly responsible for the sand production and related to aeolian geomorphology of the study area. Furthermore the low amounts of Cr, Co, V, Ni, Ge, Mo and Sb, agree with the findings of *Kovalenko et al.* (2006). But not the elements are fitting perfectly to the investigations. The high amount of Ba, Zr and Sr is remarkable but in contrast to a general alkaline granitoide spectrum of elements (*Kozlovsky et al.*, 2006). To show the slight differences of several source areas, coupling the values of certain elements is a common way to cluster the samples. For the most element couples, the values donï£¡t vary in a significant way. The slight differences of Al, Na, Mg, Zr, Hf, Ba and U / Th point out slight differences of the

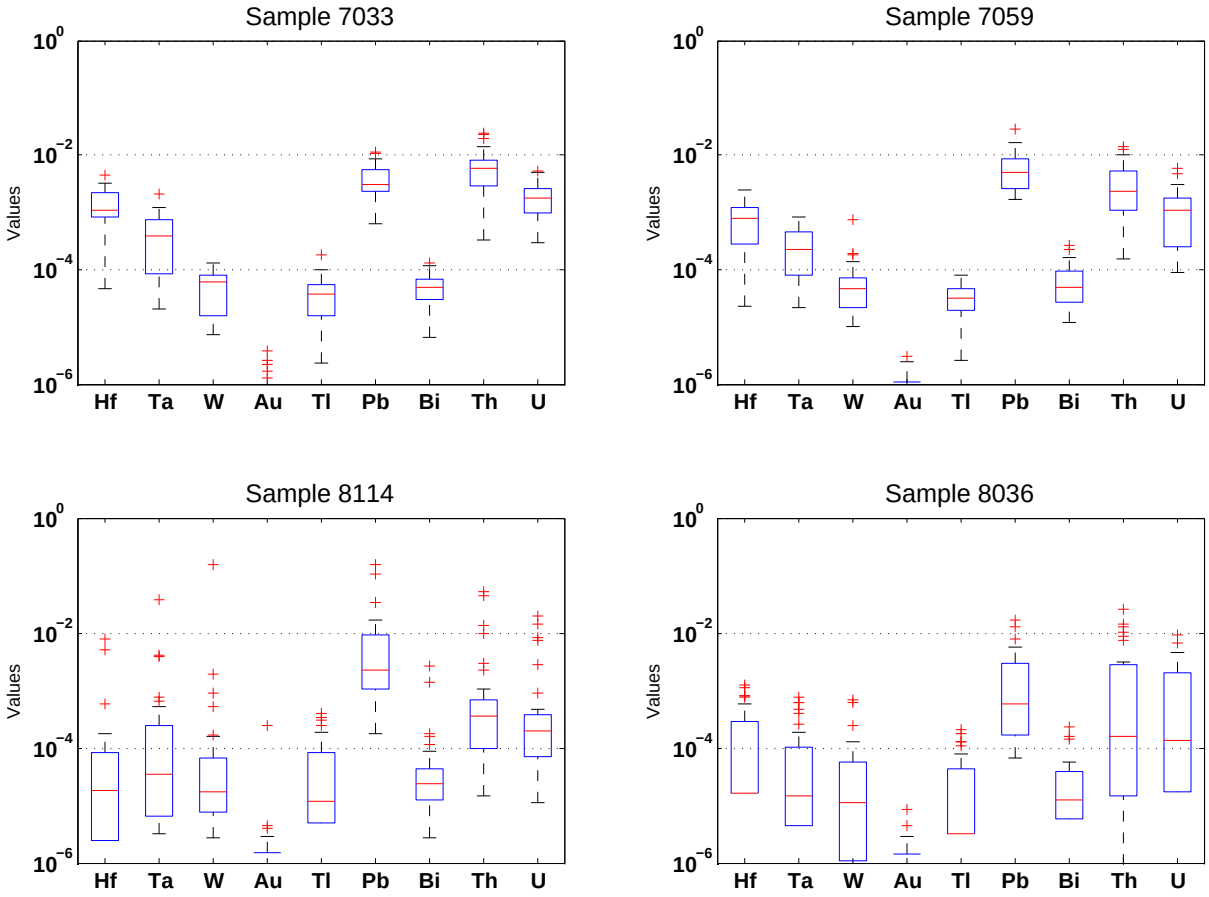

Fig. 4.17.: Single grain determination. Values of other trace elements

different source areas.

4.3.3. Quartz content, crystallinity index and electron spin resonance

After the investigations focusing on the heavy mineral determination and the investigations to determine the contents of several elements the focus was set on the quartz content itself. Quartz is relatively resistant for chemical weathering and therefore it was assumed, that the quartz content should be the main mineral consisting in the particle substrate. It was thought, that the determination of differences of the quartz component should be a possibility to detect significant differences in the samples. The focus of the quartz, determinate the properties of quartz was for the Mongolian Gobi first performed by *Sun et al.* (2007) and also investigated by *Nagashima et al.* (2007); *Maher et al.* (2009). This investigations were also focusing on the detection of source areas to investigate the transport mechanisms of particles. But

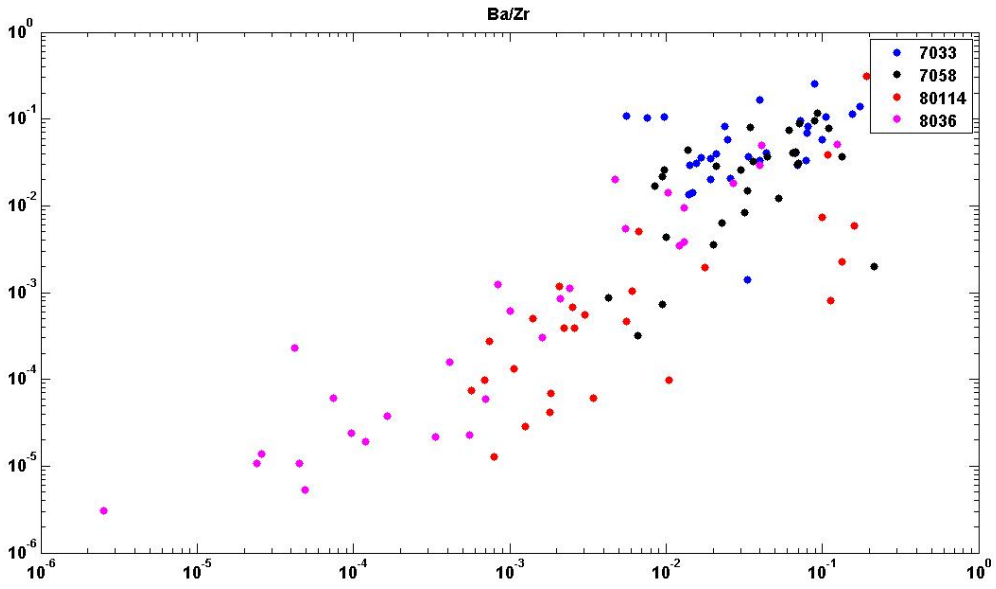

(a)

Fig. 4.18.: Coupling of amount values of elements Ba and Zr

still the number of samples out of the Mongolian Gobi is very low and therefore the necessity of further investigations are given; reducing the uncertainties of particle transport mechanism as well as improving the technique to investigate the ESR signals for challenges in geosciences.

In this study the focus is set on the E'_1 -center in the defect oxygen vacancies. The paramagnetic character of the quartz crystal allows the detection of the electron spin under a magnetic environment (comp.: refsec:labesr). Basically the signal is increasing if the number of E'_1 -centers in defect oxygen vacancies of the quartz crystal grid is increasing. Due to the stratigraphy of the geological formations the plutonic rocks are formed during several phases (*Jahn et al.*, 2009; *James H.S. Blight and Quentin G. Crowley and Michael G. Petterson and Dickson Cunningham*, 2010). Besides the surprising homogeneity of the the mineral and element distribution in the investigated samples, the signal of the ESR should show the differences of source areas or due to weathering processes (increasing of oxygen vacancies) differences of the separated grain sizes.

Unfortunately the search of clusters were not showing a significant difference. It was already mentioned in the element analyses that a high content of Al, Na, Mg and Fe lead to several other minerals. They have to be related to the quartz crystal structure and can by caused out of the development processes of the granitoide rocks. High temperatures ($1000 - 1100°$) and several melting phases (*Jahn et al.*, 2009) can be responsible for the contaminations of the minerals and the unstructured grid system. The quartz

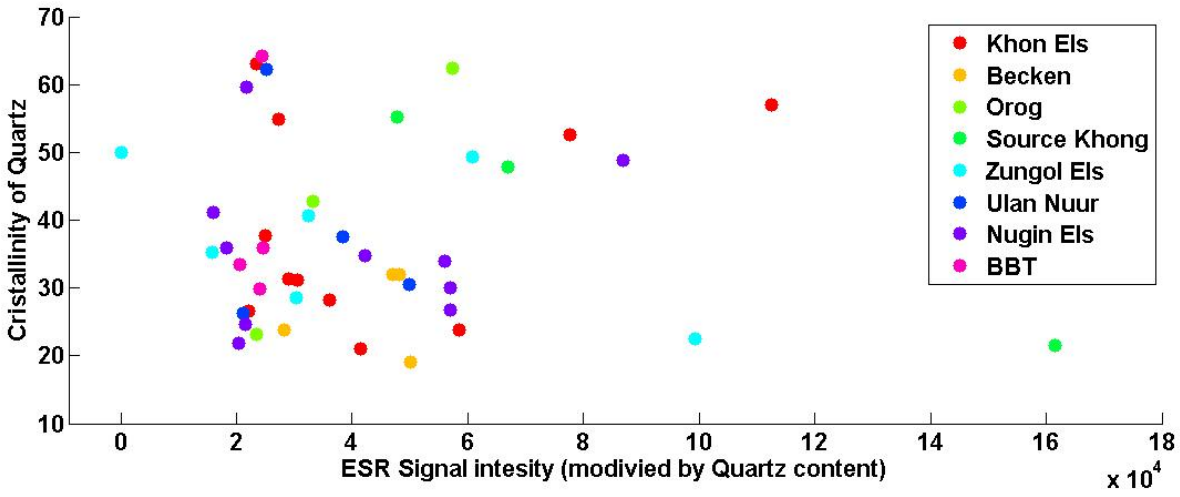

Fig. 4.19.: Coupling of ESR signal intensity (Quartz content modified) and the Crystallinity of Quartz

content even in the quartz enriched light mineral fraction and the averaged amount of quartz crystals is astonishingly low with values of 35 - 40 % for the differnt grain size fractions (fig.: A.21). The values are nesseary to equalise the later on following ESR signal.

A similar unsatisfactory picture is obtained out while determining the crystallinity index (CI). Uncertainties of the values (A.3) in case of a low CI for the quartz standard and high uncertain variations of the grain sized fractionated light mineral sub samples can be recorded. A clear picture is not really detectable.

Furthermore, the electron spin resonance (ESR) were conducted for several samples. The determinated value results out of the peak to peak difference of the detected signal line, while performing the investigation. To make sure every possible oxygen vacancy is trapped by an electron, the samples were radiated in advance. But even radiated samples were increasing the signals just in a very slight way (A.20). That matter can either be a sign for no defect oxygen vacancies or the radiation were performed with a too low intensity. The shape of the lines of the radiated samples can be found in the attachment (126). The signal had to be modified depending at the determined quartz content. This modified ESR signal values can be coupled with the values of the CI to cluster the samples significantly due to their corresponding source as suggested by *Sun et al.* (2007). Even with the modified ESR signal intensity due to the quartz content, the coupling with the crystallinity index of the quartz do not cluster a significant picture; neither due to the source region (fig.:4.19) nor in context of the grain size (fig.: A.24), fractionated sub samples.

Thus there is no significant picture detectable in the ESR signal intensity as well as for the crystallinity index in contrast to the very homogeneous values in case of other geochemical properties. Also the values connected to the quartz structure vary enormous (fig.: A.23 and figure A.22).

5. Discussion

The thesis is a part of a DFG - Project focusing on the landscape development in endorheic basins of the Mongolian Gobi desert. It points out the main ongoing phenomenon of aeolian geomorphodynamic in context of landscape development.

The concept of the thesis, as outlined in the introduction, was based on the idea to combine modelling techniques with laboratory and field investigations to understand the process interaction in more detail and simulate the phenomenons with higher precision. Therefore this chapter is divided into two main sections. In the first section the several steps done to determine the required input data to calculate the particle production of the surfaces and to simulate the motion of particles is discussed in detail. The second section deals with the results of the geochemical fingerprint.

5.1. Modelling of aeolian geomorphodynamics

The following subsections discuss the single steps used in this thesis to simulate particle dispersion on a regional scale. These steps are the determination of particle production, the modelling of diagnostic 3D wind fields and the calculation of particle distribution. The required input parameter are the grain size distribution of the surface particles, the gravel cover and some additional soil parameter (pH-value, contents of organic matter and carbonate) for the particle production calculation. Wind velocity and wind direction are needed for the distribution calculation and additionally, precipitation respectively soil moisture to calculate the moisture corrections. Furthermore atmospheric temperature gradients were taken to investigate the atmospheric stability. These input parameter were taken to calculate several other necessary values. The uncertainties or items to consider are discussed in the following subsections.

5.1.1. Diagnostic wind field

The main problem of modelling process interactions for selected regions is the availability of usable data. Despite the sparsely populated region, the spatial resolution of Mongolian governmental weather stations is, compared to other desert regions, very high (fig.: A.2). They were built in the $60^{th} - 70^{th}$ during the Soviet occupation. Three to five, or even more governmental employees observe and measure a variety of meteorological quantities at fixed times of the day (every 3 and 6 h, respectively). During the expeditions in April 2008 and in August 2009 I visited several stations and got into contact with the meteorologists. The stations are generally in good condition and the governmental employees are proud of their work. These are necessary requirements of a trustful data set. Nevertheless the delivered data sheets had several inconsistencies. It was tried to get rid of them while building up the database. But no reference is available to validate the values. Obviously the main phenomena are determined in a way correct enough to perform the simulations. Nevertheless some conclusions have to be pointed out. The time resolution every three hours is in case of the wind conditions general very rough and the precision of the values due to the manual determination just an objective value with uncertainty. Furthermore wind direction values are determinate stepwise, while the step range is changing from station to station, or even during several time periods within one station. The star form shown in the resulting simulation maps of dust distribution are resulting from the low determined stepwise values. Furthermore the station itself chosen for the diagnostic wind field simulation (ID 45200800) is situated south west of a small hill. For determinate wind values the terrain should be flat $100m \cdot h_a$ (height of the anemometer) in radius around the anemometer. The small hilly terrain is influencing the wind direction in a small scale. Therefore the calculated wind fields have a general bias.

The Blackman Turkey frequency analysis points out two main wind seasons (fig.: 4.4), which is, due to the geographical position of the area of interest within the influence of the westerlies. Furthermore the averaged wind velocity of all stations in the area of interest during the day(fig.: 4.5), also show an expectable picture of increasing wind velocity while the development of a night boundary layer reduces the wind velocity at the near ground atmosphere. Therefore it is justified to take the data set of the governmental meteorological stations as a serious data set, yet keeping the uncertainties in mind.

Wind values are available for 10m above ground and detailed investigations of vertical wind profiles are missing. Besides the kite borne measurements of profiles up to 400m above ground during the expedition in August 2009, the dust development in case of horizontal air mass motion is connected with neutral atmospheric stability. The wind fields were calculated with a neutral stability in general. The generaliza-

tion is another uncertainty, leading the particle distribution away from reality.

The diagnostic wind fields were always calculated with the estimation of a neutral stability, which is an uncertain estimation because of the alternately variation of the energy balances during night and day. As shown in the generalized averaged daily wind velocity (fig.: 4.5) and the kite borne profiles, the deviance to the estimated logarithmic profile is given in most of the cases. For the particle dispersion coincidental to the particle emission, it is justified to calculate the wind field with an neutral stability estimation. The particle emission were calculated due to the wind friction velocity (U*) which is connected to the wind velocity (U). Particle emission is therefore justified to calculate with a neutral stability in case of high wind velocity. But in case of the following calm situation the sublimate airborne particles might distribute in a different order than the wind field is calculated for.

Furthermore the roughness length (z_0) is just generalized for one condition in the input parameter in LASAT®. The estimation of $z_0 = 0.02$ might be in a general calculation right, but certain profile investigations are missing for that value (*Darmenova et al.*, 2009).

Wind shears and microscale meteorological phenomena are neglected and the resulting error for the particle distribution has to be considered.

5.1.2. Estimation of particle production

The estimations of particle production assumed in the simulations were basically made in context of the grain size distribution of the surface sediment, their gravel cover and the soil moisture. Several aspects were not taken into account, and have to be mentioned in further invsetigations.

A very substantial suggestion is published by *Marticorena and Bergametti* (1995) and improved in several further investigations. The theoretical equation are based on investigations in wind tunnels, improved in the Sahara desert and also validated experimentally in the Mu Us Desert of China (*Mei et al.*, 2006). It is a composition of three physically explicit submodes. A very important parameter is the saltation flux (F_h) leading basically to the sand fraction of the sediment. The F_h is determined with the saltation model (5.1) describing basically the kinetic energy of sand grains in motion as a factor.

$$F_h = E \cdot C \cdot \rho_a / g \cdot U^{*3} \int_{Dp} (1+R)(1-R^2) \cdot dS_{rel}(D_P) \cdot dD_p \tag{5.1}$$

As it has been done by determining the dust production factor for the simulations in this paper, the

saltation model 5.1 is also taken the fraction of erodible surface (E), wind friction velocity (U*), U_t^* and the D_p into account. Furthermore a consideration of the air density (ρ_a) as well as the Reynolds number (Re) are noticed as important factors to calculate the saltation flux. C is a dimensional constant and the acceleration of gravity (g) can be taken as the international convention of $9,81 m/s^2$.

The value of the saltation flux is taken in their suggestion to calculate two physically sandblasting sub models; (5.2) to determinate the dust number flux (N_i) and (5.3) to determinate the F_p where N_i is a necessary input parameter.

$$N_i = \beta / e_i \int_{D_{p=0}}^{\infty} p_i(D_p) \cdot dF_h(D_p) \tag{5.2}$$

$$F_{dust,i} = \pi \cdot \rho_p \cdot d_i^3 / 6 \cdot N_i \tag{5.3}$$

In case of using this kind of equation a huge number of input values are considered.

But still more factors are influencing the aeolian geomorphodynamic, focusing the sand and dust transport. Soil moisture is one of the very important values to be considered. Different equations to taking into account the moisture correction were suggested in literature (*Shao and Dong*, 2006; *Fecan et al.*, 1999). The main effect of moisture is related to the clay content in the soil. The chemical structure of clay leads the particles to soak and increases the volume of the whole sediment body. Further more it leads the water to build hydrogen bridges creating aggregates. Thus the soil moisture is influencing the binding energy of the particles and while the soil water content is increasing, the potential dust production is decreasing *Ishizuka et al.* (2009). A suggestion to correct the particle production is published by *Fecan et al.* (1999) as a function of gravimetric water content and the proportion of clay (in %). It is suggested to determinate the threshold as a function of clay

$$w'(\%) = 0.0014(\%clay)^2 + 0.17(\%clay). \tag{5.4}$$

Differences in clay mineral compositions, which have a slight influence of the water behaviour. This was not taken into account. If the water content (w) is lower than the calculated threshold the water content correction ($H_{(w)}$) is equal to 1, but if the value of the water content is more or equal to w', $H_{(w)}$ can be calculated with

$$H_{(w)} = \left[1 + 1.21(w - w')^{0.68}\right]^{0.5} \tag{5.5}$$

Especially for the summer period while the wind conditions are under the south eastern monsoon influence with a higher relative humidity, higher precipitation and a higher soil moisture can be assumed. The estimated dust production is obviously overestimated for this month. The aggregate state of water is not taken into account, thus freezing is not considered. Freezing has two effects on context of aeolian geomorohodynamics. First the binding energy of the particles are increasing. Due to the hygroscopy of ice nuclei, the soil matrix is drying out, witch leads to a reduction of binding energy of particles. To the best of my knowledge, there are no investigations focusing on dust production in context of freezing by low soil moisture, which can be expected in case of the arid region.

Fig. 5.1.: Protection of the surface by gravel cover

The protection of gravel which reduces the vulnerability in two ways, has to be pointed out. First by the direct covering and within direct protecting of the sediment, second by reduction of the friction velocity due to a different displacement height due to the topography of the covering gravel (fig.: 5.1). Besides the displacement height the covered gavel has a different roughness length compared with the sandy or silty sediment surface. Therefore different turbulences and friction velocities and drag partitions have to be calculated. Thus the particle production has to be corrected according to the two surface conditions. A suggested equitation (*Darmenova et al.*, 2009) takes that point into account, by calculating a drag partition correction ($R_{(z0,z0s)}$) with as a function of the both overlying topographical characters (z0 and z0s)

$$R_{(z_0,z_{0s})} = 1 - \frac{\left(\frac{z_0}{z_{0s}}\right)}{\left[0.7\left(\frac{10cm}{z_{0s}}\right)^{0.8}\right]} \tag{5.6}$$

The simulation results in this study were calculated only while fraction of erodible surface (E) was taken as an product of the particle emission model (PEM) into account. Without including the correction factor $R_{(z0,z0s)}$ the particle production of surfaces is overestimated exponential to the size of the covered gravel. The surface roughness is more responsible for the particle production frequency because it is influencing the erosion threshold while the rate of dust production is related to the grain size distribution of the surface sediment.

It is assumed, that the particle emission is therefor overestimated in case of the sites situated in the

depression as well as in case of the sites situated at the alluvial fans. The grain size distribution is a problem by its own. In this thesis three types of determination methods were used, and all of them have their specific advantages and disadvantages. Particles of a sediment are normally in any case of aggregation with each other. Especially the clay content is responsible for stabilization of the surface, by building soil microaggregates. At the SEM pictures, the contamination of clay can be seen. In the simulation, thresholds of particles were suggested, but the grain size distribution values were taken from the particle sizer. To perform this analysis, the sample was prepared in a water solution, and all existing aggregates destroyed. The same happened while performing the Koehn-Pipette-method. Therefore the simulated particle distribution is in case of the grain size fractions calculated with an error, while not dealing with the soil microaggregates size distribution. A parallel dry sieving is shown the under- or over-estimations of the different grain sizes, depending on the investigation method. A missing value is the micro soil aggregate grain size distribution of air borne particles. The collections of this airborne aggregates were already done, but due to the administrative problems, the investigations had never been completed. This is one of the goals for the future.

The binding energies increase not only in dependency from the presence of water or clay, but also with the amount of salt. Due to the geochemical evidences, for all of the sites the geochemical properties are connected with the acid feldspar rich alkaline granites the pH values (fig.: A.7) have to be connected with salty conditions at the surface (*Pankova*, 1994). Thus the salt also leads to increase the binding energy of the single particles. The salt content in the surface layer depends on the lateral water movement. Thus the binding energies may vary due to the slight drainage system. So there is high uncertainty about the connected binding energies which is related to an error for the estimation of the dust emission rate.

Fig. 5.2.: Dust devil as contributor to particle production

In case of no wind velocity, the presence of dust devils (fig.: 5.2) lead to an underestimation of the particle production. Especially during summer, when the soil temperature increases of more than 40° C, and no wind velocity is detectable at anemometer position dust devils increase the dust loading of the air. Due to the orographic form of the depression basin south of the Icht Bogt Mountain as well as the alluvial fans in

general, these are prime locations for the development of dust devils, which are absorbing the small (in a range of $< 125\mu m$) particles out of the surface. There are only a few publications (e.g. *Ansmann et al.*, 2009) focusing the contribution of particle emission caused by dust devils, while due to the gravel covering and the modified wind friction velocity (U*) for vertical wind velocity (U) it is expected that the dust devils play an even more important role in the Gobi regions with gravel cover and unstable stratifications during the day than they do in other desert regions.

5.1.3. Simulation of particle dispersion

Particle distribution on such a regional scale has been for the first time realized in the Mongolian Gobi desert. Other regional calculations focus on much larger scales (eg. *Darmenova et al.*, 2009). Several errors are obviously taken into account for the simulation in this thesis. Comparing to the field observations and satellite pictures, the spatial distribution of dune fields and barchans or the differences in grain size distribution of the several samples are not regarded to the simulation results. The already mentioned errors in the wind field calculation lead inescapably to errors in the calculation of particle dispersion. The errors of the time resolute and spatial differentiated particle production out of the several surfaces sites amplify these errors.

It is assumed that the dust production in case of the basin region with the dense gravel cover is overestimated, and the particle distribution might be less taken into account for this region. To the general supposed roughness length, the wind field and the wind friction velocity (U*) are over or underestimated. The resulting errors for the Prandl layer, turbulences near ground or the calculation of the boundary layer amplify these errors in case of the particle distribution. Especially in case of the generalized particle production of the single spot sites, the underestimation of turbulences lead to very straight transects. Dust distribution in case of the situation on 15.08.2007 were reported in a different spatial distribution.

The star formed radial spreading from the single spots represent the determination of the wind direction (α). For detailed particle distribution calculation this rough resolution is definitely too low.

5.2. Geochemical properties

The basic idea of this thesis was a coupling of computer based simulation techniques with field and laboratory investigations. Besides the collection of input data for several parameters needed for the simulation, a laboratory based geochemical fingerprint of the sediments were searched.

5.2.1. Mineralogy and element distribution

Until now only few rough investigations on the geochemical characteristic of the Mongolian Gobi surface sediments exist (*Baasan*, 2004). Some knowledge is already available resulting out of the dating problems of quartz samples originated from these regions. The contamination of several minerals in the light mineral fraction distract the detectable signals (*Hülle et al.*, 2009).

It worked out that the geochemical characteristics of the different contributers of particle production in the area of interest are generally very similar. The spectrum of heavy minerals, the element distribution as well as the quite difficult investigations of the ESR signal intensity of the quartz content point out Fe rich maphic and ultramaphic structures for the general particle source. The general structure of the geology in that region is very uncertain and the particle contributing basement rocks are part of the Central Asian fold belt which represents one of the largest of the word. The detailed part where the area of interest is situated, belongs to the Gobi–Tein Shan rift as a structure of the Central Asian fold belt. The area is characterized by a high tectonic activity (*Vassallo et al.*, 2005, 2007; *Demoux et al.*, 2009a,b) and a high presence of volcanic basaltic rock formations (*Yarmolyuk et al.*, 2007). The area is characterized by alkaline granites with high contents of feldspar. The determination of maphic and ultramaphic heavy minerals are underlining the occurrence and responsibility of these rock formations for particle distribution. Furthermore the difficulty for the determination of the electron spin resonance (ESR) signal is leads to the high contamination of Fe, which irritates the signal of the E'_1 -center in defect oxygen vacancies. Furthermore the high content of alterite (multi mix minerals) point out the melting processes of the fragments of the old crust of the Paleo-Asian Ocean, which leads to the plutons or as their volcanic equivalents to the basaltic hot spots situated in the south Khangei. The high presence of alterites also point out a short transport way. The sharp edges of the single grains, shown in the SEM pictures supporting such assumption too, as well as the missing of crust contamination on the surfaces of the single grains.

The pH values the sediments are basic for all samples even when the $CaCO_3$ content is very low. That is in contrast to alkalic rock formation as source region, which are extremely acid, but regarding to the salinity as well as the presence of carbonate, the pH values can be equalized.

6. Conclusion and outlook

In context of landscape development the aeolian geomorphodynamic in endorheic basins of the Mongolian Gobi desert focus particle sizes in a range of 20 – 630μm. A huge number on different process interactions has to be consider. Due to high end software and a realistic possibility to compute such a complex phenomenon on a standard computer, modelling of particle emission and their dispersion is a high potential tool to understand the process of aeolian geomorphodynamics in detail. In this study the interaction of basin sediments and hill slopes depositions suggested by *Grunert and Lehmkuhl* (2004) are simulated for an exemplary study site in the northern Gobi desert in south Mongolia.

There are two expected wind seasons during the year; in spring and in autumn, when the westerlies influence the weather conditions in the study site. The more important period is the spring time due to higher wind velocities (*Han et al.*, 2008b) in combination with low soil moisture and the absence of vegetation. High wind velocities are expected from the north west due to the westerlies influence and the orientation of the mountain ranges as orographic barriers. Soil moisture increases during the summer and reduces the particle emission due to an assumed increasing of the binding energy of the micro soil aggregates during that time. In winter the influence of the Siberian-Mongolian anticyclone reduces the wind velocity, so the particle emission and their near ground concentration is relatively low. The radial picture of the particle distribution is a result of the relatively low resoluted wind direction determination. Furthermore the relatively low resoluted values of the wind velocity contain uncertainties; therefore errors in the modelled scenarios have to be expected. Higher resoluted data of wind conditions recording the weather conditions in the Gobi region are urgently needed in the future. But still the already available data set is relatively well resoluted (in time and space) compared to other remote desert regions in the world and therefore has a high potential to be used for further investigations.

Besides the wind conditions with their main wind period and relatively regular annual frequency, the different geomorphological system parts differ in their responsibility to their contribution of particle emission. The main contributors are the highly vulnerable lake sediments in the dried out endorheic lake basin, but still the alluvial fans are contributing to the total particle concentration of the near ground air

masses too. Due to the main wind direction the dispersion of the particles move in a south west direction, but the simulation shows a dispersion to other directions too. The basin as the main contributers emit particles during spring, while the lack of precipitation dries out the lake basin surface. Furthermore the alluvial fans contribute to the total particle production as well, independent of the lake water level. The transect from the bottom of the valley up to the alluvial fans shows a shifting in the grain size distribution. With an increasing of the altitude while shifting to the alluvial fan the silt fractions dominate the spectrum in contrast to the sand dominated spectrum in the valley. While performing the grain size fractionated particle dispersion it can be seen that the grain sizes get separated. The fine sand and coarse silt fractions are deposited on the hill slopes, while the finer particles move into higher atmospheric layers and take part at the intercontinental transport (*Yumimoto et al.*, 2009).

Besides the relative low resoluted wind values as input data for the simulation and the expected error, the calculation of particle emission also shows several uncertainties. It may lead to overestimation of particle emission in case of the pavement covered sites and underestimation in case of the very difficult calculable kinetic energy saltation and reptation during sand blasting processes. This underestimation is assumed for the vulnerable lake sediment in the Orog Nuur basin due to its surrounding sandy sites. Still uncertainties have to be filled and the development of general equation as well as the necessary validation of the simulations by field investigation have to be processed. Validations or verifications can be realized experimentally with field observations of natural phenomena or by investigations for example with a mobile wind tunnel (*Fister and Ries*, 2009) to focus on the processes of dust emission under different surface conditions. One of the uncertain processes is related to the influence of freezing during the very cold winter in central Asia.

Besides the uncertainties of the influence of surface conditions and the process complexity of the particle production the micrometeorological investigations have to be improved. The kite borne investigations to evaluate turbulence, missing values of exact stability conditions, roughness length and the development of micro scaled boundary layers turned out to be a powerful equipment for less infrastructural regions. Besides the advantage of organizational efficiency, the kites can lift up several applications to investigate micrometeorological processes.

Even though the geochemical fingerprint is very difficult to detect, there must be some proxies, separating the different source areas from each other. The low quartz content was not expected in the beginning of the study but compared to the results of the heavy mineral determinations and the element analyses it can be concluded, that the granitoide plutons with their several melting phases are responsible for sedi-

ment production in general for the area of interest. Regardless the fact, that the ESR application so far has not pointed out a right separation of different sources, it might be a good tool to investigate the fingerprint of the sediments. The experimental preparation of the samples focusing on smaller grain sizes, removing the Fe content more consequently the signals should be presented in more detailed shape. First ideas were collected while testing a higher dose rate to trap the E'_1 - center into the oxygen vacancy. A radiation of 2.7kGy have already been performed with an electron accelerator (MicroDrome, Institute for nuclear physics, Mainz). The lines show an expected but different shape; so these proxy have to be investigated in more detail to understand the geophysical structure of the quartz crystal grid. Furthermore a focus on Sr and Nd or Pb isotopes can be set to investigate the isotopic differences. These differences as well as the character of the quartz crystal grid probably vary due to the different conditions during the formation geological facies as well as the age of the rock formation.

Nevertheless, in this thesis was worked out a huge number of input parameters for modelling particle dispersion on a regional scale in a very little investigated area. The recalculation of the particle emission, by taking into account several correction factors (e.g. for soil moisture (as a function of clay content) and drag partition) to avoid over- or underestimations of particle emission from different geomorphological system parts, fills several gaps on uncertainties in relation to aeolian activity in endorheic basins of the Mongolian Gobi. Furthermore the data set is usable for other investigations.

References

Alfaro, S. C. (2008), Influence of soil texture on the binding energies of fine mineral dust particles potentially released by wind erosion, *Geomorphology*, *93*(3-4), 157–167.

Ansmann, A., M. Tesche, P. Knippertz, E. Bierwirth, D. Althausen, D. Müller, and O. Schulz (2009), Vertical profiling of convective dust plumes in southern morocco during samum, *Tellus B*, *61*(1), 340–353.

Baasan, T. (2004), *Aeolian sands of Mongolia*, Baasan, Tudeviin.

Badarch, G., W. D. Cunningham, and B. F. Windley (2002), A new terrane subdivision for mongolia: implications for the phanerozoic crustal growth of central asia, *Journal of Asian Earth Sciences*, *21*(1), 87 – 110, doi:10.1016/S1367-9120(02)00017-2.

Barthel, H., G. Haase, and H. Richter (1962), Die Mongolische Volksrepublik, *Erdkundeunterricht*, *8*(9), pp. 288–318.

Batima, P. (2006), Climate change vulnerability and adaptation in the livestock sector of mongolia. a final report submitted to assessments of impacts and adaptations to climate change (aiacc), project no. as 06.

Batjargal, Z., J. Dulam, and Y. Chung (2006), Dust storms are an indication of an unhealthy environment in east asia, *ENVIRONMENTAL MONITORING AND ASSESSMENT*, *114*(1-).

Batkhishig, O., and F. Lehmkuhl (2003), Degradation und Desertifikation in der Mongolei, *Petermanns Geographische Mitteilungen*, *147*(3), 48–49.

Cari, L. J. (2004), Polyphase evolution of the East Gobi basin: sedimentary and structural records of Mesozoic-Cenozoic intraplate deformation in Mongolia, *Basin Research*, *16*(1), 79–99, 10.1111/j.1365-2117.2004.00221.x.

Chung, Y.-s., H.-s. Kim, J. Dulam, and J. Harris (2003), On heavy dustfall observed with explosive sandstorms in Chongwon-Chongju, Korea in 2002, *Atmospheric Environment*, *37*(24), 3425–3433.

Dagvadorj, D., L. Natsagdorj, J. Dorjpurev, and B. Namkhainyam (2009), Mongolia assessment report on climate change. (marcc) 2009.

Darmenova, K., and I. N. Sokolik (2007), Assessing uncertainties in dust emission in the aral sea region caused by meteorological fields predicted with a mesoscale model, *Global and Planetary Change*, *56*(3-4), 297 – 310, doi:10.1016/j.gloplacha.2006.07.024, northern Eurasia Regional Climate and Environmental Change.

Darmenova, K., I. N. Sokolik, Y. Shao, B. Marticorena, and G. Bergametti (2009), Development of a physically based dust emission module within the Weather Research and Forecasting (WRF) model: Assessment of dust emission parameterizations and input parameters for source regions in Central and East Asia, *JOURNAL OF GEOPHYSICAL RESEARCH-ATMOSPHERES*, *114*, doi:10.1029/2008JD011236.

Demoux, A., A. Kroener, G. Badarch, P. Jian, D. Tomurhuu, and M. T. D. Wingate (2009a), Zircon Ages from the Baydrag Block and the Bayankhongor Ophiolite Zone: Time Constraints on Late Neoproterozoic to Cambrian Subduction- and Accretion-Related Magmatism in Central Mongolia, *JOURNAL OF GEOLOGY*, *117*(4), 377–397, doi:10.1086/598947.

Demoux, A., A. Kroener, E. Hegner, and G. Badarch (2009b), Devonian arc-related magmatism in the tseel terrane of sw mongolia: chronological and geochemical evidence, *JOURNAL OF THE GEOLOGICAL SOCIETY*, *166*(Part 3), 459–471, doi:10.1144/0016-76492008-090.

Dill, H., S. Khishigsuren, Y. Majigsuren, S. Myagmarsuren, and J. Bulgamaa (2006), Geomorphological studies along a transect from the taiga to the desert in Central Mongolia–evolution of landforms in the mid-latitude continental interior as a function of climate and vegetation, *Journal of Asian Earth Sciences*, *27*(2), 241 – 264, doi:10.1016/j.jseaes.2005.03.006.

Dobrezow, N. L. (1992), Methamorphe Formationen Mongolei.

Dulam, J. (2005), Discriminate Analysis for Dust Storm Prediction in the Gobi and Steppe Regions in Mongolia, *Water, Air, & Soil Pollution: Focus*, *5*(3), 37–49, 10.1007/s11267-005-0725-0.

Fecan, F., B. Marticorena, and G. Bergametti (1999), Parameterization of the increase of the aeolian erosion threshold wind friction velocity due to soil moisture for arid and semi-arid areas, *Ann. Geophys.*, *17*, 149–157, doi:10.1007/s005850050744.

Fister, W., and J. B. Ries (2009), Wind erosion in the central Ebro Basin under changing land use management. Field experiments with a portable wind tunnel, *JOURNAL OF ARID ENVIRONMENTS*, *73*(11), 996–1004.

Fu, P., J. Huang, C. Li, and S. Zhong (2008), The properties of dust aerosol and reducing tendency of the dust storms in northwest China, *Atmospheric Environment*, *42*(23), 5896–5904, 1352-2310 doi: DOI: 10.1016/j.atmosenv.2008.03.041.

Gerel, O., S. Myagmarsuren, S. Oyungerel, B. Munkhtsengel, B. Batkhyshig, and S. Amar-Amgalan (2006), Structural and Tectonic correlation across the Central Asian Orogenic Collage: Implications for Continental Growth and Intracontinental Deformation. Abstracts and Excursion GuideARITCLE:.

Goudie, A. S. (2009), Dust storms: Recent developments, *Journal of Environmental Management*, *90*(1), 89–94.

Grunert, J., and F. Lehmkuhl (2004), Aeolian sedimentation in arid and semi-arid environments of Western Mongolia, *Paleoecology of Quaternary Drylands*, pp. 195–218.

Haase (1983), Beiträge zur bodengeographie der mongolischen volksrepublik.

Han, Y., X. Dai, X. Fang, Y. Chen, and F. Kang (2008a), Dust aerosols: A possible accelerant for an increasingly arid climate in north china, *Journal of Arid Environments*, *72*(8), 1476–1489.

Han, Y., X. Fang, S. Kang, H. Wang, and F. Kang (2008b), Shifts of dust source regions over central asia and the tibetan plateau: Connections with the arctic oscillation and the westerly jet, *Atmospheric Environment*, *42*(10), 2358–2368.

Harmel, C. (2010), Das Klima der Mongolei - Auswirkungen des Reliefs auf das Lokalklima in der Mongolischen Gobi, Master's thesis, Universität Mainz.

Heintzenberg, J. (2009), The samum-1 experiment over southern morocco: overview and introduction, *Tellus B*, *61*(1), 2–11.

Helo, C., E. Hegner, A. Kroner, G. Badarch, O. Tomurtogoo, B. F. Windley, and P. Dulski (2006), Geochemical signature of paleozoic accretionary complexes of the central asian orogenic belt in south mongolia: Constraints on arc enviroments and crustal growth, *Chemical Geology*, *227*(3-4), 236–257.

Hülle, D., A. Hilgers, U. Radtke, C. Stolz, N. Hempelmann, J. Grunert, T. Felauer, and F. Lehmkuhl (2009), OSL dating of sediments from the Gobi Desert, Southern Mongolia, journal = Quaternary Geochronology, *5*(2-3), 107–113.

Hoffmann, C., R. Funk, M. Sommer, and Y. Li (2008), Temporal variations in PM10 and particle size distribution during Asian dust storms in Inner Mongolia, *ATMOSPHERIC ENVIRONMENT*, *42*(36), 8422–8431, doi:{10.1016/j.atmosenv.2008.08.014}.

Hugenholtz, C. H., S. A. Wolfe, I. J. Walker, and B. J. Moorman (2009), Spatial and temporal patterns of aeolian sediment transport on an inland parabolic dune, Bigstick Sand Hills, Saskatchewan, Canada, *Geomorphology*, *105*(1-2), 158–170, 0169-555X doi: DOI: 10.1016/j.geomorph.2007.12.017.

Ishizuka, M., M. Mikami, Y. Yamada, and F. J. Zeng (2009), Threshold Friction Velocities of Saltation Sand Particles for Different Soil Moisture Conditions in the Taklimakan Desert, *Sola*, *5*, 184–187.

Jacoby, G., R. D'Arrigo, N. Pederson, B. Buckley, C. Dugarjav, and R. Mijiddorj (1999), Temperature and precipitation in Mongolia based on dendroclimatic investigations, *IAWA JOURNAL*, *20*(3), 339–350.

Jacoby, G. C., R. D. D'Arrigo, and T. Davaajamts (1996), Mongolian tree rings and 20th-century warming, *Science*, *273*(5276), 771–773, doi:10.1126/science.273.5276.771.

Jahn, B., B. Litvinovsky, A. Zanvilevich, and M. Reichow (2009), Peralkaline granitoid magmatism in the Mongolian-Transbaikalian Belt: Evolution, petrogenesis and tectonic significance, *Lithos*, *113*(3-4), 521 – 539, doi:{DOI:10.1016/j.lithos.2009.06.015}, .

James H.S. Blight and Quentin G. Crowley and Michael G. Petterson and Dickson Cunningham (2010), Granites of the Southern Mongolia Carboniferous Arc: New geochronological and geochemical constraints, *Lithos*, *116*(1-2), 35 – 52, doi:{DOI:10.1016/j.lithos.2010.01.001}, .

Janicke (2008), *Dispersion Model LASAT, Reference ARITCLE for Version 3.0*, Janicke Consulting, Alter Postweg 21, D-26427 Dunum.

Jäkel, D. (2006), Dünenwüsten und Löss in China. Gedanken eines Geowissenschaflters zu geomedizinisch bedingten Gefahren und Risiken, *Naturwissenschaftliche Rundschau*, *59*(11), 594–601.

Johnson, C., J. Amory, D. Zinniker, M. Lamb, S. Graham, M. Affolter, and G. Badarch (2007), Sedimentary response to arc-continent collision, Permian, southern Mongolia.

Jones, T. A., and S. A. Christopher (2007), Modis derived fine mode fraction characteristics of marine, dust, and anthropogenic aerosols over the ocean, constrained by gocart, mopitt, and toms, *JOURNAL OF GEOPHYSICAL RESEARCH-ATMOSPHERES*, *112*(D22), doi:10.1029/2007JD008974.

Kahl, J. (2007), Die Mongolei im Reformtief: Dauerkrise oder "zweiter Aufbruch"?, *FES-Analyse: Mongolei. Internationale Politikanalyse. Friedrich- Ebert-Stiftung*.

Kim, J. (2008), Transport routes and source regions of Asian dust observed in Korea during the past 40 years (1965-2004), *Atmospheric Environment*, *42*(19), 4778–4789.

Kimura, R., and M. Shinoda (2010), Spatial distribution of threshold wind speeds for dust outbreaks in northeast Asia, *Geomorphology*, *114*(3), 319–325.

Kinoshita, K., W. Ning, Z. Gang, A. Tupper, N. Iino, S. Hamada, and S. Tsuchida (2005), Long-Term Observation of Asian Dust in Changchun and Kagoshima, *Water, Air, & Soil Pollution: Focus*, *5*(3), 89–100, 10.1007/s11267-005-0728-x.

Klug, H. P., and L. E. Alexander (1974), X-Ray diffraction procedures for polycrystalline and amorphous materials.

Koren, I., Y. J. Kaufman, R. Washington, M. C. Todd, Y. Rudich, J. V. Martins, and D. Rosenfeld (2006), The bodélé depression: a single spot in the sahara that provides most of the mineral dust to the amazon forest, *Environemtnal Res. Lett.*, *1*, 5.

Kovalenko, V., V. Yarmoluyk, E. Salt'nikova, A. Kozlovsky, A. Kotov, V. Kovach, V. Savatenkov, N. Vladykin, and V. Ponomarchuk (2006), Geology, geochronology, and geodynamics of the khan bogd alkali granite pluton in southern mongolia, *Geotectonics*, *40*(6), 450–466.

Kovalenko, V., V. Yarmolyuk, A. Kozlovsky, V. Kovach, E. Salt'nikova, A. Kotov, and N. Vladykin (2007), Two types of magma sources of rare-metal alkali granites, *Geology of Ore Deposits*, *49*(6), 442–466.

Kozakov, I., et al. (2008), Vendian stage in formation of the Early Caledonian superterrane in Central Asia, *Stratigraphy and Geological Correlation*, *16*(4), 360–382.

Kozlovsky, A. M., V. V. Yarmolyuk, V. M. Savatenkov, and V. P. Kovach (2006), Sources of basaltoid magmas in rift settings of an active continental margin: Example from the bimodal association of the Noen and Tost ranges of the Late Paleozoic Gobi-Tien Shan rift zone, Southern Mongolia, *Petrology*, *14*(4), 337–360.

Lamb, M. A., G. Badarch, T. Navratil, and R. Poier (2008), Structural and geochronologic data from the Shin Jinst area, eastern Gobi Altai, Mongolia: Implications for Phanerozoic intracontinental deformation in Asia, *Tectonophysics*, *451*(1-4), 312 – 330, doi:10.1016/j.tecto.2007.11.061, asia out of Tethys: Geochronologic, Tectonic and Sedimentary Records.

Laurent, B., B. Marticorena, G. Bergametti, and F. Mei (2006), Modeling mineral dust emissions from chinese and mongolian deserts, *Global and Planetary Change*, *52*(1-4), 121–141.

Laurent, B., B. Marticorena, G. Bergametti, J. F. Léon, and N. M. Mahowald (2008), Modeling mineral dust emissions from the sahara desert using new surface properties and soil database, *J. Geophys. Res.*, *113*, 10.1029/2007JD009484.

Lee, E.-H., and B.-J. Sohn (2009), Examining the impact of wind and surface vegetation on the asian dust occurrence over three classified source regions, *J. Geophys. Res.*, *114*, 10.1029/2008JD010687.

Liang, M., Z. Guo, A. J. Kahmann, and F. Oldfield (2009), Geochemical characteristics of the Miocene eolian deposits in China: Their provenance and climate implications, *Geochem. Geophys. Geosyst.*, *10*, 10.1029/2008GC002331.

Livingstone, I., G. F. S. Wiggs, and C. M. Weaver (2007), Geomorphology of desert sand dunes: A review of recent progress, *Earth-Science Reviews*, *80*(3-4), 239–257, dOI: 10.1016/j.earscirev.2006.09.004.

Livingstone, J., and A. Warren (1996), Aeolian geomorphology, an introduction.

Maher, B. A., T. J. Mutch, and D. Cunningham (2009), Magnetic and geochemical characteristics of gobi desert surface sediments: Implications for provenance of the chinese loess plateau, *Geology*, *37*(3), 279–282, iSI Document Delivery No.: 414CT Times Cited: 0 Cited Reference Count: 27.

Marin, A. (2010), Riders under storms: Contributions of nomadic herders' observations to analysing climate change in mongolia, *Global Environmental Change*, *20*(1), 162–176.

Marticorena, B., and G. Bergametti (1995), Modeling the atmospheric dust cycle. 1. Design of a soil-derived dust emission scheme, *JOURNAL OF GEOPHYSICAL RESEARCH-ATMOSPHERES*, *100*(D8), 16,415–16,430.

Mei, F., J. Rajot, S. Alfaro, L. Gomes, X. Zhang, and T. Wang (2006), Validating a dust production model by field experiment in Mu Us Desert, China, *Chinese Science Bulletin*, *51*(7), 878–884, 10.1007/s11434-006-0878-x.

Mikami, M., Y. Yamada, M. Ishizuka, T. Ishimaru, W. Gao, and F. Zeng (2005), Measurement of saltation process over gobi and sand dunes in the taklimakan desert, china, with newly developed sand particle counter, *J.of Geophysical research*, *10*, 12.

Mukai, S., I. Sano, and B. Holben (2005), Aerosol Properties Over Japan Determined by Sun/Sky Photometry, *Water, Air, & Soil Pollution: Focus*, *5*(3), 133–143, 10.1007/s11267-005-0731-2.

Murata, K. J., and M. B. Norman (1976), Index of crystallinity for quartz, *American Journal of Science*, *276*(9), 1120–1130, iSI Document Delivery No.: CL052 Times Cited: 98 Cited Reference Count: 46.

Nagashima, K., R. Tada, A. Tani, S. Toyoda, Y. Sun, and Y. Isozaki (2007), Contribution of aeolian dust in Japan Sea sediments estimated from ESR signal intensity and crystallinity of quartz, *Geochem. Geophys. Geosyst.*, *8*, 10.1029/2006GC001364.

Nakano, T., M. Nishikawa, I. Mori, K. Shin, T. Hosono, and Y. Yokoo (2005), Source and evolution of the "perfect asian dust storm" in early april 2001: Implications of the sr-nd isotope ratios, *Atmospheric Environment*, *39*(30), 5568–5575, 1352-2310 doi: DOI: 10.1016/j.atmosenv.2005.05.050.

Natsagdorj, L., D. Jugder, and Y. Chung (2003), Analysis of dust storms observed in Mongolia during 1937-1999, *Atmospheric Environment*, *37*, 1401–1411.

Okrusch, M., and S. Matthes (2009), Mineralogie: eine Einührung in die spezielle Mineralogie, Petrologie und Lagerstättenkunde, literaturangaben.

on Climate Change, I. P. (2007), Fourth assessment report: Climate change 2007: The ar4 synthesis report.

Pankova, Y. (1994), Degradation processes on cropland in mongolia, *Eurasian Soil Science*, *26*(8), 88–98.

Pederson, N., G. C. Jacoby, R. D. DArrigo, E. R. Cook, B. M. Buckley, C. Dugarjav, and R. Mijiddorj (2001), Hydrometeorological Reconstructions for Northeastern Mongolia Derived from Tree Rings: 1651 - 1995, *Journal of Climate*, *14*(5), 872–881.

Prospero, J., P. Ginoux, O. Torres, S. Nicholson, and T. Gill (2002), Environmental characterization of global sources of atmospheric soil dust identified with the nimbus 7 total ozone mapping spectrometer (toms) absorbing aerosol product, *REVIEWS OF GEOPHYSICS*, *40*(1), doi:10.1029/2000RG000095.

Pye, K. (1995), The nature, origin and accumulation of loess, *Quaternary Science Reviews*, *14*(7-8), 653 – 667, doi:10.1016/0277-3791(95)00047-X, aeolian Sediments in the Quaternary Record.

Rudra, J. K., and W. B. Fowler (1987), Oxygen vacancy and the E1' center in crystalline SiO2, *Physical Review B*, *35*(Copyright (C) 2010 The American Physical Society), 8223, pRB.

Schlütz, F., and F. Lehmkuhl (2009), Holocene climatic change and the nomadic Anthropocene in Eastern Tibet: palynological and geomorphological results from the Nianbaoyeze Mountains, *Quaternary Science Reviews*, *28*(15-16), 1449 – 1471, doi:10.1016/j.quascirev.2009.01.009.

Schwanghart, W., M. Frechen, N. J. Kuhn, and B. Schï£¡tt (2009), Holocene environmental changes in the ugii nuur basin, mongolia, *Palaeogeography, Palaeoclimatology, Palaeoecology*, *In Press, Corrected Proof*, 0031-0182 doi: DOI: 10.1016/j.palaeo.2009.05.007.

Shao, Y. (2004), Simplification of a dust emission scheme and comparison with data, *J. Geophys. Res.*, *109*(D10), D10,202–.

Shao, Y., and C. Dong (2006), A review on east asian dust storm climate, modelling and monitoring, *Global and Planetary Change*, *52*, 1–22.

Stull (1988), An introduction to boundary layer meteorology.

Sun, J. (2002), Provenance of loess material and formation of loess deposits on the chinese loess plateau, *Earth and Planetary Science Letters*, *203*(3-4), 845–859, 0012-821X doi: DOI: 10.1016/S0012-821X(02)00921-4.

Sun, Y., et al. (2007), Distinguishing the sources of asian dust based on electron spin resonance signal intensity and crystallinity of quartz, *Atmospheric Environment*, *41*(38), 8537–8548.

Sun, Y. B., R. J. Tada, J. C. Chen, Q. S. Liu, S. Toyoda, A. Tani, J. F. Ji, and Y. Isozaki (2008), Tracing the provenance of fine-grained dust deposited on the central chinese loess plateau, *Geophysical Research Letters*, *35*(1), iSI Document Delivery No.: 248UT Times Cited: 3 Cited Reference Count: 32 L01804.

Todd, M. C., R. Washington, V. Martins, O. Dubovik, G. Lizcano, S. McBainayel, and S. Engelstaedter (2006), Properties of mineral dust from the Bodélé depression, Northern Chad during BodEx 2005.

Trauth, M. M. (2008), Matlab. recieps for earth sciense.

Vandenberghe, J., H. Renssen, K. van Huissteden, G. Nugteren, M. Konert, H. Lu, A. Dodonov, and J.-P. Buylaert (2006), Penetration of Atlantic westerly winds into Central and East Asia, *Quaternary Science Reviews*, *25*(17-18), 2380 – 2389, doi:10.1016/j.quascirev.2006.02.017.

Vassallo, R., J. F. Ritz, R. Braucher, and S. Carretier (2005), Dating faulted alluvial fans with cosmogenic Be-10 in the Gurvan Bogd mountain range (Gobi-Altay, Mongolia): climatic and tectonic implications, *Terra Nova*, *17*(3), 278–285.

Vassallo, R., M. Jolivet, J. F. Ritz, R. Braucher, C. Larroque, C. Sue, M. Todbileg, and D. Javkhlanbold (2007), Uplift age and rates of the Gurvan Bogd system (Gobi-Altay) by apatite fission track analysis, *Earth and Planetary Science Letters*, *259*(3-4), 333–346.

Vostokova, E., P. Gunin, and E. Rachkovskaya (1995), Ekosistemy mongolii. rasprostranenie i sovremennoe sostoyanie.

Wang, X., D. Xia, T. Wang, X. Xue, and J. Li (2008a), Dust sources in arid and semiarid china and southern mongolia: Impacts of geomorphological setting and surface materials, *Geomorphology*, *97*(3-4), 583–600.

Wang, Y. Q., X. Y. Zhang, S. L. Gong, C. H. Zhou, X. Q. Hu, H. L. Liu, T. Niu, and Y. Q. Yang (2008b), Surface observation of sand and dust storm in east asia and its application in cuace/dust, *Atmospheric Chemistry and Physics*, *8*(3), 545–553.

Wang, Z., H. Ueda, and M. Huang (2000), A deflation module for use in modeling long-range transport of yellow sand over east asia, *JOURNAL OF GEOPHYSICAL RESEARCH-ATMOSPHERES*, *105*(D22), 26,947–26,959.

Warren, A., A. Chappell, M. C. Todd, C. Bristow, N. Drake, S. Engelstaedter, V. Martins, S. M'bainayel, and R. Washington (2007), Dust-raising in the dustiest place on earth.

Washington, R., and M. C. Todd (2005), Atmospheric controls on mineral dust emission from the bodélé depression, chad: The role of the low level jet, *GEOPHYSICAL RESEARCH LETTERS*, *32*.

Washington, R., M. C. Todd, S. Engelstaedter, S. Mbainayel, and F. Mitchell (2006a), Dust and the low-level circulation over the bodélé depression, chad: Observations from bodex 2005, *JOURNAL OF GEOPHYSICAL RESEARCH*, *111*.

Washington, R., et al. (2006b), Links between topography, wind, deflation, lakes and dust: The case of the bodÃl'lÃl' depression, chad, *GEOPHYSICAL RESEARCH LETTERS*, *33*, 4.

Wehrden, H., and K. Wesche (2007), Relationships between climate, productivity and vegetation in southern mongolian drylands, *Basic and Applied Dryland Research*, *2*, 100–120, doi:ISSN1864-3191.

Wesche, K., and V. Retzer (2005), Is degradation a major problem in semi-desert environments of the gobi region in southern mongolia?, *Biologische Ressourcen der Mongolei*, *9*, 133–146.

Wesche, K., K. Ronnenberg, and V. Retzer (2001), Effects of herbivore exclusion in southern mongolian desert steppes.

Yang, X., Y. Liu, C. Li, Y. Song, H. Zhu, and X. Jin (2007), Rare earth elements of aeolian deposits in northern china and their implications for determining the provenance of dust storms in beijing, *Geomorphology*, *87*(4), 365–377.

Yarmolyuk, V. V., E. A. Kudryashova, A. M. Kozlovsky, and V. M. Savatenkov (2007), Late Cretaceous-Early Cenozoic Volcanism of Southern Mongolia: A Trace of the South Khangai Mantle Hot Spot, *JOURNAL OF VOLCANOLOGY AND SEISMOLOGY*, *1*(1), 1–27, doi:{10.1134/S0742046307010010}.

Yumimoto, K., K. Eguchi, I. Uno, T. Takemura, Z. Liu, A. Shimizu, and N. Sugimoto (2009), An elevated large-scale dust veil from the taklimakan desert: Intercontinental transport and three-dimensional structure as captured by calipso and regional and global models, *Atmospheric Chemistry and Physics*, *9*(21), 8545–8558, doi:10.5194/acp-9-8545-2009.

Zhang, B., A. Tsunekawa, and M. Tsubo (2008), Contributions of sandy lands and stony deserts to long-distance dust emission in China and Mongolia during 2000-2006, *Global and Planetary Change*, *60*(3-4), 487–504.

A. Appendix

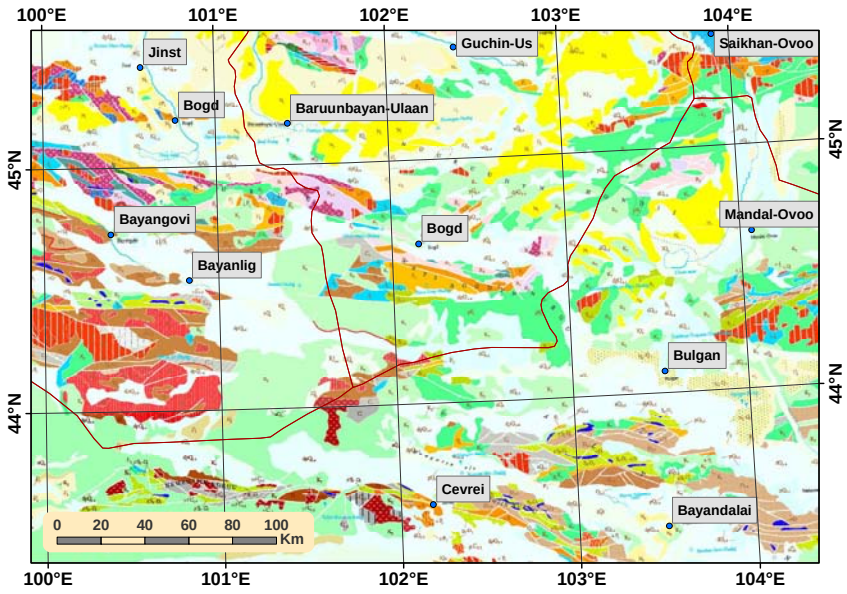

Fig. A.1.: Geology in the area of interest.
Source: Geological map of Mongolia 1998 (transformed and Geo referenced pdf-file). Legend next page

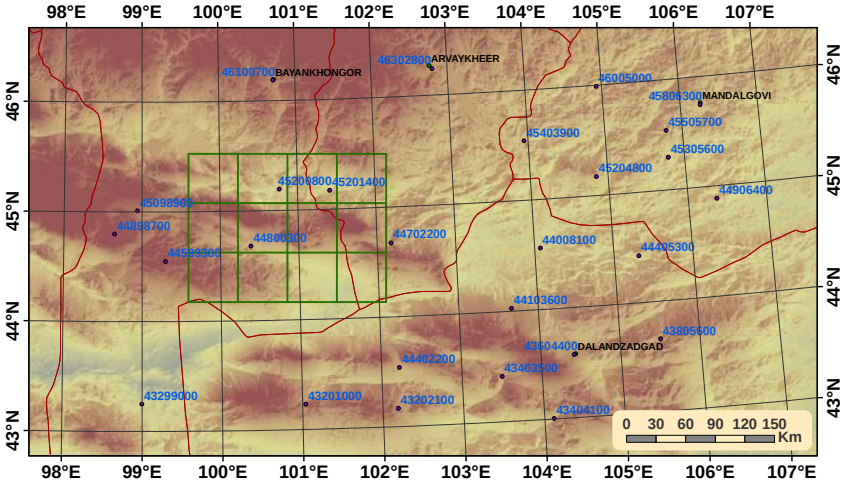

Fig. A.2.: Mongolian governmental weather stations (index numbers) in the study area. Simulation area as green grid

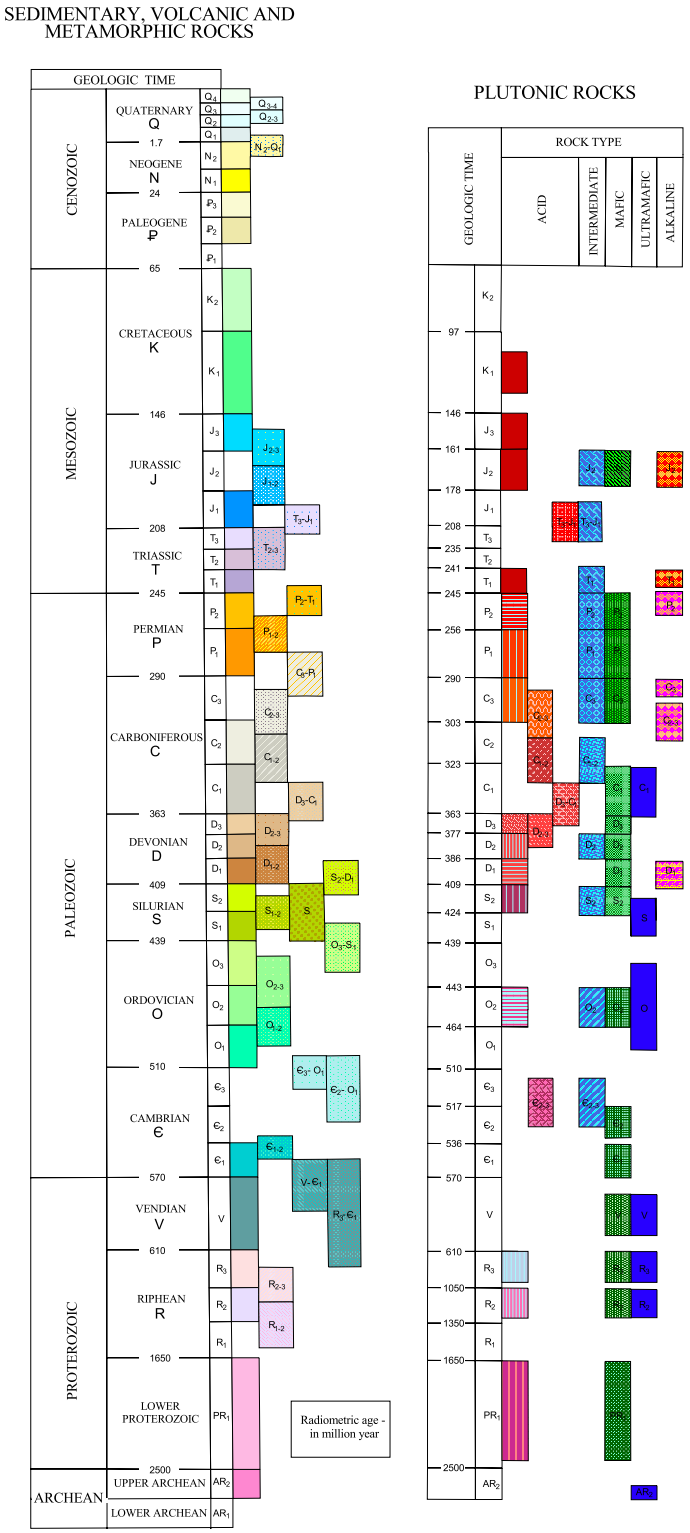

Fig. A.3.: Geology Map Legend

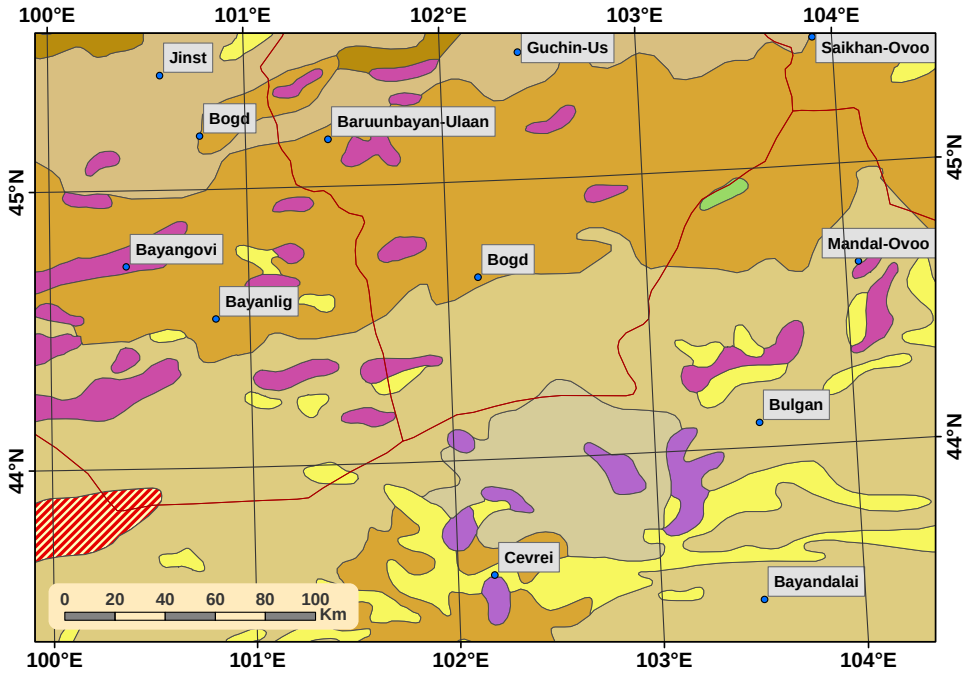

Fig. A.4.: Soils in the area of interest. Source: digital soil map of Mongolia 2007

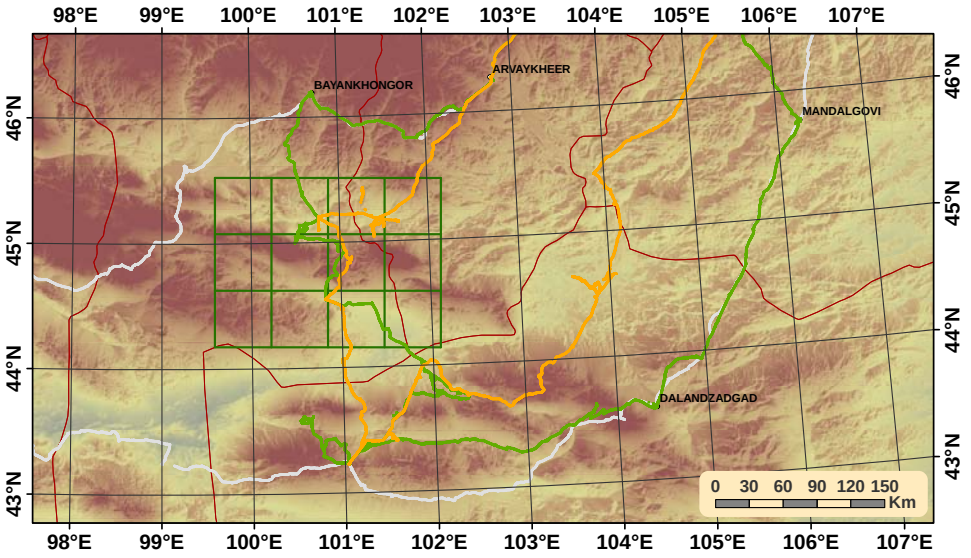

Fig. A.5.: Tracks of the field expeditions April 2008 (green), Aug2008 (orange) and Aug 2009 (white). Track of expedition Aug 2007 was not recorded,and therefore is not shown in the figure. Green squares = simulation area

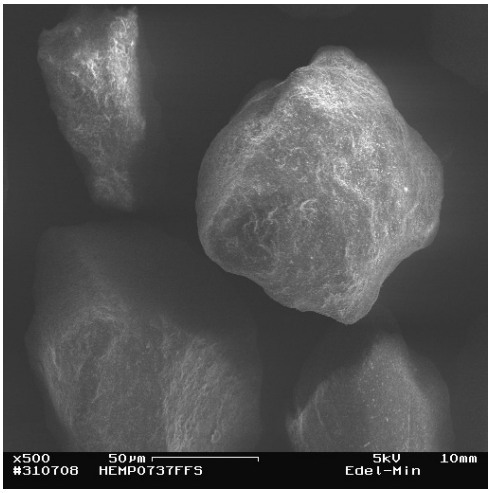
x500 50µm 5kV 10mm
#310708 HEMP0737FF5 Edel-Min

(a)

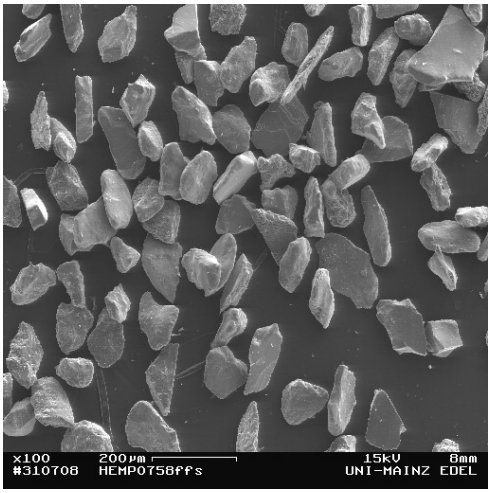
x100 200µm 15kV 8mm
#310708 HEMP0758ffs UNI-MAINZ EDEL

(b)

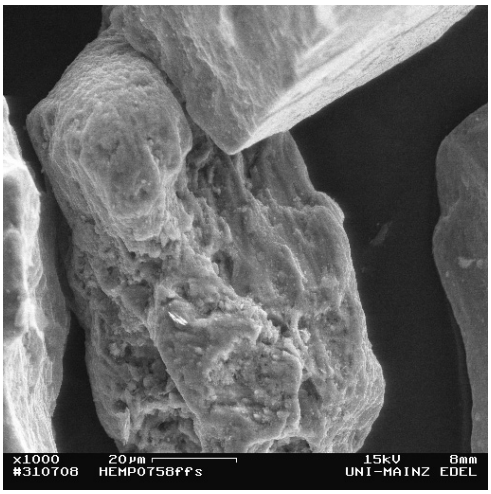
x1000 20µm 15kV 8mm
#310708 HEMP0758ffs UNI-MAINZ EDEL

(c)

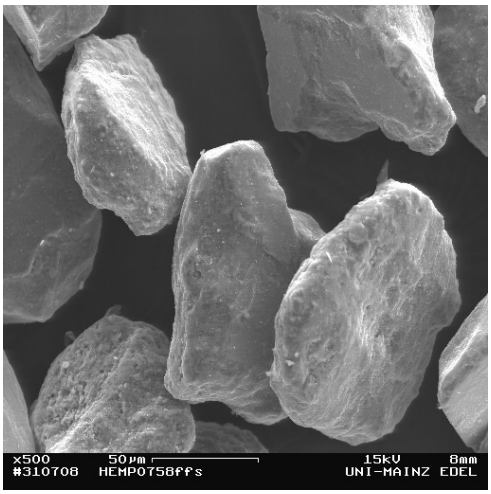
x500 50µm 15kV 8mm
#310708 HEMP0758ffs UNI-MAINZ EDEL

(d)

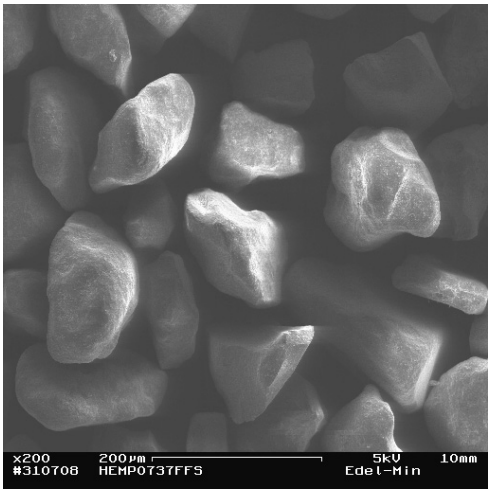
x200 200µm 5kV 10mm
#310708 HEMP0737FF5 Edel-Min

(e)

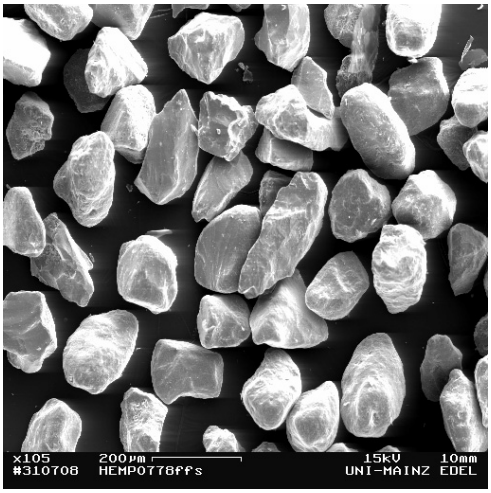
x105 200µm 15kV 10mm
#310708 HEMP0778ffs UNI-MAINZ EDEL

(f)

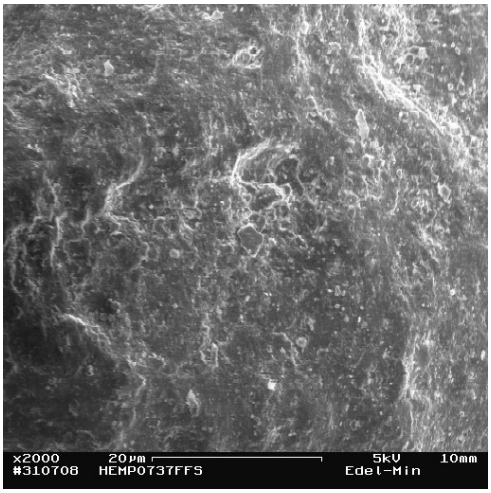
x2000 20µm 5kV 10mm
#310708 HEMP0737FFS Edel-Min

(g)

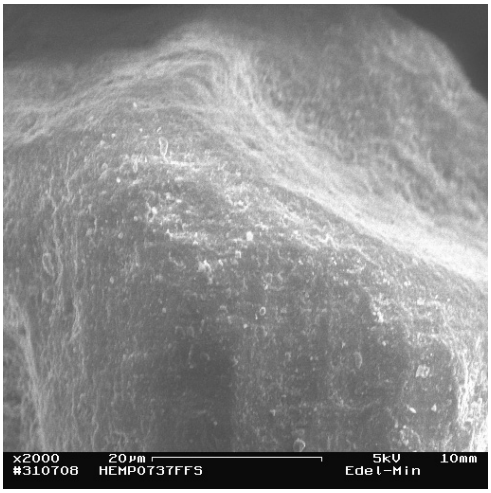
x2000 20µm 5kV 10mm
#310708 HEMP0737FFS Edel-Min

(h)

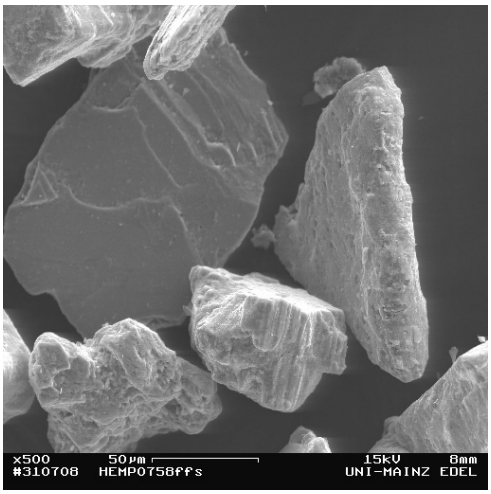
x500 50µm 15kV 8mm
#310708 HEMP0758ffs UNI-MAINZ EDEL

(i)

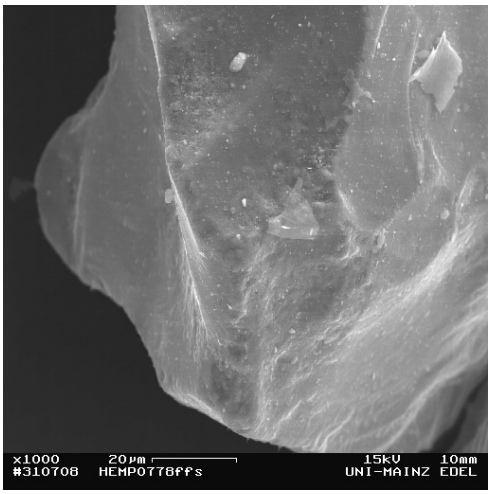
x1000 20µm 15kV 10mm
#310708 HEMP0778ffs UNI-MAINZ EDEL

(j)

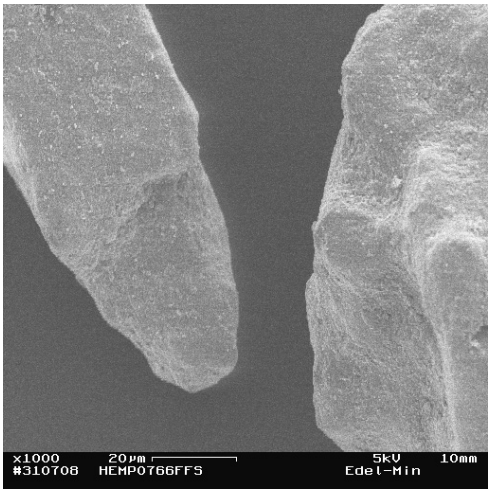
x1000 20µm 5kV 10mm
#310708 HEMP0766FFS Edel-Min

(k)

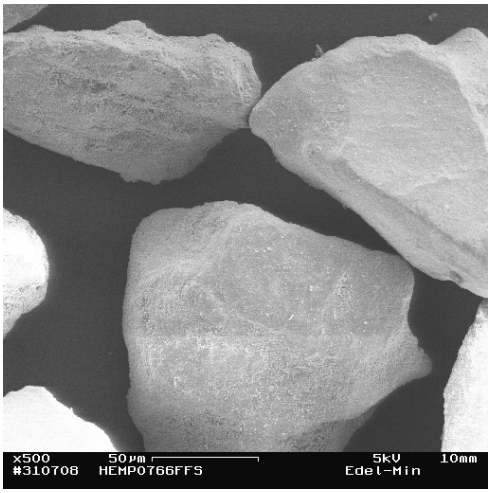
x500 50µm 5kV 10mm
#310708 HEMP0766FFS Edel-Min

(l)

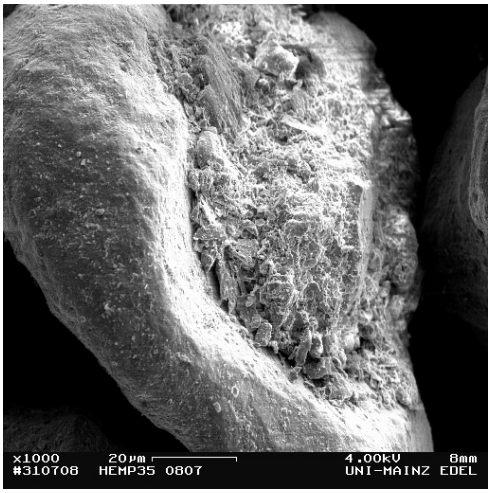

(m)

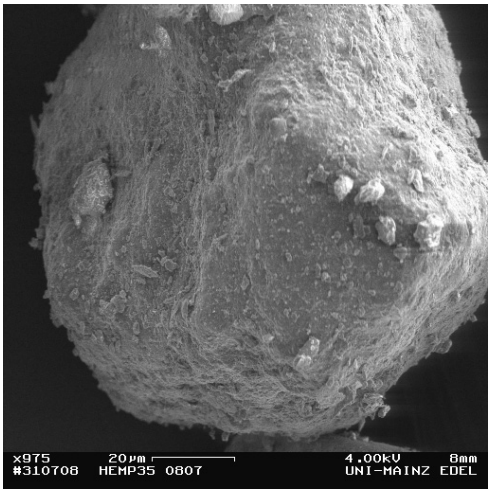

(n)

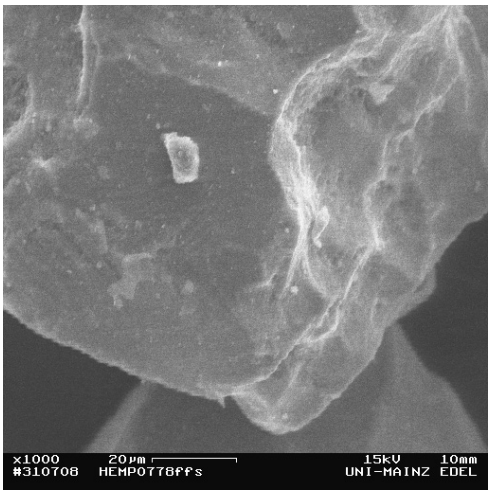

(o)

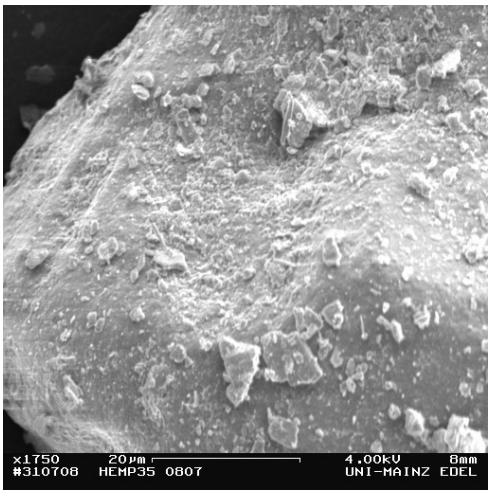

(p)

Fig. A.6.: SEM pictures of sand grains

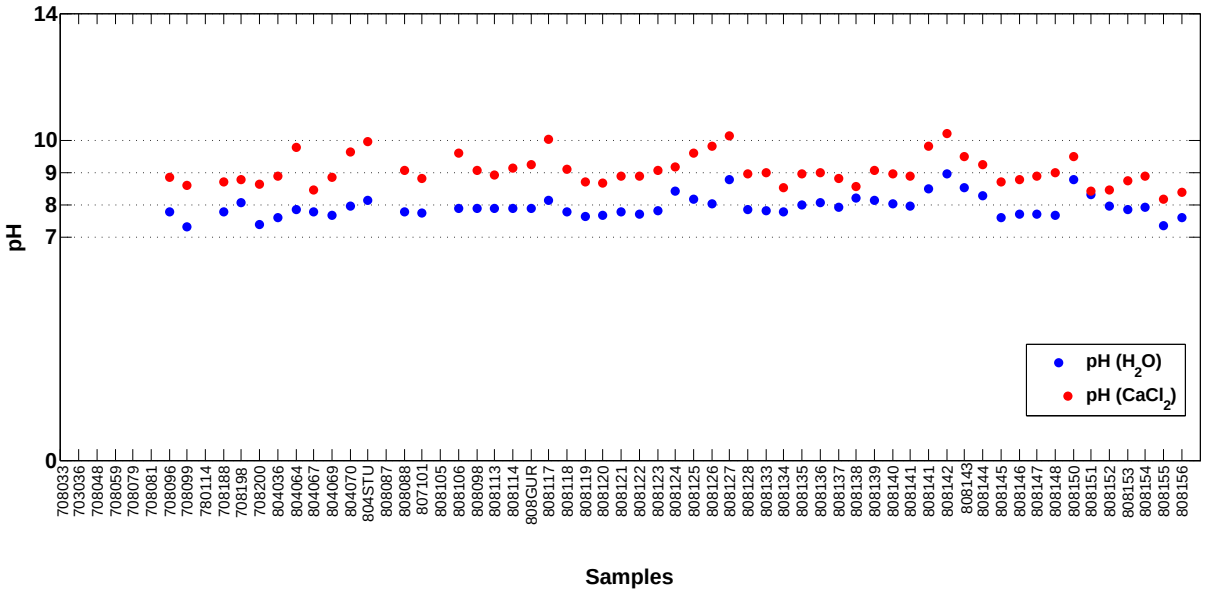

Fig. A.7.: pH - Values of the surface samples

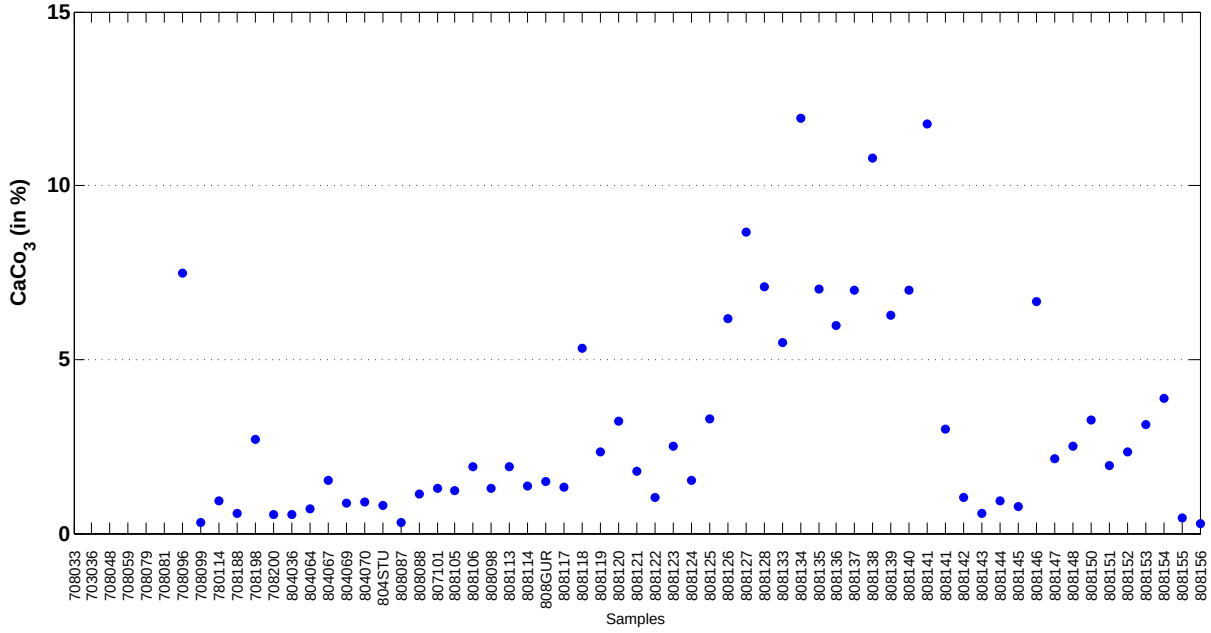

Fig. A.8.: Values of $CaCo_3$ content (in %)

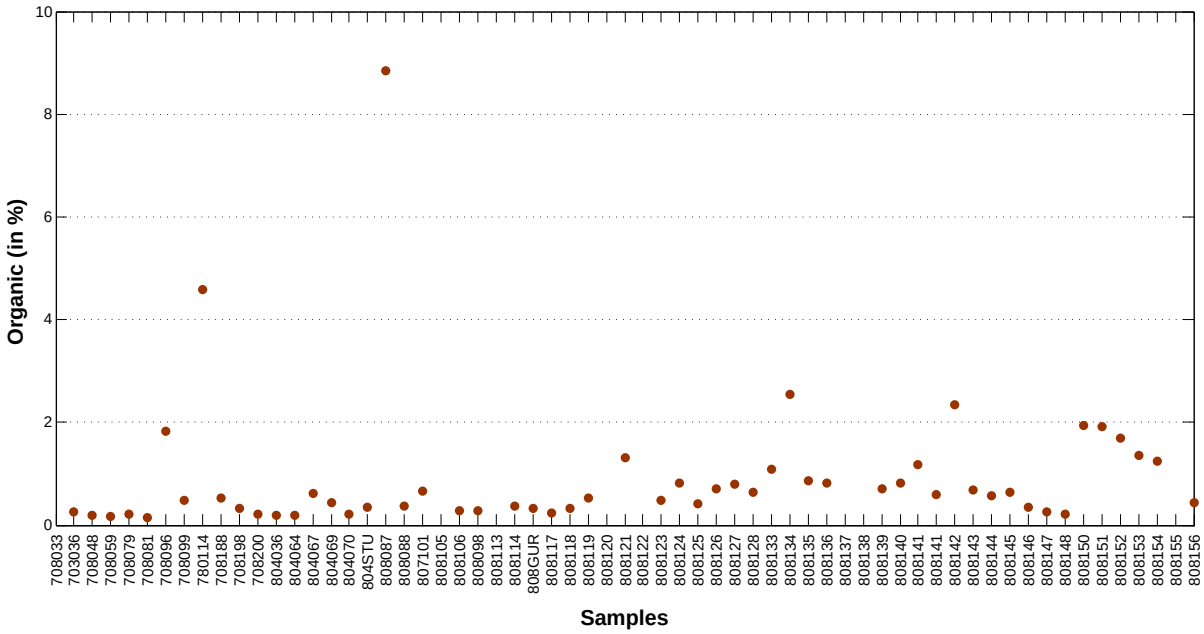

Fig. A.9.: Values of the organic content (in %)

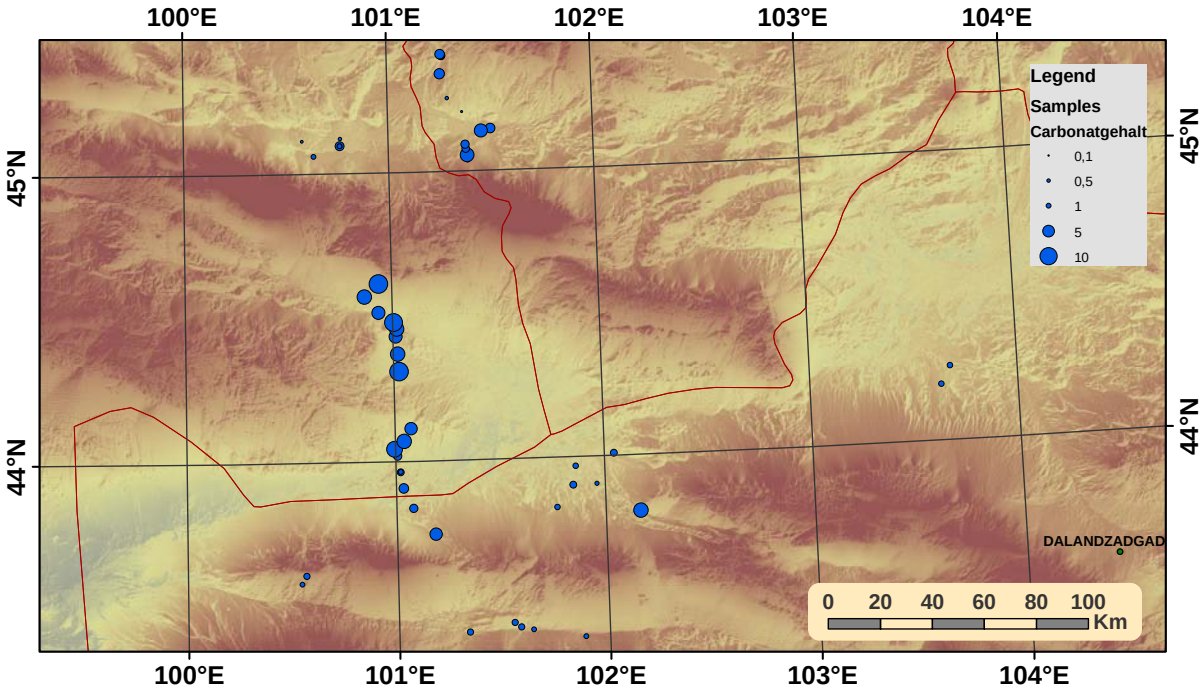

Fig. A.10.: Spatial distribution of the $CaCO_3$ contents. (Values in %)

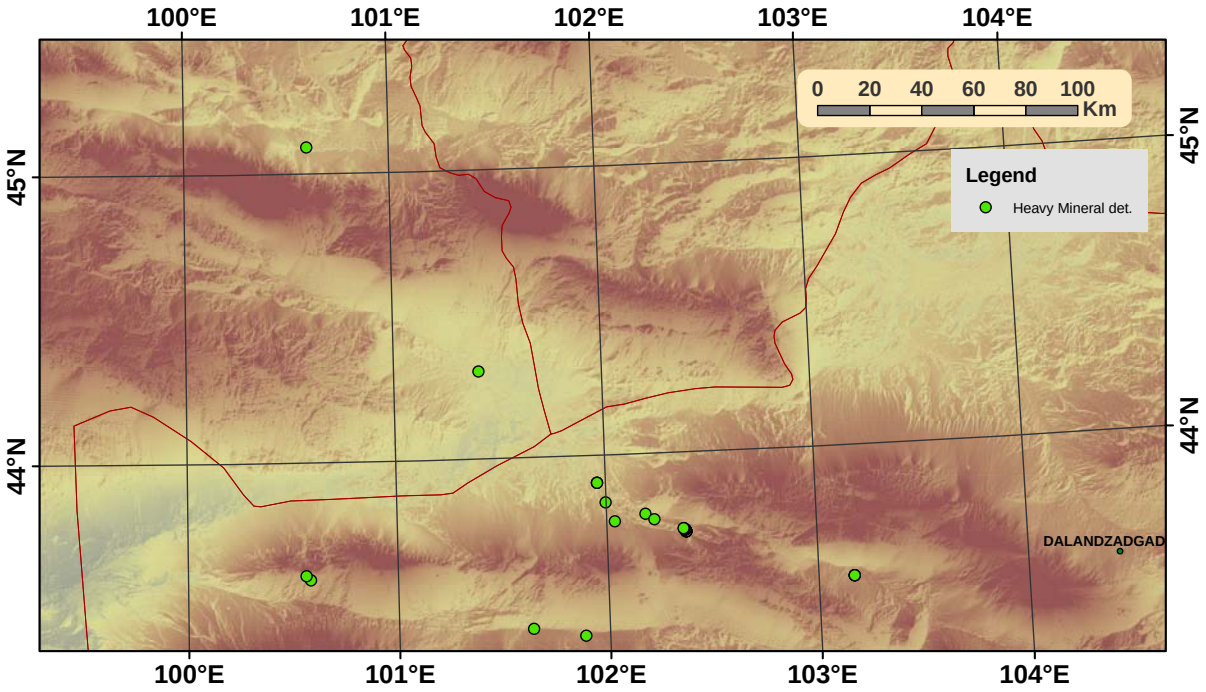

Fig. A.12.: Spatial distribution of the sites taken for heavy mineral determination

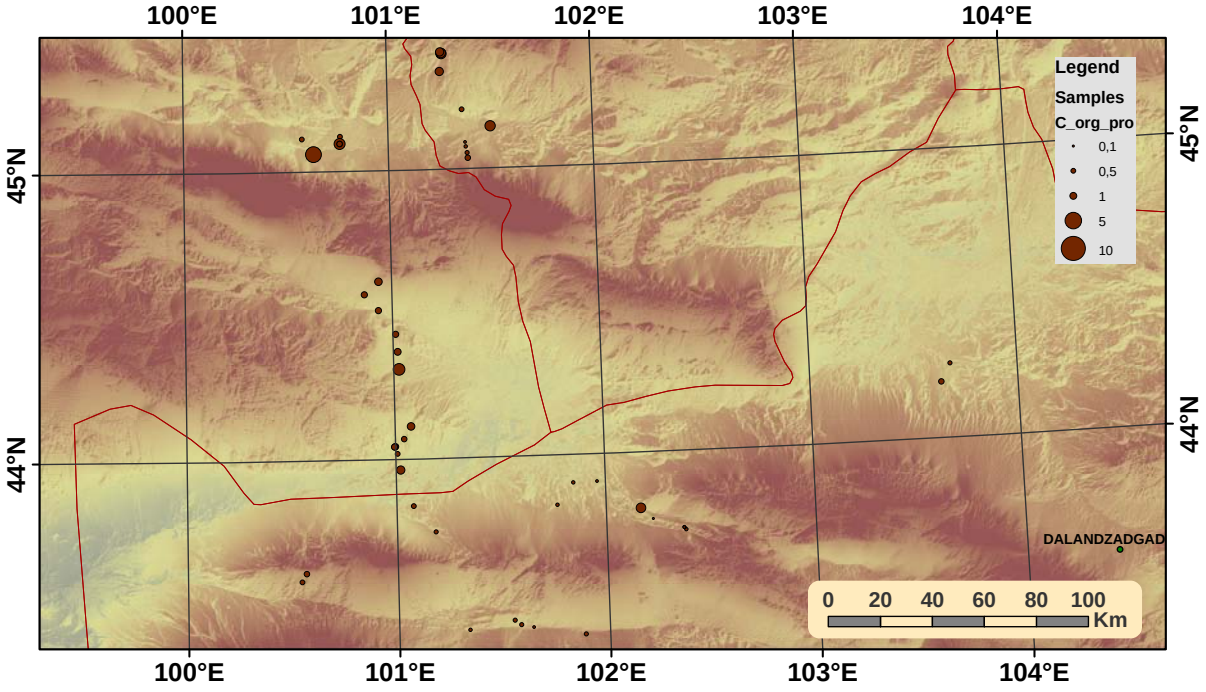

Fig. A.11.: Spatial distribution of the organic contents. (Values in %)

Fig. A.13.: Rock formation in the study area pointing out the main wind direction

Fig. A.14.: Surface condition in the Orog Nuur lake basin. Highly vulnerable bare surface, with particle emission in the background

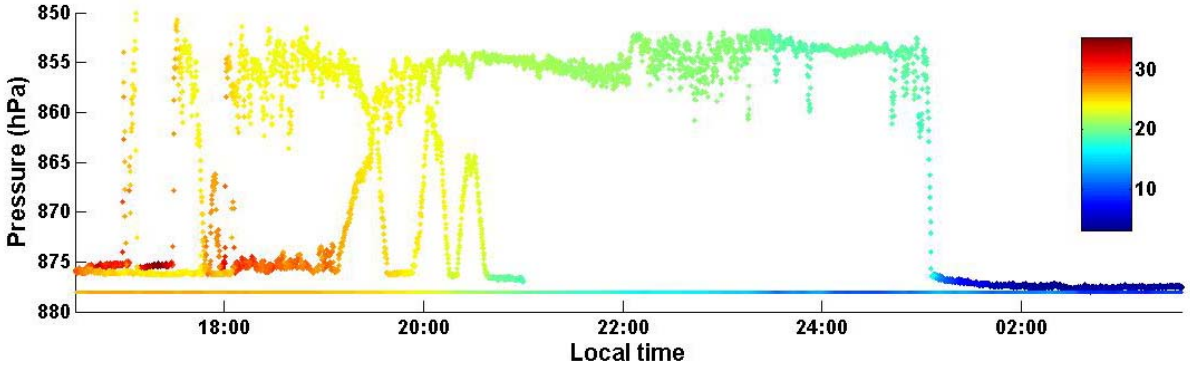

Fig. A.15.: Kite and lift borne measured temperature profile showing a low level jet (values in C)

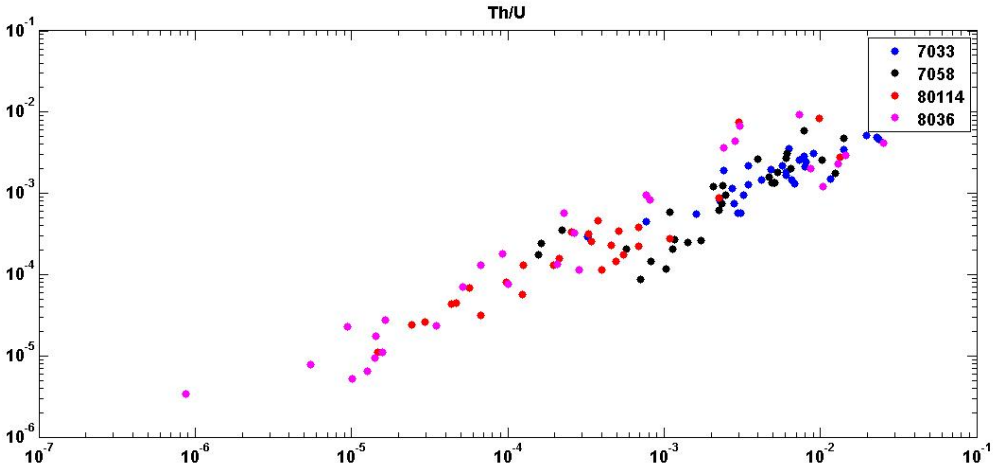

Fig. A.16.: Coupling of amount values of elements Th and U

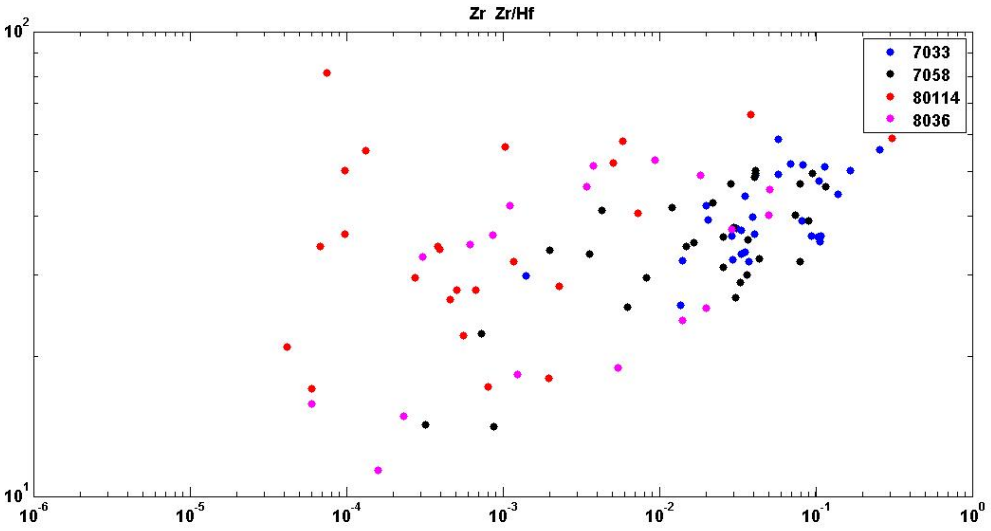

Fig. A.17.: Coupling of amount values of Zr and the couple of Zr/Hf

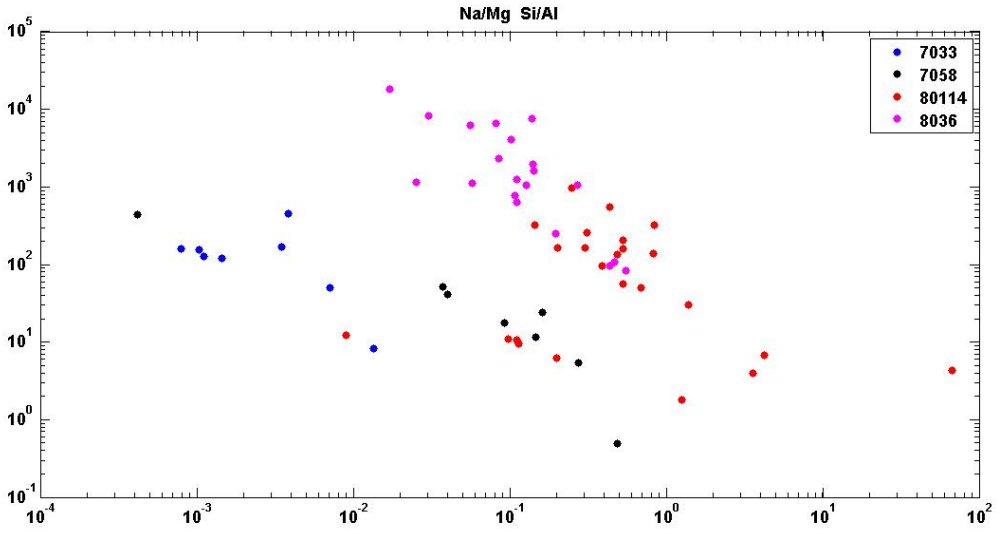

Fig. A.18.: Coupling of amount values of element couples Na/Mg and Si/Al

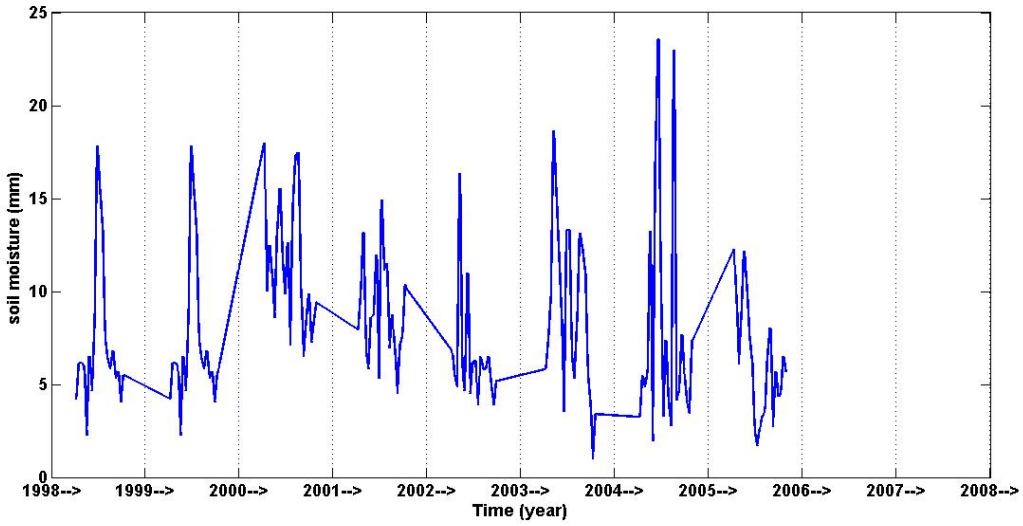

Fig. A.19.: Interpolated soil moisture. Values of the weather station in Dalanzadgat

unradieated.pdf

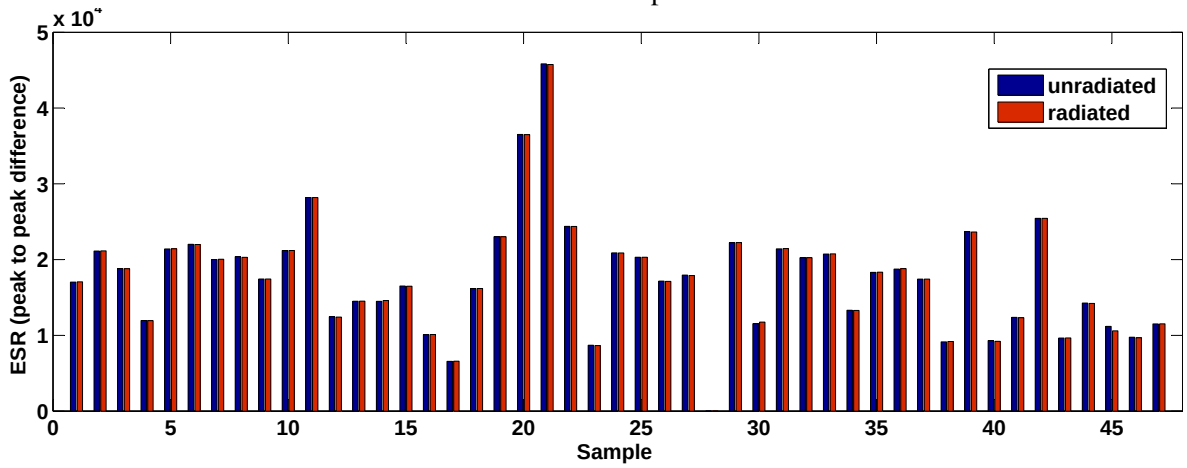

Fig. A.20.: Comparing of the values of unradiated (neutral) and radiated samples

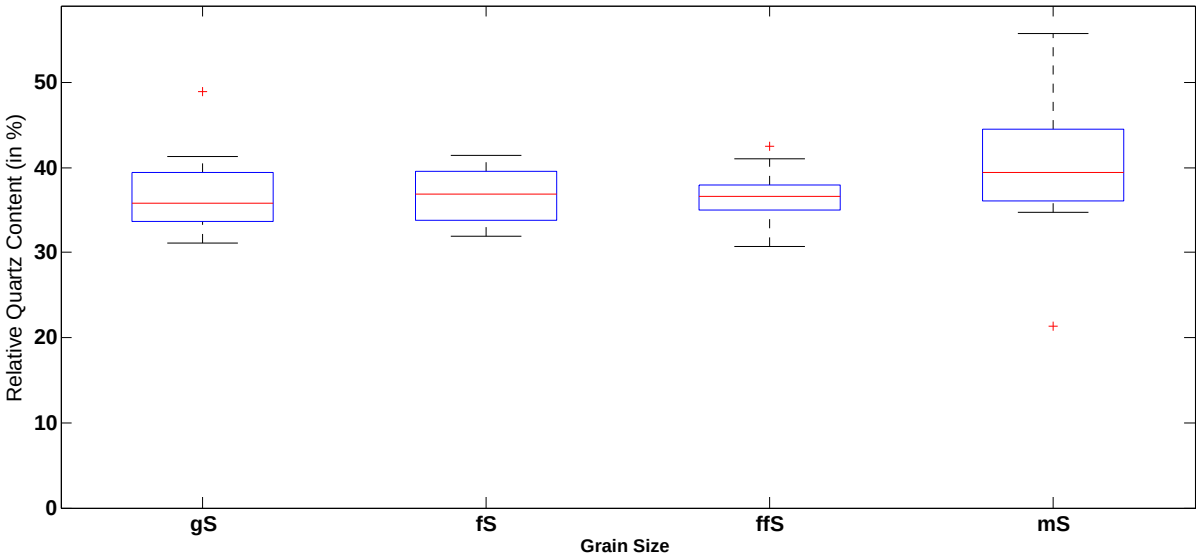

Fig. A.21.: Values of the quartz content, separated by grain size (in %)

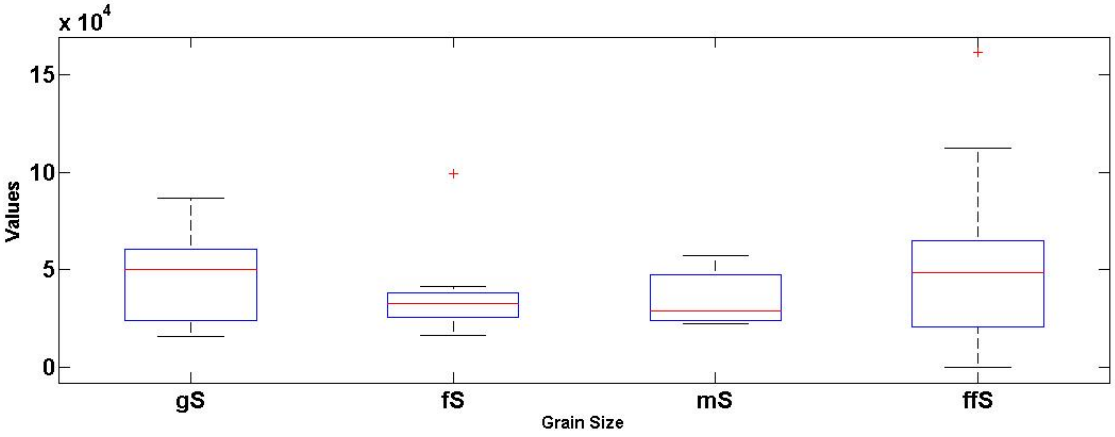

Fig. A.22.: ESR signal in intensity of different grain size fractions

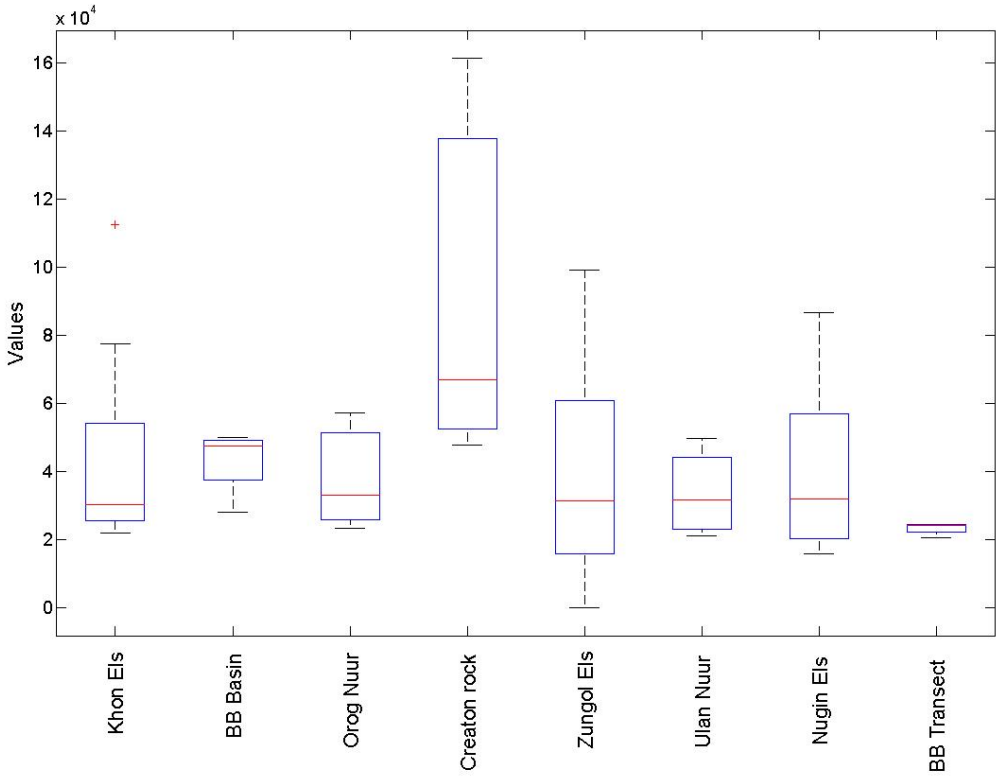

Fig. A.23.: ESR signal in intensity of different source areas

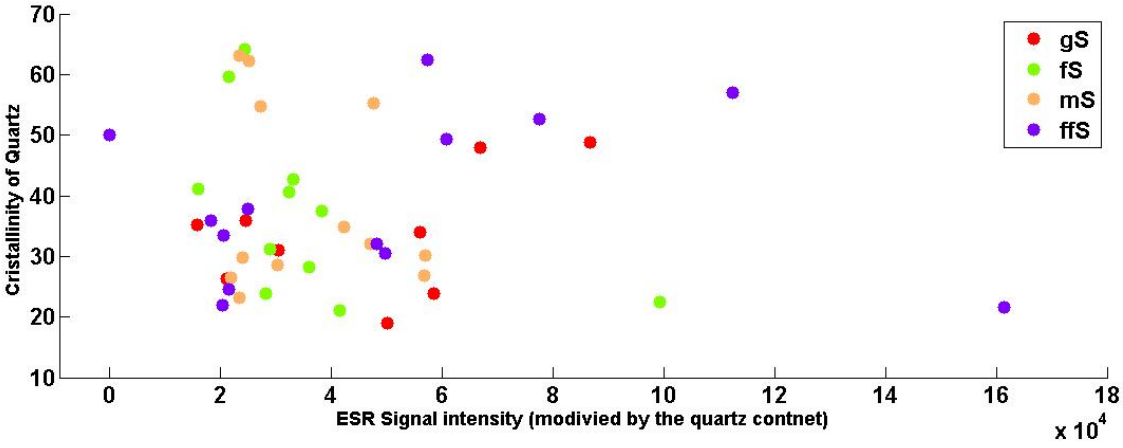

Fig. A.24.: ESR CI grain size depending

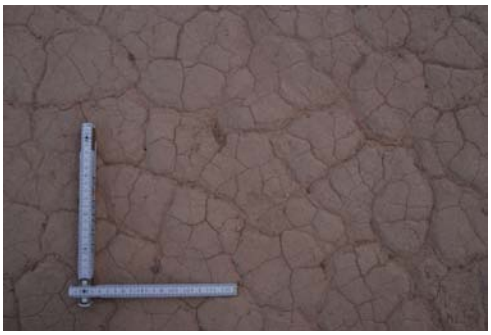

(a)

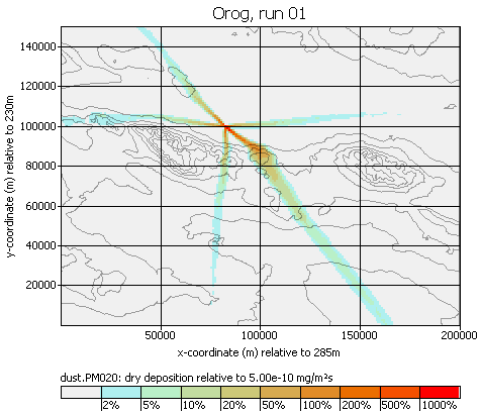

(b)

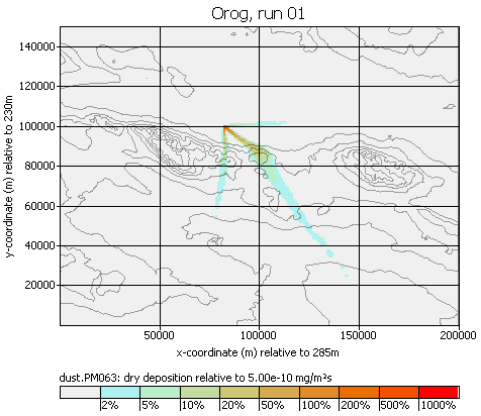

(c)

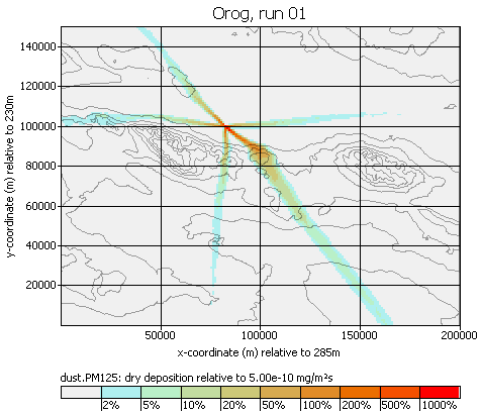

(d)

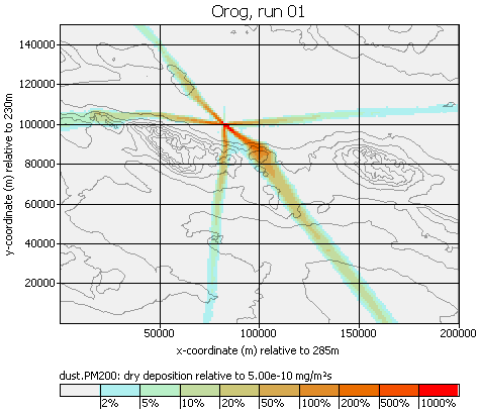

(e)

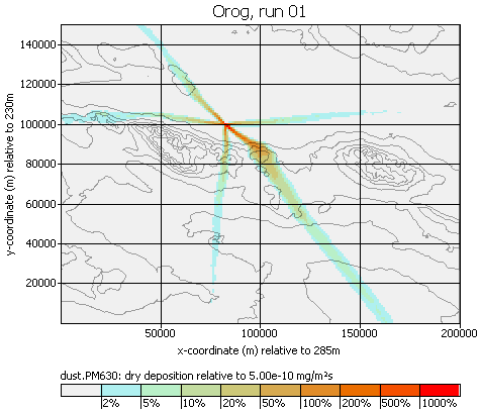

(f)

Fig. A.25.: Surface condition and particle dispersion. WP 0708099. Dry deposition Apr 2001 PM020 PM063 PM125 PM200 PM630 (fig b-g). Sources in Fig a

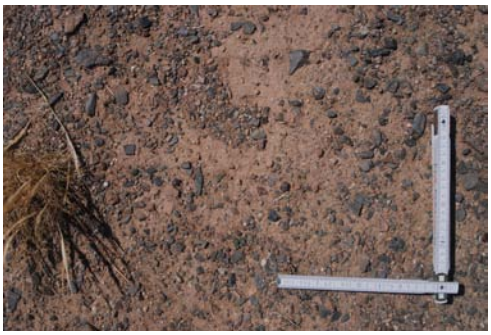

(a)

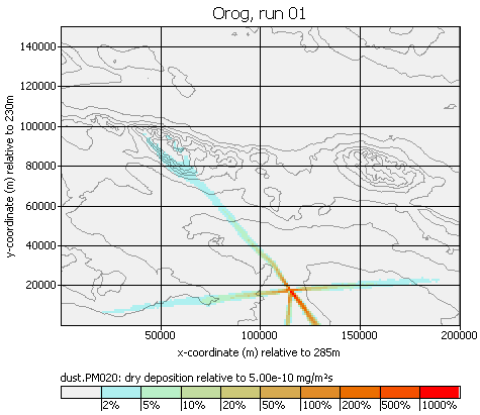

(b)

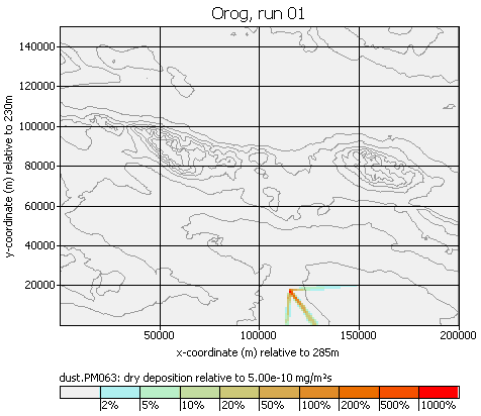

(c)

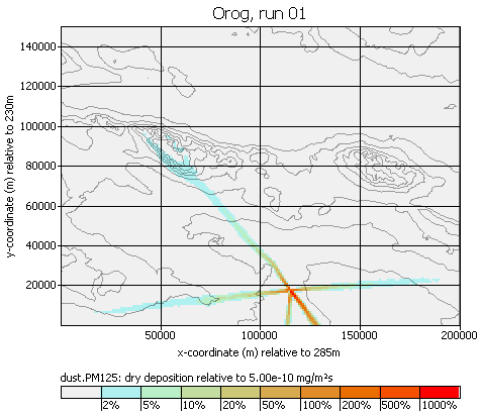

(d)

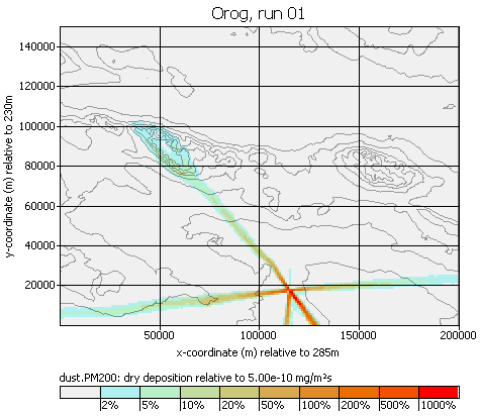

(e)

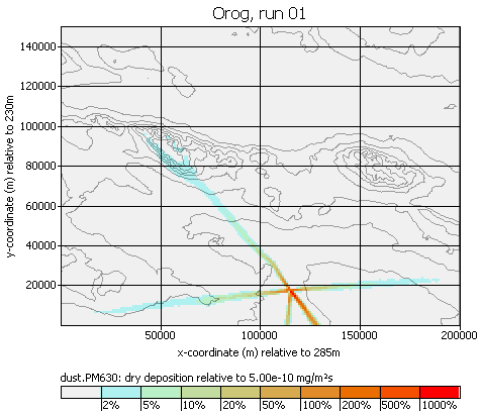

(f)

Fig. A.26.: Surface condition and particle dispersion. WP 0808133. Dry deposition Apr 2001 PM020 PM063 PM125 PM200 PM630 (fig b-g). Sources in Fig a

(a)

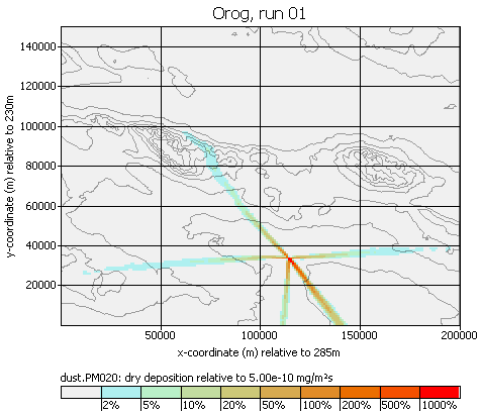

(b)

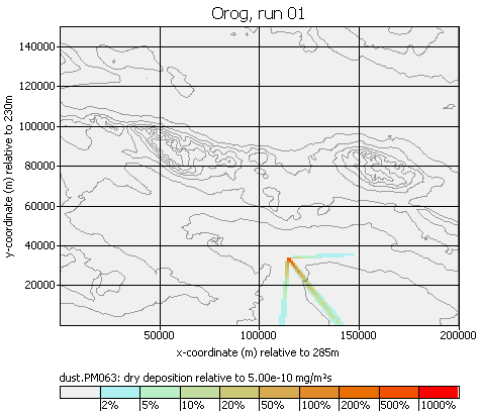

(c)

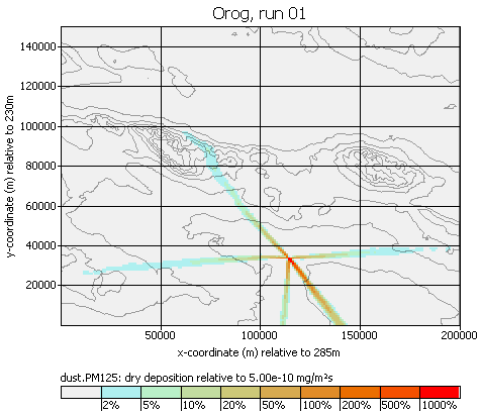

(d)

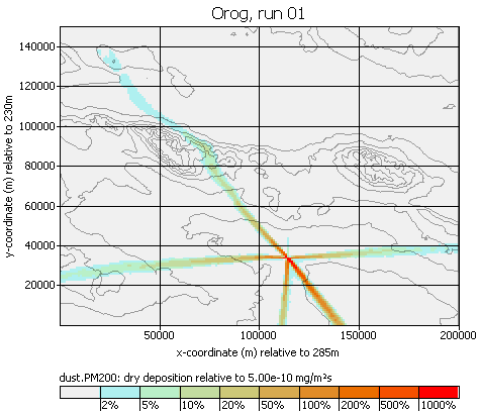

(e)

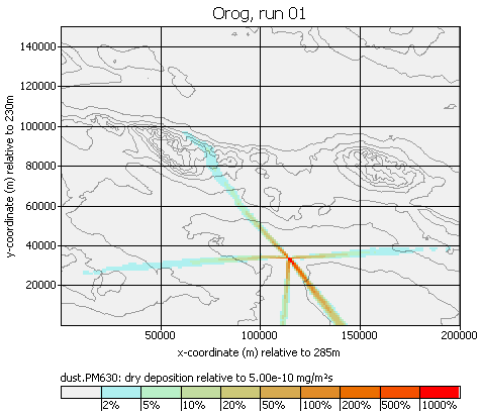

(f)

Fig. A.27.: Particle dispersion. WP 0808136. Dry deposition Apr 2001 PM020 PM063 PM125 PM200 PM630 (fig b-g). Sources in Fig a

(a)

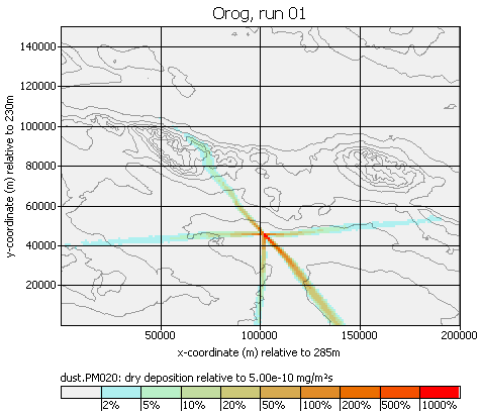

(b)

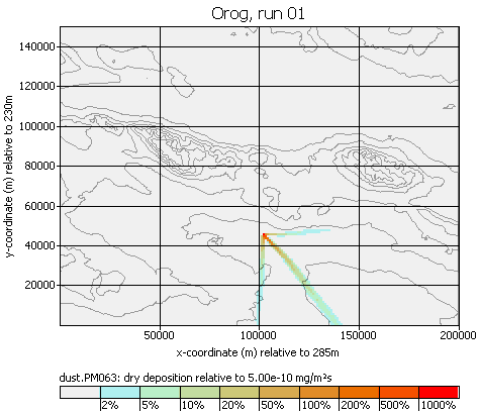

(c)

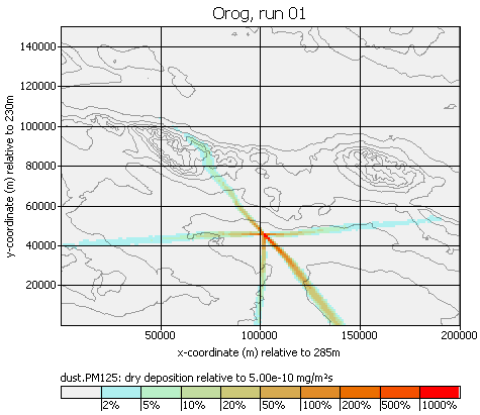

(d)

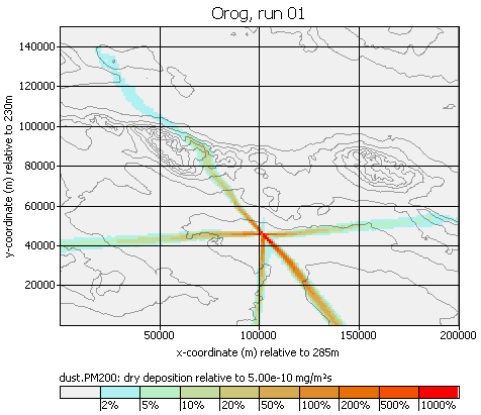

(e)

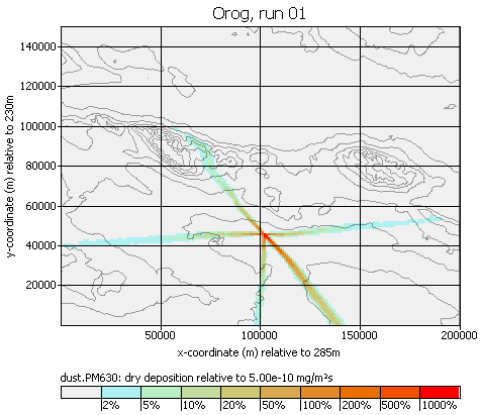

(f)

Fig. A.28.: Surface condition and particle dispersion. WP 0808139. Dry deposition Apr 2001 PM020 PM063 PM125 PM200 PM630 (fig b-g). Sources in Fig a

(a)

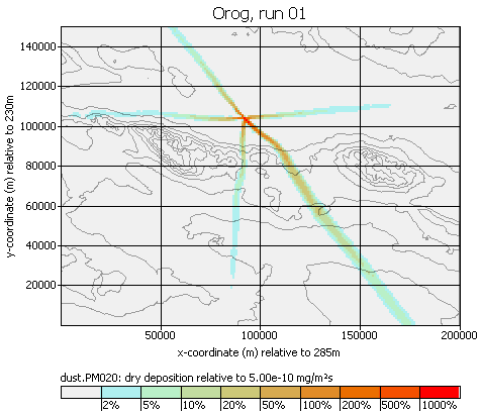

(b)

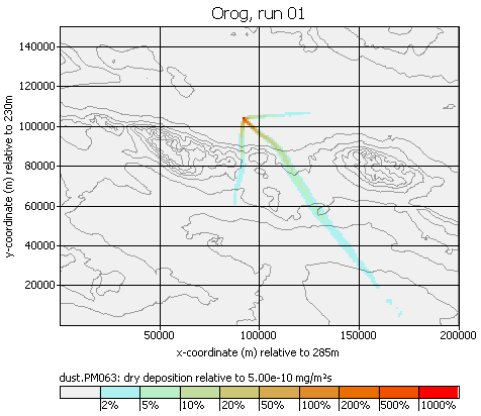

(c)

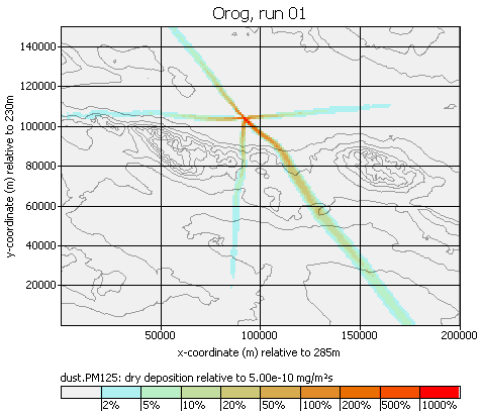

(d)

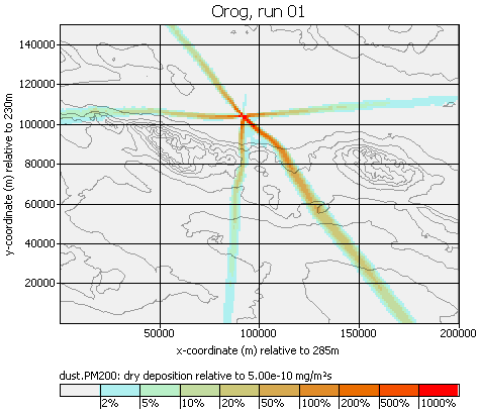

(e)

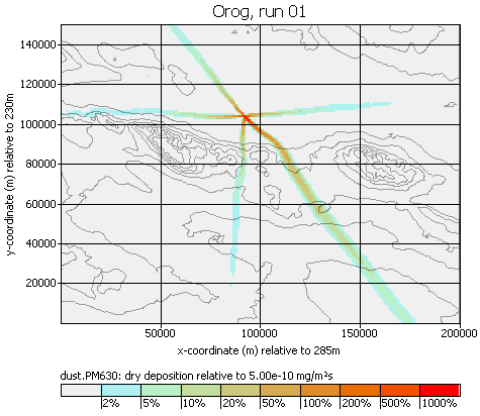

(f)

Fig. A.29.: Surface condition and particle dispersion. WP 0808141. Dry deposition Apr 2001 PM020 PM063 PM125 PM200 PM630 (fig b-g). Sources in Fig a

(a)

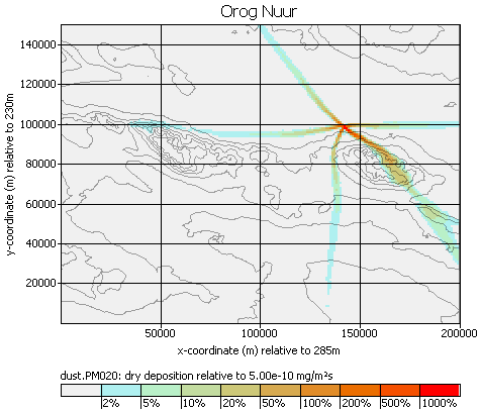

(b)

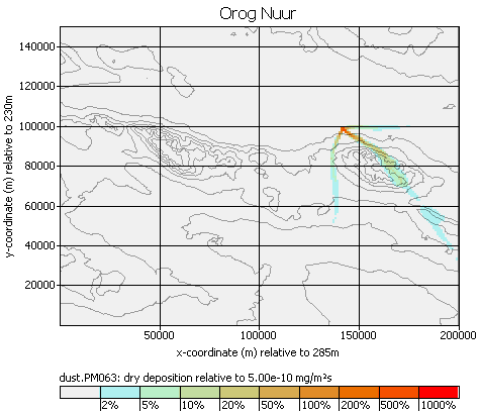

(c)

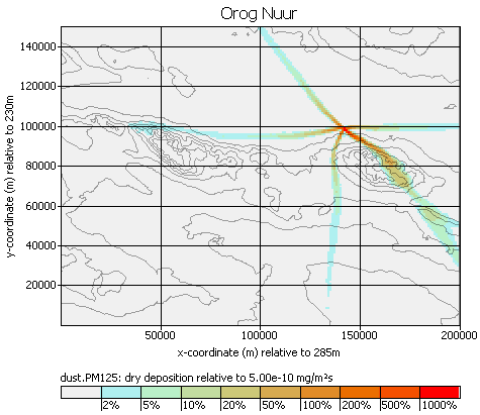

(d)

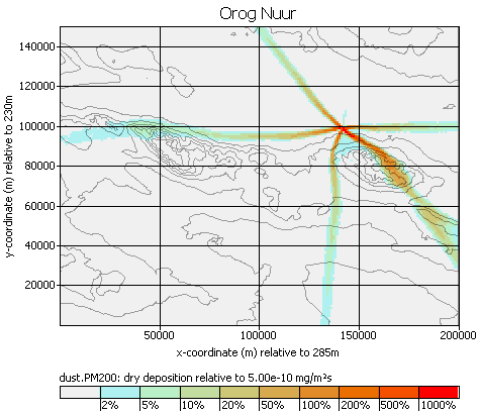

(e)

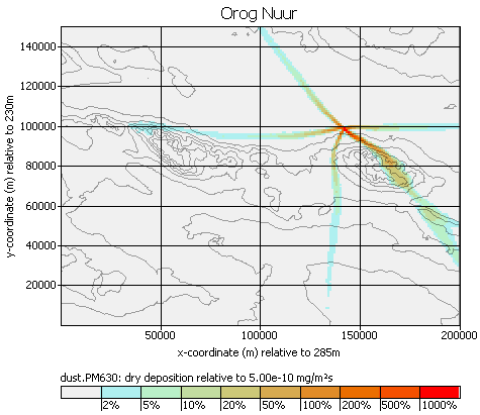

(f)

Fig. A.30.: Surface condition and particle dispersion. WP 0808144. Dry deposition Apr 2001 PM020 PM063 PM125 PM200 PM630 (fig b-g). Sources in Fig a

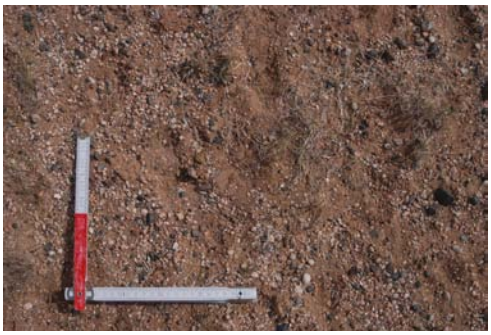

(a)

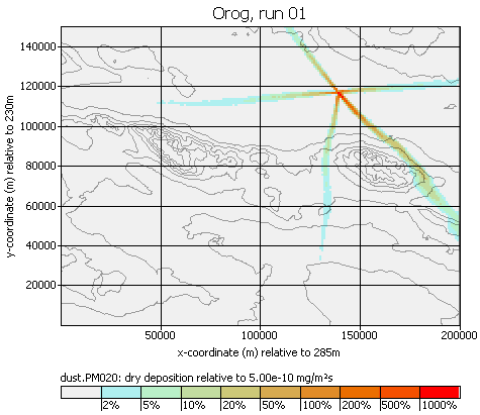

(b)

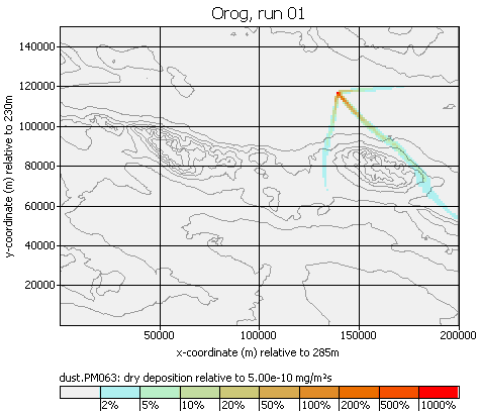

(c)

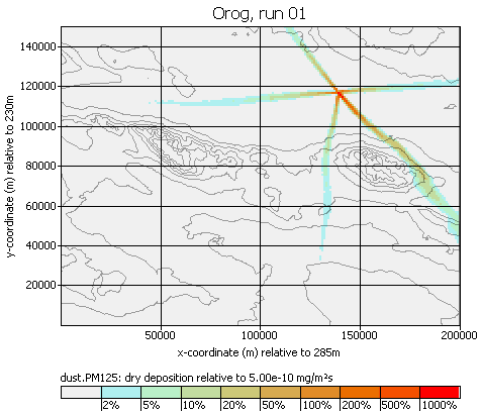

(d)

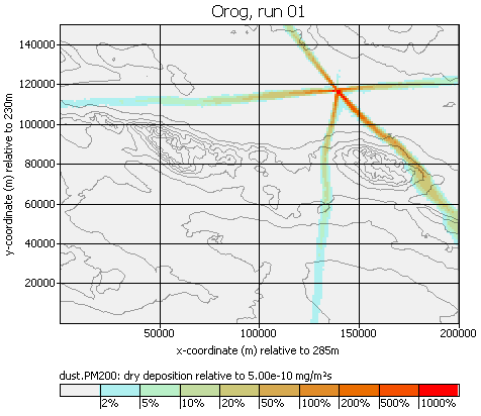

(e)

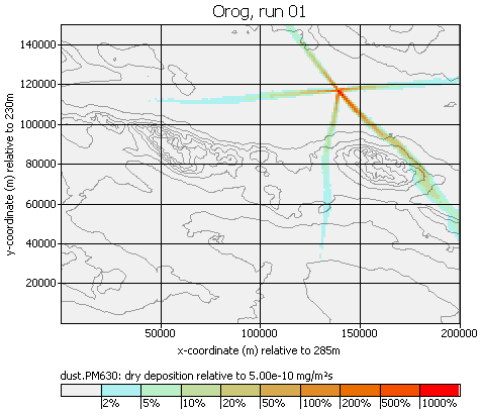

(f)

Fig. A.31.: Surface condition and particle dispersion. WP 0808156. Dry deposition Apr 2001 PM020 PM063 PM125 PM200 PM630 (fig b-g). Sources in Fig a

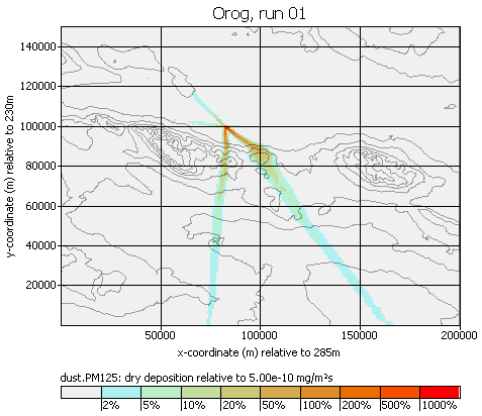
Orog, run 01
y-coordinate (m) relative to 230m
x-coordinate (m) relative to 285m
dust.PM125: dry deposition relative to 5.00e-10 mg/m²s
2% 5% 10% 20% 50% 100% 200% 500% 1000%

(a)

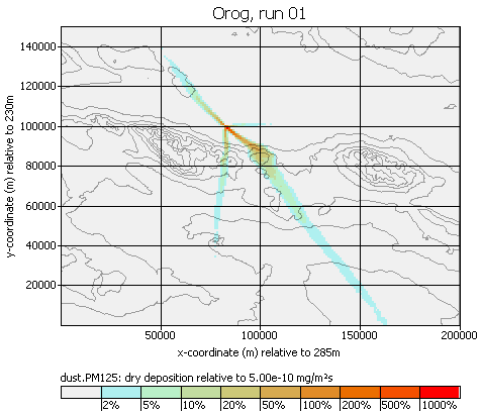
Orog, run 01
y-coordinate (m) relative to 230m
x-coordinate (m) relative to 285m
dust.PM125: dry deposition relative to 5.00e-10 mg/m²s
2% 5% 10% 20% 50% 100% 200% 500% 1000%

(b)

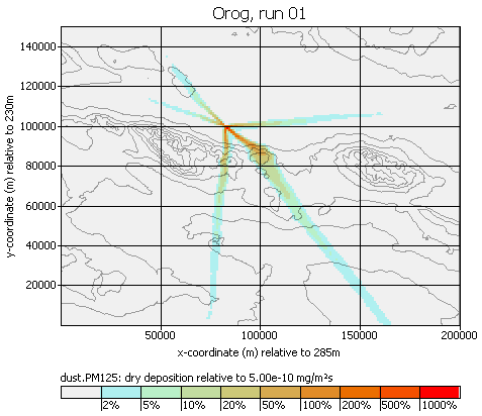
Orog, run 01
y-coordinate (m) relative to 230m
x-coordinate (m) relative to 285m
dust.PM125: dry deposition relative to 5.00e-10 mg/m²s
2% 5% 10% 20% 50% 100% 200% 500% 1000%

(c)

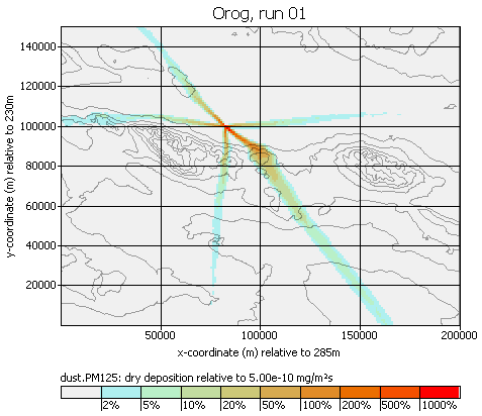
Orog, run 01
y-coordinate (m) relative to 230m
x-coordinate (m) relative to 285m
dust.PM125: dry deposition relative to 5.00e-10 mg/m²s
2% 5% 10% 20% 50% 100% 200% 500% 1000%

(d)

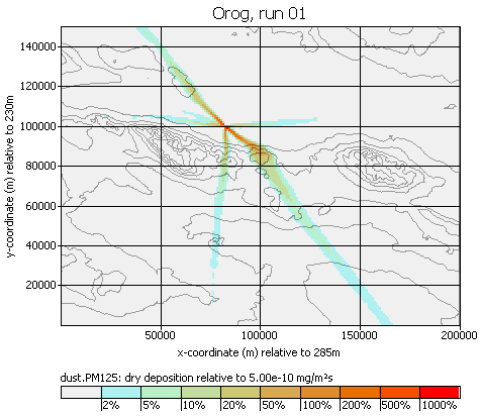
Orog, run 01
y-coordinate (m) relative to 230m
x-coordinate (m) relative to 285m
dust.PM125: dry deposition relative to 5.00e-10 mg/m²s
2% 5% 10% 20% 50% 100% 200% 500% 1000%

(e)

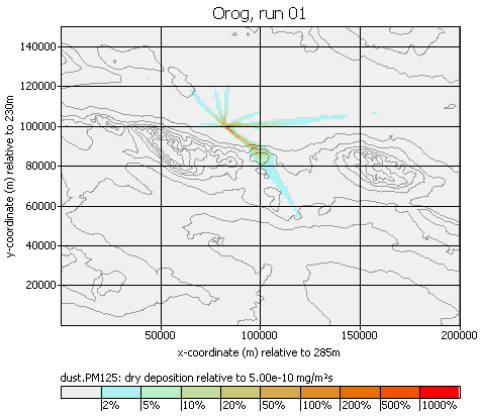
Orog, run 01
y-coordinate (m) relative to 230m
x-coordinate (m) relative to 285m
dust.PM125: dry deposition relative to 5.00e-10 mg/m²s
2% 5% 10% 20% 50% 100% 200% 500% 1000%

(f)

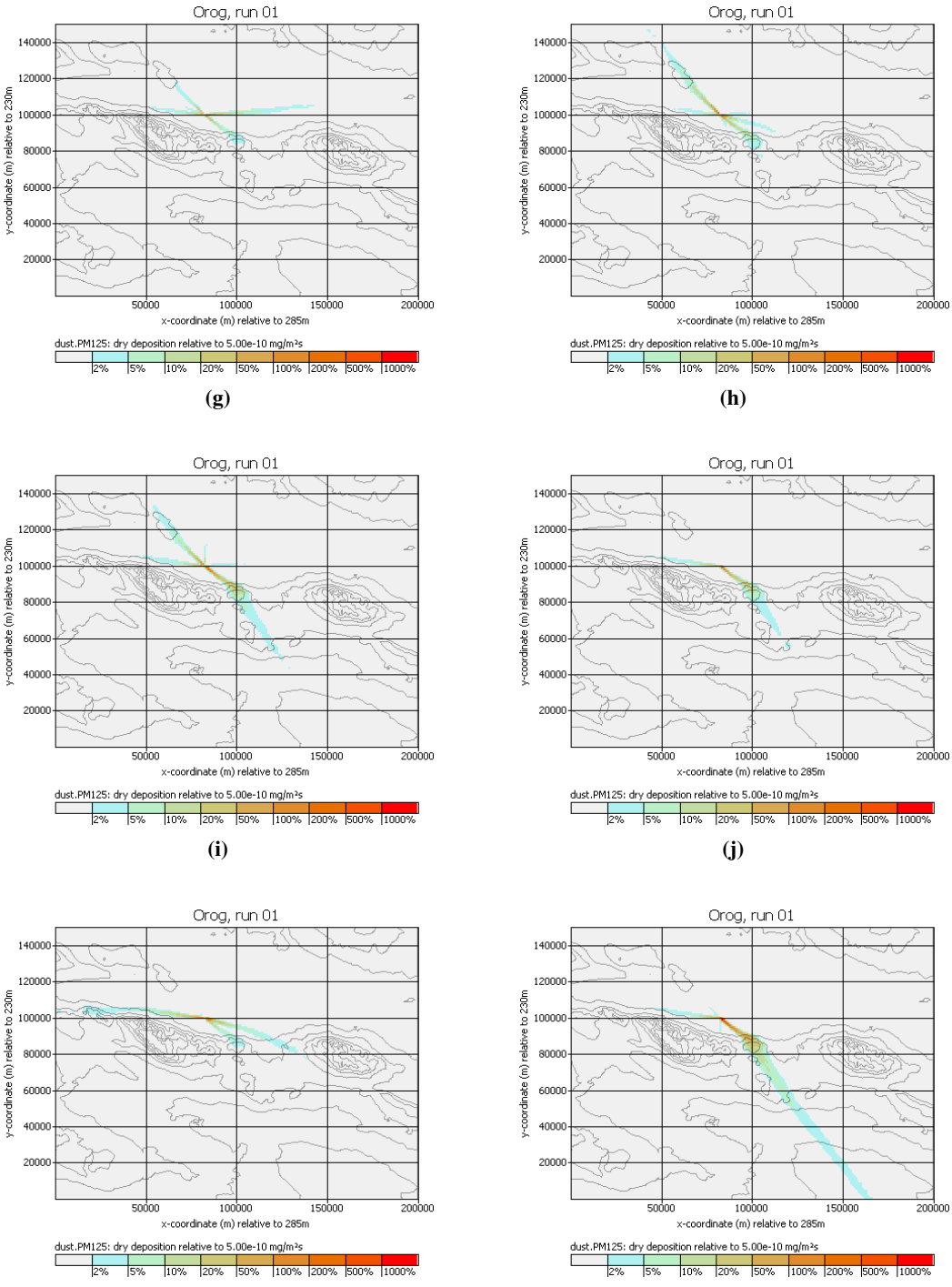

Fig. A.32.: Particle dispersion. WP 0708099. PM 125 dry deposition. Jan to Dec 2001 (Fig a - l)

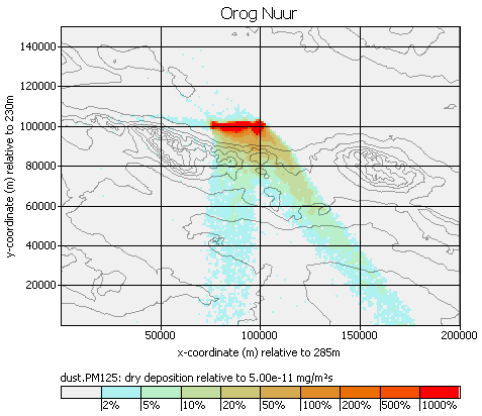
Orog Nuur
y-coordinate (m) relative to 230m
140000
120000
100000
80000
60000
40000
20000
50000
100000
150000
200000
x-coordinate (m) relative to 285m
dust.PM125: dry deposition relative to 5.00e-11 mg/m²s
2%
5%
10%
20%
50%
100%
200%
500%
1000%

(a)

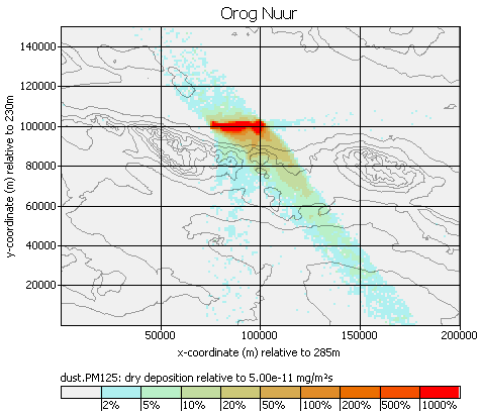
Orog Nuur
y-coordinate (m) relative to 230m
140000
120000
100000
80000
60000
40000
20000
50000
100000
150000
200000
x-coordinate (m) relative to 285m
dust.PM125: dry deposition relative to 5.00e-11 mg/m²s
2%
5%
10%
20%
50%
100%
200%
500%
1000%

(b)

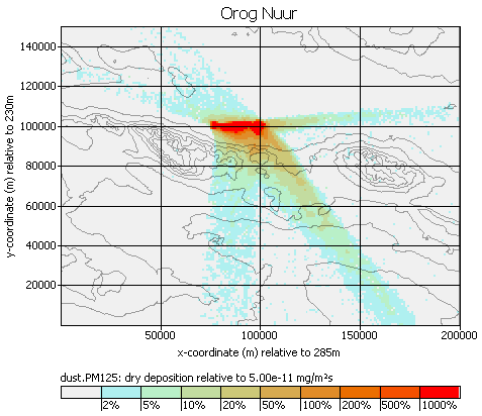
Orog Nuur
y-coordinate (m) relative to 230m
140000
120000
100000
80000
60000
40000
20000
50000
100000
150000
200000
x-coordinate (m) relative to 285m
dust.PM125: dry deposition relative to 5.00e-11 mg/m²s
2%
5%
10%
20%
50%
100%
200%
500%
1000%

(c)

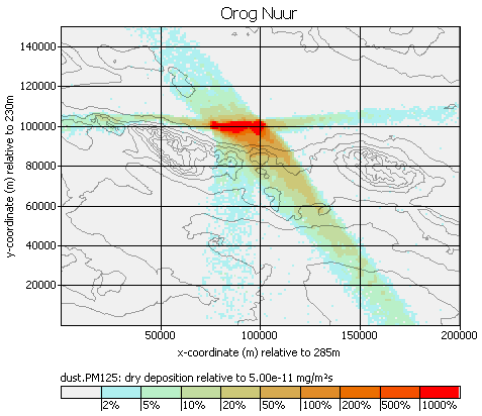
Orog Nuur
y-coordinate (m) relative to 230m
140000
120000
100000
80000
60000
40000
20000
50000
100000
150000
200000
x-coordinate (m) relative to 285m
dust.PM125: dry deposition relative to 5.00e-11 mg/m²s
2%
5%
10%
20%
50%
100%
200%
500%
1000%

(d)

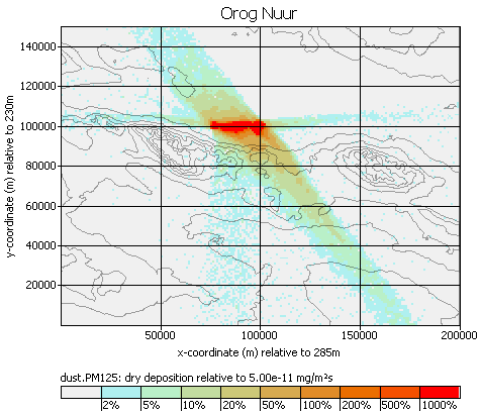
Orog Nuur
y-coordinate (m) relative to 230m
140000
120000
100000
80000
60000
40000
20000
50000
100000
150000
200000
x-coordinate (m) relative to 285m
dust.PM125: dry deposition relative to 5.00e-11 mg/m²s
2%
5%
10%
20%
50%
100%
200%
500%
1000%

(e)

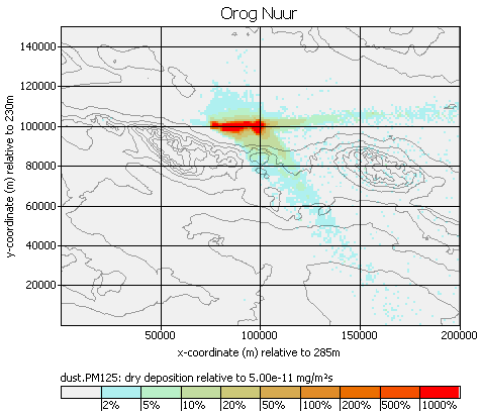
Orog Nuur
y-coordinate (m) relative to 230m
140000
120000
100000
80000
60000
40000
20000
50000
100000
150000
200000
x-coordinate (m) relative to 285m
dust.PM125: dry deposition relative to 5.00e-11 mg/m²s
2%
5%
10%
20%
50%
100%
200%
500%
1000%

(f)

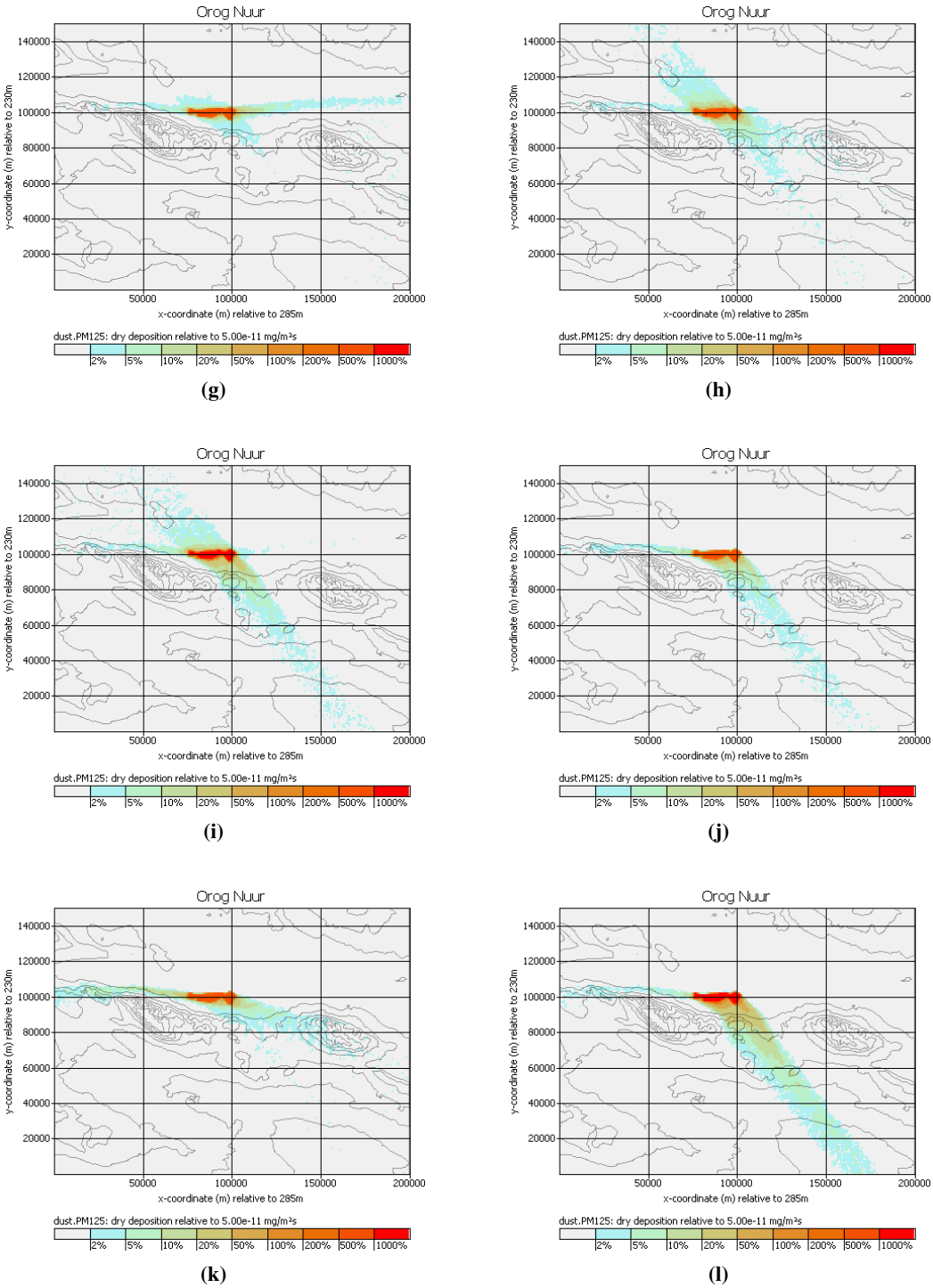

Fig. A.33.: Particle disperstion. Orog Nuur lake basin. PM 125 dry deposition (mg/m^2/sec). Jan to Dec 2001 (Fig a - l)

Table A.1.: Site Coordinates of the taken ESR Samples

ID	name	region	north	west	altitude
1	708033	KhongorienEls	43,725071	102,379017	1523
2	708036	KhongorienEls	43,731546	102,373706	1474
3	708048	KhongorienEls	43,733767	102,370074	1462
4	708059	KhongorienEls	43,733509	102,370428	0
5	708081	KhongorienEls	43,805076	102,167541	0
6	708096	OrogNuur	45,113270	100,580424	0
7	804036	sourcearea	43,903720	101,961350	1098
8	804064	ZungolEls	43,608580	100,565950	1736
9	804069	ZungolEls	43,406500	101,638220	1361
10	808088	UlanNuur	44,192450	103,632260	1162
11	808121	BBtras	43,962860	101,024730	1132
12	808144	NuginEls	45,036560	101,388450	1396
13	808145	NuginEls	45,054770	101,385470	1335
14	808150	NuginEls	45,399520	101,272310	1394

Table A.3.: Crystallinity index

Sample name	Caption	Angle 2theta	d value Å	Intensity Count	Intensity % %	average
Quarzstand	d=1,38268	67,71200	1,38268	47,50000	100,00000	43,96667
ci 0708033 gS	d=1,38305	67,69100	1,38305	24,90000	100,00000	23,83333
ci 0708036 ffS	d=1,38217	67,74000	1,38217	38,40000	99,00000	37,76667
ci 0708036 fS	d=1,38222	67,73700	1,38222	29,20000	99,20000	28,16667
ci 0708036 mS	d=1,38228	67,73400	1,38228	53,40000	88,30000	54,80000
ci 0708048 ffS	d=1,38248	67,72300	1,38248	47,00000	81,80000	52,56667
ci 0708048 fS	d=1,38235	67,73000	1,38235	19,50000	89,70000	21,03333
ci 0708048 gS	d=1,38182	67,76000	1,38182	42,80000	97,30000	41,20000
ci 0708048 mS	d=1,38203	67,74800	1,38203	74,70000	100,00000	63,10000
ci 0708059 ffS	d=1,38213	67,74300	1,38213	56,70000	88,40000	57,00000
ci 0708059 fS	d=1,38218	67,74000	1,38218	28,90000	84,60000	31,26667
ci 0708059 gS	d=1,38197	67,75100	1,38197	31,30000	85,80000	31,10000
ci 0708059 mS	d=1,38206	67,74700	1,38206	23,40000	78,40000	26,56667
ci 0708081 ffS	d=1,38325	67,68000	1,38325	32,90000	100,00000	32,00000
ci 0708081 fS	d=1,38231	67,73200	1,38231	25,20000	98,60000	23,86667
ci 0708081 gS	d=1,38253	67,72000	1,38253	17,80000	77,80000	19,06667
ci 0708081 mS	d=1,38169	67,76700	1,38169	37,70000	100,00000	32,03333
ci 0708096 ffS	d=1,38220	67,73900	1,38220	55,00000	82,00000	62,43333
ci 0708096 fS	d=1,38204	67,74800	1,38204	54,20000	100,00000	42,70000
ci 0708096 mS	d=1,38215	67,74200	1,38215	23,40000	90,50000	23,16667
ci 0804036 ffS	d=1,38242	67,72600	1,38242	20,50000	91,70000	21,60000
ci 0804036 fS	d=1,38215	67,74100	1,38215	49,90000	97,20000	47,86667
ci 0804036 gS	d=1,38224	67,73600	1,38224	52,00000	86,80000	55,20000

Continued on next page

Table A.3 – continued from previous page

Sample name	Caption	Angle 2Theta	d value Å	Intensity Count	Intensity % %	average
ci 0804036 mS	d=1,38169	67,76700	1,38169	42,60000	95,30000	43,86667
ci 0804064 ffS	d=1,38233	67,73100	1,38233	48,10000	86,60000	49,33333
ci 0804064 fS	d=1,38263	67,71500	1,38263	18,20000	72,00000	22,50000
ci 0804064 gS	d=1,38210	67,74400	1,38210	39,20000	100,00000	35,26667
ci 0804064 mS	d=1,38223	67,73700	1,38223	26,10000	86,20000	28,60000
ci 0804069 ffS	d=1,38169	67,76700	1,38169	52,10000	100,00000	50,03333
ci 0804069 fS	d=1,38197	67,75200	1,38197	58,30000	100,00000	40,10000
ci 0804069 mS	d=1,38224	67,73600	1,38224	49,20000	100,00000	46,43333
ci 0808088 ffS	d=1,38189	67,75600	1,38189	35,70000	100,00000	30,56667
ci 0808088 fS	d=1,38216	67,74100	1,38216	38,40000	88,20000	37,50000
ci 0808088 gS	d=1,38211	67,74400	1,38211	23,90000	82,30000	26,30000
ci 0808088 mS	d=1,38244	67,72500	1,38244	63,20000	98,20000	62,23333
ci 0808121 ffS	d=1,38095	67,80800	1,38095	37,10000	100,00000	33,50000
ci 0808121 fS	d=1,38204	67,74800	1,38204	66,50000	100,00000	64,16667
ci 0808121 gS	d=1,38227	67,73500	1,38227	54,40000	100,00000	35,86667
ci 0808121 mS	d=1,38259	67,71700	1,38259	35,90000	100,00000	29,80000
ci 0808144 ffS	d=1,38144	67,78100	1,38144	21,90000	99,40000	21,86667
ci 0808144 fS	d=1,38194	67,75300	1,38194	38,00000	86,20000	39,90000
ci 0808144 gS	d=1,38238	67,72800	1,38238	29,50000	78,10000	33,93333
ci 0808144 mS	d=1,38221	67,73800	1,38221	36,40000	87,60000	34,80000
ci 0808145 ffS	d=1,38230	67,73300	1,38230	40,20000	100,00000	35,96667
ci 0808145 fS	d=1,38209	67,74500	1,38209	37,50000	85,20000	41,20000
ci 0808145 mS	d=1,38180	67,76100	1,38180	32,70000	100,00000	30,10000
ci 0808150 ffS	d=1,38206	67,74600	1,38206	24,30000	91,60000	24,56667
ci 0808150 fS	d=1,38192	67,75400	1,38192	62,30000	100,00000	59,66667
ci 0808150 gS	d=1,38163	67,77000	1,38163	48,40000	97,90000	48,80000
ci 0808150 mS	d=1,38289	67,70000	1,38289	21,30000	69,00000	26,80000

Table A.2.: Averaged grain size values of particle scans. The raw data, with resolution of 200 steps are not listed here

	μ m (in %)	≤ 2	2 – 6,3	6,3 – 20	20 – 63	63 – 125	125 – 200	200 – 630	630 – 2000
2008807WP098	BBeast	29,86	27,67	14,75	7,22	7,85	5,18	5,67	1,78
2008807WP101	BBeast	13,74	12,07	6,18	5,90	15,69	17,74	27,05	1,64
2008810WP117	BBT	1,36	1,30	1,07	1,54	4,59	6,16	42,23	41,76
2008810WP118	BBT	5,16	5,21	3,78	4,87	21,27	22,58	28,32	8,80
2008810WP119	BBT	2,50	1,98	1,70	3,72	20,38	23,50	37,45	8,77
2008810WP120	BBT	17,01	20,06	12,21	4,49	9,90	9,25	21,92	5,16
2008810WP121	BBT	4,03	3,63	2,20	4,07	20,79	20,83	37,33	7,12
2008810WP122	BBT	2,40	2,40	2,18	4,15	13,13	13,34	37,93	24,47
2008810WP123	BBT	4,32	8,45	7,45	6,14	7,37	21,17	41,16	3,94
2008810WP124	BBT	2,09	3,47	3,58	2,94	3,83	6,83	63,98	13,28
2008810WP125	BBT	3,16	4,36	3,84	3,64	5,25	8,80	53,43	17,53
2008810WP126	BBT	5,21	8,74	9,95	10,48	32,22	27,13	5,55	0,73
2008810WP127	BBT	3,43	3,41	3,03	5,78	12,34	11,27	36,09	24,65
2008810WP128	BBT	6,99	7,66	11,15	18,75	20,66	10,25	17,53	7,00
2008810WP133	BBT	11,56	15,70	27,69	22,49	9,19	5,88	5,25	2,24
2008810WP134	BBT	7,05	6,87	5,12	5,42	10,82	10,03	27,54	27,15
2008810WP135	BBT	23,64	5,15	26,54	36,40	7,37	0,90	0,00	0,00
2008810WP136	BBT	65,27	15,69	11,01	3,81	3,06	1,17	0,00	0,00
2008810WP137	BBT	27,27	9,36	43,57	19,11	0,69	0,00	0,00	0,00
2008810WP138	BBT	6,49	6,96	4,28	4,36	19,49	22,19	31,57	4,65
2008810WP139	BBT	12,65	11,90	6,54	5,83	16,60	16,58	23,18	6,72
2008810WP140	BBT	47,58	10,67	19,77	12,13	6,76	3,09	0,00	0,00
2008811WP141	Orog	2,31	2,04	2,15	2,79	15,11	26,49	41,34	5,81
2008811WP141	Orog	16,73	22,57	27,05	20,33	5,10	3,23	4,60	0,39
2008811WP142	Orog	2,52	2,17	2,15	4,78	31,06	34,49	22,70	0,13
2008811WP143	Orog	2,88	2,58	2,42	3,87	23,74	31,17	33,23	0,12
2007823WP099	Orog	1,39	1,17	1,15	2,76	9,70	8,60	40,56	34,67
2008812WP144	NugE	2,10	1,10	0,93	5,52	31,72	46,36	11,69	0,59
2008812WP145	NugE	1,25	0,42	0,25	1,12	18,85	57,42	20,68	0,00
2008812WP146	NugE	0,72	0,27	0,25	1,67	6,61	15,40	70,17	4,92
2008812WP147	NugE	0,18	0,03	0,03	0,22	1,60	29,19	68,73	0,00
2008814WP148	NugE	13,59	12,95	6,80	5,18	14,86	16,38	23,53	6,69
2008815WP150	NugE	3,71	3,93	5,56	13,55	25,14	24,13	23,88	0,08
2008815WP151	NugE	4,97	5,24	6,84	16,98	30,43	20,59	13,14	1,80
2008815WP152	NugE	11,85	13,21	12,24	13,52	15,85	9,82	14,40	9,12
2008815WP153	NugE	12,80	13,54	9,22	9,97	15,10	10,77	18,25	10,35
2008815WP155	NugE	2,25	1,42	0,99	3,20	21,11	24,61	36,62	9,79
2008816WP156	NugE	7,21	7,30	5,26	5,02	5,52	23,94	45,73	0,02

Table A.4.: Values of the X-Ray fluorescence analyses

samplename	Sc	V	Cr	Co	Ni	Cu	Zn	Ga	Rb	Sr	Y	Zr	Nb	Ba	Pb	Th	U
804036xla	5,0	45,0	34,0	2,0	10,0	6,0	24,0	14,0	97,0	269,0	11,0	223,0	8,0	490,0	17,0	4,8	0,5
708033 gS	8,0	55,0	17,0	7,0	9,0	15,0	37,0	12,0	54,0	245,0	24,0	185,0	8,0	580,0	9,0	5,4	1,2
708048 fS	2,0	21,0	16,0	4,0	6,0	6,0	16,0	10,0	96,0	222,0	9,0	73,0	3,0	608,0	15,0	2,1	0,1
708048 mS	3,0	16,0	10,0	2,0	4,0	5,0	13,0	8,0	85,0	154,0	7,0	54,0	2,0	551,0	15,0	1,7	0,0
708081 mS	13,0	90,0	55,0	11,0	26,0	27,0	58,0	14,0	91,0	288,0	20,0	152,0	9,0	583,0	18,0	5,3	0,6
708081 mS	12,0	86,0	54,0	10,0	25,0	25,0	56,0	13,0	87,0	255,0	21,0	134,0	8,0	555,0	15,0	6,4	1,4
708096ffS	12,0	64,0	65,0	9,0	22,0	11,0	38,0	15,0	66,0	364,0	20,0	152,0	8,0	543,0	17,0	7,6	0,7
708096 fS	5,0	37,0	25,0	4,0	13,0	8,0	27,0	14,0	73,0	362,0	10,0	73,0	4,0	542,0	15,0	4,0	0,8
808088 fS	5,0	33,0	24,0	3,0	10,0	6,0	20,0	11,0	103,0	194,0	11,0	89,0	6,0	590,0	18,0	3,3	0,0
808088 mS	3,0	26,0	21,0	2,0	6,0	5,0	16,0	7,0	82,0	142,0	7,0	58,0	3,0	517,0	13,0	3,2	0,2
808088ffS	7,0	73,0	61,0	5,0	20,0	10,0	36,0	13,0	89,0	266,0	19,0	499,0	14,0	543,0	17,0	5,0	1,6
808144ffS	12,0	137,0	200,0	11,0	31,0	11,0	58,0	16,0	75,0	380,0	32,0	514,0	20,0	531,0	18,0	8,6	1,7
808145ffS	12,0	83,0	111,0	7,0	25,0	9,0	42,0	15,0	78,0	384,0	22,0	218,0	13,0	548,0	16,0	5,4	1,6
808145 fS	4,0	34,0	26,0	2,0	11,0	5,0	23,0	13,0	82,0	365,0	11,0	70,0	4,0	637,0	16,0	2,6	0,0
804036 fS	4,0	29,0	13,0	3,0	6,0	4,0	16,0	12,0	106,0	230,0	8,0	75,0	4,0	560,0	18,0	3,2	1,4
804036ffS	5,0	41,0	26,0	4,0	9,0	6,0	22,0	14,0	95,0	263,0	10,0	206,0	8,0	515,0	17,0	4,3	0,0
804069 fS	4,0	30,0	13,0	4,0	6,0	7,0	18,0	11,0	98,0	236,0	11,0	66,0	4,0	615,0	17,0	3,3	0,0
804069ffS	5,0	55,0	27,0	6,0	9,0	10,0	26,0	12,0	86,0	266,0	16,0	250,0	10,0	571,0	15,0	3,9	2,0
804069 mS	1,0	20,0	12,0	2,0	7,0	5,0	14,0	8,0	90,0	192,0	8,0	58,0	2,0	622,0	11,0	1,9	0,0
804064 fS	6,0	37,0	21,0	3,0	7,0	6,0	22,0	12,0	94,0	263,0	14,0	166,0	9,0	695,0	16,0	3,5	0,6
804064ffS	8,0	54,0	32,0	6,0	11,0	7,0	30,0	13,0	85,0	273,0	19,0	377,0	10,0	531,0	15,0	5,4	0,7
804036 mS	2,0	19,0	16,0	1,0	7,0	3,0	12,0	9,0	104,0	173,0	6,0	55,0	3,0	607,0	13,0	1,4	0,0
804064 mS	4,0	27,0	21,0	4,0	6,0	6,0	18,0	10,0	89,0	203,0	9,0	91,0	4,0	671,0	14,0	2,2	0,0
808121ffS	10,0	71,0	49,0	9,0	17,0	11,0	39,0	13,0	85,0	241,0	30,0	376,0	15,0	506,0	18,0	9,1	1,6
808121 mS	4,0	14,0	12,0	2,0	5,0	4,0	14,0	9,0	110,0	144,0	9,0	61,0	4,0	544,0	15,0	2,2	0,0
808144 fS	7,0	43,0	40,0	6,0	17,0	7,0	27,0	14,0	79,0	367,0	13,0	89,0	6,0	674,0	15,0	2,5	1,3
708096 mS	3,0	24,0	15,0	3,0	8,0	5,0	21,0	13,0	78,0	337,0	9,0	73,0	3,0	686,0	18,0	3,1	1,1
708059 mS	1,0	15,0	11,0	1,0	5,0	5,0	13,0	8,0	79,0	151,0	8,0	55,0	2,0	513,0	11,0	1,5	0,0
708059 fS	4,0	26,0	20,0	4,0	8,0	7,0	18,0	10,0	93,0	227,0	10,0	66,0	4,0	609,0	15,0	1,9	0,0
808121 fS	6,0	32,0	17,0	4,0	9,0	7,0	25,0	11,0	106,0	196,0	19,0	101,0	8,0	573,0	19,0	5,1	0,4

Table A.5.: General soil parameter of the investigated surface samples

ID	SampleID	Sample	region	north	east	alt	date	Ca	pH	pH	Org
1	2007 8 17 WP 033	708033	KhonEls	43,725071	102,379017	1523	17.08.2007				0,26
2	2007 8 17 WP 036	703036	KhonEls	43,731546	102,373706	1474	17.08.2007				0,19
3	2007 8 17 WP 048	708048	KhonEls	43,733767	102,370074	1462	17.08.2007				0,16
4	2007 8 17 WP 059	708059	KhonEls	43,733509	102,370428	0	17.08.2007				0,21
5	2007 8 18 WP 079	708079	KhonEls	43,766806	102,223422	1450	18.08.2007				0,14
6	2007 8 19 WP 081	708081	KhonEls	43,805076	102,167541	0	19.08.2007	7,48	8,86	7,76	1,83
7	2007 8 23 WP 096	708096	OrogNuur	45,113270	100,580424	0	23.08.2007	0,31	8,59	7,32	0,47
8	2007 8 23 WP 99	708099	OrogNuur	45,060516	100,636058	0	23.08.2007	0,94			4,58
9	2007 8 25 WP 114	780114	OrogNuur	45,120324	100,767492	1221	25.08.2007	0,57	8,71	7,76	0,53
10	2007 8 28 WP 188	708188	Cp070829	45,714594	97,399914	1380	28.08.2007	2,71	8,80	8,07	0,34
11	2007 8 31 WP 198	708198	MungolEls	47,335635	95,738361	1470	31.08.2007	0,55	8,65	7,38	0,21
12	2007 8 31 WP 200	708200	MungolEls	47,334005	95,738667	1500	31.08.2007	0,53	8,89	7,59	0,20
13	08 4 13 WP 036	804036	SKHEl	43,903720	101,961350	1098	13.04.2008	0,71	9,80	7,83	0,18
14	08 4 19 WP 064	804064	Zung els	43,608580	100,565950	1736	19.04.2008	1,51	8,45	7,78	0,61
15	08 4 19 WP 067	804067	Zung els	43,581080	100,543220	1574	19.04.2008	0,86	8,86	7,67	0,45
16	2008 4 20 WP 069	804069	Zung els	43,406500	101,638220	1361	20.04.2008	0,91	9,67	7,94	0,21
17	2008 4 20 WP 070	804070	Zung els	43,376450	101,885560	1408	20.04.2008	0,81	9,96	8,14	0,34
18	2008 4 28 WP St	804stu	BajanOn	47,052190	105,941040	1186	28.04.2008	0,32			8,84
19	2008 8 05 WP 087	808087	Ulan Nuur	44,255460	103,678220	1092	05.08.2008	1,12	9,08	7,78	0,38
20	2008 8 05 WP 088	808088	Ulan Nuur	44,192450	103,632260	1162	05.08.2008	1,28	8,83	7,74	0,65
21	2008 8 07 WP 101	807101	BlBasinea	43,966550	101,862830	1060	07.08.2008	1,23			
22	2008 8 07 WP 105	808105	SKHEl	43,901860	101,848200	1101	07.08.2008	1,93	9,63	7,89	0,27
23	2008 8 07 WP 106	808106	SKHEl	43,826270	101,769100	1181	07.08.2008	1,31	9,09	7,87	0,28
24	2008 8 07 WP 98	808098	BlBasinea	44,007900	102,047540	1073	07.08.2008	1,90	8,94	7,88	
25	2008 8 08 WP 113	808113	Zung els	43,415470	101,580740	1324	08.08.2008	1,37	9,15	7,88	0,38
26	2008 8 08 WP 114	808114	Zung els	43,431840	101,550510	1374	08.08.2008	1,50	9,25	7,87	0,33
27	2008 8 09 WP Gur	808gur	Zung els	43,402640	101,337150	1320	09.08.2008	1,34	10,04	8,12	0,23

Continued on next page

Table A.5 – continued from previous page

ID	SampleID	Sample	region	north	east	alt	date	Ca	pH	pH	Org
28	2008 8 10 WP 117	808117	BBTran	43,744580	101,1857201182		10.08.2008	5,31	9,10	7,78	0,32
29	2008 8 10 WP 118	808118	BBTran	43,836820	101,0816701071		10.08.2008	2,34	8,70	7,64	0,52
30	2008 8 10 WP 119	808119	BBTran	43,905690	101,0375801099		10.08.2008	3,21	8,69	7,67	
31	2008 8 10 WP 120	808120	BBTran	43,962230	101,0250200		10.08.2008	1,77	8,90	7,76	1,32
32	2008 8 10 WP 121	808121	BBTran	43,962860	101,0247301132		10.08.2008	1,04	8,89	7,72	
33	2008 8 10 WP 122	808122	BBTran	44,018500	101,0108701174		10.08.2008	2,49	9,06	7,80	0,47
34	2008 8 10 WP 123	808123	BBTran	44,043290	101,0024501203		10.08.2008	1,53	9,18	8,41	0,82
35	2008 8 10 WP 124	808124	BBTran	44,042330	100,9985501186		10.08.2008	3,30	9,60	8,18	0,42
36	2008 8 10 WP 125	808125	BBTran	44,042380	100,9986301188		10.08.2008	6,18	9,83	8,02	0,71
37	2008 8 10 WP 126	808126	BBTran	44,041960	100,9973001186		10.08.2008	8,67	10,16	8,79	0,80
38	2008 8 10 WP 127	808127	BBTran	44,069330	101,0451701220		10.08.2008	7,10	8,98	7,83	0,63
39	2008 8 10 WP 128	808128	BBTran	44,111980	101,0791201243		10.08.2008	5,49	9,01	7,81	1,08
40	2008 8 10 WP 133	808133	BBTran	44,310170	101,0286901263		10.08.2008	11,93	8,55	7,76	2,56
41	2008 8 10 WP 134	808134	BBTran	44,371790	101,0232401257		10.08.2008	7,02	8,95	8,01	0,87
42	2008 8 10 WP 135	808135	BBTran	44,432490	101,0153601237		10.08.2008	5,99	9,01	8,07	0,82
43	2008 8 10 WP 136	808136	BBTran	44,458530	101,0208001221		10.08.2008	6,99	8,81	7,91	
44	2008 8 10 WP 137	808137	BBTran	44,481240	101,0075301242		10.08.2008	10,78	8,57	8,21	
45	2008 8 10 WP 138	808138	BBTran	44,515270	100,9347601277		10.08.2008	6,26	9,07	8,14	0,71
46	2008 8 10 WP 139	808139	BBTran	44,571800	100,8697301387		10.08.2008	7,01	8,95	8,04	0,83
47	2008 8 10 WP 140	808140	BBTran	44,615030	100,9384801519		10.08.2008	11,77	8,90	7,94	1,18
48	2008 8 11 WP 141	808141	Orog Nuur	45,095420	100,7646801220		11.08.2008	3,01	9,83	8,51	0,60
49	2008 8 11 WP 141	808141	Orog Nuur	45,095420	100,7646801220		11.08.2008	1,03	10,23	8,98	2,34
50	2008 8 11 WP 142	808142	Orog Nuur	45,095280	100,7647301218		11.08.2008	0,57	9,50	8,54	0,68
51	2008 8 11 WP 143	808143	Orog Nuur	45,095520	100,7646601221		11.08.2008	0,94	9,26	8,27	0,57
52	2008 8 12 WP 144	808144	NuginEls	45,036560	101,3884501396		12.08.2008	0,76	8,71	7,61	0,64
53	2008 8 12 WP 145	808145	NuginEls	45,054770	101,3854701335		12.08.2008	6,66	8,77	7,69	0,34

Continued on next page

Table A.5 – continued from previous page

ID	SampleID	Sample	region	north	east	alt	date	Ca	pH	pH	Org
54	2008 8 12 WP 146	808146	NuginEls	45,075230	101,3811201306		12.08.2008	2,14	8,90	7,69	0,25
55	2008 8 12 WP 147	808147	NuginEls	45,091760	101,3784001304		12.08.2008	2,49	8,99	7,65	0,21
56	2008 8 14 WP 148	808148	NuginEls	45,145050	101,5022601233		14.08.2008	3,27	9,51	8,78	1,94
57	2008 8 15 WP 150	808150	NuginEls	45,399520	101,2723101394		15.08.2008	1,96	8,44	8,33	1,91
58	2008 8 15 WP 151	808151	NuginEls	45,401860	101,2705701391		15.08.2008	2,35	8,47	7,96	1,69
59	2008 8 15 WP 152	808152	NuginEls	45,404670	101,2664301407		15.08.2008	3,14	8,74	7,84	1,36
60	2008 8 15 WP 153	808153	NuginEls	45,336950	101,2607201377		15.08.2008	3,87	8,91	7,91	1,23
61	2008 8 15 WP 154	808154	NuginEls	45,252870	101,2956801353		15.08.2008	0,43	8,19	7,36	
62	2008 8 15 WP 155	808155	NuginEls	45,204090	101,3661201297		15.08.2008	0,27	8,39	7,58	0,44
63	2008 8 16 WP 156	808156	NuginEls	45,136800	101,4576501227		16.08.2008	6,20			

Table A.6.: Grain size analyses (Koehn method)

lfd. Nr	**Probe**	**Datum**	**T**	**fU**	**mU**	**gU**	**ffS**	**fS**	**mS**	**gS**	**Skelett**	**organic**
1	WP007	OrogNuur	06.04.08 2,29	0,00	0,22	0,22	36,66	47,89	12,61	0,10	0,00	0,27
2	WP08	OrogNuur	06.04.08 2,86	0,00	0,18	0,52	41,85	46,68	7,86	0,05	0,00	0,32
3	WP09	OrogNuur	06.04.08 2,95	0,03	0,14	0,40	36,53	49,94	9,94	0,07	0,00	0,46
4	WP10	OrogNuur	06.04.08 2,88	0,00	0,08	0,41	37,55	46,22	12,71	0,14	0,00	0,42
5	WP11	OrogNuur	06.04.08 2,38	0,12	0,00	0,34	18,69	38,88	39,42	0,17	0,00	0,24
6	WP12	OrogNuur	06.04.08 1,95	0,08	0,02	0,29	20,23	38,08	39,15	0,20	0,00	0,31
7	WP13	OrogNuur	06.04.08 1,25	0,02	0,12	0,04	11,05	31,73	54,14	1,66	0,00	1,00
8	WP14	OrogNuur	06.04.08 2,74	0,05	0,10	0,67	24,02	37,45	33,37	1,59	0,00	0,41
9	WP15	OrogNuur	06.04.08 2,60	0,18	0,05	1,15	32,86	41,00	21,05	1,11	0,00	0,29
10	WP16	OrogNuur	06.04.08 2,33	0,00	0,11	0,49	18,08	33,92	41,12	3,96	0,00	0,51
11	WP17	OrogNuur	06.04.08 9,47	1,65	1,84	5,51	34,05	29,99	17,44	0,06	0,00	0,93
12	WP19	OrogNuur	06.04.08 26,50	9,34	11,74	41,00	11,15	0,26	0,00	0,00	0,00	6,72
13	WP18	OrogNuur	06.04.08 33,68	19,40	18,78	21,16	6,67	0,31	0,00	0,00	0,00	5,84
14	WP20	OrogNuur	06.04.08 15,46	1,33	2,21	36,99	34,82	5,83	2,99	0,37	0,00	3,37
15	WP21	OrogNuur	06.04.08 15,34	2,06	3,89	42,00	27,62	6,53	2,41	0,15	0,00	2,03
16	WP31	Kuping	09.04.08 4,04	0,47	0,32	0,79	14,77	17,92	46,30	15,40	0,00	0,55

Continued on next page

Table A.6 – continued from previous page

lfd. Nr	Probe		Datum	T	fU	mU	gU	ffS	fS	mS	gS	Skelett	organic
17	WP32	Sed.	11.04.08	6,62	0,70	0,62	1,29	11,18	26,05	52,82	0,71	0,00	0,21
18	WP34	senFl.	11.04.08	1,35	0,00	0,00	0,04	8,97	43,25	46,01	0,39	0,64	0,37
19	WP44	PassZugol	15.04.08	10,17	2,19	6,23	16,23	43,84	17,22	4,12	0,00	0,00	0,69
20	WP48	all. fan	17.04.08	14,39	8,08	25,82	23,75	2,61	0,74	4,07	20,55	11,99	3,95
21	WP61	sedim	18.04.2008	7,60	1,40	1,65	12,05	46,84	22,83	7,43	0,20	0,00	0,46
22	WP65	sed fot	19.04.08	31,35	16,25	12,60	10,37	10,80	8,27	9,32	1,04	0,00	0,94
23	WP99	OrogNuur	23.08.07	46,28	27,10	13,41	4,19	5,02	1,79	1,35	0,86	0,00	3,91
24	WPst		28.04.08	8,12	1,32	1,89	2,85	20,58	29,47	32,47	3,30	0,00	7,54
25	WP33	fel	11.04.08	7,63	1,04	1,87	5,43	30,25	31,24	21,21	1,33	3,62	0,35
26	WP34	Sed	11.04.08	2,39	0,00	0,32	0,27	26,48	47,59	22,93	0,03	0,00	0,30
27	WP35	Sed	12.04.08	3,59	0,93	1,00	2,20	26,40	43,72	21,17	0,99	0,00	0,39
28	WP36	Sed	13.04.08	3,88	0,16	0,69	1,17	11,28	31,58	51,18	0,07	0,00	0,27
29	WP36	Erros	14.04.08	5,33	0,48	1,39	2,50	18,61	25,11	38,30	8,28	0,22	0,26
30	WP66	Verw	19.04.08	26,88	9,38	13,50	27,17	20,01	2,70	0,23	0,13	0,00	1,17
31	WP66	VerwiII)	19.04.2008	23,98	8,81	11,24	25,78	28,29	1,66	0,13	0,11	0,00	1,15
32	WP67	Sed	19.04.08	7,43	1,37	1,56	2,00	41,05	44,26	2,33	0,00	0,00	0,52
33	WP68	Sed	19.04.08	7,83	1,72	2,06	10,15	34,97	31,32	9,70	2,25	1,54	0,42
34	WP69	alte	20.04.08	5,08	0,00	0,14	1,87	26,96	34,15	31,65	0,15	0,00	0,26
35	WP69	Sed	20.04.08	2,42	0,14	0,19	0,43	12,29	33,28	51,09	0,17	0,00	0,23
36	WP70	Dune	20.04.08	2,48	0,17	0,00	0,33	7,01	25,70	64,31	0,00	0,00	0,29
37	WP70	SeeSed	20.04.08	15,40	22,25	23,77	19,96	7,24	6,07	4,23	1,09	0,00	3,32
38	WPWet	Flasche	23.04.08	9,20	3,33	3,73	33,74	33,98	8,02	7,01	0,98	0,00	3,59
39	WPSed	Breck	12.04.08	18,60	13,77	8,37	6,64	20,51	17,37	10,63	4,12	0,32	1,40
40	WP94Fl	OrogNuur	23.08.07	0,73	0,00	0,34	0,00	21,24	46,45	31,12	0,12	0,00	0,52
41	WP9632	OrogNuur	23.08.07	2,12	0,17	0,34	0,00	24,06	46,70	26,50	0,11	0,00	1,09
42	WP9634	OrogNuur	23.08.07	1,49	0,11	0,06	0,17	21,51	45,80	30,78	0,08	0,00	0,89
43	WP96Pr.35	OrogNuur	23.08.07	1,34	0,17	0,17	0,00	21,19	45,10	31,98	0,05	0,00	0,53
44	WP9636	OrogNuur	23.08.07	1,52	0,25	0,25	0,00	20,46	44,65	32,84	0,02	0,00	0,63
45	WP9653	OrogNuur	23.08.07	2,25	0,00	0,41	0,00	20,66	46,98	29,68	0,02	0,00	0,88

Continued on next page

Table A.6 – continued from previous page

lfd. Nr	Probe	Datum	T	fU	mU	gU	ffS	fS	mS	gS	Skelett	organic
46	WP9654	OrogNuur23.08.07	2,06	0,00	0,66	0,00	22,26	46,25	28,76	0,00	0,00	0,96
47	WP9655	OrogNuur23.08.07	1,31	0,06	0,24	0,12	16,03	48,26	33,99	0,00	0,00	1,00
48	WP9656	OrogNuur23.08.07	1,92	0,08	0,48	0,00	20,29	47,53	29,71	0,00	0,00	0,79
49	WP9657	OrogNuur23.08.07	2,05	0,25	0,16	0,16	20,72	46,64	30,01	0,00	0,00	0,92
50	WP981	OrogNuur23.08.07	40,71	21,58	10,38	6,24	9,86	5,81	5,16	0,26	0,00	2,26
51	WP1141	OrogNuur25.08.07	3,02	1,30	1,19	4,48	21,26	23,64	44,55	0,56	0,00	0,44
52	WP1163	OrogNuur25.08.07	5,61	1,31	1,50	5,55	32,61	29,42	22,41	1,59	0,23	0,45
54	Camp12	12.04.2008	16,54	11,06	7,21	8,41	23,61	18,68	10,59	3,89	1,34	1,25

Table A.7.: Rare earth element analyses on single grains

Sample	0733 n=30			0759 n=30			08114 n=30			0836 n=30		
	$\bar{x}$	Var	σ	$\bar{x}$	Var	σ	$\bar{x}$	Var	σ	$\bar{x}$	Var	σ
Na23	1,37E+00	7,59E+00	2,71E+00	4,30E-01	1,51E+00	1,21E+00	4,52E-01	2,85E+00	1,66E+00	6,96E-03	8,31E-05	8,96E-03
Mg25	6,67E-02	1,79E-02	1,32E-01	4,77E-01	3,38E-01	5,71E-01	9,67E-02	2,86E-02	1,66E-01	3,28E-02	9,60E-03	9,63E-02
Al27	2,99E+00	1,98E+01	4,37E+00	2,68E+00	1,94E+01	4,33E+00	5,47E-01	5,90E+00	2,39E+00	5,04E-01	4,49E+00	2,08E+00
Si29	1,00E+00	0,00E+00	0,00E+00	1,00E+00	0,00E+00	0,00E+00	1,00E+00	0,00E+00	0,00E+00	1,00E+00	0,00E+00	0,00E+00
Si30	1,03E+00	1,49E-04	1,20E-02	1,06E+00	1,45E-04	1,19E-02	9,65E-01	6,90E-02	2,58E-01	1,08E+00	1,26E-04	1,11E-02
Ca43	5,59E-03	8,60E-05	9,12E-03	1,76E-02	1,30E-03	3,54E-02	1,17E-02	1,01E-03	3,12E-02	3,49E-04	3,41E-07	5,74E-04
Ti47	7,10E-02	1,20E-02	1,08E-01	1,14E-01	2,75E-02	1,63E-01	3,20E-02	9,48E-03	9,57E-02	6,64E-03	2,17E-04	1,45E-02
V51	1,05E-02	2,75E-04	1,63E-02	4,17E-02	2,88E-03	5,27E-02	1,84E-02	7,52E-04	2,70E-02	7,15E-03	3,05E-04	1,72E-02
Cr53	1,66E-04	5,93E-08	2,39E-04	3,42E-03	1,72E-04	1,29E-02	1,88E-03	1,81E-05	4,18E-03	1,66E-04	1,51E-07	3,81E-04
Fe57	1,10E-01	2,16E-02	1,44E-01	4,50E-01	1,29E-01	3,53E-01	1,06E-01	6,38E-02	2,48E-01	7,93E-02	3,75E-02	1,90E-01
Co59	1,37E-03	6,67E-06	2,54E-03	8,73E-03	9,97E-05	9,82E-03	3,78E-03	8,40E-05	9,01E-03	9,30E-04	8,25E-06	2,82E-03
Ni62	5,98E-05	9,81E-09	9,74E-05	7,08E-04	1,50E-06	1,20E-03	1,47E-04	9,47E-08	3,03E-04	4,29E-05	1,10E-08	1,03E-04
Cu65	7,17E-04	6,20E-07	7,74E-04	2,62E-03	6,77E-06	2,56E-03	5,52E-04	8,14E-07	8,87E-04	3,32E-04	3,36E-07	5,70E-04
Ga71	1,63E-03	9,84E-07	9,75E-04	2,66E-03	4,45E-06	2,07E-03	2,28E-03	9,43E-06	3,02E-03	6,22E-04	1,06E-06	1,01E-03
Ge74	9,90E-05	3,85E-09	6,10E-05	1,36E-04	1,66E-08	1,27E-04	1,38E-04	2,44E-08	1,54E-04	7,86E-05	1,62E-09	3,96E-05
Rb85	2,63E-02	5,37E-04	2,28E-02	2,22E-02	2,29E-04	1,49E-02	4,89E-02	6,74E-03	8,07E-02	1,83E-02	1,16E-03	3,34E-02
Sr88	1,51E-01	3,15E-02	1,75E-01	1,72E-01	8,62E-02	2,89E-01	1,10E-01	8,22E-02	2,82E-01	2,05E-02	1,88E-03	4,26E-02
Y89	1,63E-02	1,34E-04	1,14E-02	1,93E-02	9,43E-04	3,02E-02	2,91E-02	8,12E-03	8,86E-02	3,65E-03	4,88E-05	6,87E-03
Zr90	6,66E-02	2,97E-03	5,35E-02	3,46E-02	9,84E-04	3,08E-02	1,44E-02	3,16E-03	5,53E-02	6,98E-03	1,92E-04	1,36E-02
Nb93	4,22E-03	1,85E-05	4,23E-03	2,86E-03	7,48E-06	2,69E-03	8,33E-03	6,46E-04	2,50E-02	1,02E-03	3,10E-06	1,73E-03
Mo95	3,93E-05	1,46E-09	3,75E-05	3,58E-05	3,18E-09	5,54E-05	8,08E-05	8,51E-08	2,87E-04	1,35E-05	7,31E-10	2,66E-05

Continued on next page

Table A.7 – continued from previous page

Sample	0733 n=30			0759 n=30			08114 n=30			0836 n=30		
	$\bar{x}$	Var	σ	$\bar{x}$	Var	σ	$\bar{x}$	Var	σ	$\bar{x}$	Var	σ
Sn118	3,97E-04	4,83E-08	2,16E-04	5,68E-04	2,14E-07	4,55E-04	3,20E-03	9,05E-05	9,35E-03	2,09E-04	5,65E-08	2,34E-04
Sb121	1,19E-04	1,89E-08	1,35E-04	7,02E-05	5,60E-09	7,36E-05	1,78E-04	1,11E-07	3,27E-04	9,55E-05	1,05E-08	1,01E-04
Cs133	9,03E-04	8,43E-07	9,03E-04	1,03E-03	1,13E-06	1,05E-03	3,67E-03	2,37E-05	4,78E-03	5,41E-04	7,49E-07	8,51E-04
Ba137	4,99E-02	1,89E-03	4,27E-02	5,04E-02	2,10E-03	4,51E-02	3,57E-02	3,30E-03	5,64E-02	1,32E-02	8,16E-04	2,81E-02
La139	1,89E-02	9,29E-04	3,00E-02	1,08E-02	3,08E-04	1,73E-02	1,18E-02	1,12E-03	3,29E-02	5,62E-03	2,08E-04	1,42E-02
Ce140	3,70E-02	2,68E-03	5,09E-02	2,43E-02	1,31E-03	3,56E-02	2,30E-02	4,31E-03	6,45E-02	9,51E-03	5,61E-04	2,33E-02
Pr141	5,50E-03	6,05E-05	7,65E-03	3,82E-03	3,92E-05	6,16E-03	1,34E-02	1,62E-03	3,96E-02	1,52E-03	1,42E-05	3,71E-03
Nd146	3,50E-03	2,28E-05	4,69E-03	2,71E-03	2,13E-05	4,54E-03	9,00E-03	7,76E-04	2,74E-02	8,89E-04	4,83E-06	2,16E-03
Sm147	5,84E-04	4,89E-07	6,87E-04	5,48E-04	8,22E-07	8,91E-04	1,48E-03	2,24E-05	4,66E-03	1,50E-04	1,23E-07	3,45E-04
Eu151	3,33E-04	1,43E-07	3,71E-04	4,89E-04	7,60E-07	8,57E-04	1,75E-03	2,33E-05	4,75E-03	9,06E-05	4,26E-08	2,03E-04
Gd157	8,27E-04	7,34E-07	8,42E-04	9,15E-04	2,47E-06	1,55E-03	2,44E-03	5,62E-05	7,37E-03	1,85E-04	1,64E-07	3,99E-04
Tb159	8,42E-04	5,86E-07	7,53E-04	9,63E-04	2,50E-06	1,55E-03	2,61E-03	6,19E-05	7,73E-03	1,84E-04	1,39E-07	3,66E-04
Dy163	1,25E-03	1,06E-06	1,01E-03	1,44E-03	5,12E-06	2,22E-03	3,71E-03	1,13E-04	1,04E-02	2,69E-04	2,56E-07	4,97E-04
Ho165	1,01E-03	5,63E-07	7,38E-04	1,16E-03	3,13E-06	1,74E-03	3,08E-03	8,56E-05	9,10E-03	2,20E-04	1,61E-07	3,95E-04
Er167	6,94E-04	2,31E-07	4,73E-04	7,49E-04	1,09E-06	1,03E-03	2,02E-03	3,76E-05	6,03E-03	1,54E-04	7,59E-08	2,71E-04
Tm169	4,52E-04	8,17E-08	2,81E-04	4,65E-04	3,41E-07	5,74E-04	9,84E-04	7,82E-06	2,75E-03	1,10E-04	3,68E-08	1,89E-04
Yb173	4,89E-04	8,52E-08	2,87E-04	4,78E-04	3,02E-07	5,40E-04	9,27E-04	6,29E-06	2,47E-03	1,19E-04	4,13E-08	2,00E-04
Lu175	4,49E-04	7,85E-08	2,75E-04	4,19E-04	2,04E-07	4,44E-04	8,17E-04	4,96E-06	2,19E-03	1,09E-04	3,35E-08	1,80E-04
Hf178	1,55E-03	1,19E-06	1,07E-03	8,87E-04	5,53E-07	7,31E-04	4,84E-04	2,79E-06	1,64E-03	2,15E-04	1,33E-07	3,59E-04
Ta181	4,93E-04	2,02E-07	4,42E-04	2,70E-04	4,70E-08	2,13E-04	1,63E-03	4,66E-05	6,71E-03	1,29E-04	4,68E-08	2,13E-04
W182	5,67E-05	1,40E-09	3,68E-05	7,80E-05	1,71E-08	1,28E-04	5,38E-03	8,22E-04	2,82E-02	7,37E-05	2,76E-08	1,63E-04
Au197	4,61E-07	8,50E-13	9,06E-07	6,15E-07	8,25E-13	8,93E-07	8,83E-06	1,96E-09	4,35E-05	9,66E-07	3,31E-12	1,79E-06
Tl203	4,19E-05	1,44E-09	3,73E-05	3,48E-05	3,88E-10	1,94E-05	6,99E-05	1,25E-08	1,10E-04	3,52E-05	3,37E-09	5,71E-05
Pb208	4,32E-03	7,98E-06	2,78E-03	6,99E-03	3,43E-05	5,76E-03	1,30E-02	1,07E-03	3,22E-02	2,32E-03	1,48E-05	3,79E-03
Bi209	5,19E-05	8,88E-10	2,93E-05	7,25E-05	4,02E-09	6,23E-05	1,71E-04	2,87E-07	5,26E-04	3,39E-05	2,76E-09	5,17E-05
Th232	6,94E-03	3,63E-05	5,92E-03	3,80E-03	1,32E-05	3,57E-03	4,44E-03	1,54E-04	1,22E-02	3,02E-03	3,47E-05	5,79E-03
U238	1,98E-03	1,74E-06	1,30E-03	1,35E-03	1,94E-06	1,37E-03	1,91E-03	2,12E-05	4,53E-03	1,34E-03	5,22E-06	2,25E-03

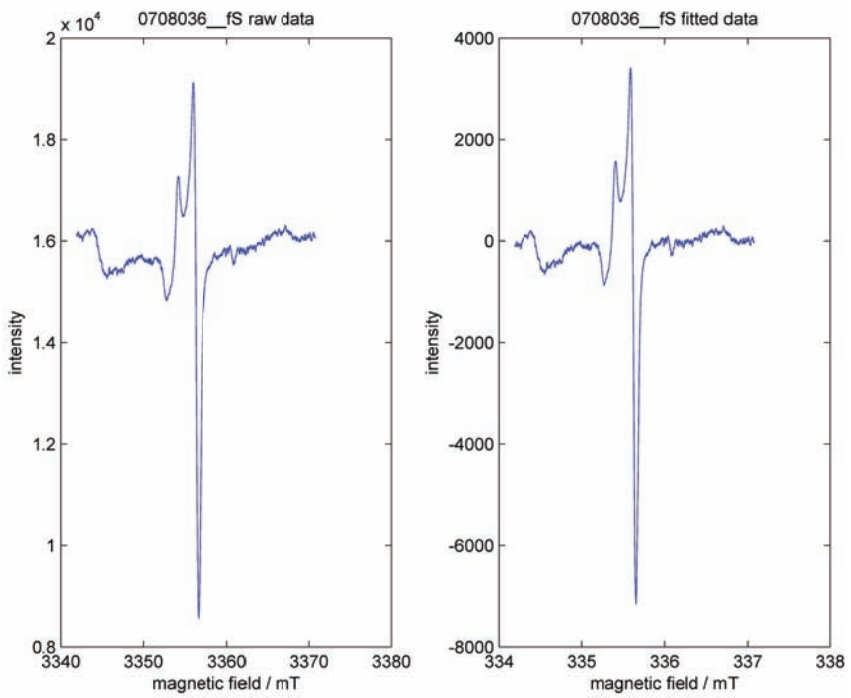
x 10^4
0708036__fS raw data
intensity
magnetic field / mT
0708036__fS fitted data
intensity
magnetic field / mT

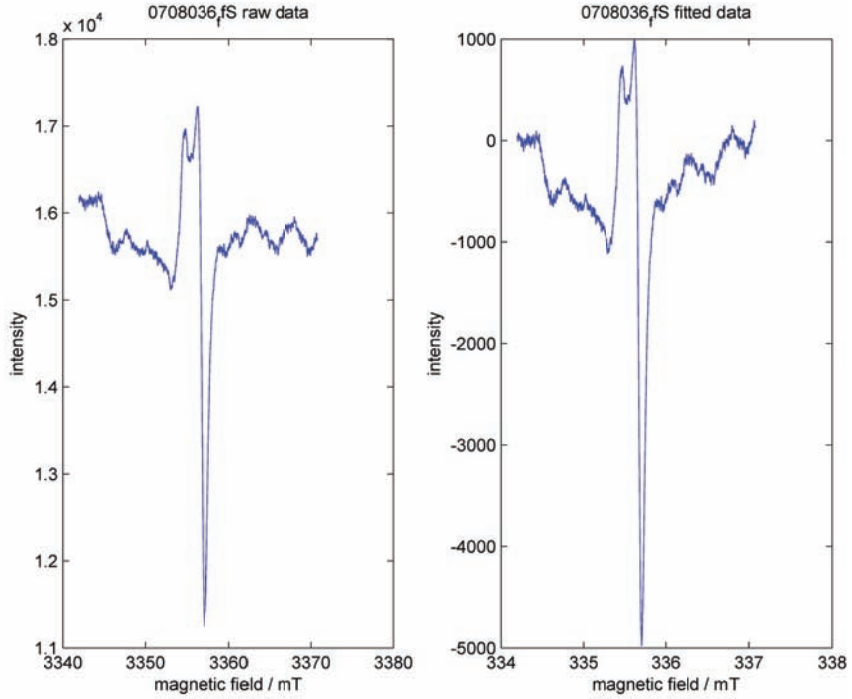
x 10^4
0708036_fS raw data
intensity
magnetic field / mT
0708036_fS fitted data
intensity
magnetic field / mT

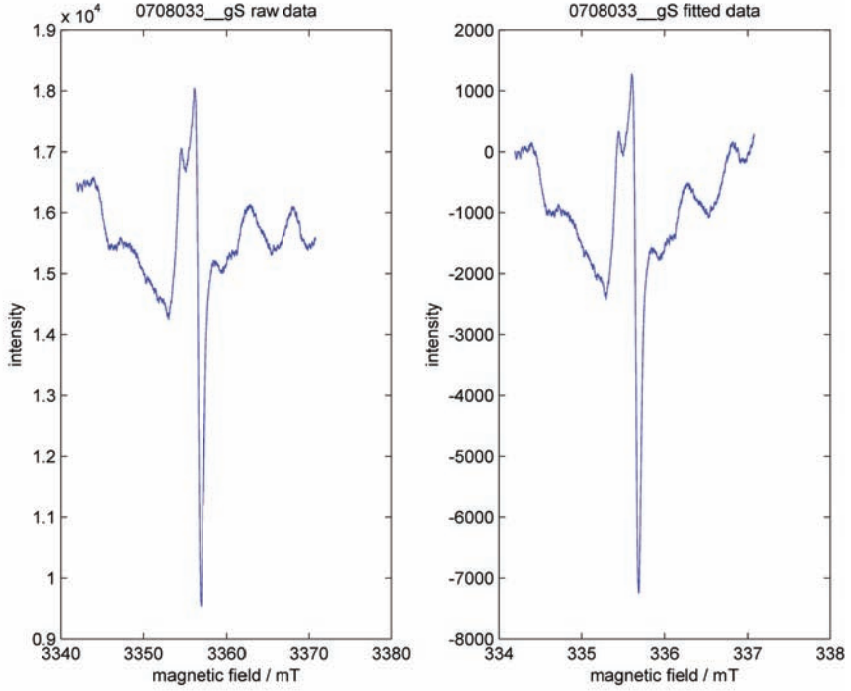
x 10^4
0708033__gS raw data
intensity
magnetic field / mT
0708033__gS fitted data
intensity
magnetic field / mT

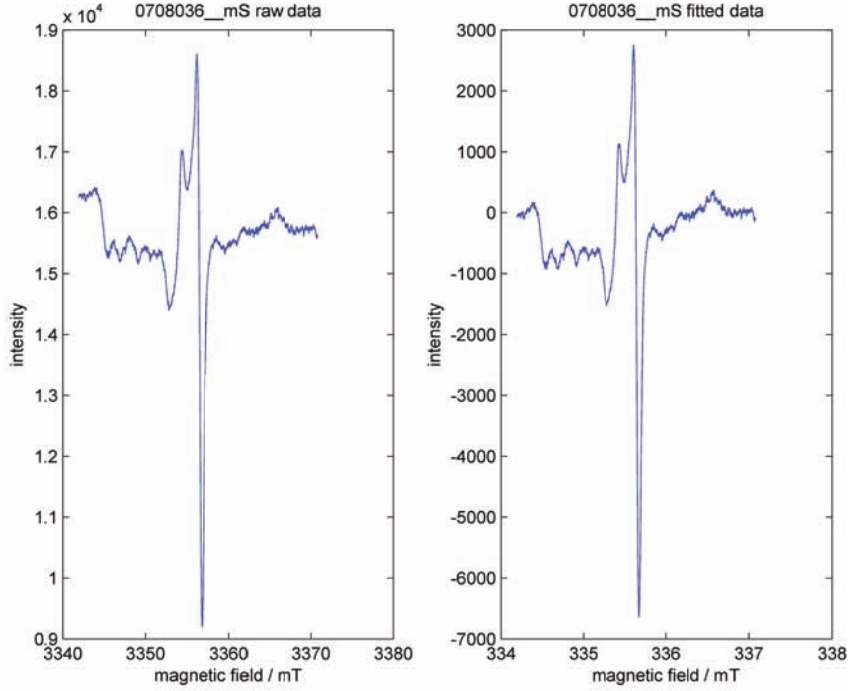
x 10^4
0708036__mS raw data
intensity
magnetic field / mT
0708036__mS fitted data
intensity
magnetic field / mT

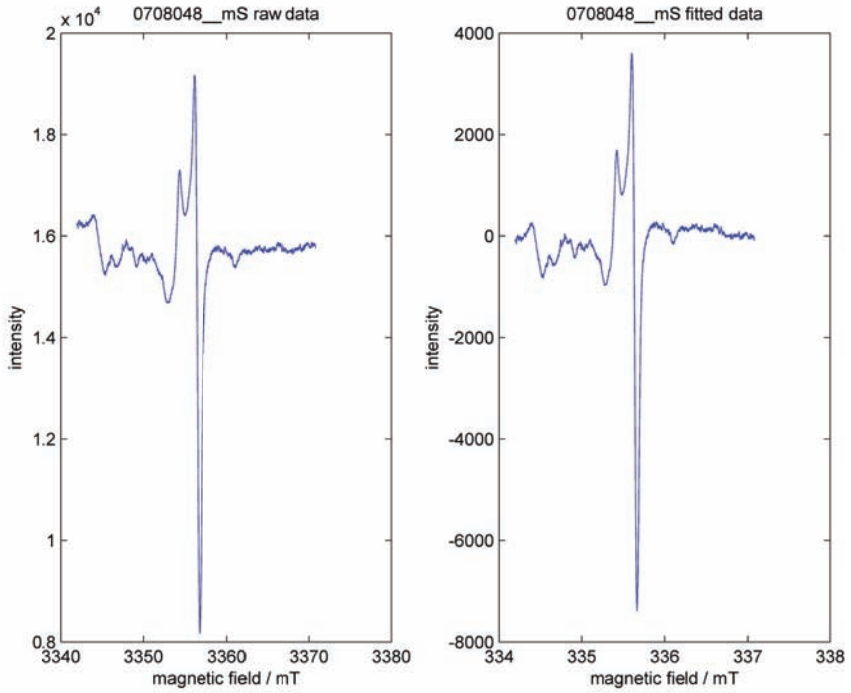
x 10^4
0708048__mS raw data
intensity
magnetic field / mT
0708048__mS fitted data
intensity
magnetic field / mT

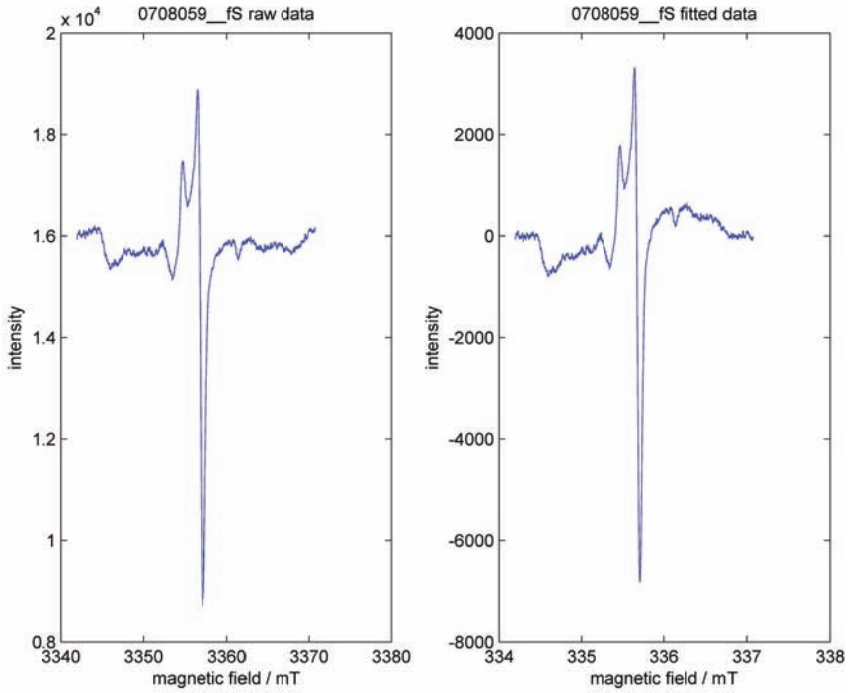
x 10^4
0708059__fS raw data
intensity
magnetic field / mT
0708059__fS fitted data
intensity
magnetic field / mT

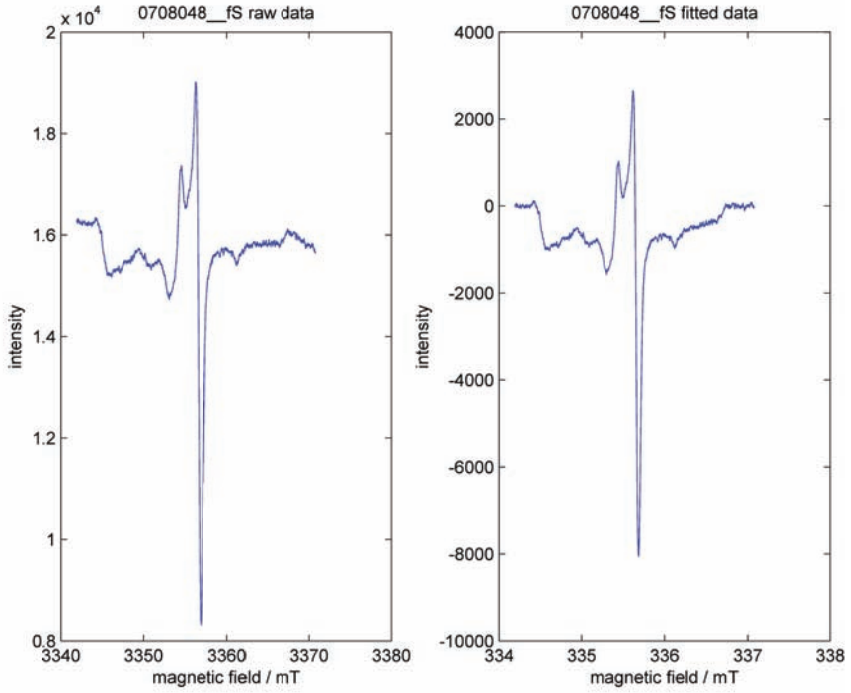
x 10^4
0708048__fS raw data
intensity
magnetic field / mT
0708048__fS fitted data
intensity
magnetic field / mT

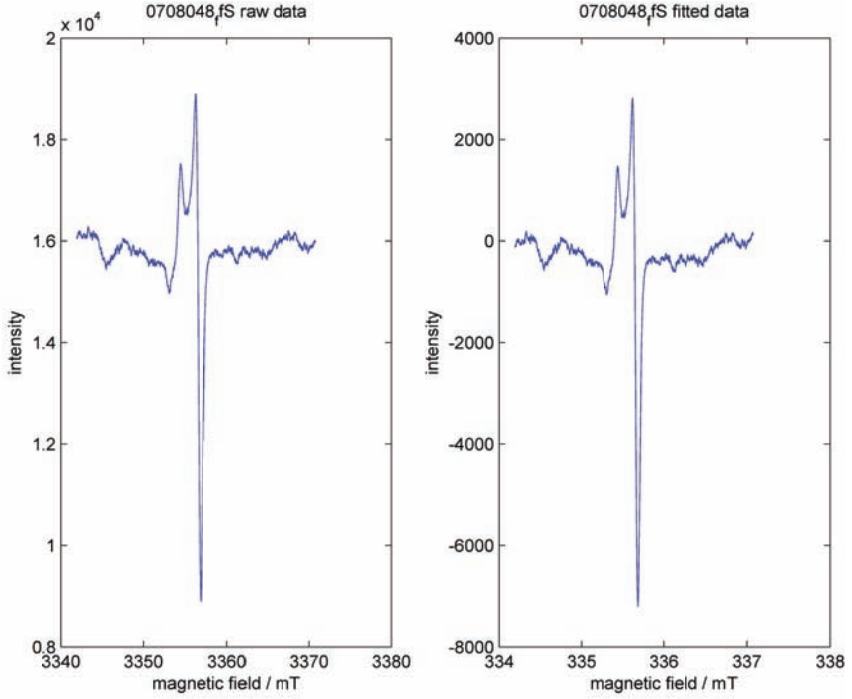
x 10^4
0708048_fS raw data
intensity
magnetic field / mT
0708048_fS fitted data
intensity
magnetic field / mT

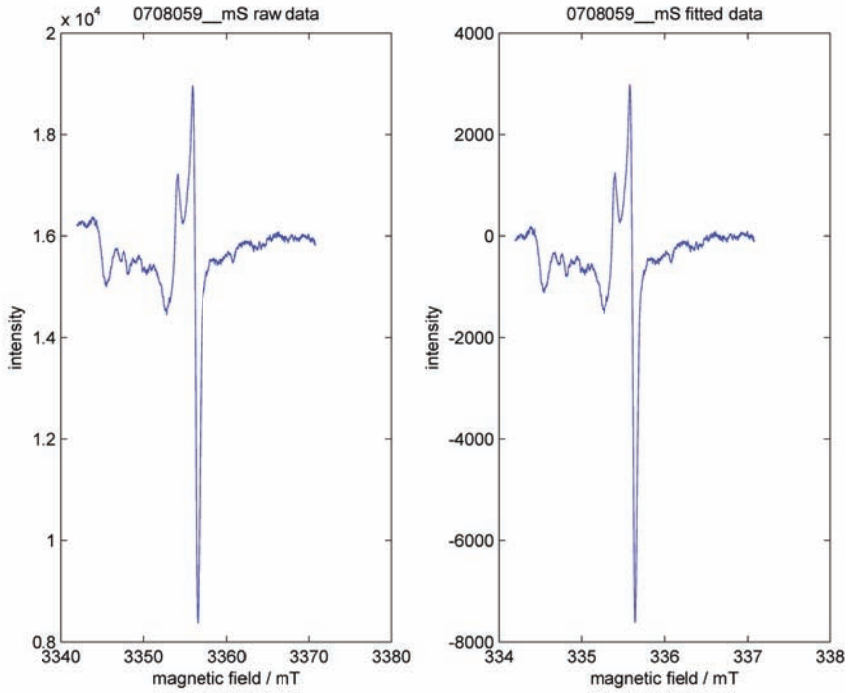
x 10^4
0708059__mS raw data
intensity
magnetic field / mT
0708059__mS fitted data
intensity
magnetic field / mT

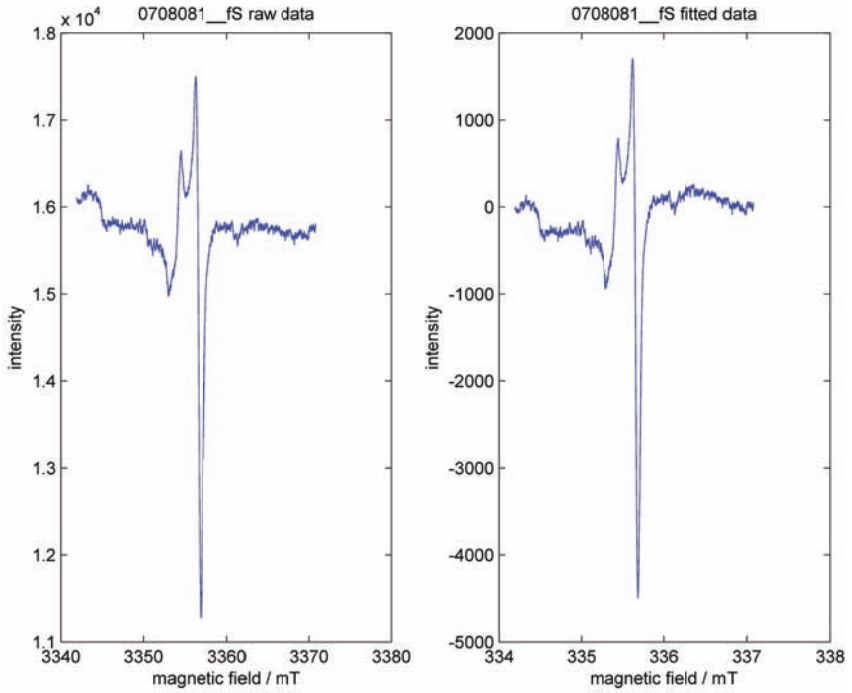
x 10^4
0708081__fS raw data
intensity
magnetic field / mT
0708081__fS fitted data
intensity
magnetic field / mT

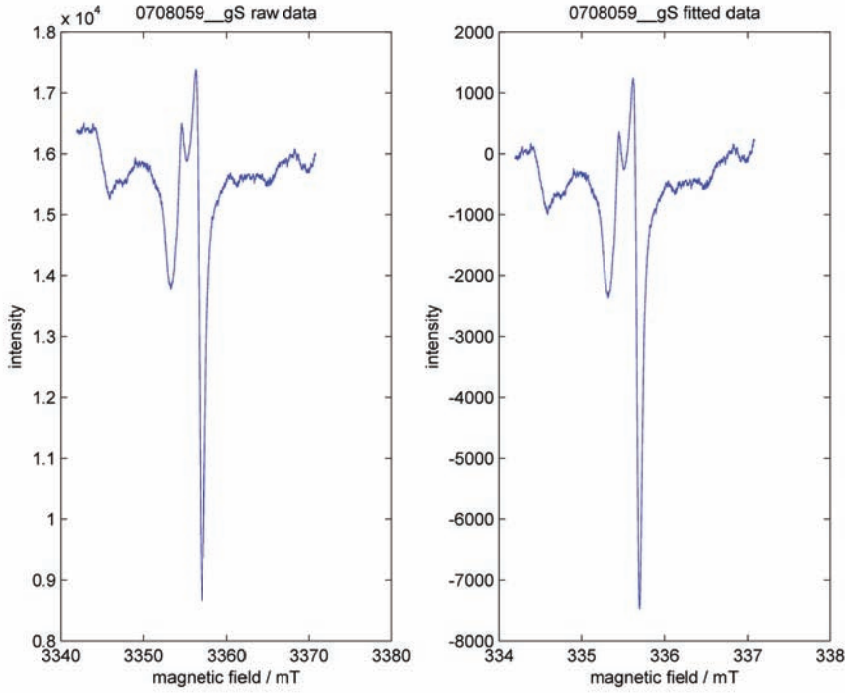
x 10^4
0708059__gS raw data
intensity
magnetic field / mT
0708059__gS fitted data
intensity
magnetic field / mT

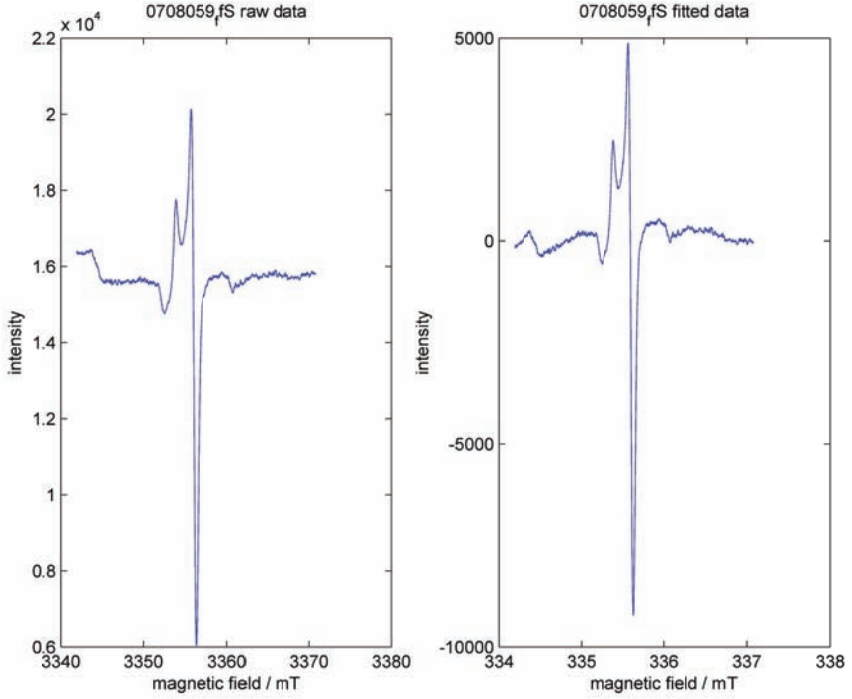
x 10^4
0708059_fS raw data
intensity
magnetic field / mT
0708059_fS fitted data
intensity
magnetic field / mT

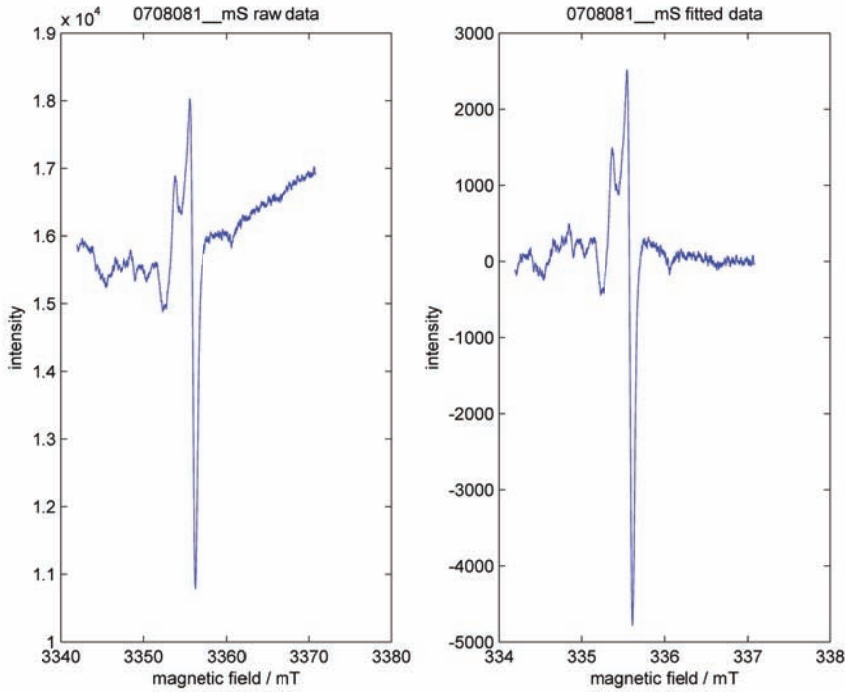
x 10^4
0708081__mS raw data
intensity
magnetic field / mT
0708081__mS fitted data
intensity
magnetic field / mT

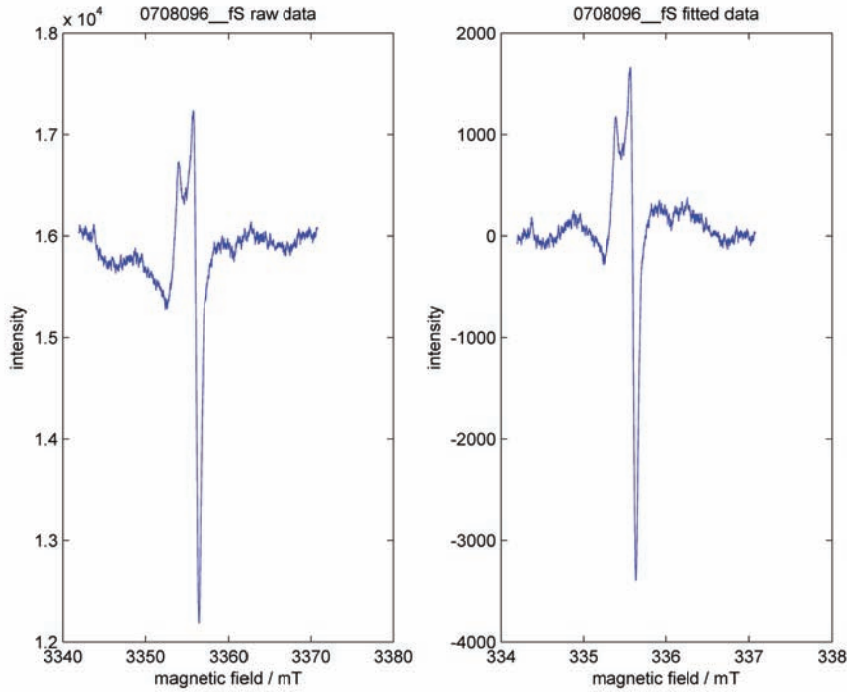
x 10^4
0708096__fS raw data
intensity
magnetic field / mT
0708096__fS fitted data
intensity
magnetic field / mT

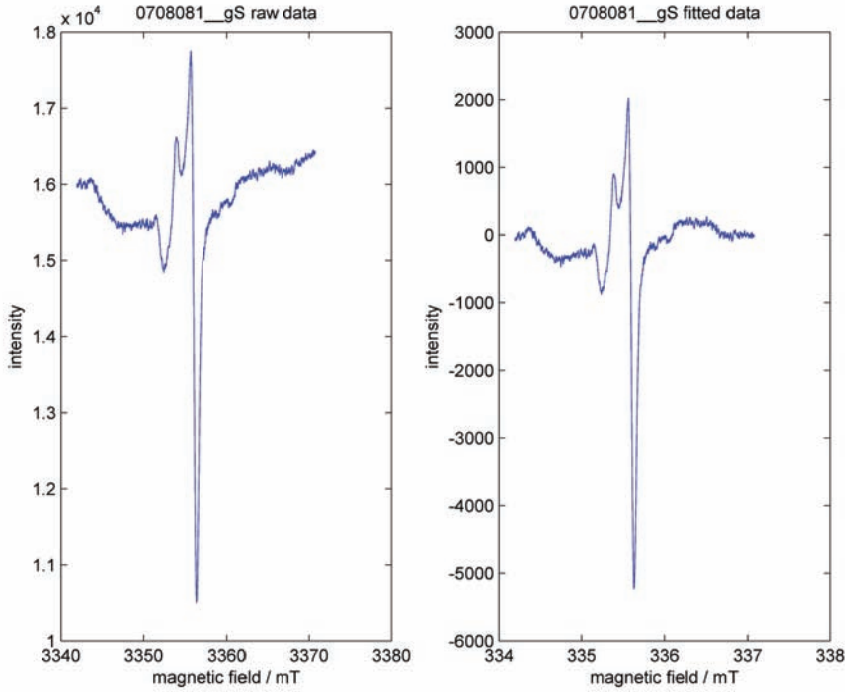
x 10^4
0708081__gS raw data
intensity
magnetic field / mT
0708081__gS fitted data
intensity
magnetic field / mT

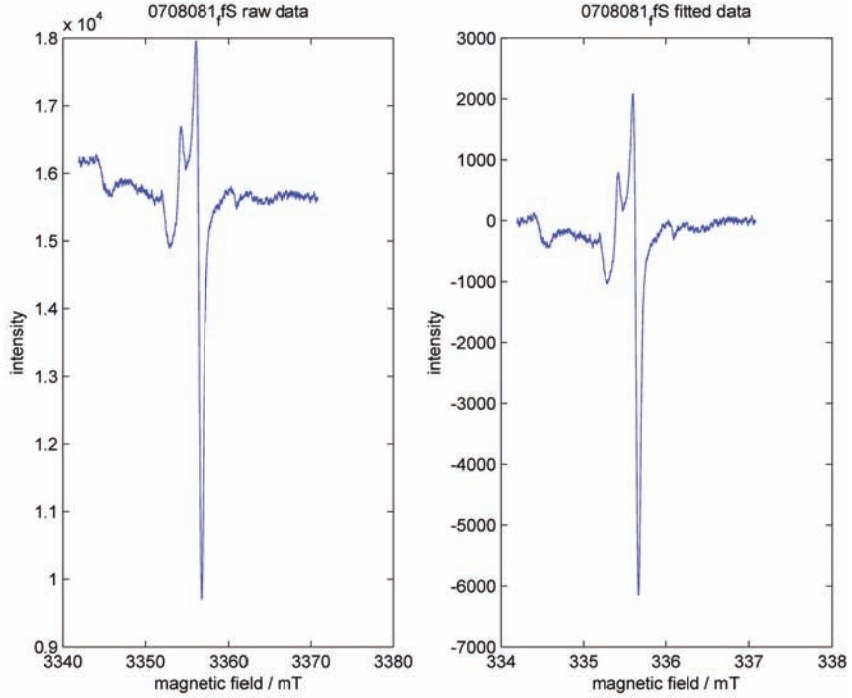
x 10^4
0708081_fS raw data
intensity
magnetic field / mT
0708081_fS fitted data
intensity
magnetic field / mT

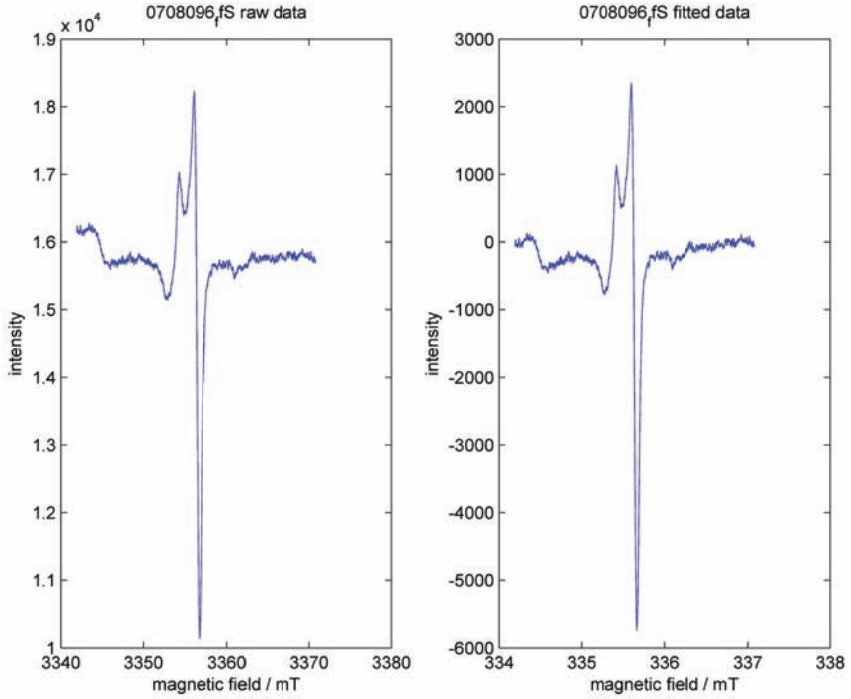
0708096_fS raw data
x 10^4
intensity
magnetic field / mT
0708096_fS fitted data
intensity
magnetic field / mT

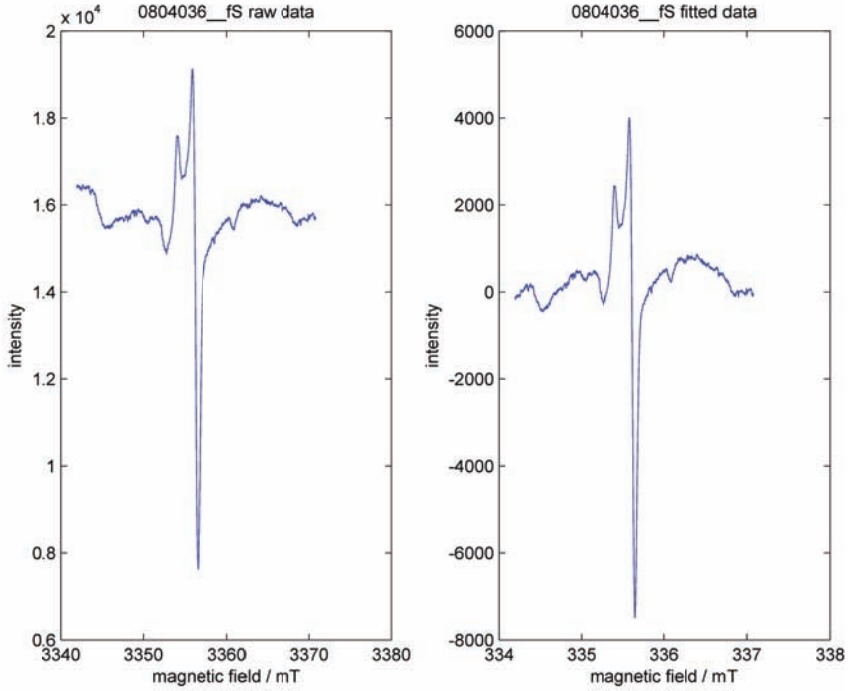
0804036__fS raw data
x 10^4
intensity
magnetic field / mT
0804036__fS fitted data
intensity
magnetic field / mT

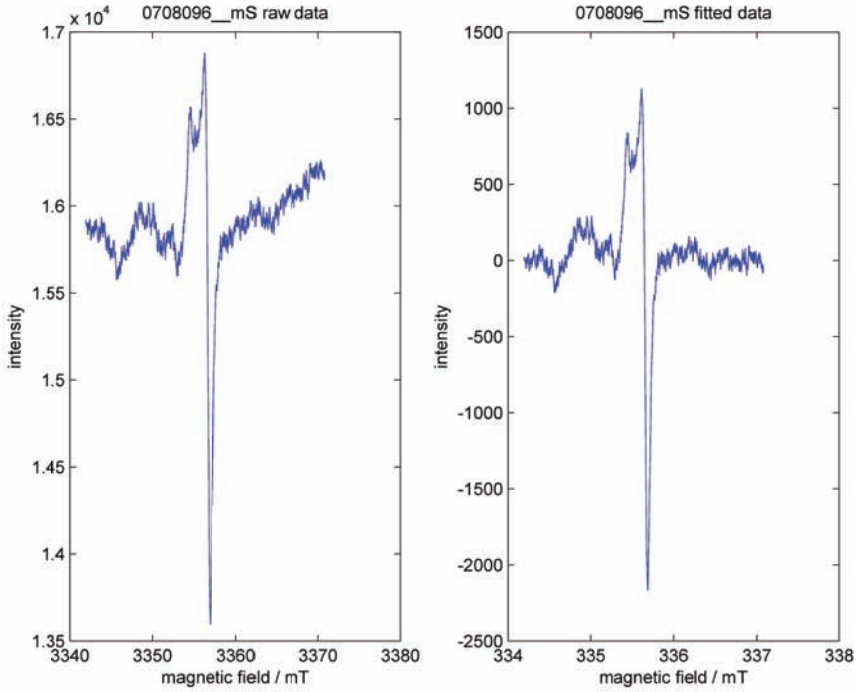
0708096__mS raw data
x 10^4
intensity
magnetic field / mT
0708096__mS fitted data
intensity
magnetic field / mT

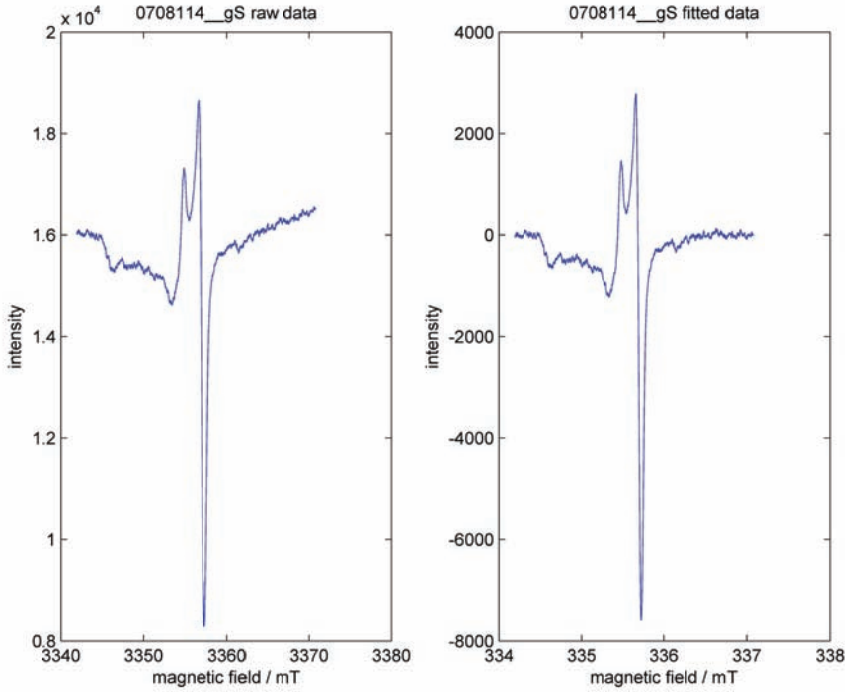
0708114__gS raw data
x 10^4
intensity
magnetic field / mT
0708114__gS fitted data
intensity
magnetic field / mT

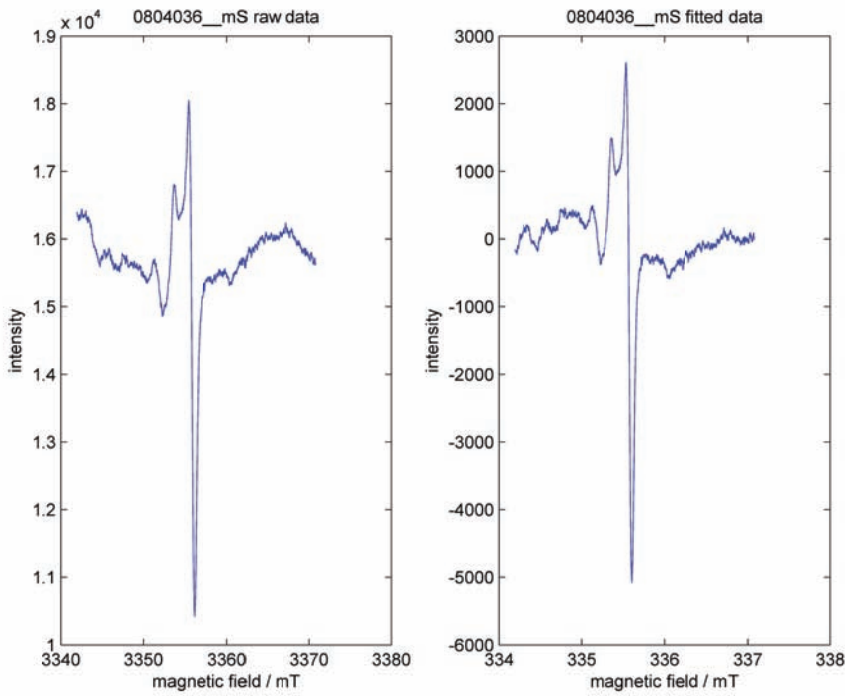
0804036__mS raw data
x 10^4
intensity
magnetic field / mT

0804036__mS fitted data
intensity
magnetic field / mT

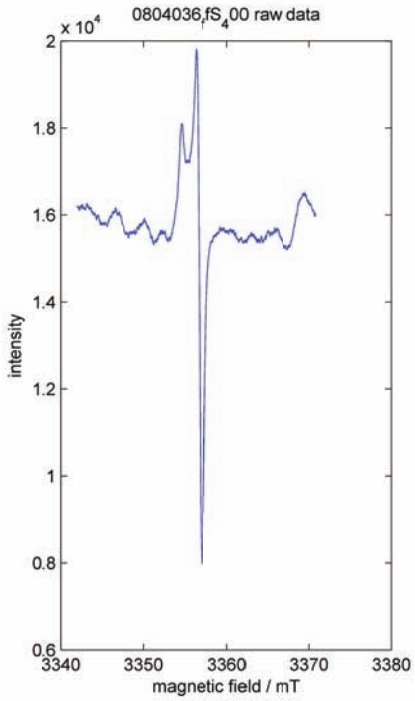
0804036_fS_400 raw data
x 10^4
intensity
magnetic field / mT

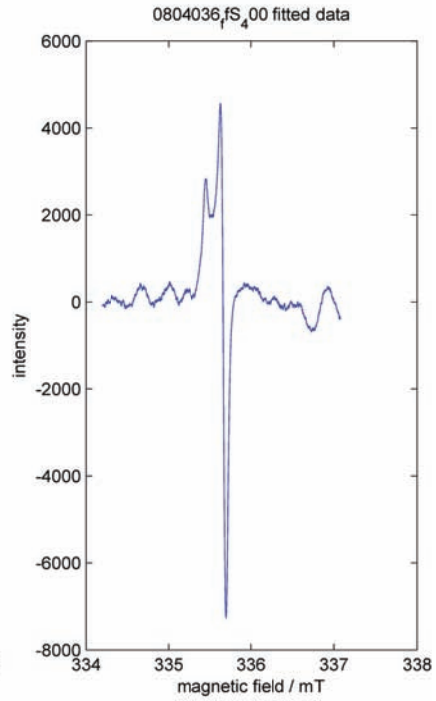
0804036_fS_400 fitted data
intensity
magnetic field / mT

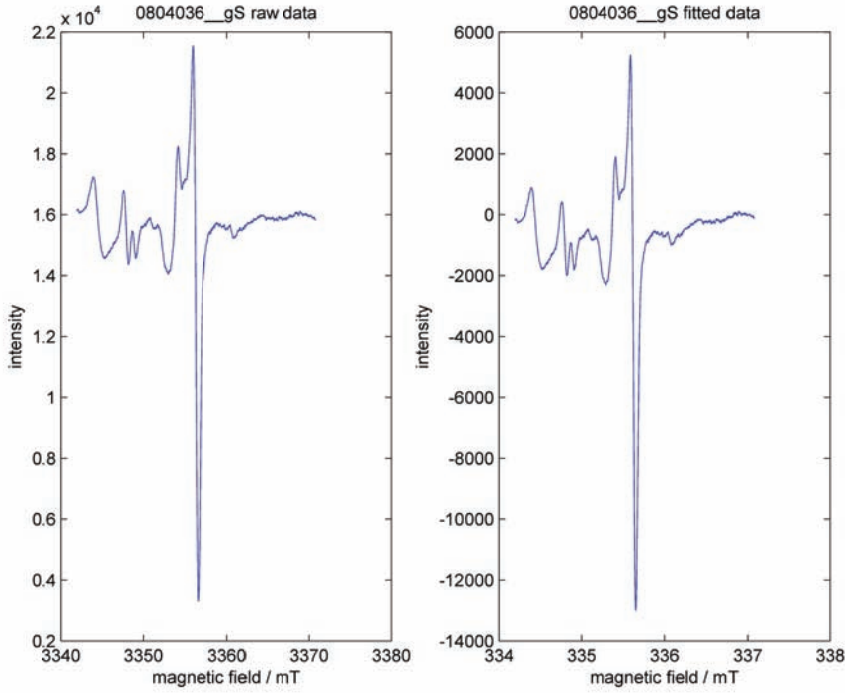
0804036__gS raw data
x 10^4
intensity
magnetic field / mT

0804036__gS fitted data
intensity
magnetic field / mT

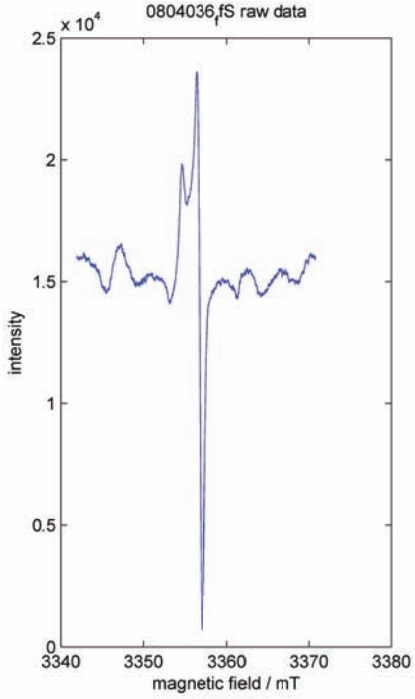
0804036_fS raw data
x 10^4
intensity
magnetic field / mT

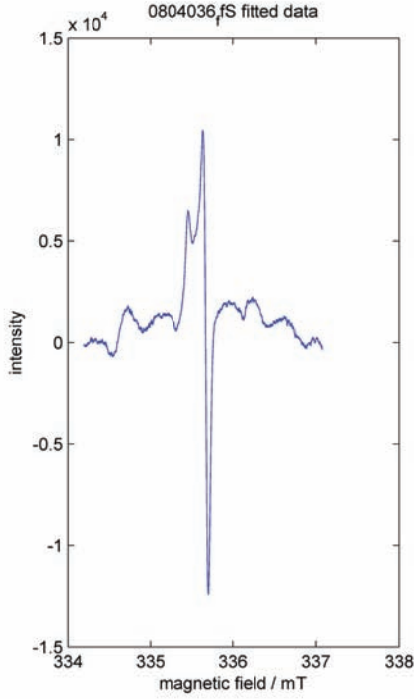
0804036_fS fitted data
x 10^4
intensity
magnetic field / mT

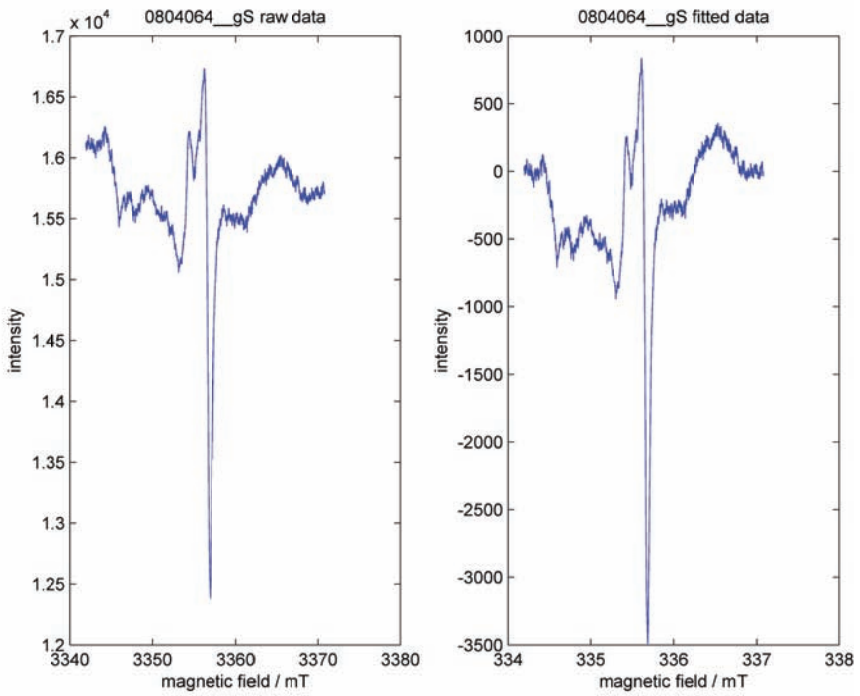
x 10^4
0804064__gS raw data
intensity
magnetic field / mT
0804064__gS fitted data
intensity
magnetic field / mT

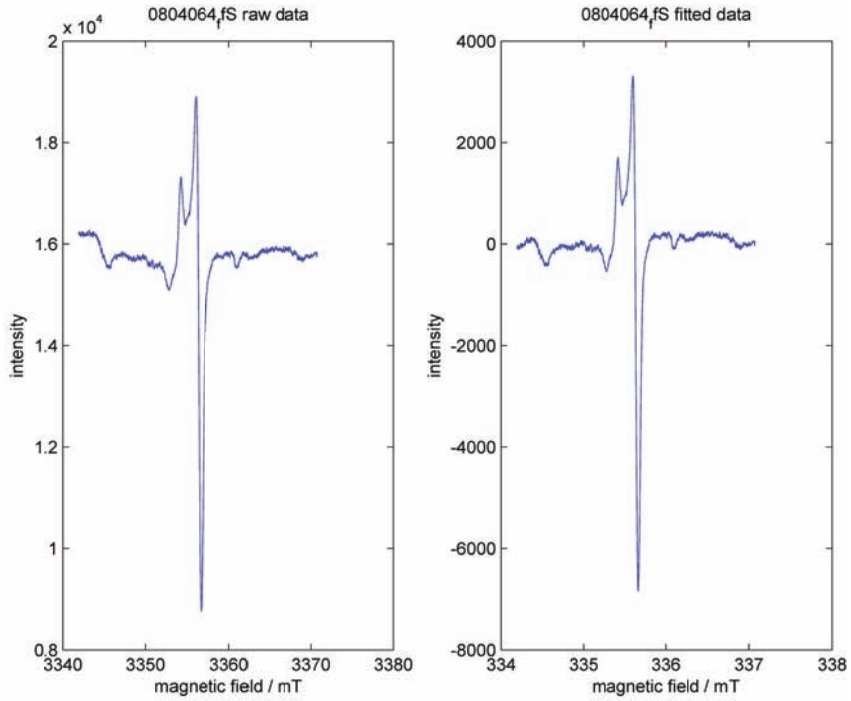
x 10^4
0804064_fS raw data
intensity
magnetic field / mT
0804064_fS fitted data
intensity
magnetic field / mT

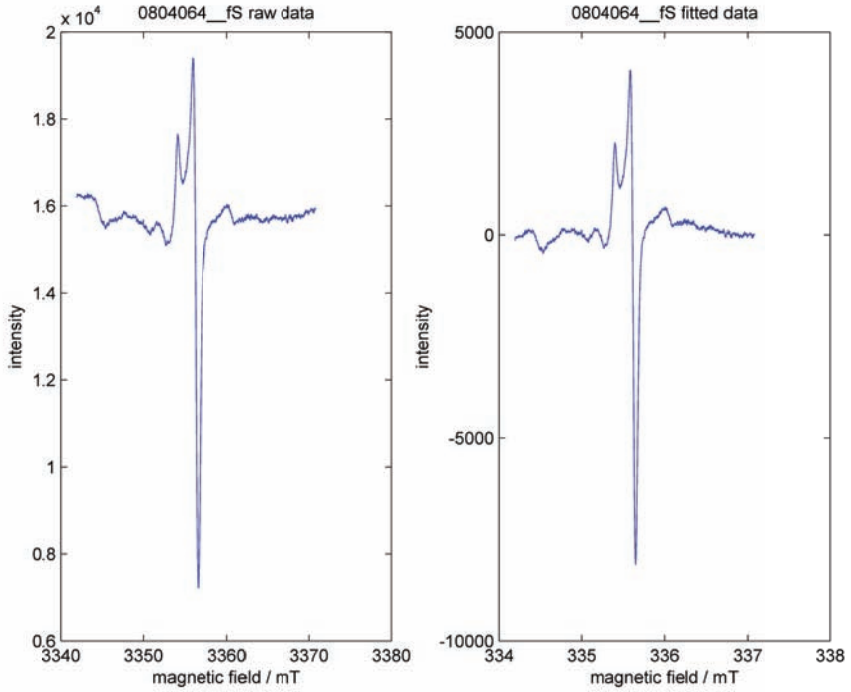
x 10^4
0804064__fS raw data
intensity
magnetic field / mT
0804064__fS fitted data
intensity
magnetic field / mT

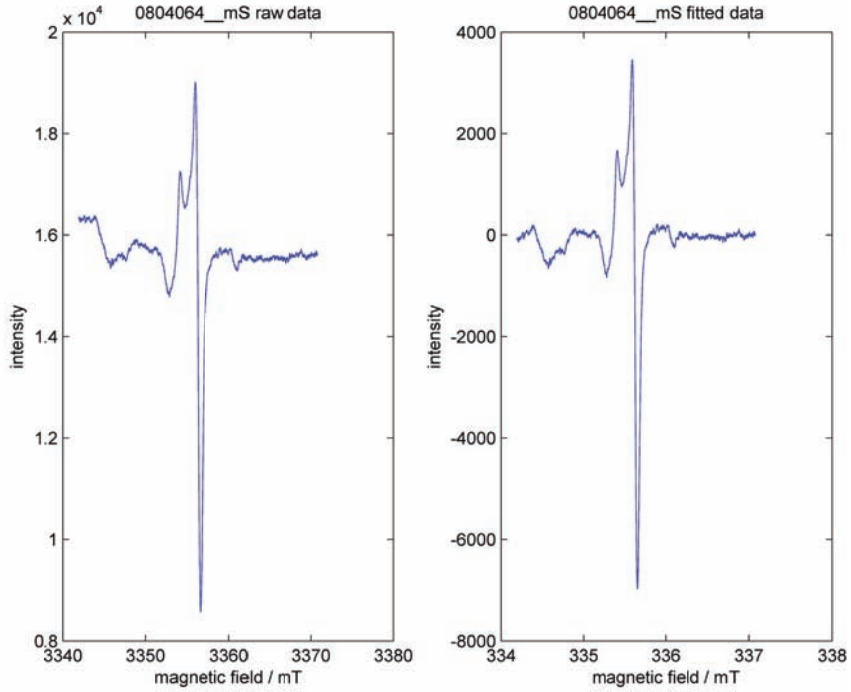
x 10^4
0804064__mS raw data
intensity
magnetic field / mT
0804064__mS fitted data
intensity
magnetic field / mT

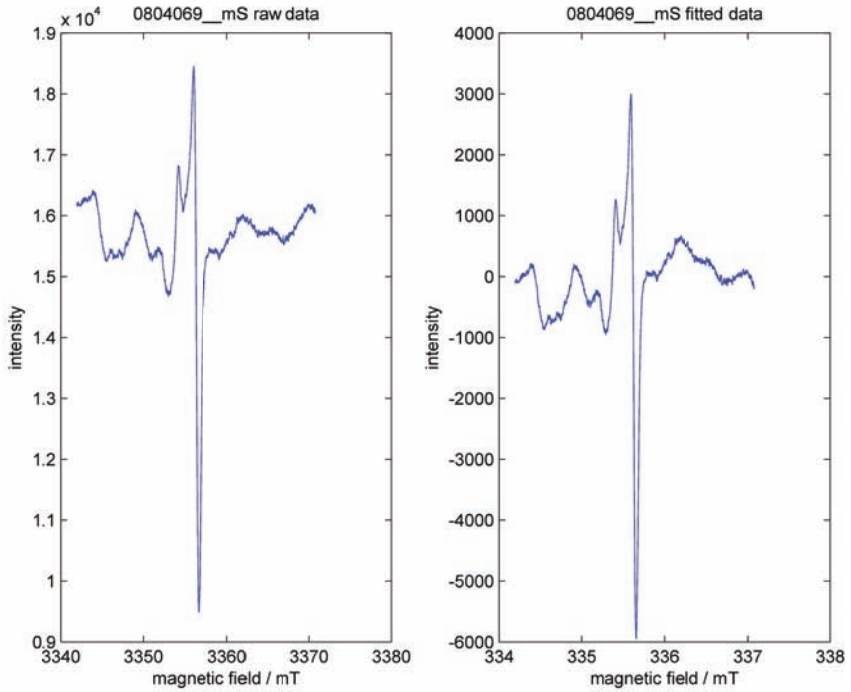
x 10^4
0804069__mS raw data
intensity
magnetic field / mT
0804069__mS fitted data
intensity
magnetic field / mT

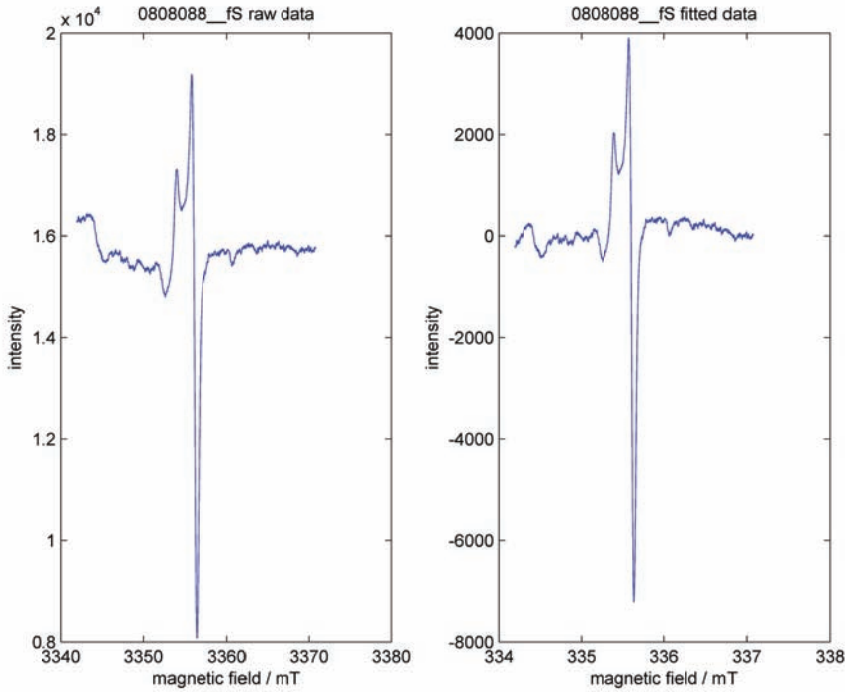
x 10^4
0808088__fS raw data
intensity
magnetic field / mT
0808088__fS fitted data
intensity
magnetic field / mT

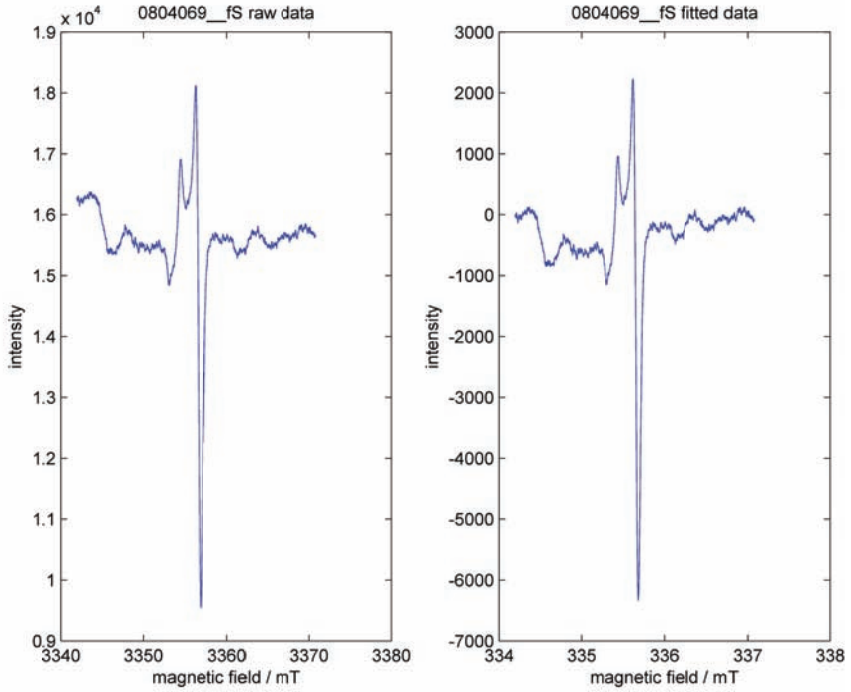
x 10^4
0804069__fS raw data
intensity
magnetic field / mT
0804069__fS fitted data
intensity
magnetic field / mT

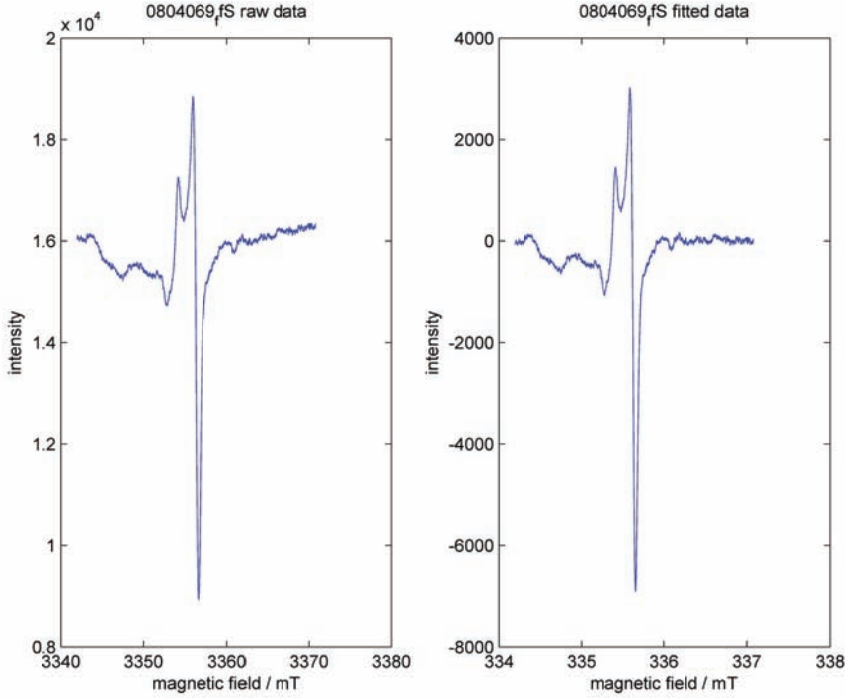
x 10^4
0804069_fS raw data
intensity
magnetic field / mT
0804069_fS fitted data
intensity
magnetic field / mT

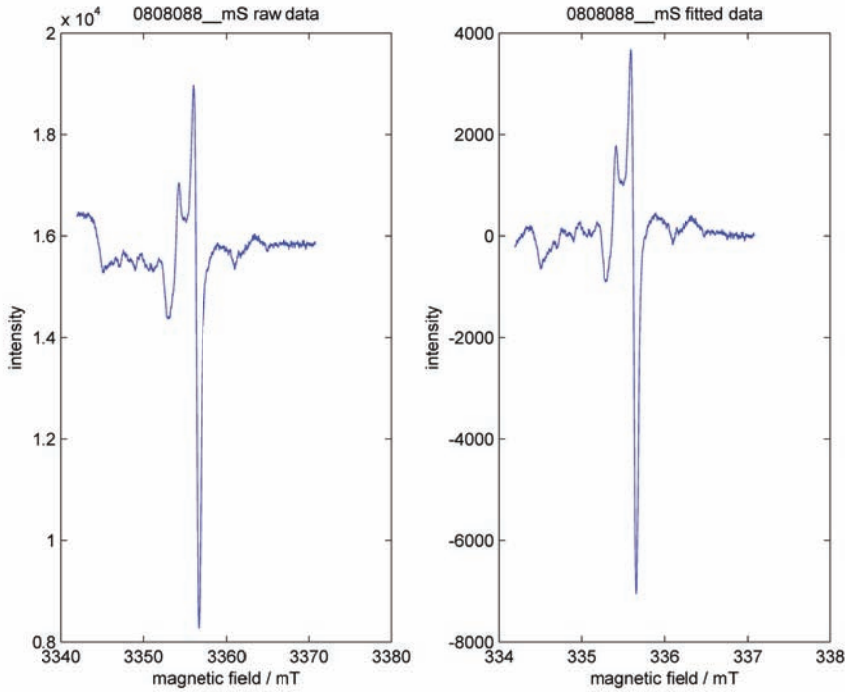
x 10^4
0808088__mS raw data
intensity
magnetic field / mT
0808088__mS fitted data
intensity
magnetic field / mT

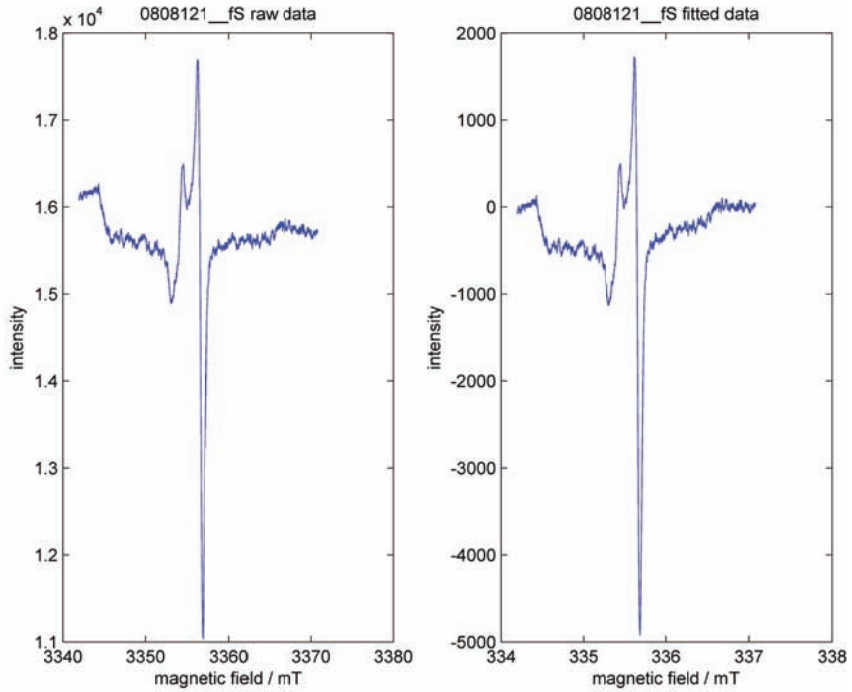
x 10^4
0808121__fS raw data
intensity
magnetic field / mT
0808121__fS fitted data
intensity
magnetic field / mT

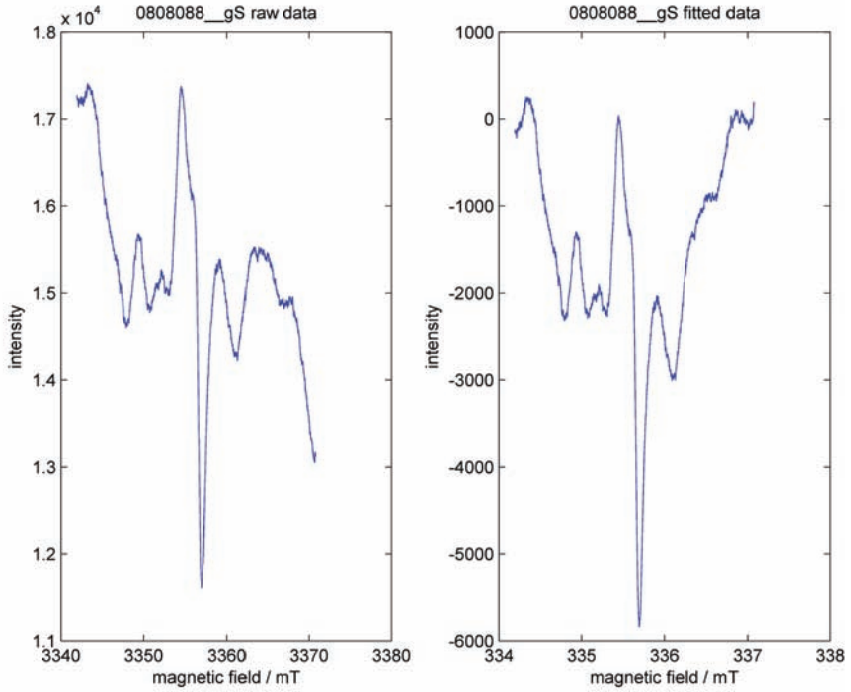
x 10^4
0808088__gS raw data
intensity
magnetic field / mT
0808088__gS fitted data
intensity
magnetic field / mT

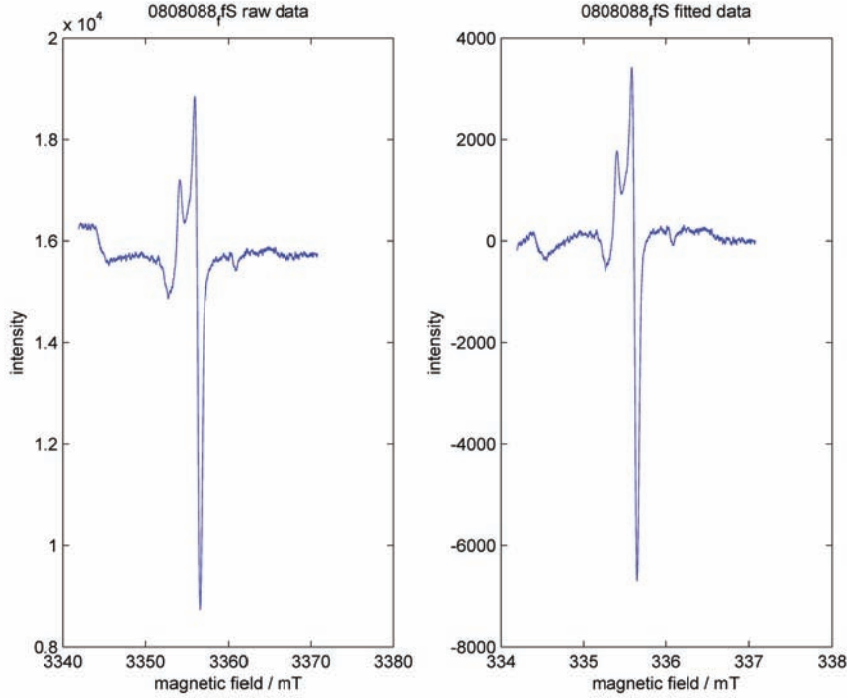
x 10^4
0808088_fS raw data
intensity
magnetic field / mT
0808088_fS fitted data
intensity
magnetic field / mT

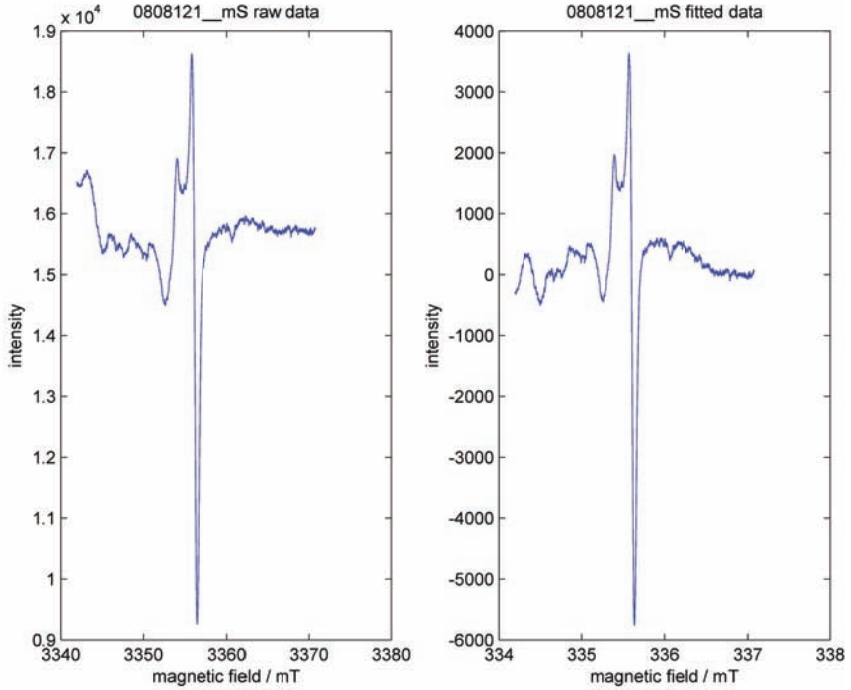
x 10^4
0808121__mS raw data
intensity
magnetic field / mT
0808121__mS fitted data
intensity
magnetic field / mT

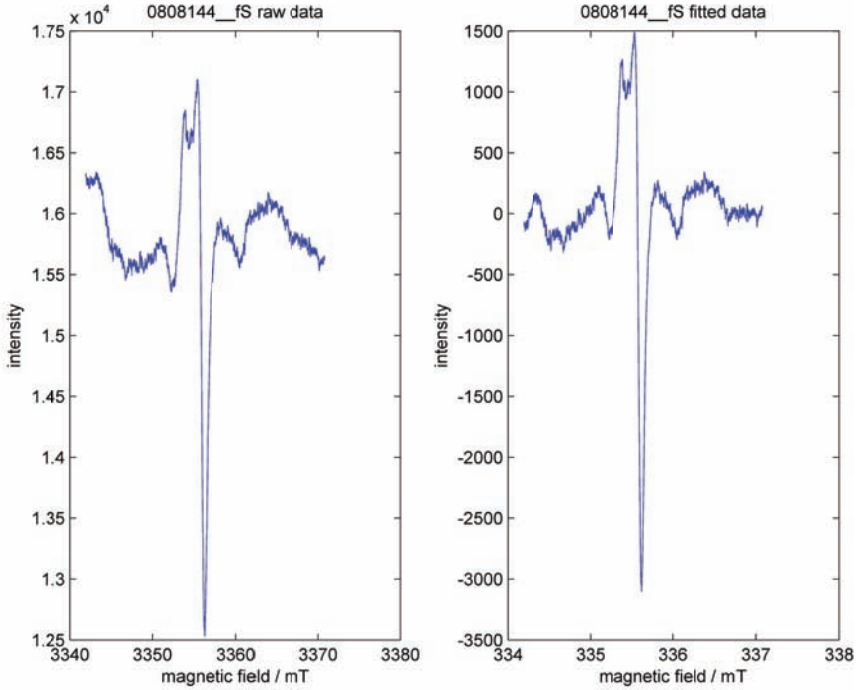
x 10^4
0808144__fS raw data
intensity
magnetic field / mT
0808144__fS fitted data
intensity
magnetic field / mT

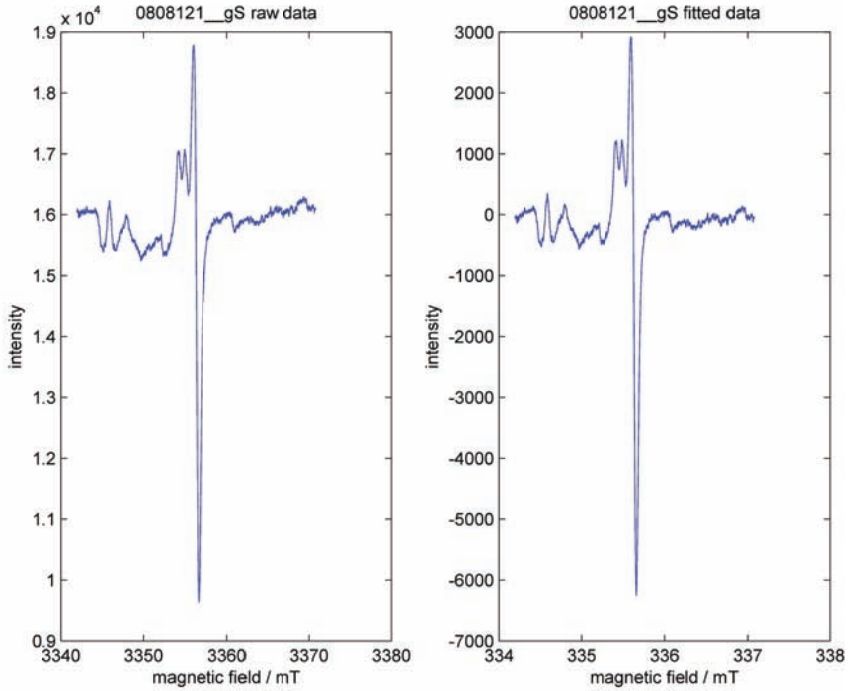
x 10^4
0808121__gS raw data
intensity
magnetic field / mT
0808121__gS fitted data
intensity
magnetic field / mT

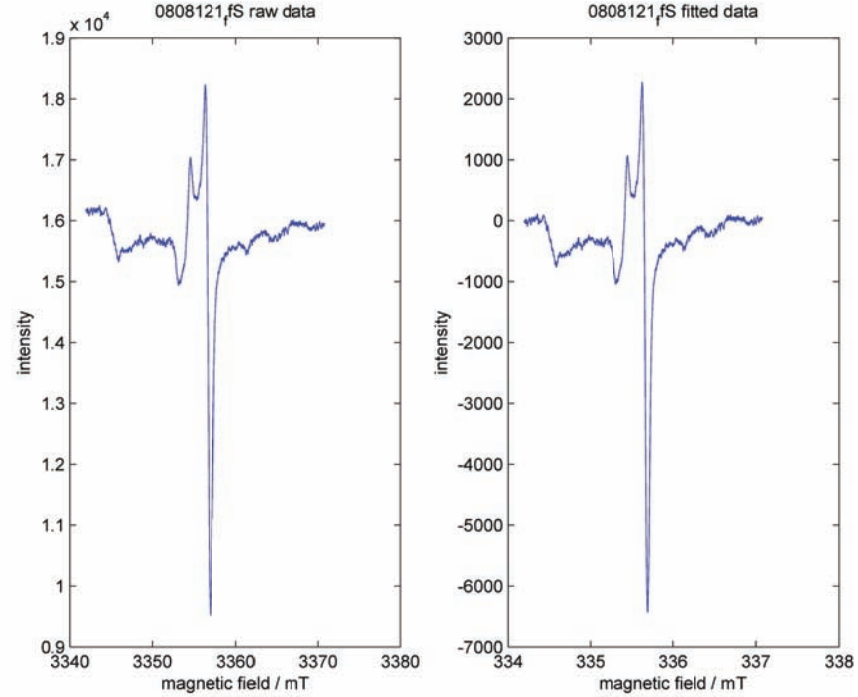
x 10^4
0808121_fS raw data
intensity
magnetic field / mT
0808121_fS fitted data
intensity
magnetic field / mT

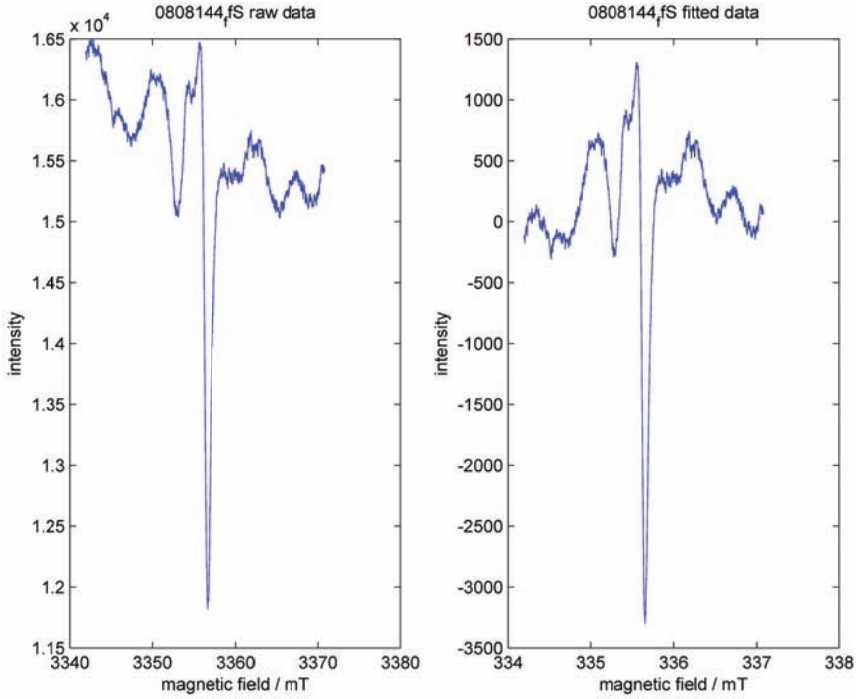
0808144_fS raw data
x 10^4
intensity
magnetic field / mT
0808144_fS fitted data
intensity
magnetic field / mT

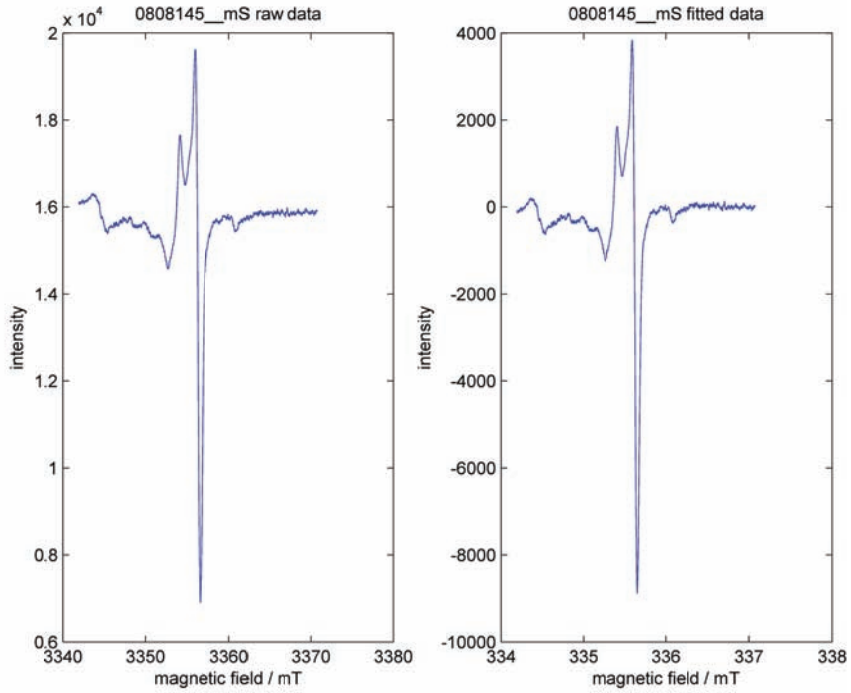
0808145__mS raw data
x 10^4
intensity
magnetic field / mT
0808145__mS fitted data
intensity
magnetic field / mT

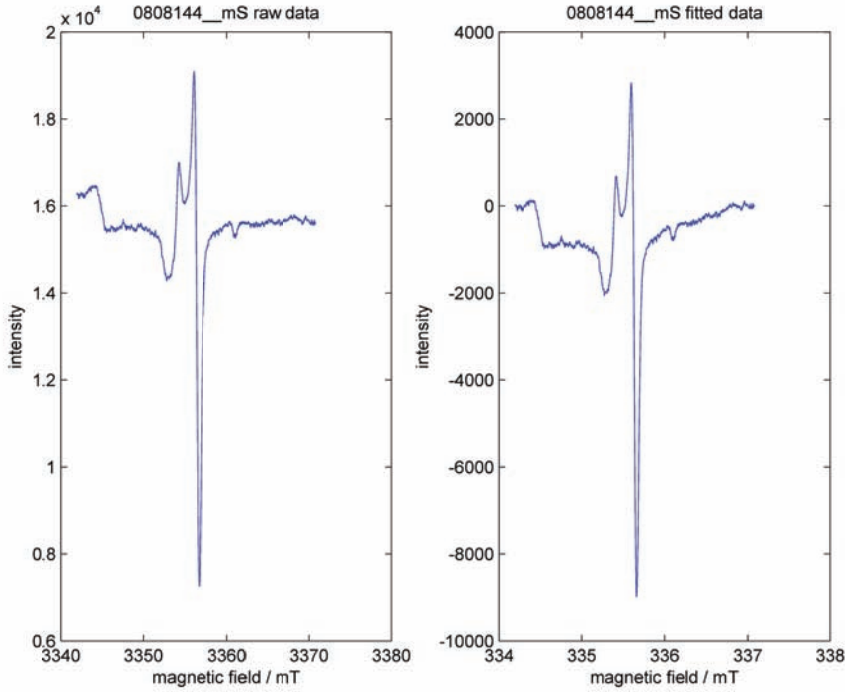
0808144__mS raw data
x 10^4
intensity
magnetic field / mT
0808144__mS fitted data
intensity
magnetic field / mT

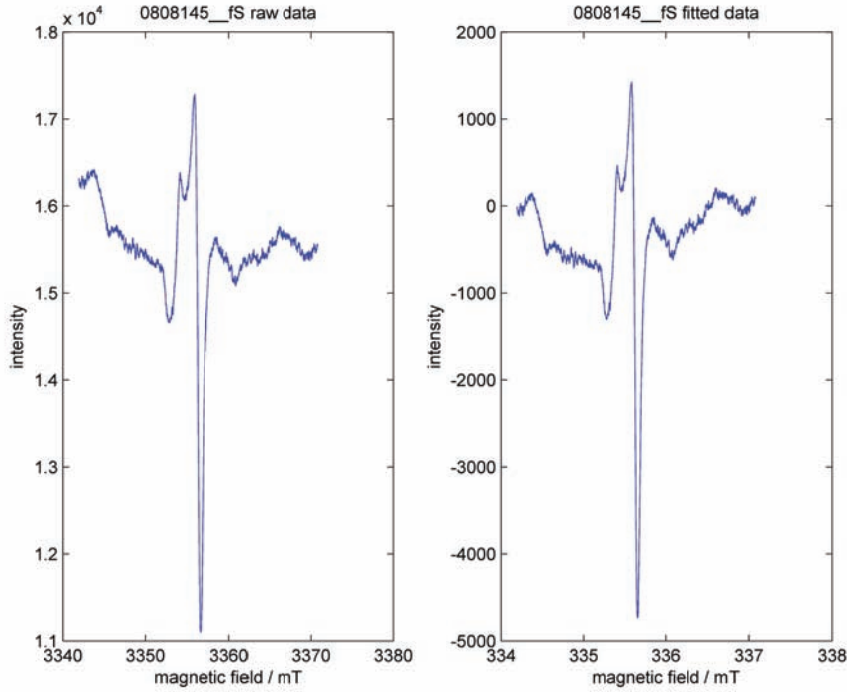
0808145__fS raw data
x 10^4
intensity
magnetic field / mT
0808145__fS fitted data
intensity
magnetic field / mT

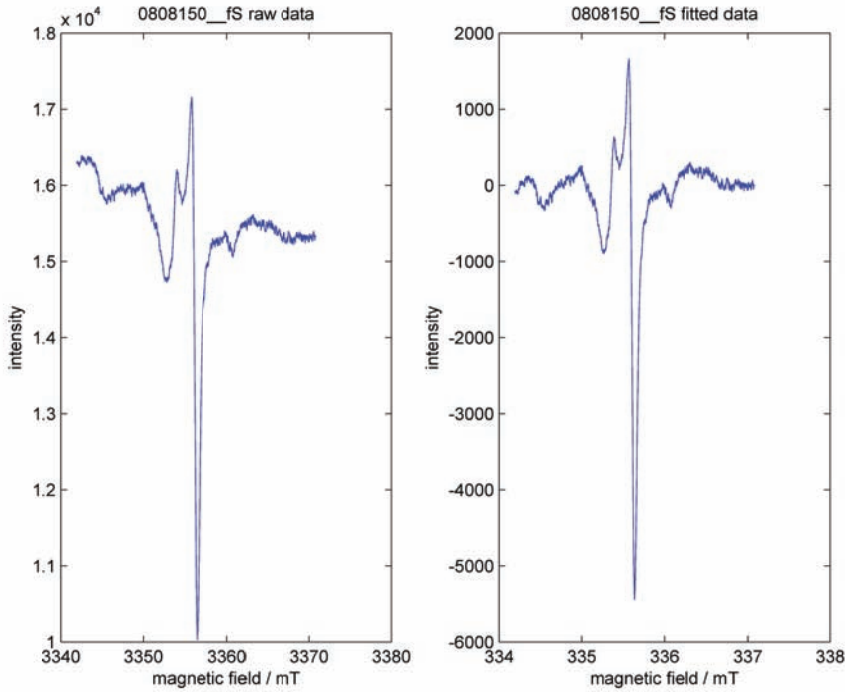
0808150__fS raw data
x 10^4
intensity
magnetic field / mT
0808150__fS fitted data
intensity
magnetic field / mT

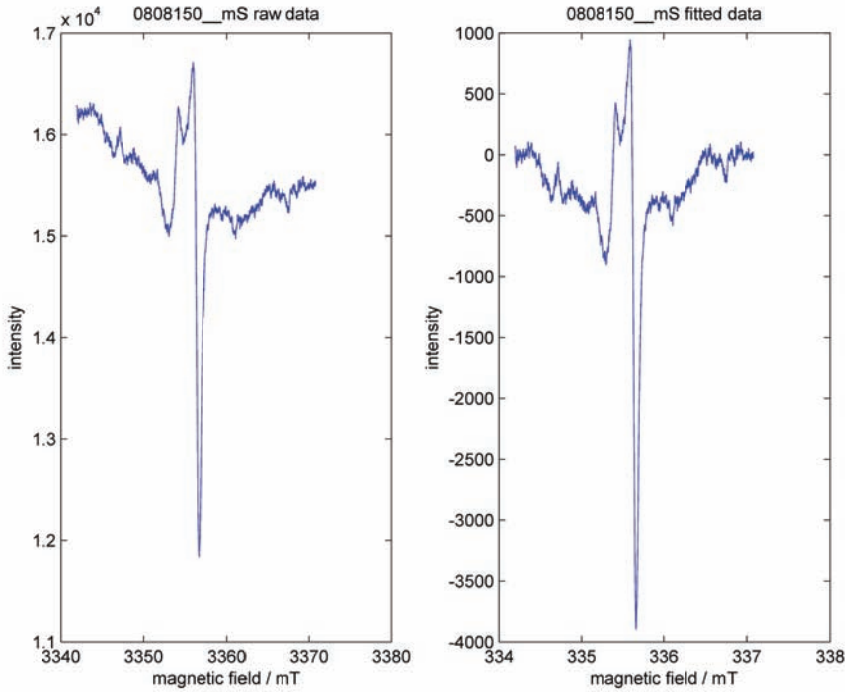
0808150__mS raw data
x 10^4
intensity
magnetic field / mT
0808150__mS fitted data
intensity
magnetic field / mT

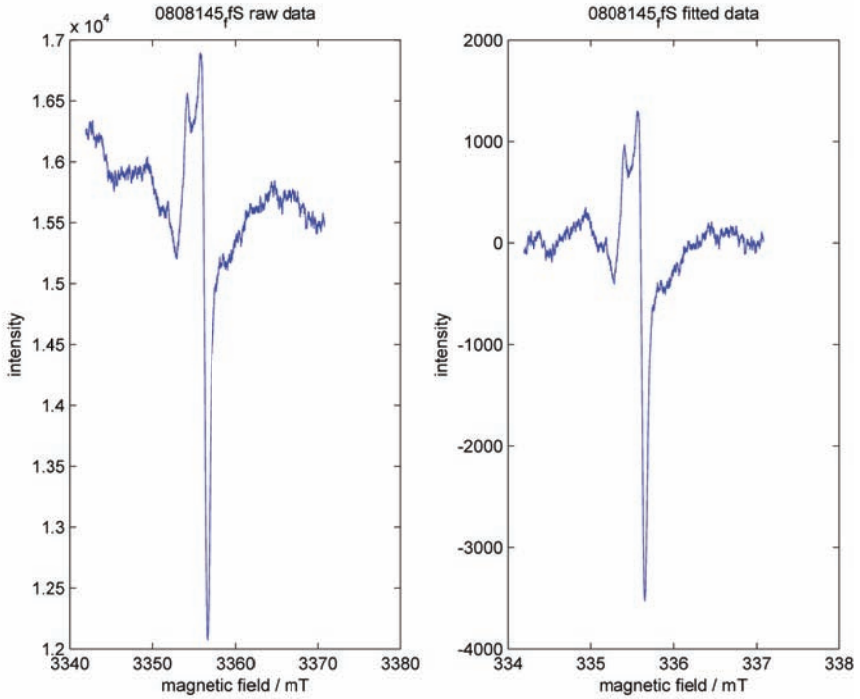
0808145_fS raw data
x 10^4
intensity
magnetic field / mT
0808145_fS fitted data
intensity
magnetic field / mT

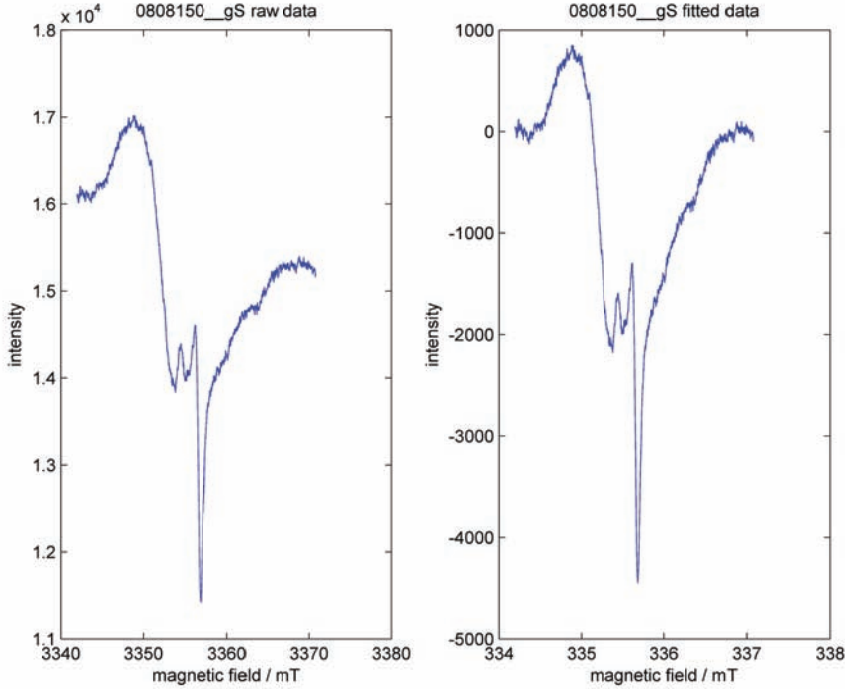
0808150__gS raw data
x 10^4
intensity
magnetic field / mT
0808150__gS fitted data
intensity
magnetic field / mT

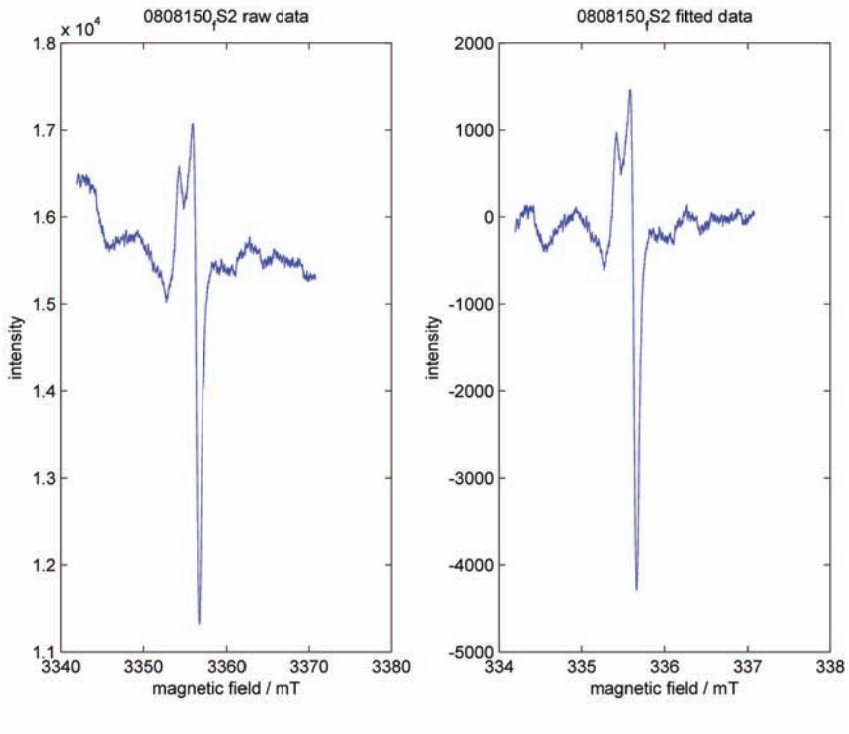
0808150_fS2 raw data
x 10^4
1.8
1.7
1.6
1.5
1.4
1.3
1.2
1.1
intensity
3340
3350
3360
3370
3380
magnetic field / mT
0808150_fS2 fitted data
2000
1000
0
-1000
-2000
-3000
-4000
-5000
intensity
334
335
336
337
338
magnetic field / mT

B. Curriculum Vitae

The Curriculum Vitae is not published in the online version.

C. Publications

Papers

Hülle, D., A. Hilgers, U. Radtke, C. Stolz, **Hempelmann, N.**, J. Grunert, T. Felauer, and F. Lehmkuhl (2009), OSL dating of sediments from the Gobi desert, Southern Mongolia, Quaternary Geochronology, 5 (2–3), 107–113.

Grunert, J. , C. Stolz, **N. Hempelmann**, A. Hilgers, D. Hülle, F. Lehmkuhl, T. Felauer, D. Dasch (2009): The evolution of small lake basins in the Gobi desert in Mongolia. In: Quaternary Sciences, Vol. 29, No. 4, 677–686

Oral presentations

N. Hempelmann (2009): Ongoing aeolian geomorphodynamics in endorheic basins of the mongolian Gobi desert, Methods and Results. Forschungskolloquium Physische Geographie Universität Trier.

N. Hempelmann, A.Hilgers, D. Hinderberger, T. Felauer, J. Grunert (2009): Geochemical properties of surface sediments in the Mongolian Gobi desert. In: Opp, Ch. & Groll, M. (Eds) (2009): Dust & Sand Storms and Desertification. Proceedings oft the Marburg International Dust and Sandstorm Symposium, 29th September–3rd October, Marburg.

Hempelman, N., Felauer, Th., Hülle, D., Hilgers, A., Stolz, Chr., Grunert, F. Meixner, F., Bruse, M. & Lehmkuhl, F.(2009): Aktuelle äolische Geomorphodynamik in abflusslosen Becken der Wüste Gobi, Mongolei. Annual Meeting Arbeitskreis Wüstenränder, Rauischholzhausen.

N. Hempelmann (2008): Ongoing aeolian geomorphodynamics in endorheic basins of the Mongolian Gobi desert. Problems and preliminary results. 3. Meeting of the "Junge Geomorphologen", Herrischried

Posters

Hempelmann, N., F.X. Meixner, M. Bruse, D. Dorjgotov, D. Jugder, T. Felauer, J. Grunert (2009): Modelling of mineral dust distribution on regional scale. In: Opp, Ch. & Groll, M. (Eds) (2009): Dust & Sand Storms and Desertification. Proceedings oft the Marburg International Dust and Sandstorm Symposium, 29th September–3rd October, Marburg.

Hempelmann, N., Meixner, F., Bruse, M., Dorjgotov, D., Grunert, J., Jugder, D., Felauer, T., Lehmkuhl, F.(2009): Aeolian geomorphodynamics in endorheic basins of the Gobi Desert, Mongolia; Regional modelling of sediment transport. In: 7th International Conference on Geomorphology (ANZIAG) 6 – 11

July 2009 Melbourne Convention and Exhibition Centre, Melbourne, Australia. 59

Grunert, J., Stolz, C., **Hempelmann, N.**, Lehmkuhl, F., Felauer, T., Hilgers, A., Hülle, D. (2009): Interaction of aeolian and lacustrine processes in endorheic basins of the Gobi (Mongolia), new results. In: 7th International Conference on Geomorphology (ANZIAG) 6 – 11 July 2009 Melbourne Convention and Exhibition Centre, Melbourne, Australia.

Felauer, T., Lehmkuhl, F., Murad, W., Schlütz, F., Stolz, C., **Hempelmann, N.**, Grunert, J., Hülle, D., Hilgers, A.(2009): Pleistocene to Holocene climate transition reconstructed from the Bayan Tohomiin Nuur core (southern Mongolia). In: 7th International Conference on Geomorphology (ANZIAG) 6 – 11 July 2009 Melbourne Convention and Exhibition Centre, Melbourne, Australia.

M. Allspach, G. Feig, A. Bargsten, **Hempelmann, N.**, K. Emde, J. Grunert, M. O. Andreae, E. Tamirbaeva, and F. X.Meixner (2009): Biogenic Emissions of Nitric Oxide from Continental Steppe and Desert Soils of Mongolia. In: Geophysical Research Abstracts Vol. 12, EGU General Assembly 2009

Hempelmann, N., F.X. Meixner, M. Bruse, D. Dorjgotov, D. Jugder, T. Felauer, J. Grunert, and F. Lehmkuhl (2009): Regional wind field simulation and modelling of sediment distribution as a record of ongoing aeolian geomorphodynamics in endorheic basins of the Gobi desert. In: Geophysical Research Abstracts Vol. 12, EGU General Assembly 2009

Christian Stolz, Daniela Hülle, Jörg Grunert, Alexandra Hilgers, **Nils Hempelmann**, Thomas Felauer & Frank Lehmkul(2009): Paläoseen und Dünen in der Gobi (Mongolei). Annual Meeting Arbeitskreis Wüstenränder, Rauischholzhausen.

Hülle, D., Stolz, C., Felauer, T. **Hempelmann, N.**, Hilgers, A., Grunert, J.; Lehmkuhl, F., Radtke, U.(2008): Reconstruction of aeolian and fluvial interactrion in the Gobi Desert, south Mongolia. International Conference and annual meeting of DGG and GV (Geo 2008 – Resources and Risks in the Earth Systhem)–Aachen.

Hülle, D., Hilgers, A., Radtke, U., Stolz, C., **Hempelmann, N.**, Grunert, J., Felauer, T., Lehmkuhl, F.,(2008): OSL dating of sediments from the Gobi desert, Southern Mongolia. 12th International Conference on Luminescence and Electron Spin Resonance Dating (LED 2008) – Beijing.

N. Hempelmann, J. Grunert, F. Meixner, D. Jugder, D. Hülle, T. Felauer, F. Lehmkuhl(2008): Ongoing aeolian geomorphodynamics in endorheic basins of the Gobi desert, Mongolia. In: Proceedings of the INTERNATIONAL CONFERENCE. Natural Resources and Sustainable Development in Surrounding Regions of the Mongolian Plateau SEPTEMBER 12–16, 2008 ULAANBAATAR, MONGOLIA

Hempelmann, N., Meixner, F., Bruse, M., Dorjgotov, D., Grunert, J., Jugder, D., Felauer, T., Lehmkuhl, F.(2008): Modeling of mineral dust distribution on regional scale Tagungsband der 3. Mitteleuropäischen Geomorphologietagung, Universität Salzburg, 23.–28. September 2008, S. 95, Salzburg.

Felauer, T., Lehmkuhl, F., **Hempelmann, N**., Hülle, D., Hilgers, A., Grunert, J., Radtke, U. Schlütz, F. & H. Rother (2008): Jungpleistozäne und holozäne Dynamik äolischer und fluvialer Sedimente in den Gebirgen und Gebirgsvorländern der mongolischen Gobi. Tagungsband der 3. Mitteleuropäischen Geomorphologietagung, Universität Salzburg, 23.-28. September 2008, S. 95, Salzburg.

Hülle, D., C. Stolz, T. Felauer, **Hempelmann, N.**, A. Hilgers, J. Grunert, F. Lehmkuhl & U. Radtke (2008): Reconstruction of aeolian and fluvial interaction in the Gobi Dessert Southern Mongolia. In: Schriftenreihe der Deutschen Gesellschaft für Geowissenschaften 60:337.

Hempelmann, N.; Opp, Ch.; Vorderbrügge Th. (2005): Entwicklung eines Validierungsverfahrens für eine Methode zur Bestimmung der Verschlämmungsneigung auf Basis der Klassenzeichen der Bodenschätzung. In: Mitteilungen der Deutschen Bodenkundlichen Gesellschaft. Band 107, S 337–338